THE UNIVERSITY *of* EDINBURGH

The growth dynamics of *E. coli* in the presence of cell wall-targeting antibiotics

Rebecca Brouwers

Doctor of Philosophy
The University of Edinburgh
2019

Abstract

This thesis investigates the growth dynamics of *Escherichia coli* bacteria in the presence of cell wall-targeting antibiotics, using experiments and mathematical modelling in order to understand quantitatively how these antibiotics interact with growing bacterial cells. In the experiments *E. coli* were grown in various growth media (which result in different growth rates), with a range of antibiotic concentrations. Measurements of optical density and viable colony counts revealed complex growth medium-dependent inhibition dynamics for the different antibiotics, contrary to the "standard" picture that cell wall-targeting antibiotics are more effective against fast growing bacteria. Complementary microscopy analysis suggested a strong correlation between the antibiotic mechanism of action and changes in cell morphology, and consequently the population's inhibition dynamics.

To link the mechanism of antibiotic action to bacterial population dynamics, a mathematical model is presented, guided by the experiments. The model is able to reproduce the inhibition dynamics and morphological changes observed in the presence of mecillinam and aztreonam. The model's robustness and generality is tested by applying it to other growth conditions, to other antibiotics such as fosfomycin, and to combinations of antibiotics. The model performs very well, capturing many of the inhibition dynamics and morphology changes as observed experimentally, as well as testing different hypotheses for the mechanism triggering division in *E. coli*.

In summary this thesis presents a unified experimental and theoretical approach to understanding the effects of cell wall-targeting antibiotics on growing bacterial cells.

Lay summary

This thesis investigates how *Escherichia coli* bacteria grow in the presence of antibiotics. The antibiotics studied here target the *E. coli* cell wall, which is a support structure that completely surrounds the bacterial cell. When antibiotics target the cell wall, the support structure becomes compromised leading to changes in the shape of the bacteria, and eventually death of the bacteria. In our experiments we measured the number of viable *E. coli* via colony counts, the total biomass via optical density readings and quantified the changes in *E. coli* cell shape using phase contrast microscopy. We performed these experiments at different antibiotic concentrations and in different growth media (where the nutrient quality was varied, resulting in the bacteria growing at different rates) primarily for two antibiotics: mecillinam and aztreonam. The combination of experiments suggested a strong correlation between the mechanism of antibiotic action, changes in cell shape and the population dynamics.

In order to better understand the interplay between the mechanism of antibiotic action, cell shape changes and the observed population dynamics we developed a mathematical model, guided by our experimental observations. The model was able to reproduce the population dynamics and shape changes observed in the presence of mecillinam and aztreonam, by considering the surface area and volume dynamics of the average *E. coli* cell and simplifying the biochemical processes going on within the bacterium. The model's robustness and generality was tested by applying it to other growth conditions, to other antibiotics and to combinations of antibiotics. The model performs very well, capturing many of the population dynamics and shape changes as observed experimentally, as well as testing different mechanisms for triggering division in *E. coli*.

In summary this thesis presents a unified experimental and theoretical approach to understanding the effects of cell wall-targeting antibiotics on growing bacterial cells.

Declaration

I declare that this thesis was composed by myself, that the work contained herein is my own except where explicitly stated otherwise in the text, and that this work has not been submitted for any other degree or professional qualification except as specified.

(*Rebecca Brouwers, 2019*)

Acknowledgements

My first thanks are extended to my supervisor Professor Rosalind Allen who has been an invaluable source of support, guidance and encouragement throughout my PhD, and my second supervisor Dr Bartek Waclaw who provided experimental guidance and was extremely helpful in analysing the gene sequencing data.

I would like to thank everyone who helped me to get started in the microbiology lab: in particular Dr Angela Dawson who kept me right on all the basics of microbiology, Dr Diarmuid Lloyd who taught me the basics of phase contrast microscopy and image processing and Dr Alys Jepson who taught me how to use the plate reader. I would also like to thank Elizabeth Tatham for her enthusiasm throughout her Senior Honours project and helping us to explore more avenues than time would otherwise have allowed. Further thanks are extended to Dr Meriem El Karoui for giving me time on the MACS set-up, and especially to Sebastían Jaramillo-Riveri for teaching me how to use the MACS set-up and providing continuous assistance. Thank you also to Hugh Vass for performing the Raman spectroscopy. A massive thanks also has to be made to Dr Sharareh Tavaddod who performed the bulk of the phase contrast microscopy and provided steady state cultures for the later stages of the project, without which the main conclusions of this thesis would not have been reached.

A big thank you also to Professor Waldemar Vollmer for our invaluable discussions and for providing a biologist's perspective on our model and experimental results. Also thanks to everyone attending the Population Dynamics group meetings for your insightful questions and feedback.

Thank you to all my friends, in office 2618, in the swing dancing world and from high school, who encouraged me, sympathised when things went wrong and provided random conversations when I needed to think about anything other than my own PhD. I am also extremely grateful for my family who supported me throughout, and particularly for their loving generosity when I finished my funding.

Finally, thanks to Adam for his unwavering faith in my ability, for being a fantastic dance partner and for encouraging me to dance hard and work hard.

This project was supported by an EPSRC grant.

Contents

Abstract i

Lay summary ii

Declaration iii

Acknowledgements iv

Contents v

1 Introduction 1

1.1 The broad context of this work 1

1.1.1 The antibiotic crisis..... 1

1.1.2 Ways to overcome the antibiotic crisis 1

1.2 Key background biology of *E. coli* 2

1.2.1 The *E. coli* cell envelope 2

1.2.1.1 The cell wall synthesis pathway 4

1.2.1.2 The Penicillin Binding Proteins 5

1.2.1.3 The PBPs and growth rate 6

1.2.1.4 Role of hydrolases 7

1.2.2 Typical *E. coli* growth dynamics 8

1.2.3 Mechanisms of division initiation 9
1.2.3.1 Timer hypothesis 10
1.2.3.2 Sizer hypothesis 10
1.2.3.3 Adder hypothesis 10
1.2.3.4 Mixed models 11
1.2.3.5 Precursor hypothesis 12
1.2.4 Proteome-partitioning 12
1.3 Cell wall-targeting antibiotics 13
1.3.1 Prevalence of cell wall-targeting antibiotics 13
1.3.2 Targets in the cell wall synthesis pathway 13
1.3.2.1 Antibiotics that act within the cytoplasm 14
1.3.2.2 Antibiotics that act at the periplasmic face of the cytoplasmic membrane 15
1.3.3 Beta-lactams and growth rate 18
1.3.4 Resistance mechanisms to cell wall-targeting antibiotics 19
1.4 Modelling antibiotic-bacteria interactions 19
2 Experimental Methods 22
2.1 Culturing *E. coli* 22
2.1.1 *E. coli* strains 22
2.1.2 Growth media 22
2.1.3 Preparing bacterial cultures for experimental use: steady state versus non-steady state 23
2.2 Protocols for measuring population dynamics 26
2.2.1 Optical density 26
2.2.1.1 Spectrophotometer 26
2.2.1.2 Plate reader 27

2.2.1.3 Growth rate calculations 28
2.2.2 Colony forming units 29
2.3 Antibiotic preparation 32
2.3.1 Stock solutions 32
2.3.2 MIC measurement 32
2.4 Microscopy 34
2.4.1 Phase contrast 34
2.4.2 MACS 35
2.5 Raman Spectroscopy 37
2.6 Whole genome sequencing 39

3 Initial characterisation of *E. coli* population dynamics in the presence of cell wall-targeting antibiotics 40

3.1 Literature observations of population dynamics with cell wall-targeting antibiotics 40
3.2 Initial growth curves in LB medium 42
3.3 Understanding the bumps 45
3.3.1 Characterising the bumps: Inoculum effect 45
3.3.2 How the bump depends on growth medium 48
3.4 Understanding "regrowth" 52
3.4.1 Re-inoculation experiments 53
3.4.1.1 Whole genome sequencing 55
3.4.2 Antibiotic degradation 56
3.4.2.1 Mecillinam degradation 59
3.4.2.2 Increasing mecillinam stability 59
3.4.2.3 Cefotaxime degradation 62

3.4.2.4 Aztreonam degradation 63

3.5 Summary of our initial series of experiments..... 63

4 Mecillinam: population dynamics and morphology 65

4.1 Introduction 65

4.2 Population dynamics..... 66

4.2.1 Population dynamics observed in the plate reader 67

4.2.2 Population dynamics observed via OD measurements in the shake flask 68

4.2.3 Population dynamics observed via colony forming units in the shake flask 71

4.2.4 Key data from population dynamics observations..... 72

4.3 Dynamical changes in *E. coli* morphology..... 73

4.3.1 Phase contrast microscopy 73

4.3.2 High-throughput MACS microscopy..... 75

4.3.3 Key morphology observations 79

5 Aztreonam: population dynamics and morphology 80

5.1 Introduction 80

5.2 Population dynamics..... 80

5.2.1 Population dynamics observed in the plate reader 81

5.2.2 Population dynamics observed in the shake flask..... 83

5.2.3 Population dynamics observed via colony forming units..... 86

5.2.4 Summary of population dynamics observations..... 87

5.3 Morphology dynamics: phase contrast microscopy 87

5.3.1 Key data from morphology dynamics observations..... 91

6 Mathematical model: development 93

6.1 Introduction 93

6.1.1 Linking cell physiology, cell morphology and population dynamics 93

6.2 The Model 95

6.2.1 Model set-up 95

6.2.1.1 Precursor synthesis 95

6.2.1.2 Precursor incorporation 97

6.2.1.3 Volume and surface area growth 98

6.2.1.4 Lysis rates 99

6.2.2 Division criteria..... 101

6.2.3 Fatness threshold..... 101

6.2.4 Determining the cell length and width..... 102

6.3 Parameterising the model in the absence of antibiotics..... 103

6.3.1 Constraining the parameter space..... 104

6.3.2 Finding the best fit parameters..... 105

6.4 Observations about the model..... 111

7 Mathematical model: fitting the antibiotic parameters 113

7.1 Simulation protocol 114

7.2 Parameter fits for mecillinam 114

7.2.1 Fitting process for mecillinam morphology dynamics..... 115

7.2.2 Sphere and fatness thresholds 117

7.2.3 Best fit morphology dynamics in detail 121

7.2.4 Lysis rates: fitting population dynamics in the presence of mecillinam 121

7.2.4.1 Value of R corresponding to low mecillinam . . . 122

7.3 Parameter fits for aztreonam 123

7.3.1 Best fit morphology dynamics for fast growing bacteria in high aztreonam 124

7.3.2 Fitting the lysis rates for aztreonam-like inhibition 124

7.3.2.1 Value of n_D corresponding to low aztreonam . . . 124

7.4 Discussion 127

8 Mathematical model: results and predictions 130

8.1 Mecillinam 130

8.1.1 Morphology predictions 130

8.1.1.1 Low mecillinam morphology predictions for fast and slow growing bacteria 131

8.1.2 Predicted population dynamics for slow growing cells in the presence of mecillinam 133

8.1.3 Predicting the population dynamics in MOPSgluCAA..... 134

8.2 Aztreonam 135

8.2.1 Morphology tracks 136

8.2.1.1 Improving the aztreonam morphology tracks . . . 136

8.2.2 Population dynamics in the presence of aztreonam 141

8.2.2.1 Without elongation during pole formation 141

8.2.2.2 With elongation during pole formation 141

8.2.3 Further predictions for population dynamics with aztreonam 143

8.2.3.1 MOPSgluCAA 143

8.2.3.2 Growth-medium dependent inhibition 145

8.2.3.3 Long filaments on rich media 146
8.3 The adder division model 147
8.3.1 Mecillinam 147
8.3.2 Aztreonam 150
8.4 Summary 151

9 Expanding the project to more antibiotics 153

9.1 Population dynamics with other cell wall-targeting antimicrobials . . 153
9.1.1 The six antimicrobials on rich media 154
9.1.2 The six antimicrobials on poor media 155
9.1.3 Comparing population dynamics on rich and poor media 156
9.1.4 Conclusions regarding the six antimicrobials 157
9.2 Microscopy with cefotaxime and fosfomycin 158
9.2.1 Cefotaxime 158
9.2.2 Fosfomycin 160
9.3 Modelling fosfomycin morphology dynamics 162

10 Ideas for further work 164

10.1 Short term future work 164
10.2 Long term future work 165
10.2.1 Extending our work with the current antibiotics 165
10.2.2 Antibiotic combinations 165
10.2.2.1 Population dynamics with fosfomycin in conjunction with mecillinam 166
10.2.2.2 Testing the model for fosfomycin and mecillinam synergy 166

10.3 Conclusions 167

10.3.1 Novelty with respect to other models in the literature 169

A Papers in preparation 170

B Early experiments 171

B.1 Population dynamics in 50ml tubes with mecillinam in LB and M9 variants 171

B.2 *E. coli* population dynamics in M9 media variants 171

B.2.1 Fosfomycin Summary 171

B.2.2 Cefotaxime Summary 174

B.2.3 Mecillinam Summary 174

B.3 MOPS variants - supplementary curves 174

B.4 Supplementary curves from the delay-time bioassay 174

B.5 Full data from genome sequencing 180

C Extra MACS data analysis 181

D Supplementary model results 183

E Additional data analysis for the combination of fosfomycin and mecillinam 190

Bibliography 191

Chapter 1

Introduction

1.1 The broad context of this work

1.1.1 The antibiotic crisis

The emergence and spread of antibiotic resistant bacteria is one of the most serious clinical problems currently facing the world's population. By 2050 it has been projected that more people will die from infections caused by antibiotic resistant bacteria than from cancer [13]. From a biological point of view, antibiotic resistance is pervasive and difficult to counteract because it can arise in a variety of different ways. These can include modification of the antibiotic's target, production of enzymes that degrade the antibiotic (beta-lactamases), over-expression of efflux pumps to remove antibiotic from the bacteria and loss of porins which are channels that antibiotics diffuse through to enter the bacterial cell [129].

1.1.2 Ways to overcome the antibiotic crisis

When antibiotics were first discovered in the 1940s, resistance evolution was already recognised as a problem [75, 157]. Since the 1940s, the problem has generally been overcome by developing new antibiotics [24]. Over time, finding new antibiotics has become increasingly challenging, but drug discovery is still an important part of our strategy to counteract resistant bacteria [153].

Combinations of antibiotics are another promising approach to resolving the resistance problem. Some combinations of antibiotics behave synergistically, meaning that lower concentrations of each antibiotic can be used in combination to yield a greater effect than either antibiotic on its own [92, 100]. In theory this should reduce the selection pressure for resistance as less of each antibiotic

is being used. Antibiotics can also be combined with other drugs that inhibit antibiotic-degrading enzymes, thus allowing the antibiotic to work unhindered. This approach is used in clinical practice, although it has been found to lead to even more complicated resistance mechanisms, when resistance occurs [121].

Another way to reduce the amount of antibiotic required (to treat an infection) could be by the provision of tailored treatment plans, which are based on a detailed understanding of the antibiotic-bacteria interaction throughout an infection. For example, during an infection the growth rate of the infecting bacteria may change; as some antibiotics are more effective against slowly growing bacteria it would not be effective to prescribe these antibiotics if the bacteria are growing quickly [48]. Biofilm infections are another example where bacterial growth state can be important [103]. For this reason, it is important to understand how bacteria respond to antibiotics under different environmental and growth conditions. This is one area where a physical modelling approach can help.

1.2 Key background biology of *E. coli*

This thesis focuses on the bacterium *Escherichia coli* (*E. coli*). *E. coli* is one of the most studied, and best understood, micro-organisms. Strains of *E. coli* are responsible for a significant number of clinical infections (especially of the urinary tract) and have developed extended-spectrum resistance, i.e. resistance to a wide range of antibiotics, in clinical settings [13].

1.2.1 The *E. coli* cell envelope

Bacteria can be generally sub-divided into two categories, based on the structure of the cell envelope: Gram-negative and Gram-positive [106]. *E. coli* is a rod-shaped Gram-negative bacterium.

The structure of the cell envelope in *E. coli*, and other Gram-negative bacteria, consists of three layers: an inner (cytoplasmic) membrane which is composed of a phospholipid bilayer and integrated membrane proteins; a thin cell wall composed of peptidoglycan (PG); and an outer membrane which is an asymmetric bilayer of phospholipids and lipopolysaccharides (Fig. 1.1). The PG cell wall is anchored to the outer membrane via lipoproteins. The space between the inner and outer membranes, within which the cell wall is found, is called the periplasm. The periplasm contains a variety of proteins in a gel-like solution. The periplasmic proteins include the penicillin binding proteins (PBPs) which are some of the main targets of cell wall-targeting antibiotics. The outer membrane provides a protective layer but to enable the entry of nutrients and other necessary small molecules, the outer membrane contains porin protein channels. It is through

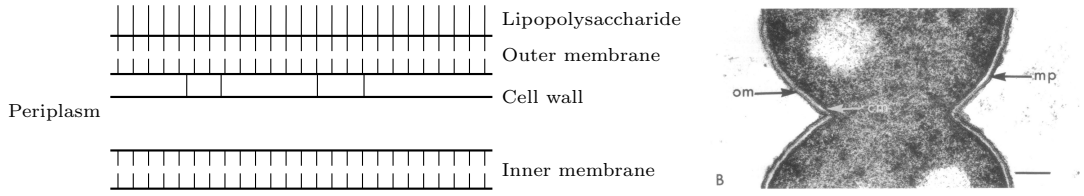

Figure 1.1: Left: A simple schematic of the *E. coli* cell envelope depicting the inner phospholipid membrane which surrounds the cytoplasm, which in turn is surrounded by the periplasm containing the peptidoglycan (PG) cell wall. The entire cell is then surrounded by the outer phospholipid membrane which is decorated with lipopolysaccharides [23]. The PG cell wall is anchored to the outer membrane with lipoproteins. Right: An electron micrograph of the *E. coli* cell wall showing the outer membrane (om), periplasm (mp) and cell membrane (cm). Bar, 0.1μm. From Burdett and Murray [10]

these porin channels that antibiotics enter the periplasmic space and disrupt the cell wall synthesis machinery [96].

In *E. coli*, the cell wall, made of peptidoglycan (PG), is generally considered to have a simple single-layered molecular architecture. Peptidoglycan consists of a network of glycan strands composed of alternating Mur*N*Ac (NAM) and Glc*N*Ac (NAG) sugar residues, which are connected by peptide bonds [33], as shown in Fig. 1.2. New cell wall material is required for cell elongation and also for cell division.

The peptidoglycan network forms a strong, but dynamic, macromolecular mesh that is able to withstand pressures greater that 20 atmospheres [30]. This is crucial as bacterial cells are under osmotic turgor pressure of several atmospheres [57]. The PG cell wall is thus the structure that ensures that *E. coli* are able to maintain their shape and integrity in a variety of environments (Figure 1.3). As mentioned, *E. coli* is rod-shaped and can be considered a spherocylinder i.e. a cylindrical body with hemispheres on each end (Figure 1.3) forming the poles. *E. coli* divides by building a septum at mid-cell. The septum is composed of new cell wall and will form two new poles once division occurs (Figure 1.3).

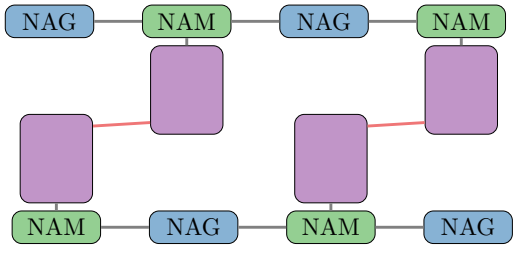

Figure 1.2: Schematic representing the structure of peptidoglycan. NAG represents the Glc*N*Ac residue while NAM represents the Mur*N*Ac residue, and the larger, lilac unlabeled rectangle represents the pentapeptide chain. Peptide bonds between peptidoglycan units are shown in orange.

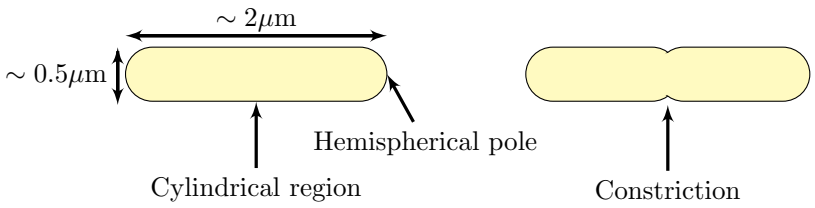

Figure 1.3: Schematic of a typical rod-shaped bacterium which can be considered as a cylinder with two hemispheres capping the ends. A stereotypical *E. coli* bacterium is approximately 2μm long and 0.5μm wide, although this depends on the growth conditions and the phase of growth. Constriction occurs at the mid-cell during division, forming two new poles.

1.2.1.1 The cell wall synthesis pathway

The synthesis pathway of peptidoglycan is depicted in Fig. 1.4. The precursor UDP-Glc*N*Ac (UDP stands for uridine diphosphate) arises from the conversion of fructose-6-phosphate, which is made from glucose which the cell ingests. UDP-

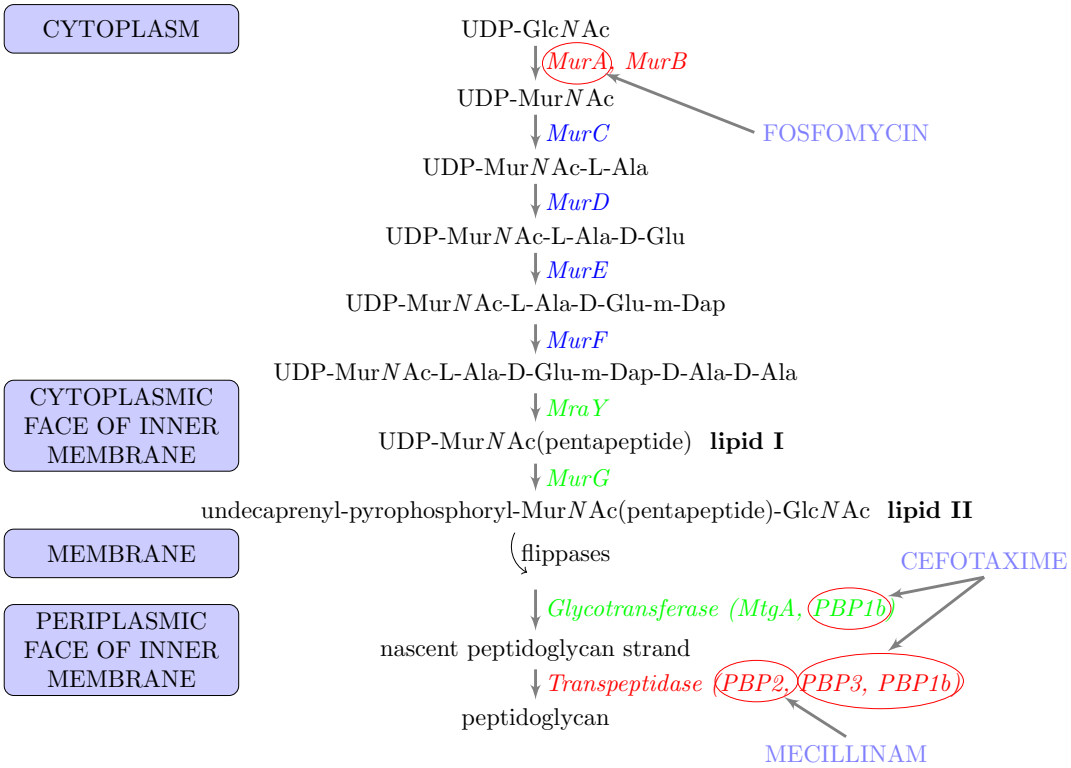

Figure 1.4: Schematic of the biosynthesis pathway of peptidoglycan indicating the regions of the cell where the reactions occur and differentiating between different enzyme types with different colours. Blue indicates a ligase, green indicates a transferase and red indicates other enzyme types. UDP stands for uridine diphosphate and is a nucleoside. The diagram also shows where some of the antibiotics used in this study act i.e. fosfomycin, cefotaxime and mecillinam.

PBP class	Activity	Examples
A	bifunctional GTase/TPase	PBP1a, PBP1b, PBP1c
B	monofunctional TPase	PBP2, PBP3
C	monofunctional GTase	MtgA

Table 1.1: Summary of *E. coli* PBPs (penicillin binding proteins) and their classifications [33]. GTase refers to a glycotransferase and TPase to a transpeptidase. PBP2 is the target of mecillinam, PBP3 and PBP1b are the targets of cefotaxime and PBP3 is the target of aztreonam.

Glc*N*Ac is converted to UDP-Mur*N*Ac-pentapeptide by the sequential activity of the MurA transferase, MurB reductase and MurC-MurF ligases in the cytoplasm. At the membrane, MraY catalyses the reaction of UDP-Mur*N*Ac-pentapeptide with undecaprenylpyrophosphate (a carrier lipid) to generate Lipid I, and this is coupled to Glc*N*Ac by the MurG transferase to yield Lipid II [64]. Figure 1.4 shows that there are various different geographic points within the cell where a cell wall-targeting antibiotic could disrupt the pathway: within the cytoplasm, at the cytoplasmic face of the inner membrane or at the periplasmic face of the inner membrane. In this project we study one antibiotic with a cytoplasmic target (fosfomycin) and various antibiotics which act at the periplasmic face of the inner membrane (including aztreonam, cefotaxime and mecillinam) (Figure 1.4).

1.2.1.2 The Penicillin Binding Proteins

Some of the more important enzymes in the context of the action of cell wall-targeting antibiotics are the penicillin binding proteins (PBPs). As the name suggests these were discovered after the mechanism of action of penicillin was elucidated [125]. PBPs are peptidoglycan synthases, of which there are three classes as summarised in Table 1.1. In order for the cell wall to grow successfully, both glycosidic and peptide bonds need to be synthesised, therefore peptidoglycan synthesis requires both transpeptidase (TPase) and glycotransferase (GTase) enzymes. PBPs can be monofunctional, or bifunctional TPase/GTase enzymes [57]. PBPs play various roles in cell division and peptidoglycan synthesis. Importantly, different sets of PBPs are involved in elongation and cell division.

A schematic illustration of how the PBPs and auxiliary enzymes are organised into the two main cell wall synthesis machineries can be found in Figure 1.5, these are often called the "elongasome" and the "divisome" [16]. PBP2 and PBP1a are thought to provide the main peptidoglycan synthesis activities for elongation [147], while PBP3 and PBP1b are thought to provide the main PG synthesis activity for cell division [33]. PBP3 is essential for cell division while PBP1b has a semi-redundant role in peptidoglycan synthesis [33].

Another important player in the synthesis and maintenance of the cell wall is the

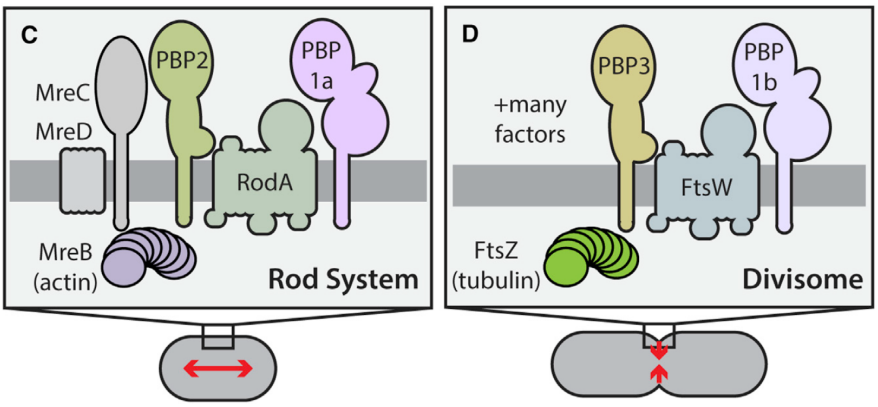

Figure 1.5: An excerpt of Figure 1 from Cho et al. [16] depicting the elongation ('Rod System') and division ('Divisome') associated cell wall synthesis machineries. PBP2 and PBP3 are transpeptidases while PBP1a and PBP1b are bifunctional transpeptidase/glycotransferases. FtsW is a Lipid II flippase. RodA is thought to be a glycotransferase [17].

actin-like protein - MreB. MreB is required for rod-shaped growth and interacts with a host of other proteins (MreC, MreD, RodZ and lipid II synthesis enzymes MraY and MurG). MreB is thought to play a structural role and is hypothesised to guide the localisation of the cell wall elongation machinery around the cell wall [102, 117]. A similar structural protein, FtsZ, guides the localisation of the cell division machinery [116].

1.2.1.3 The PBPs and growth rate

Bacteria grow at different rates depending on their environmental conditions (e.g. the richness of the nutrient media). In this thesis we explore the impact of growth rate on the efficacy of cell wall-targeting antibiotics. It is therefore useful to know how the abundances of the main targets (the PBPs) of the cell wall-targeting antibiotics are impacted by growth rate. Dougherty et al. [28] calculated the numbers of PBPs (1a, 1b, 2, 3, 4, 5, 6, 7 and 8) per cell of *E. coli* MC4100 in different growth media (M9 glucose and LB) by radiolabelling the PBPs, separating the PBPs by gel electrophoresis and comparing PBP abundance to cell number as determined by colony counts. They found that slower growing cells contain significantly less of each PBP per cell, in terms of absolute number.

The growth rate of *E. coli* can also impact the cell wall synthesis machinery by affecting the rate at which each PBP is synthesised. We have performed a sub-analysis of absolute protein synthesis rate data that was produced by Li et al. [82] using ribosome profiling on rich and poor media (MOPSgluRDM and MOPSgluMIN respectively). This is shown in Figure 1.6, for cell wall related proteins. Li et al. [82] determined the absolute synthesis rate on two growth media (in units of molecules produced per generation) by normalising the average ribosome density for each protein in the proteome by the total amount of proteins

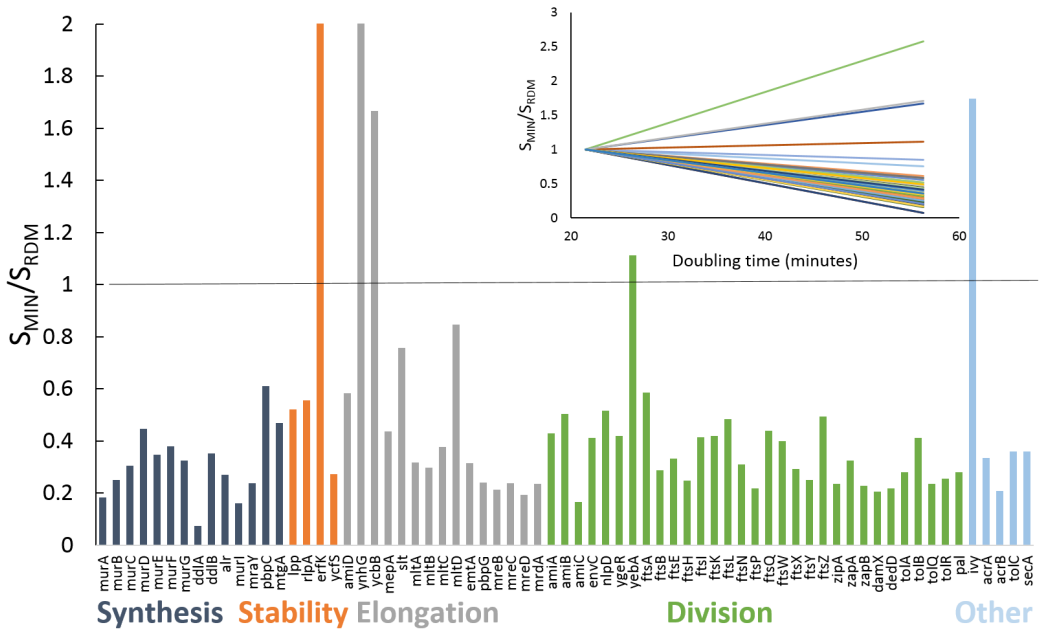

Figure 1.6: The ratio between the absolute synthesis rates (units of molecules produced per generation) on the poor growth media MOPSgluMIN (S_{MIN}) and on the rich media MOPSgluRDM (S_{RDM}) for cell wall associated proteins using data from Li et al. [82]. The proteins have been grouped according to their primary function: synthesis of PG precursors, maintaining stability (e.g. associated with lipoproteins and anchoring of the cell wall to the outer membrane), elongation, division and other. A value less than 1 indicates a decrease in synthesis rate for that protein at slower growth rate. The inset shows the ratio between poor and rich synthesis rates as a function of doubling time.

synthesised during the cell doubling time. In our analysis we determined which genes were associated with the cell wall using the Ecocyc database [67], and grouped them by their primary function. To visualise the impact of growth rate on the synthesis rates we took the ratio of the synthesis rate on poor medium to the rate on rich medium (Figure 1.6). Figure 1.6 shows that the rate at which the majority of cell wall associated proteins are synthesised decreases when the bacteria are growing at a slower rate (in a poor growth medium, compared to a rich medium).

1.2.1.4 Role of hydrolases

Hydrolases are enzymes which cut the peptidoglycan network - an activity that is necessary for the insertion of new material during growth, and in separating the two daughter cells during division [57, 140]. In *E. coli* as much as 40-50% of the total peptidoglycan material is removed in each generation [104]. The resulting soluble fragments of PG are reused via the peptidoglycan-recycling pathway [64, 104]. *E. coli* has more than 20 hydrolases which include amidases (e.g. AmiA-EnvC), lytic transglycosylases (e.g. Slt), carboxypeptidases (e.g. AmpH) and

endopeptidases (e.g. PBP4 and PBP7) [105].

It has been observed that PG hydrolases can help or hinder the action of cell wall-targeting antibiotics. For example, Heidrich et al. [53] investigated the role of the three amidases that are linked with the divisome machinery in *E. coli*, finding a balance between PBP3, the three amidases and the lytic transglycosylase (Slt70). If PBP3 and Slt70 were inhibited, the amidases became uncontrolled resulting in lysis, while if PBP3 and an amidase were inhibited then Slt70 was unregulated triggering lysis. This indicates that to achieve fast cell death when inhibiting PBP3 it is necessary to also inhibit one of the hydrolases. Conversely, Dörr et al. [27] found that endopeptidases in the bacterium *Vibro cholerae* enabled the organism to tolerate cell wall synthesis targeting antibiotics, by remodelling the peptidoglycan network into an osmotically stable sphere.

These observations suggest a balance between the activities of PBPs and hydrolases, with two possible outcomes when PBPs are inhibited. Firstly, the hydrolases may slowly remodel the PG when PBPs are inhibited resulting in spherical bacteria which are relatively stable [27]. Alternatively, active hydrolases may quickly out-balance PBP activity, leading to lysis [53].

1.2.2 Typical *E. coli* growth dynamics

A typical growth curve for *E. coli* in the absence of antibiotics can be seen in Fig. 1.7 highlighting the different growth phases. Here, the optical density at 600 nm (OD_{600}) is used as a measure of the number of cells present in the culture. Optical density is a measure of how much light at a given wavelength is scattered by the cells in a suspension [50]. If a culture is well dispersed, and assuming cell shape does not change, optical density is proportional to bacterial density throughout most of the initial growth phase. Thus, optical density measurements provide a way of estimating the number of bacteria per milliliter of suspension [93].

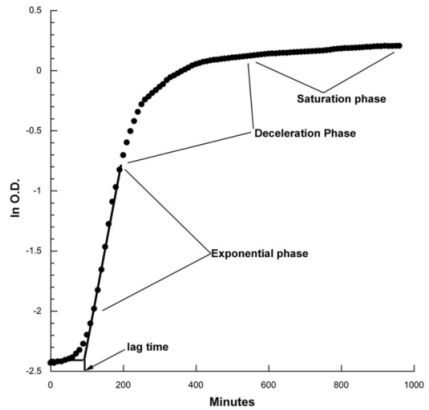

Figure 1.7: An illustrative bacterial population growth curve from Hall et al. [50] with the different growth phases labelled.

Bacterial growth curves are normally characterised by three stages [96]. First there is a 'lag phase', in which little growth is seen as the bacteria become accustomed to the growth medium. Next there is a period of exponential growth, followed by a 'stationary phase' where bacteria either do not grow or the rates of growth and death balance.

During the exponential growth phase, cells proliferate at a rate proportional to the number of cells present at a particular time:

$$\frac{\mathrm{d}N}{\mathrm{d}t} = \lambda N \tag{1.1}$$

where N is the concentration of cells, t the time and λ a constant of proportionality, which is called the specific growth rate. If this expression is integrated between the limits of 0 and t and N_1 and N_2 the result is:

$$\ln\left(N_2/N_1\right) = \lambda\left(t_2 - t_1\right) \tag{1.2}$$

Therefore, if the natural logarithm of the number of cells present in a culture (or of the optical density of the culture) is plotted against time, a straight line should result during the exponential phase, where the gradient is the specific growth rate.

Another common measure of the growth rate of a bacterial culture is the doubling time, T_d. This is the time required for the number of cells to increase by a factor of 2 and can be determined by:

$$T_d = \ln 2/\lambda \approx 0.693/\lambda. \tag{1.3}$$

Under optimum conditions *E. coli* can achieve a doubling time of 20 minutes [96]. By altering the environmental conditions e.g. nutrient quality, one can alter the growth rate in a controlled manner. We will use this approach in Chapters 3, 4 and 5 of this thesis.

1.2.3 Mechanisms of division initiation

As some cell wall-targeting antibiotics interfere with cell division, it is important to discuss how *E. coli* initiates and controls its division process. The initiation of division is still a topic of debate, with the added complication that bacteria may employ different division triggering mechanisms under different growth conditions [1, 12, 68, 128].

The general mechanism underlying *E. coli* cell division is as follows. An initial group of divisome proteins assemble at the mid-cell, orchestrated by the MinCDE system [116], before a constriction is visible [33]. This group includes FtsZ, which is a structural, cytoskeleton-like protein that forms what is called the "Z-ring" around the circumference of the cell, guiding the localisation of the other division enzymes. Then, immediately before constriction, the divisome "matures"

by incorporating the remaining divisome proteins, including the transpeptidase PBP3 [33].

Much of the debate around the initiation of cell division centres on the "signal" used by the cell to trigger division.

1.2.3.1 Timer hypothesis

The "timer paradigm" suggests that a bacterial cell attempts to grow for a fixed amount of time between birth and division [128] - the rationale being that it is necessary for the genome to be fully duplicated and separated before division can occur. This paradigm is inspired by the work of Cooper and Helmstetter [20] who suggested that the time between the end of a round of DNA replication and cell division is constant and independent of the growth rate, assuming that the rate of DNA synthesis per replication origin is a constant independent of the overall cellular growth rate [20] (although the number of replication origins that are active within the cell increases with growth rate [1, 20]).

Regarding the mechanism of *E. coli* division control, the timer hypothesis simply states that division is initiated a fixed time after birth, and this fixed "division time" is growth-rate dependent. No specific molecular mechanism is proposed.

1.2.3.2 Sizer hypothesis

The "sizer paradigm" suggests, instead, that a bacterial cell monitors its size and triggers division once a critical size is reached [128]. The sizer model is generally dismissed, as single cell data shows that the cell size at division is not fixed but is instead positively correlated with the size at birth [6].

1.2.3.3 Adder hypothesis

The "adder paradigm" proposed by Campos et al. [12], suggests that bacterial cells add a fixed volume between birth and division, irrespective of their newborn size. Experiments using a microfluidic 'mother machine' in which many individual *E. coli* and *Bacillus subtilis* cells can be observed growing under a range of growth conditions, suggest that the adder model explains experimental data at both the population and single-cell levels [128]. Taheri-Araghi et al. [128] also argue against the sizer and timer division models. Firstly, they observed that the newborn cell size was negatively correlated with the doubling time, which disagrees with the timer model. Secondly, a positive correlation between the dividing size and the newborn cell size was measured, counteracting the sizer model.

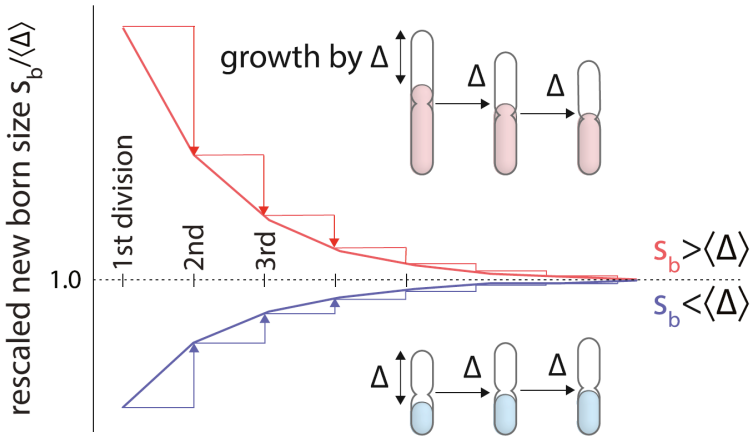

Figure 1.8: An excerpt from Figure 3 of Taheri-Araghi et al. [128] demonstrating the principle of the adder division model. Division occurs after a constant volume Δ is added, and this results in convergence to a steady state cell size, s_b.

1.2.3.4 Mixed models

Further work in the field has attempted to elucidate the mechanism underlying the adder model by mapping the chromosome replication cycle at the single cell level [148]. Applying the Cooper-Helmstetter model on a single cell level, Wallden et al. [148] suggest that the underlying mechanism is actually a combination of the timer and sizer pictures. They suggest that replication is initiated when the cell has grown to a fixed volume per origin of replication (sizer-like). Then, the cell divides at a growth-rate dependent fixed time after replication initiation (timer-like). When *E. coli* cells are growing quickly replication is initiated in a previous generation [1]. Therefore the volume at division becomes uncorrelated with the birth volume. Thus this combined mechanism reproduces "adder-like" dynamics for fast growing cells. In contrast, when cells are growing slowly, replication initiation occurs in the same generation as the corresponding division initiation. In this scenario, the division volume will be proportional to the initiation volume and independent of growth rate. In this case the cells are expected to behave as "sizers". The data of Wallden et al. [148] indeed supports this view.

An improvement on the work of Wallden et al. [148] is found in Micali et al. [89]. In this improved model the assumption of growth-rate dependent division after replication initiation is removed. Instead the model consists of two size-dependent processes which occur concurrently, with division being determined by the slowest of the two processes [89]. With this model formulation the correlation between C+D period duration and growth rate, as well as the correlation between cell growth during the C+D period and the cell size at initiation, are succesfully captured.

1.2.3.5 Precursor hypothesis

The "precursor threshold model" is an alternative idea that has been suggested by Harris and Theriot [51]. Based on careful examination of the surface area and volume of growing *E. coli*, *C. crescentus* and *B. subtilis* cells, they hypothesise that the surface area to volume ratio (SA/V) is the key variable in bacterial growth. With this hypothesis they develop a simple model for SA/V determination which attempts to explain how cells reach a steady state SA/V over time.

Harris and Theriot [51] suggest that the rate of synthesis of new surface area material per unit volume may be relatively constant over a cell cycle, such that during cell elongation there will be an accumulation of excess surface area "precursors". Once a threshold "precursor level" is reached, Harris and Theriot [51] suggest that division is initiated and the excess material used up in the production of the new cell end-caps (poles). This mechanism is predicted to lead to adder-like behaviour [51]. While there are no direct measurements of precursor levels to back this hypothesis, it does provide a potential molecular mechanism for division triggering. A similar concept has been discussed in Chien et al. [15] using FtsZ as the molecule of interest.

1.2.4 Proteome-partitioning

As discussed, the growth rate of the bacteria can impact the synthesis rate of proteins. However, there is a limit to how fast proteins can be synthesised based on the need of the bacteria to also synthesise ribosomes, in order to synthesise those proteins. This idea has led to the concept of "proteome-partitioning", in which the proteome is considered to consist of a number of distinct segments: ribosome-affiliated proteins whose fractional abundance increases with growth rate, a fixed "core" whose fractional abundance is independent of growth rate and the remaining proteins whose fractional abundance decreases with growth rate [9, 118]. These patterns of abundances can by explained by growth rate-dependent partitioning of the cell's translational resources between the production of new ribosomes and the production of other proteins [118].

Scott et al. [118] showed that this partitioning can be described by a set of empirically determined constraint functions [118]. Firstly, the RNA/protein ratio r is linearly correlated with the specific growth rate λ:

$$r = r_0 + \frac{\lambda}{\kappa_t} \tag{1.4}$$

This is expected if the ribosomes are growth-limiting and are engaged in translation at a constant rate (κ_t) [118]. Here r_0 is the minimal RNA to protein

ratio. There is also another linear relation linked to the nutritional capacity κ_n:

$$r = r_{max} - \frac{\lambda}{\kappa_n} \tag{1.5}$$

Here, r_{max} is the (extrapolated) maximal RNA/protein ratio. These linear relations can be combined to give the prediction that the maximal growth rate is proportional to $r_{max}\kappa_t$ [118]. These relations have previously been employed to aid our understanding of antibiotic mechanism of action. Greulich et al. [48] showed that these relations, combined with a simple model for antibiotic action, could explain several non-trivial features of the growth-medium dependent action of ribosome-targeting antibiotics.

1.3 Cell wall-targeting antibiotics

1.3.1 Prevalence of cell wall-targeting antibiotics

Cell wall-targeting antibiotics are the most widely used class of antibiotics in a clinical setting [11]. Of the antibiotics studied in this thesis, for example, fosfomycin and mecillinam are used for uncomplicated urinary tract infections [38, 132]. Cell wall-targeting antibiotics are clinically successful because cell walls are structures unique to bacteria leading to high target specificity [11] and reduced toxicity to the patient [86]. Furthermore, cell wall-targeting antibiotics are often bactericidal (i.e. they kill bacteria, rather than just preventing growth), leading to complete bacterial clearance [11].

However, the effectiveness of antibiotic treatment has become diminished due to ever increasing levels of resistance [11]. For example, the widespread use of the cell wall-targeting antibiotic cefotaxime is thought to be the major cause of the spread of extended-spectrum beta-lactamases [69]. Beta-lactamases are enzymes produced by many strains of multi-drug resistant bacteria that degrade the beta-lactam class of cell wall-targeting antibiotics.

Cell wall-targeting antibiotics include intracellular antibiotics, beta-lactams and glycopeptides (Figure 1.9). Beta-lactams, which form the main topic of this thesis, are a large family of antibiotics including cephalosporins, carbapenems, penicillins and monobactams (see Figure 1.9 and later discussions). Glycopeptides predominantly target Gram-positive bacteria, and as such they will not be discussed any further.

1.3.2 Targets in the cell wall synthesis pathway

As we have seen, the cellular pathway which synthesises peptidoglycan is fairly complex (Section 1.2.1.1), and thus it provides many possible targets for

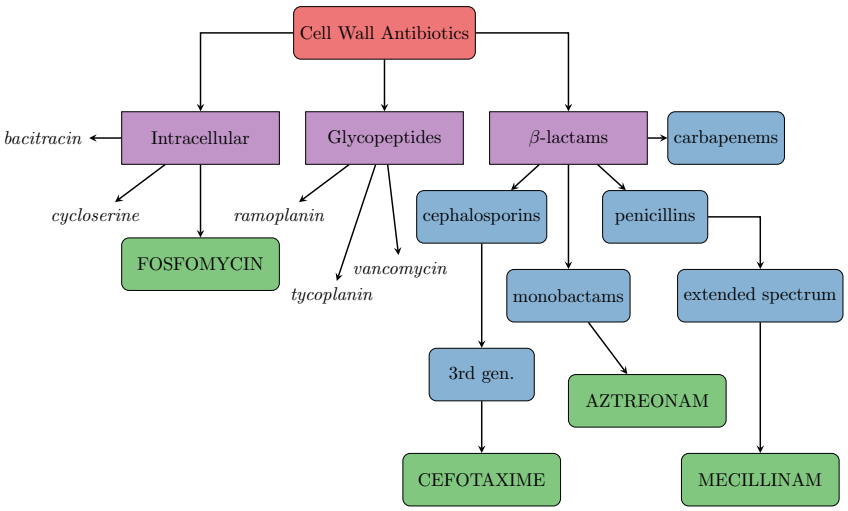

Figure 1.9: Cell wall-targeting antibiotic "family tree" - lilac boxes differentiate different antibiotics by general mode of action; blue boxes refer to the further sub-categories in the beta-lactam class; italicised text shows named examples that are not studied here; green boxes highlight the key antibiotics studied in this thesis. This is not a fully comprehensive picture of the large class of cell wall-targeting antibiotics but helps with visualising where the antibiotics of interest fit in.

antibiotics. However, there is some redundancy in the cell wall synthesis pathway (as might be expected as it is a life-critical system of the cell) [33, 75]. Therefore, many cell wall-targeting antibiotics have affinity to multiple targets [72, 133]. To keep our study as simple as possible, in this thesis we focus mainly on antibiotics which have a single major molecular target. In the following we briefly discuss the chosen antibiotics in more detail.

1.3.2.1 Antibiotics that act within the cytoplasm

Fosfomycin (Fos.) (Fig. 1.10) is a hydrophobic molecule that is imported into the cytoplasm via membrane bound transporters [99]. Fos. irreversibly inhibits MurA, an enzyme found in the cytoplasm at the start of the biosynthesis pathway of peptidoglycan (Fig. 1.4) [38]. As Fos. acts at a critical early stage of the peptidoglycan pathway, which is found in all bacteria, it has a broad spectrum of activity [90].

The chemical structure of fosfomycin can be seen in Figure 1.10. Fosfomycin has been reported to result in lysis of *E. coli* grown in rich media [79].

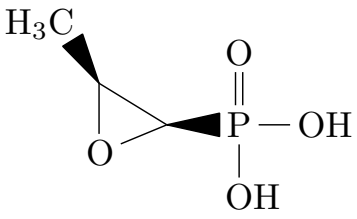

Figure 1.10: The chemical structure of fosfomycin.

1.3.2.2 Antibiotics that act at the periplasmic face of the cytoplasmic membrane

The beta-lactams are a large class of antibiotics which work by inhibiting PBPs (penicillin binding proteins) [99]. Beta-lactams function by structurally mimicking the D-Ala-D-Ala component of the peptidoglycan stem peptide, to form an irreversible intermediate within the active site of the PBPs. Beta-lactams have a long history: the original beta-lactam, penicillin, paved the way for the discovery of many more chemically related beta-lactam antibiotics [24]. For example, cephalosporins were discovered when beta-lactamase enzymes started to make penicillins ineffective [45]. The core structures of the penicillin, cephalosporin and monobactam classes of beta-lactams are shown in Figure 1.11. Three beta-lactams are studied in this thesis: mecillinam, aztreonam and cefotaxime.

Mecillinam (Mec.) (Figure 1.12) is classified as a penicillin but it deviates from the core penicillin chemical structure (Fig 1.11), as it has a side chain joined to the beta-lactam ring by an amidine bond rather than a β-acylamino group (see Figure 1.12) [5]. Mecillinam is also known as amdinocillin [132] and FL 1060 [136]. Mec. specifically targets the transpeptidase (TPase) active site of PBP2 [33]. Blocking PBP2 function with mecillinam is lethal [16, 147].

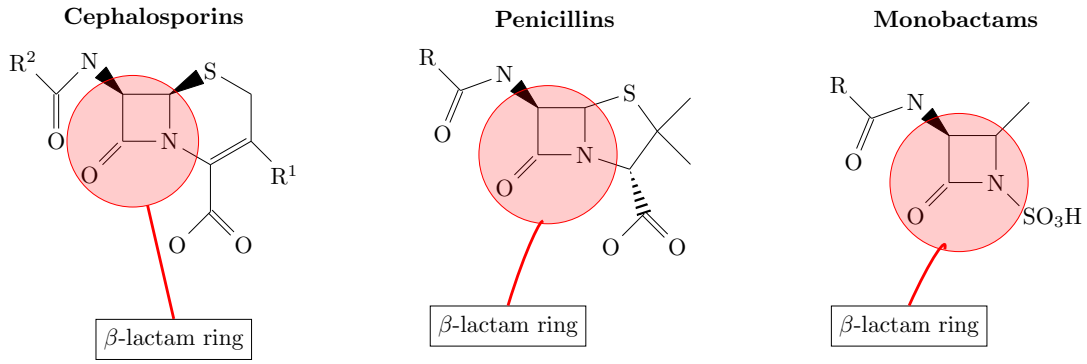

Figure 1.11: The core structures of the cephalosporin, penicillin and monobactam classes of beta-lactam antibiotics. Monobactams have no secondary ring attached to the beta-lactam ring [4], while penicillins have a five-membered thiazolidine ring fused to the beta-lactam ring and cephalosporins have a six-membered dihydrothiazine ring fused to the beta-lactam ring [143].

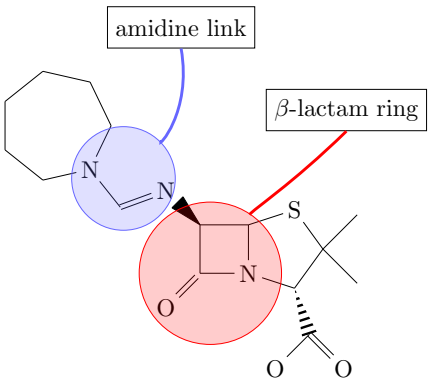

Figure 1.12: Mecillinam chemical structure.

The population dynamics of *E. coli* growing in the presence of mecillinam have been previously described [14, 46, 137]. These studies report that a cell culture continues to increase in optical density for some time after Mec. is added. Later, the OD decreases (creating a 'bump') and, ultimately, apparent recovery of the population ('regrowth') happens (Figure 1.13). The hypothesis has been put forward that the bump is due to the formation of large spherical cells that divide more slowly and eventually lyse [46]. The "regrowth" has been attributed to cells that happened to have lower osmotic pressure, were therefore more osmotically stable as spheres and thus tolerated mecillinam [46]. Others have suggested that the regrowth may be due to decay of mecillinam [14].

Aztreonam (Azt.) (Fig. 1.14) is a monobactam that binds PBP3 irreversibly, thus preventing cell division [107]. The mechanism behind the prevention of division has been partly elucidated as it has been found that antibiotics which

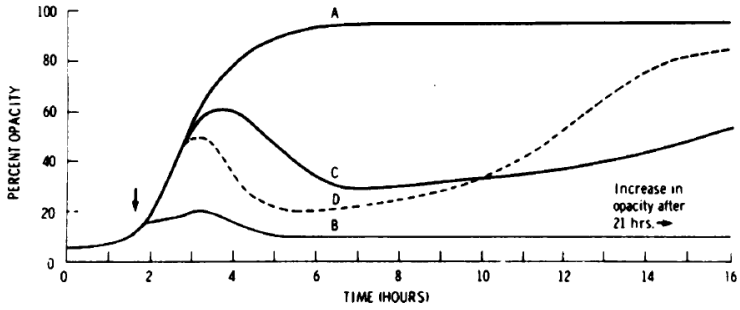

FIG. 1. ***Continuous opacity records of E. coli strain ECSA 2. (A) Normal growth curve; (B,C,D) mecillinam was added (arrow) to achieve a concentration of 10 μg/ml. Medium contained (A,B) no addition; (C) 10% sucrose; (D) 1% NaCl.***

Figure 1.13: Figure 1 from Greenwood [46] demonstrating the population dynamics of *E. coli* in the presence of 10μg/ml mecillinam in growth media of varying osmolarity.

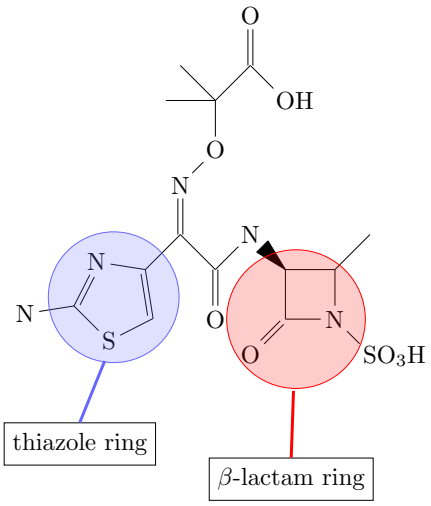

Figure 1.14: The chemical structure of aztreonam.

target PBP3 reduce the localisation of PBP3 approximately two-fold at septation sites [150], therefore these antibiotics prevent the complete maturation of the divisome.

Exposure to sub-MIC levels of aztreonam results in the production of long filaments, for levels of aztreonam corresponding to inhibition of 60% of the total PBP3 [107]. These filaments eventually become unstable and lyse.

Cefotaxime (Ctx.) (Figure 1.15) is a third generation cephalosporin beta-lactam (Figure 1.11) that targets several different PBPs. In particular, cefotaxime shows a high affinity for PBP3 and PBP1b [72]. Therefore, like aztreonam, cefotaxime directly inhibits cell division. Consistent with this, several studies have shown that *E. coli* cells exposed to cefotaxime form filaments [45, 69] - for an example see Fig. 1.16.

Another interesting morphological change in the presence of cephalosporins is bulge formation (Figure 1.16). Yao, Kahn and Kishony (2012) argue that beta-lactam killing of *E. coli* has four stages: cell elongation, bulge formation, bulge stagnation and lysis; and that both the cell wall and the outer membrane affect

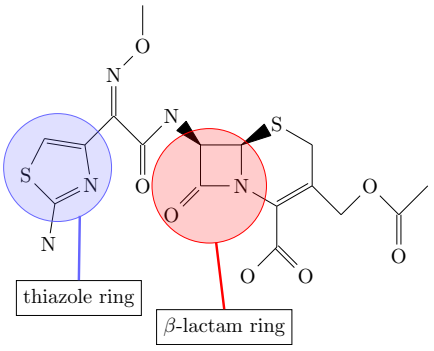

Figure 1.15: The chemical structure of cefotaxime.

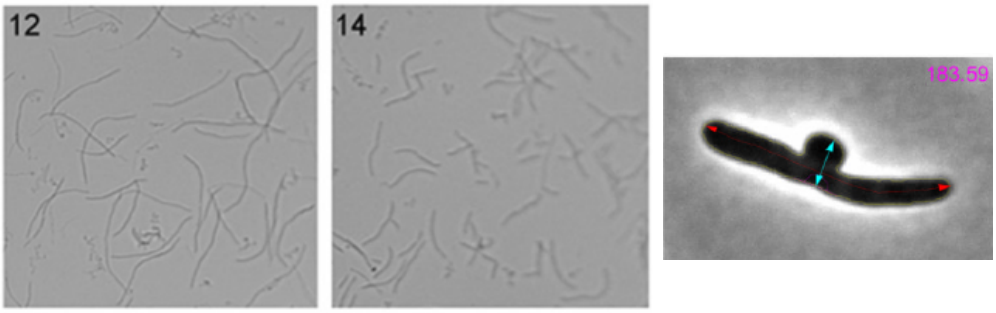

Figure 1.16: Left: Images taken from Kjeldsen et al. [69] Fig. 1 showing filamentation of two sensitive strains cells at sub-MIC cefotaxime concentrations [69]. Right: An example of bulge formation under the action of cephalexin (another cephalosporin) taken from [154].

the observed dynamics. They argue that the outer membrane plays an important role in stabilising bulges, thus delaying lysis due to the antibiotic activity. Bulges are found to form abruptly at potential dividing sites and it has been suggested that they might allow for recovery of normal growth once the antibiotic pressure is removed [154]. It is however not clear why formation of a bulge should protect a cell from killing by an antibiotic.

1.3.3 Beta-lactams and growth rate

An important focus of this thesis is on the growth-rate dependence of antibiotic action. There are several reasons to expect that the activity of beta-lactams should be different for fast-growing versus slow-growing bacteria. Firstly, mecillinam, aztreonam and cefotaxime all target PBPs, whose abundance varies with growth rate as discussed in Section 1.2.1.3. For example, Dougherty [28] measured the numbers of PBP$\{1a, 1b, 2, 3, 4, 5, 6, 7, 8\}$s per cell of *E. coli* in different growth media, finding that slower growing cells contain a significantly lower number of each PBP per cell.

Direct evidence also exists for growth-rate dependent beta-lactam action. Cozens et al [22] investigated how growth rate affects the killing activity of beta-lactam antibiotics. By growing cells in a range of growth limiting conditions, mimicking the conditions in a real, in vivo infection, they concluded that only a few antibiotics remained effective at killing slow growing cells. Additionally, slow growing bacteria were killed proportionately more slowly. In similar work, Tuomanen et al. [134] found that the beta-lactam killing rates were proportional to the bacterial generation time and that slow growing bacteria become progressively more phenotypically tolerant to beta-lactam activity [134]. Therefore, in general, faster growing bacteria are more easily killed by cell wall-targeting antibiotics. This contrasts with the naive expectation that slow-growing cells have fewer PBPs and should thus be easier to kill.

1.3.4 Resistance mechanisms to cell wall-targeting antibiotics

Because beta-lactams often bind to multiple PBPs these antibiotics typically circumvent single-mutation resistance mechanisms. However, bacteria can become resistant via reduced membrane permeability or efflux increase, expression of PBPs with reduced affinity for the antibiotic, bypassing of cross-linking the stem peptide with transpeptidases, or degradation of the antibiotic by β-lactamase enzymes [129]

For intracellular antibiotics, transport provides a potential target for mutation. As an example, the requirement for transport of fosfomycin into the cytoplasm is a potential weakness in the efficacy of the antibiotic; decreasing the expression of transporters can reduce the cell's antibiotic susceptibility [99].

1.4 Modelling antibiotic-bacteria interactions

In Chapters 6, 7 and 8 of this thesis, we will develop a mathematical model for the action of cell wall-targeting antibiotics. While mathematical modelling of antibiotic action is far from new, our model is unusual in that it combines cell-level physiology and cell morphology, with population dynamics. To set our work in context, we briefly review the types of models that have previously been developed for antibiotic action, with an emphasis on cell wall-targeting antibiotics.

A number of models have been developed with the aim of optimising antibiotic treatments. These are population-based, with no description of the internal workings of the target bacteria. For example, Levin and Udekwu [80] developed a model that combined the known pharmacodynamics (the in vitro relationship between antibiotic concentration and the growth or death rate of the target bacteria) of antibiotics with the population dynamics of bacteria in order to evaluate the efficacy of antibiotics and improve data on the minimum inhibitory concentration (MIC) [80]. Their model consists of differential equations describing different sub-populations of bacteria experiencing an environment with varying antibiotic concentrations, as depicted in Figure 1.17. This model allows the generation of testable hypotheses for how the density of viable bacteria changes in a range of situations e.g. bacteriostatic versus bacteriocidal antibiotics, batch versus continuous culture, low versus high initial bacterial density.

On the level of individual bacteria, various models have been developed that look closely at the structure of the *E. coli* cell wall. Typically these model the peptidoglycan mesh as a network of springs (see Figure 1.17) and predict morphological changes when the peptidoglycan is perturbed (i.e. in the presence of an antibiotic) [58]. One can also include the action of cell wall synthesis enzymes and determine which enzymes need to coordinate for a cell to grow in a stable fashion [98]. The growth dynamics of the cell wall have also been studied

with more theoretical models: for example one can try to calculate the changes in free energy when adding new peptidoglycan sub-units and how this determines the interplay between cell wall growth and the structural MreB filaments [62].

Less modelling effort has been focused on the interaction of antibiotics with the entire "cell system". However, some work has been done for other antibiotic classes. For example, Greulich et al [48] developed a model which simplifies the bacterial cell as a box into which ribosome-targeting antibiotics diffuse in and out. In the model, ribosomes produce proteins at a certain rate (including more ribosomes), and the cell grows at a rate determined by the rate of protein production. This results in a series of coupled differential equations which link the mechanism of action of the antibiotic with the observable population dynamics. The outcome of the model is a non-trivial prediction of the growth medium-dependence of ribosome-targeting antibiotics that is in agreement with experimental data. To our knowledge this kind of model does not yet exist for cell wall-targeting antibiotics.

To summarise the field, mathematical models, tend to be constrained to one of the zones depicted in Figure 1.17: population dynamics, cell structure or cell physiology. The aim of this thesis is to develop a thorough understanding of the action of cell wall-targeting antibiotics and hence build a mathematical model which combines these zones. i.e. which uses the intracellular dynamics of the antibiotic, with the target, to predict a change in cell structure, and thus a change in the population dynamics.

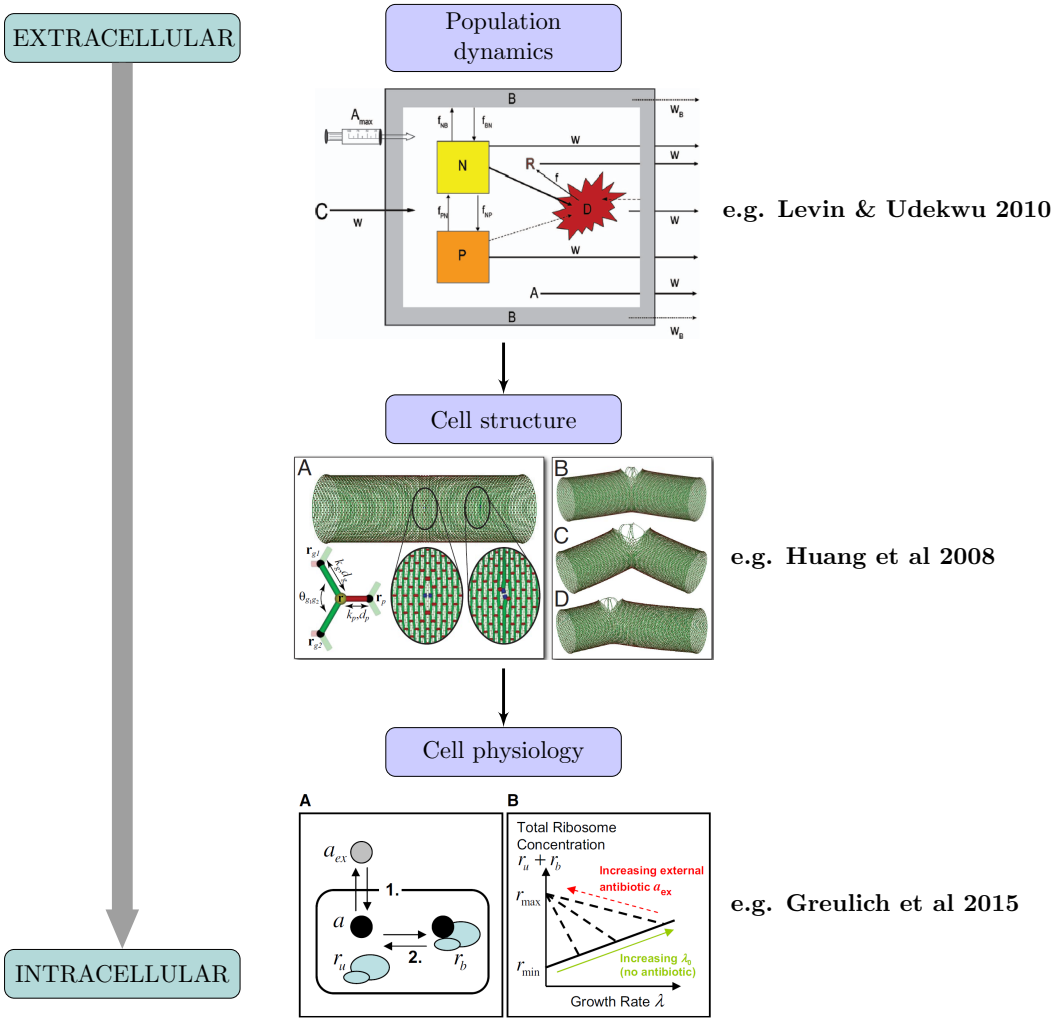

Figure 1.17: Various examples of mathematical models looking at antibiotic interactions with bacteria on different scales. Firstly, Figure 2 from Levin and Udekwu's 2010 paper [80] depicting a representation of their mathematical model investigating the dynamics of bacterial sub-populations in the presence of changing antibiotic concentrations. Secondly, Figure 1 from Huang et al's 2008 paper [58] depicting a representation of their elastic model for the peptidoglycan network and the predictions for a cracked cell. Glycan strands are shown in green and peptide crosslinks in red. Thirdly, Figure 2 from Greulich et al's 2015 paper [48] depicting a schematic of their model and its dynamics.

Chapter 2

Experimental Methods

2.1 Culturing *E. coli*

2.1.1 *E. coli* strains

Two strains of the bacterium *Escherichia coli* (*E. coli*) were used for the majority of the work in this project. These were *E. coli* MG1655 wild type, chosen because it is a widely studied *E. coli* strain and therefore easy to compare and contrast with the literature, as well as *E. coli* RJA002, which is an MG1655 strain carrying a chromosomal yellow fluorescent protein (YFP)/chloramphenicol resistance reporter. The reporter is under the control of the constitutive λP_R promoter, and was made by P1 transduction from strain MRR of Elowitz et al. [34][83].

2.1.2 Growth media

The *E. coli* strains used here can grow in a variety of growth media. Growth media can be grouped into two broad categories: undefined and defined. These terms refer to how well categorised the growth media composition is: for example, growth media derived from yeast products or from blood are undefined, whereas defined growth media are put together from a list of known chemical constituents. One of the standard undefined growth media used worldwide is Lysogeny Broth (LB), which is a nutrient rich yeast-derived growth medium, typically with pH 7.0. This was made in-house. In this project LB was used in both liquid and agar forms. We used liquid cultures to measure bacterial population dynamics or prepare bacteria for microscopy. LB agar plates were used to either isolate individual colonies or to count the number of colony forming units present in a sample.

To investigate the population dynamics of *E. coli* in liquid culture, in the presence of antibiotics, it was deemed best to use a defined growth medium. Using a defined growth medium removed any potential batch differences in LB and gave us more control over the nutrients present in the media. This was achieved by using MOPS (potassium morpholinopropane sulfonate)-based media (originally developed by Neidhardt et al. [95]), which has a defined chemical composition and in which the nutrient quality can be varied. In earlier experiments the components of MOPS media (the MOPS buffer, EZ amino acids and ACGU nucleotides) were purchased from Teknova. However, there were problems with maintaining the stability of these components in transport, so later in the project the production of these components moved in-house (Sharareh Tavaddod, Angela Dawson, Tracey Squires: University of Edinburgh). These components were made according to the recipe in Neidhardt et al. [95]. The MOPS base medium is made up of: MOPS, which acts as a pH buffer; tricine (source of iron); KOH (to buffer to pH 7.4); $FeSO_4$; NH_4Cl; K_2SO_4; $CaCl_2$:$2H_2O$; $MgCl_2$; NaCl; micronutrient stock (ammonium molybdate, boric acid, cobalt chloride, cupric sulfate, manganese chloride, zinc sulfate); sterile H_2O and K_2HPO_4. Together, these components provide many of the requirements for robust bacterial growth. The MOPS medium needs to be supplemented with a carbon source: here we used glucose or glycerol (2% w/v glucose or glycerol). Adding a carbon source to the MOPS base gives a minimal growth medium (MOPSglu/glyMIN). To achieve faster growth the minimal media is supplemented with amino acids and nucleotides (in predefined mixtures known as ACGU nucleotides and EZ amino acids) to give a rich-defined medium (MOPSglu/glyRDM). An intermediate medium (nutrient-wise) can also be made by supplementing the minimal medium with casamino acids (CAA) to a final concentration of 0.2% (w/v) from a 10% casamino acid solution (MOPSglu/glyCAA).

This standard MOPS medium has pH 7.4. For some of our experiments the medium was adjusted to pH 6.5 by gradually adding 1M HCl whilst measuring the pH using a Mettler Toledo pH meter with LE409 probe calibrated with a phthalate type buffer (pH 4.01) and a phosphate type buffer (pH 7) (both from Hach). In the end there was 2-3% 1M HCl in the total volume.

2.1.3 Preparing bacterial cultures for experimental use: steady state versus non-steady state

A bacterial population is typically genetically diverse, due to rapid mutation rates [84]; the impact of this can be reduced by starting experimental cultures with an (as close as possible) isogenic population. This is achieved by inoculating a "starter culture" with a colony that has grown from a single bacterial cell [91]. The general protocol for all experiments in this thesis is as follows. A sample is taken from a frozen aliquot of the desired strain and streaked out onto an LB agar plate (Figure 2.1). This plate is incubated at 37°C overnight for approximately 18 hours, or until single colonies are clearly visible. It can be assumed that

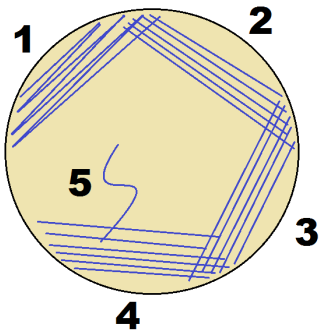

Figure 2.1: The streak plate protocol to mechanically disperse the bacteria. Streaking the sample across the LB agar gradually reduces the number of cells present in each streak.

each colony arises from a single starter cell and is therefore isogenic [91]. In my experiments, single colonies were used to inoculate 5ml LB "seed cultures" which were grown for 2 hours at 37°C and 200 rpm. 10μl of the "seed culture" was then used to inoculate 5 ml liquid cultures in the chosen growth medium, which were allowed to grow overnight in a shaker at 37°C and 200 rpm to reach a high cell density.

From this point my experiments followed one of two pathways: "steady state" and "non-steady state" growth (Figure 2.2). For non-steady state growth the overnight culture is diluted 1/1000 into fresh media pre-warmed to 37°C and allowed to grow until mid-exponential phase (this roughly corresponds to an optical density of 0.2 at 600 nm, which corresponds to a bacterial density of approximately 2×10^7 cfu/ml (cfu stands for colony forming units i.e. viable cells)). This OD$\sim$0.2 culture is then used as the inoculate for the experiment. This preparation is called "non-steady state" as the bacteria have only undergone 3 or 4 generations of exponential growth after the overnight culture and, while it is likely that most cells will be growing exponentially, some may still be in the stationary phase and not growing yet, while some may be in the early stages of growth. This leads to a heterogeneous bacterial cell population.

For some experiments this heterogeneous population can cloud the results, so in most of my work a "steady state" culture was used. To generate a steady state culture, cells were kept in the exponential growth regime for more than 10-20

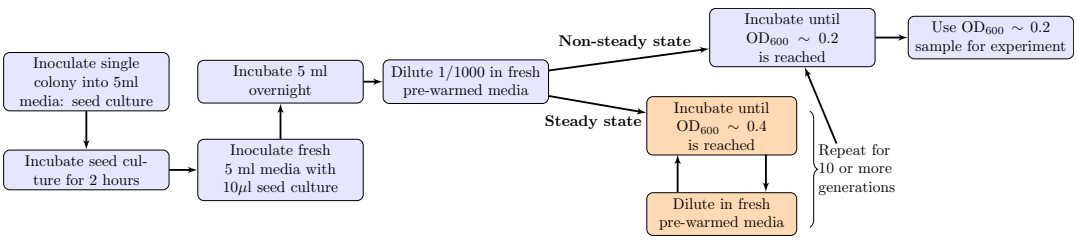

Figure 2.2: A diagram highlighting the protocols for non-steady state and steady-state bacterial culture preparation.

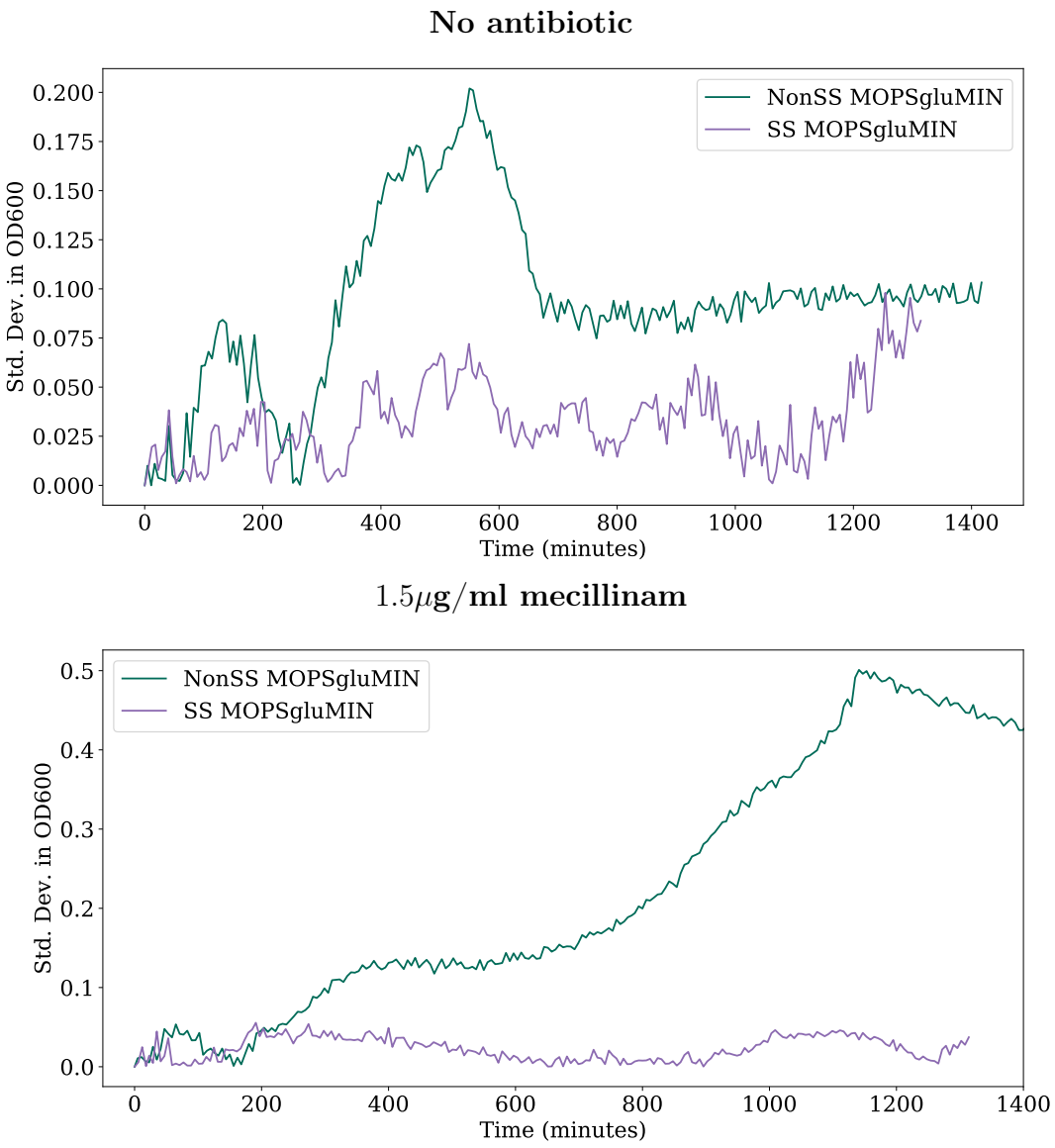

Figure 2.3: The standard deviation of the optical density for 8 wells across two independent plate reader assays (4 wells in each) with no antibiotic (top), and with 1.5μg/ml mecillinam (bottom) in MOPSgluMIN. Using a steady state (SS) culture, versus a non steady state (NonSS) culture, greatly increases the reproducibility of growth curves across experiments.

generations by diluting periodically in pre-warmed growth medium (Figure 2.2). The maximum optical density of a cell culture before each dilution was 0.4 at 450 nm. This method is used to achieve a "homogeneous bacterial culture" [49]. Figure 2.3 demonstrates the impact of having a steady state culture versus non-steady state, by plotting the standard deviation in the optical density over time. It is very clear that having a steady state culture greatly decreases the noise in the optical density measurement, and reduces the standard deviation, both with and without antibiotic (Figure 2.3). Working with steady state cells was important for comparison to the mathematical model, where steady state growth is assumed.

2.2 Protocols for measuring population dynamics

2.2.1 Optical density

In my work, a key observable of interest is the number of bacteria present at any given time. Since direct measurement of bacterial numbers is difficult, various proxy measures have been developed e.g. measuring dry weight or estimating the metabolic activity [93]. "Optical density" is a very common proxy measure for the number of bacteria in a liquid culture, due to its ease of measurement. Optical density (OD) is a measure of light scattered ($\log I_0/I$) by a sample, the simple idea being that in a well mixed, dilute, sample of bacteria, the number of bacteria present should correlate with the amount of light scattered [93]. There are several caveats to using optical density as a measure of cell number: optical density and cell number are generally only well correlated up to a certain bacterial density (due to the increasing occurrence of multiple scattering events [74]); various wavelengths of light are used in the literature (e.g. 450 nm [152], 420 nm[134] , 550 nm[108] and 600 nm[16, 48, 81, 145]) which can make it more difficult to compare results between studies; if cell size or shape changes during an experiment this will also affect optical density (indeed optical density can be argued to be a measure of total biomass) [87]. Nevertheless, OD is a convenient measure for measuring trends in population size, and can be highly informative if these caveats are properly taken into consideration.

2.2.1.1 Spectrophotometer

There are various methods for measuring optical density, two of which were used in this thesis. The first method used in this work was a benchtop spectrophotometer. A spectrophotometer sends a beam of light through a sample and measures the decrease in light intensity due to scattering, at a photodetector on the other side of the sample [74]. A benchtop spectrophotometer is commonly

used when working with larger volumes of liquid culture, and in this case was used primarily to measure the optical density of the inoculate when preparing for experiments, and during experiments where samples were periodically removed from a shake flask culture - for microscopy or for counting colony forming units. A Cary UV spectrophotometer and polystyrene cuvettes (FisherBrand, FB55146) with 1 ml of sample were used to measure the optical density at 600 nm.

2.2.1.2 Plate reader

In other experiments, high throughput growth curve measurements were carried out in plastic microplates (flat-bottomed microplates from Greiner) like that shown in Figure 2.4, using a Fluostar Optima plate reader. The microplate is made of polystyrene and consists of 96 (8x12) flat-bottomed wells, of volume 392μl, indexed by the letters A-H and the numbers 1-12 (Fig. 2.4). The plate reader incubates the plate at the desired temperature and shakes it in between automated optical density measurements. This method enabled us to carry out multiple experiments simultaneously - using different rows and/or columns. The Fluostar Optima plate reader was generally set to incubate at 37°C (or 34°C/30°C as needed) with double orbital shaking at 600 rpm. Optical density measurements at 600 nm were taken approximately every five minutes, with continuous shaking in between measurements. Each well contained 200 μl of sample or growth media. Maintaining the same volume in each well was important as the path length correction of the plate reader was calibrated for this volume and deviations from this would have lead to erroneous optical density measurements. Lids were used on the plates to reduce evaporation over the course of the experiments (various tests were carried out to ensure that evaporation was not impacting results). Lids were taped onto the microplate at four points to reduce the production of plastic dust when the microplate was shaken, but also to ensure that air could still circulate around the microplate.

A bacterial culture at an optical density of 0.2 was diluted 1:20 into the plate, resulting in a starting cell concentration corresponding to an optical density of

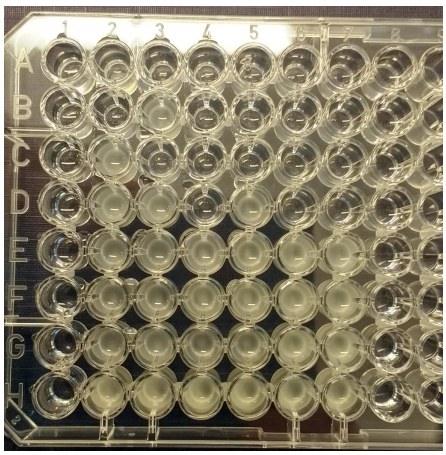

Figure 2.4: An 8x8 snapshot of a 96-well microplate.

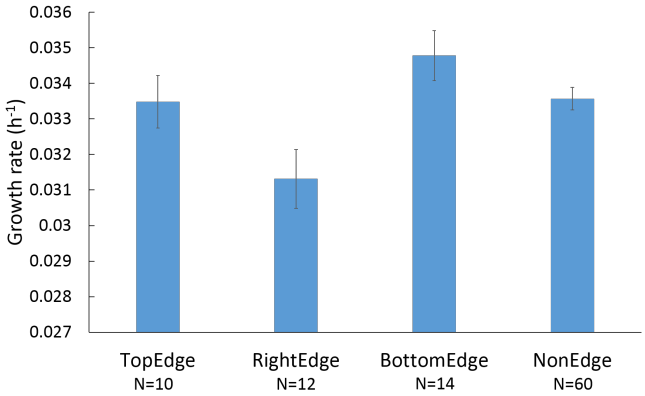

Figure 2.5: Wells grouped by location: TopEdge=Row A, RightEdge = Column 12, BottomEdge = Row H, NonEdge = all other wells. The bar charts indicate the average growth rate (h^{-1}) for *E. coli* MG1655 growing in LB medium at 37°C in wells at these different locations.

0.01. This relatively high initial cell density was chosen because of the plate reader's relatively poor detection limit [61]. The same starting cell density was also used in all other experimental set-ups for consistency.

In my experiments, all microplates contained a reference column filled with growth medium only (no bacteria). The other wells contained varying concentrations of different antibiotics, plus bacteria. The column containing only growth medium acted as a contamination control - if any growth was observed in these wells contamination had occurred and the rest of the plate had to be discarded (this occurred in approximately 17% of experiments). Samples were pipetted into the wells using an electronic multichannel pipette if > 6 wells required the same input. Considerable time was spent on pilot experiments to find the optimum set-up for recording reproducible growth curves. For example, trials were carried out comparing growth in wells at the edges of the plate to growth in the centre of the plate (Figure 2.5). From this it was observed that if the right edge of the plate was ignored, there was no clear correlation between well position and measured growth rate. As a result of this columns 11 and 12 were not used in subsequent experiments. Different shaking regimes were also tested e.g. 600 rpm and 200 rpm, for which no significant difference in the average growth rate was observed (at 200 rpm the calculated growth rate was $0.034 \pm 0.002h^{-1}$, while at 600 rpm it was $0.035 \pm 0.002h^{-1}$). 600 rpm was used to minimise the impact of sedimentation under experimental regimes where lysis occurred.

2.2.1.3 Growth rate calculations

One of the key features of the population dynamics of a bacteria culture is how quickly the bacteria grow in the exponential phase. As described in Chapter 1 (section 1.2.2) the cell number dynamics during exponential growth can be

described by

$$\frac{\mathrm{d}N}{\mathrm{d}t} = \lambda N, \text{ hence } N(t) = e^{\lambda t} \text{ and } \log \frac{N}{N_0} = \lambda t \tag{2.1}$$

where λ is the growth rate, and N the number of cells. As optical density (OD) is a proxy measure for the number of bacteria in a culture, N in this equation can be replaced by OD. By taking the natural log of the measured optical density (subtracting the background OD first), and measuring the gradient of the linear portion, the growth rate is extracted.

In this thesis different methods were used for extracting the growth rate from the benchtop spectrophotometer and plate reader optical density measurements. Benchtop spectrophotometer measurements were taken at hourly intervals and input into Microsoft Excel where the natural log of the OD was taken. The LnOD data was plotted to determine the linear portion of the data, and then the LINEST function applied to the linear portion. The LINEST function uses the least squares method to return a best fit straight line to the data. The gradient, and the standard error on the gradient, were used to describe the growth rate.

The plate reader optical density measurements were analysed using custom Python code. As before, the natural log of the background-subtracted OD was taken. The first optical density measurement for each well was taken as the background for that well. The first step in measuring the growth rate was to set the length of the "window" over which to measure the gradient. This was generally ten datapoints for fast growing bacteria, and twenty datapoints for slow growing bacteria. The next step was to determine at which datapoint the analysis could start - the earliest datapoints were generally very close to the plate reader's background OD, resulting in noisy LnOD data (see Figure 2.6). Once the initial datapoint had been determined, the gradient over the window was found using the numpy.polyfit function (also returning the residual of the least squares fit). The window was then moved along, one datapoint at a time, over the whole dataset. This generates a list of gradients, and the accompanying residuals.

To find the best-fit maximal growth rate the next step in the analysis was to find the highest gradient with the lowest residual - this was constrained to the first 300 minutes of the growth curve to remove the influence of "regrowth" (see Chapter 3). An example fit can be seen in Figure 2.6. This gradient and residual were used to describe the growth rate.

2.2.2 Colony forming units

Colony forming units (CFUs) are used to estimate the number of viable bacteria in a sample. The sample is diluted, and either spread, or pipetted in drops, onto an LB agar Petri dish. The aim is to reach a bacterial concentration that results in isolated, countable colonies after overnight incubation (Figure 2.7). Each colony

The gradient and residual for the population growing in well H2

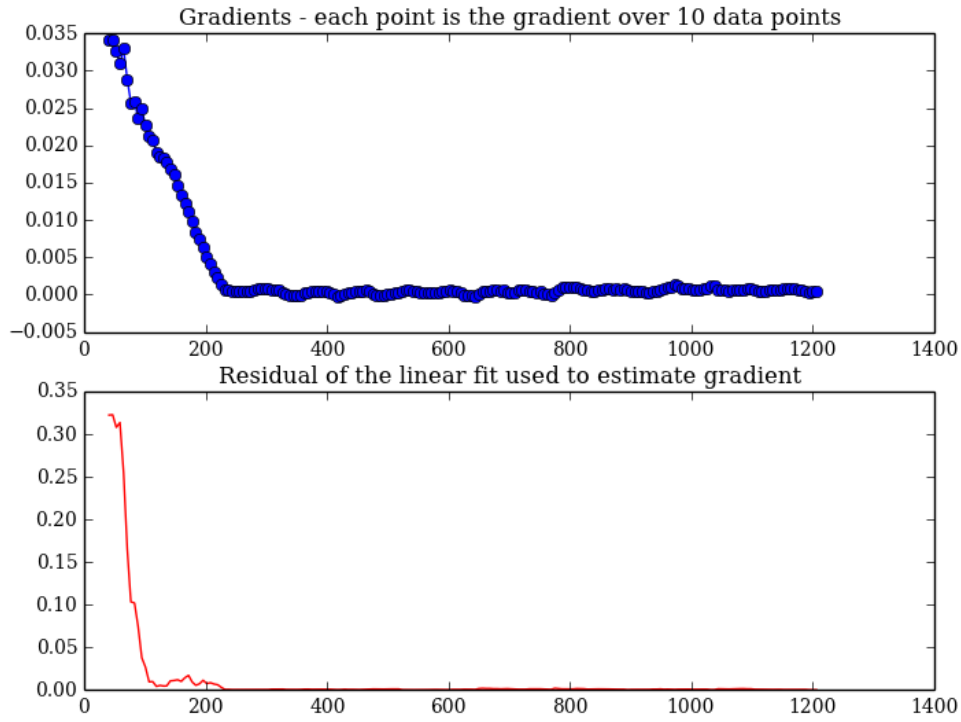

The linear fits for the populaitons growing in wells H2 and H3

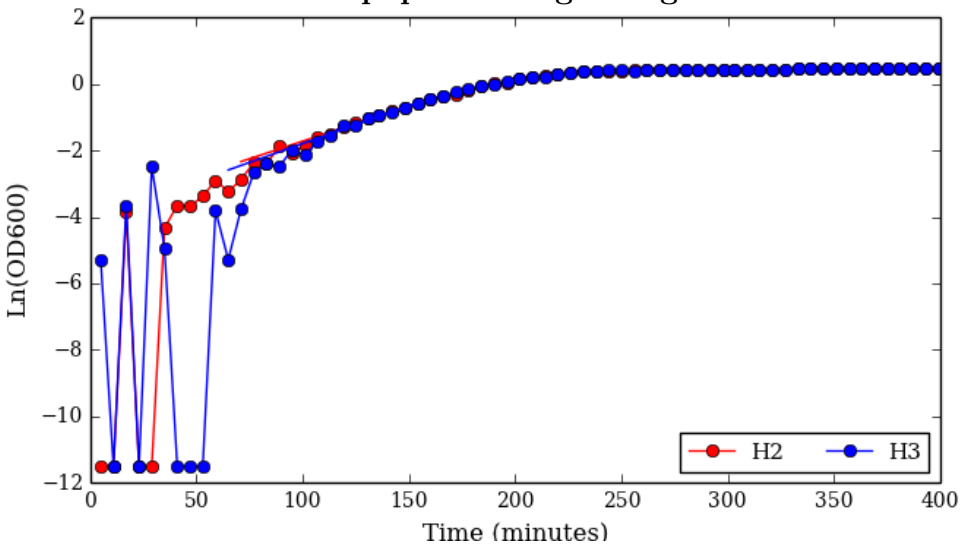

Figure 2.6: Top: A demonstration of how the gradient, and residual, can vary across a plate reader measured growth curve in the absence of antibiotic in MOPSgluRDM. Bottom: The linear fits of the LnOD curve for *E. coli* MG1655 growing in MOPSgluRDM.

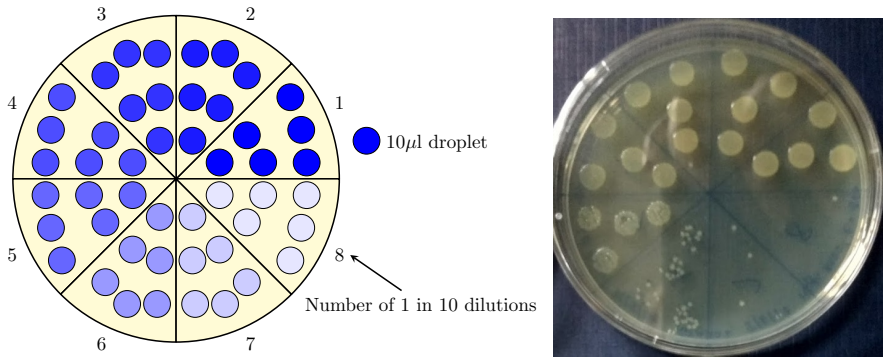

Figure 2.7: Left: A typical plate set-up with eight segments each containing six 10μl droplets. Each segment is for a different culture dilution with the number referring to the number of 1 in 10 dilutions in PBS. For example segment 7 contains droplets of the sample culture diluted 1 in 10000000. The shade of blue in the droplets is a visual guide to demonstrate the increasing diluted nature of the sample across the segments. Right: Example CFU plate from an experiment with the segments aligned with those in the diagram.

is initiated from a single, viable cell, or CFU, and thus by counting the colonies, an estimate for the number of viable bacteria is reached. CFUs are used in this thesis to elucidate the viable *E. coli* population dynamics, which may be obscured in optical density measurements due to changes in bacterial morphology.

To make a CFU measurement, the *E. coli* culture of interest was vortexed for 6 seconds before an initial 1 ml sample was extracted and serially diluted ten fold up to 10^{-8} in PBS (8x1.5 ml eppendorfs had been prepared containing 900μl PBS to which 100μl sample was added). These eight dilutions were pipetted in 6-8 10μl drops onto LB agar plates using the layout in Figure 2.7. This protocol is similar to that in Herigstad et al. [55]. It took an average of 15 minutes to serially dilute and pipette out drops for three concurrent samples. Further measurements were taken at hourly or two hourly intervals for up to six hours.

Once droplets had dried on the LB agar plates they were inverted and incubated at 30°C overnight. This temperature was used to prevent overgrowth of the colonies, which may lead to overlaps and introduce error into the colony count. Viable colony forming units were counted the following morning from whichever dilution that had 3-30 colonies per 10μl drop [55]. This number of colonies was then scaled by the corresponding dilution and drop volume to give a measure of the number of colony forming units in 1 ml of culture.

2.3 Antibiotic preparation

2.3.1 Stock solutions

The antibiotics used were mecillinam (Sigma-Aldrich, product no. 33447), cefotaxime (Fisher Bioreagents, product no. BP2951-1), fosfomycin (Abcam, product no. ab141215), aztreonam (Cambridge Bioscience, product no. 19784-1 g-CAY), ampicillin (AppliChem, product no. A0839), and the antimicrobial A22 (Calbiochem, product no. 475951). All antibiotic stock solutions that were prepared with water were filter sterilised (using Merck Millipore MillexGP 0.22μm filters) before aliquoting (ampicillin (50 mg/ml), cefotaxime (10 mg/ml), fosfomycin (25 mg/ml), mecillinam (3 mg/ml)). A22 stock solution was prepared in DMSO (10 mg/ml) and aztreonam stock solution was prepared in ethanol (25 mg/ml).

Antibiotics can degrade during storage [2], therefore care was taken with antibiotic preparation. Stock solutions were prepared at the recommended antibiotic concentration from the antibiotic powders and kept in 1 or 0.5 ml aliquots at -20°C (wrapped in foil). These stock solutions were defrosted and diluted to the required starting concentration for each experiment. Once a stock solution had been defrosted it was discarded to avoid degradation of the antibiotic.

2.3.2 MIC measurement

A common measure used when discussing antibiotic efficacy is the minimum inhibitory concentration (MIC). Theoretically, the MIC is the minimum antibiotic concentration at which no bacterial growth is observed - thus the MIC is often used to determine the antibiotic dose that should be given to treat a bacterial infection [37]. The definition of the MIC is very generic: 'the lowest concentration of an antimicrobial agent that, under defined in vitro conditions, prevents the appearance of visible growth of a microorganism within a defined period of time' [37], and it is debated whether the MIC should be used for determining clinical doses [139]. Nevertheless, the MIC is a useful number for estimating the antibiotic concentrations to be used in our experiments.

To determine MICs for our chosen antimicrobials, the plate reader and 96-well microplates were used for higher throughput. The growth medium used was Lysogeny Broth and the strain was *E. coli* MG1655. Antibiotics were added at concentrations that decreased geometrically using a protocol known as the broth microdilution technique [19]: antibiotics are added to the top row of the plate at twice the desired volume, e.g. $2x$ μl, of the highest antibiotic concentration. Then x μl of LB plus antibiotic are pipetted and diluted into the next row down, into another x μl of LB. Thus at each row the antibiotic is diluted by a factor of 2 [61](Figure 2.8).

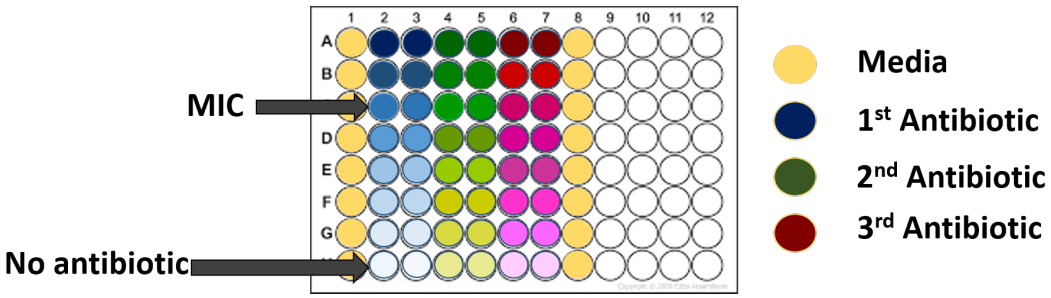

Figure 2.8: Schematic of a 96-well plate set-up with three antibiotics. The highest concentration of each antibiotic is in the top row, with subsequent one in two dilutions down the columns up to the penultimate row. The last row is the growth control with no antibiotic. Columns 1 and 8 contain only growth media as contamination controls.

Initial antibiotic concentration ranges were chosen using the MIC values reported on the EUCAST (the European Committee on Antimicrobial Susceptibility Testing) website on 2/12/2015 and can be found in Table 2.1. The final volume in every well was 200μl. To prepare the antibiotic dilutions, 190μl of growth media was first added to every row, then an additional 150μl was added to the top row giving a total of 340μl. 40μl of antibiotic was the added to the top row to give a total volume of 380μl and a starting concentration of four times the MIC. This was mixed using the electronic pipette by pipetting 190μl up and down, five times. Once mixed 190μl of the top row was pipetted up and added to the next row down, where mixing was again carried out (Figure 2.8). As described previously, this resulted in antibiotic concentrations that decreased two-fold down the columns. No antibiotic was added to the bottom row.

After the antibiotic had been distributed, each well contained 190μl, to which 10μl of *E. coli* MG1655 culture at optical density 0.2 was added, giving a starting inoculation density of optical density 0.01. The 96-well plate was then incubated at 37°C in the plate reader for 24 hours. The MIC was determined as the concentration at which there was no visible growth after the 24 hour incubation.

Antibiotic	EUCAST MIC range (μg/ml)	Our MIC (μg/ml)
Cefotaxime	0.25	0.25
Fosfomcyin	8	8
Mecillinam	1	1.5
Aztreonam	0.03-0.06	0.5
Ampicillin	2-4	8
A22	*2 [141]	0.25

Table 2.1: MIC values used as a starting estimate were found on the EUCAST website, apart from that of the antimicrobial A22. The final MIC values which were measured in this project are also listed here.

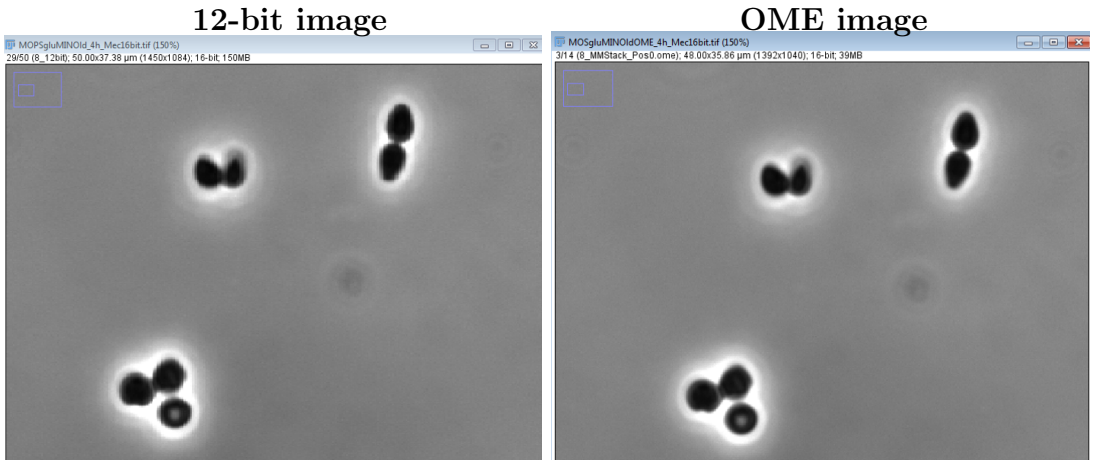

Figure 2.9: The two image formats used with the phase contrast microscopy: 12-bit and OME. The OME format results in a higher resolution image and was used when available.

2.4 Microscopy

The focus of this thesis is on cell wall-targeting antibiotics, which are known to cause changes in the *E. coli* morphology, and one of the aims of this work is to link the antibiotic mechanism of action to changes in morphology. As such, quantifying these morphological changes experimentally using microscopy is crucial to this project. To be consistent with the population dynamics experiments, the majority of the microscopy was carried out on cultures growing in MOPS media variants. MOPS had the added advantage of having little auto-fluorescence, improving the image contrast when fluorescence techniques were used. Two microscopy protocols were used, which had very different cell number throughput.

2.4.1 Phase contrast

The main microscopy protocol used here was phase contrast microscopy, which was primarily performed by Sharareh Tavaddod (University of Edinburgh). In these experiments, at every timepoint, a cell culture growing in a shake flask was sampled and an imaging "chamber" prepared. For the imaging chamber $2-4\mu$l of cell culture was sandwiched between a cover slip and microscope slide, and sealed with VALAP (1:1:1 vaseline, lanolin and beeswax). Imaging was done using an inverted phase contrast microscope (Nikon Ti-U) with a 100×, 1.45 NA phase oil objective in combination with a digital-camera (CoolSNAPHQ2). The images (1392×1040 pixels, 12 bit images are 1450×1084 pixels (Figure 2.9)) were taken from different parts of the chamber, and far from the edges. Some representative images indicating the typical bacteria density per image in rich (MOPSgluRDM) and poor (MOPSgluMIN) media can be seen in Figure 2.10.

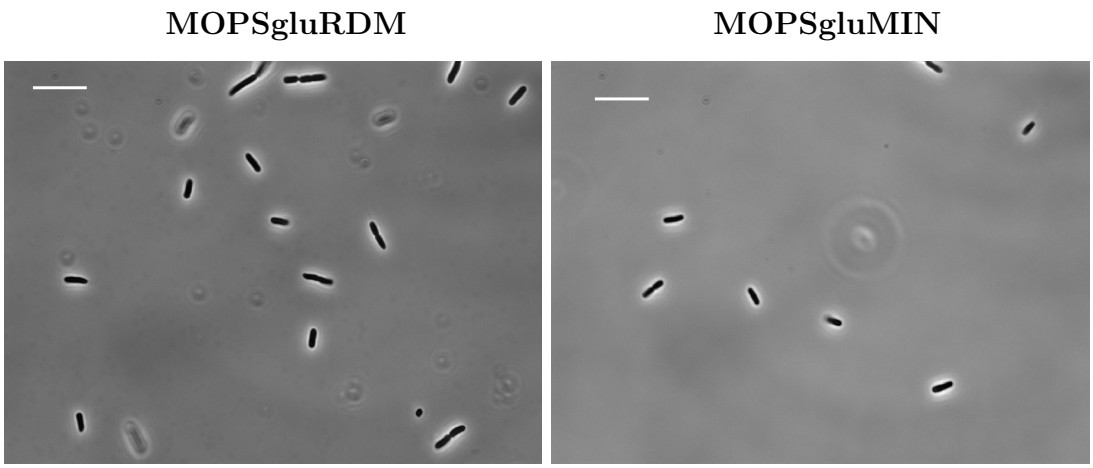

Figure 2.10: Some representative images of *E. coli* RJA002 in MOPSgluRDM and MOPSgluMIN at 100x magnification. Scale bar is 9μm.

Phase contrast microscopy images were processed using MicrobeJ [31] with a pixel conversion of 15.625 pixels per micron. The thresholding used was 'Local Default' with an offset of -20 to 0, depending on the granularity of the images. For bacteria growing in the absence of antibiotic the 'medial axis' mode of detection was used, while for antibiotic-induced morphologies the 'smoothed' mode of detection was employed. Example results of these detection modes can be seen in Figure 2.11. Detected cells were then manually binned into three types: 'septating', 'lysing' and 'normal'. Counts for the three types, and average lengths and widths (with standard deviations) were found using the MicrobeJ results analysis component.

2.4.2 MACS

The MACS (microfluidic-assisted cytoplasmic screening) microscopy protocol was also used in this thesis, in collaboration with Sebastían Jaramillo-Riveri

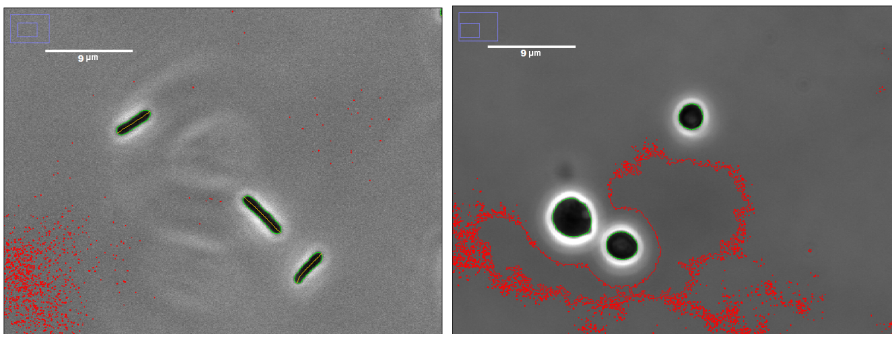

Figure 2.11: Representative images demonstrating the cell detection of MicrobeJ on normal cells (left, using Medial Axis detection) growing for 2 hours in MOPSgluRDM, and on large round cells (right, using Smoothed detection) after growing for 3 hours in MOPSgluRDM with 3μg/ml mecillinam.

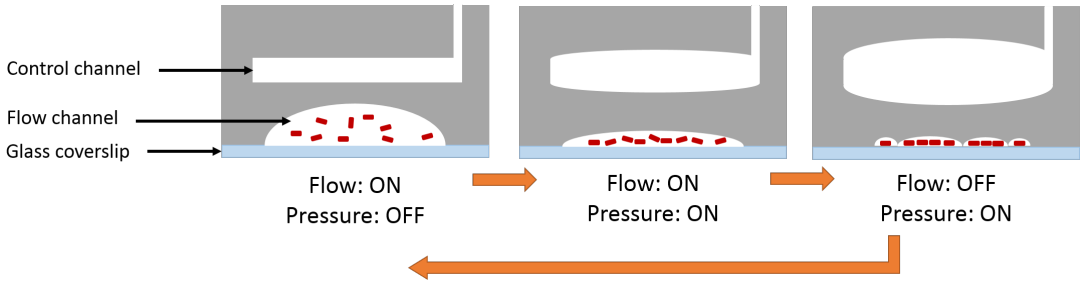

Figure 2.12: Schematic representing the trapping process in the MACS microfluidic device (adapted from Okumus et al. [101]). As pressure is applied, and the flow turned off bacteria form a monolayer on the glass coverslip.

and Meriem El-Karoui (SynthSys, University of Edinburgh). This is a high throughput, novel technique [101], which was employed in an attempt to achieve good population statistics, as many cells can be imaged at each timepoint. MACS works by trapping cells in a microfluidic channel (the "flow channel"). This trapping occurs as follows: a small volume of sample is pumped into the microfluidic device in the flow channel; pressure is applied in a channel perpendicular to the flow channel (the "control channel") deforming the device and squashing the flow channel; bacteria are now trapped in the flow channel; flow is maintained to flush out growth medium; flow ceases and imaging occurs (Figure 2.12). Once images have been taken, the pressure is released and more sample flows through the flow channel, flushing out the previous cells and replacing them with new cells to be trapped [101].

In this way a large number of cells in a sample are rapidly imaged, with the downside that the deformation of the channel to trap the cells may also be deforming the cells themselves. MACS relies on having fluorescent bacteria and a low-fluorescence growth medium in order to clearly visualise the bacteria.

The microfluidic device was used in conjunction with a Nikon Ti-E inverted microscopy and 100x oil immersion objective, maintained at 37°C. The imaging process was controlled by a custom Matlab GUI (Sebastían Jaramillo-Riveri) which controlled the flow and pressure channel, and imaged bacteria trapped

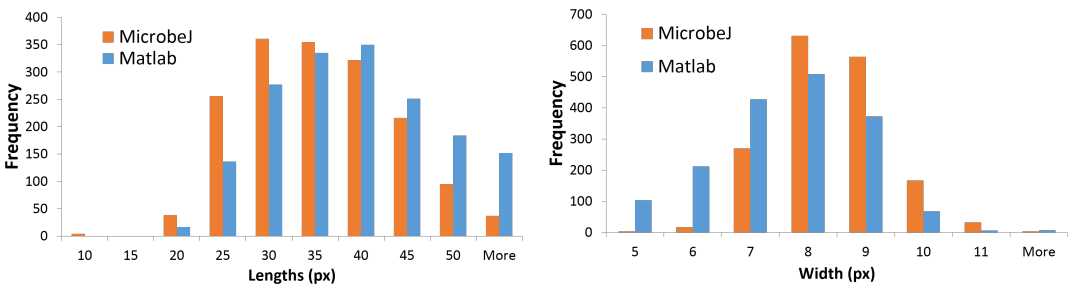

Figure 2.13: A comparison of the length and width distributions measured using the two image processing methods: Matlab GUI or MicrobeJ, for a MACS dataset for *E. coli* RJA002 in MOPSgluRDM with no antibiotic.

in two locations. MACS images were processed with a purpose-built Matlab GUI (Sebastían Jaramillo-Riveri [130]), as the images were generated using a Matlab protocol and saved as Matlab files. The Matlab GUI thresholded the images and identified cell objects using a protocol based on a Matlab routine (https://uk.mathworks.com/help/images/detecting-a-cell-using-image-segmentation.html). The thresholded results from the GUI were then converted to TIF and processed in ImageJ to find lengths and widths of the cells using 'Analyze Particles'. A sample of these images were also processed in MicrobeJ and no significant difference in the average results was found (Fig. 2.13). There is some difference in the tails of the distributions: the Matlab GUI reports a higher frequency of longer, and thinner cells. The discrepancy in the length distributions arises because the Matlab GUI does not perform well on bacteria that are very close end-to-end. In contrast MicrobeJ provides the option for the user to segment these as individual bacteria. Meanwhile, the discrepancy in the width distributions is an artifact from the severe thresholding required when cells were parallel to each other i.e. cells which were in close contact were eroded in order to distinguish the individuals, decreasing the measured width.

For both microscopy protocols cells were alive during imaging. This avoided the potential impact of any fixing procedures on the cell morphology, particularly for delicate cells in the presence of antibiotic.

2.5 Raman Spectroscopy

In this thesis Raman spectroscopy is used to investigate the degradation of antibiotics in growth media (Chapter 3). Raman spectroscopy is concerned with vibrational transitions in laser-excited molecules which appear at frequencies of $10^4 - 10^2$ cm^{-1}. These vibrational transitions originate from vibrations of atomic nuclei within the molecule. In Raman spectroscopy the sample is irradiated by an intense laser beam, and scattered light is observed in the direction perpendicular to the beam. The scattered light has two components: Rayleigh scattering, which has the same frequency as the incident beam and is strong in intensity; and Raman scattering, at the frequency of the incident beam plus/minus the vibrational frequency of the molecule, which is weak [40]. Raman spectroscopy was employed in collaboration with Hugh Vass (School of Physics and Astronomy, University of Edinburgh) to detect changing concentrations of antibiotic in our samples. As an antibiotic molecule has a unique Raman spectrum, changes in antibiotic concentration due to degradation are observable in the Raman signal.

In particular, we were interested in the degradation dynamics of mecillinam in MOPSgluRDM. The MOPSgluRDM growth medium is a complex medium with a strong Raman spectrum. In order to see the mecillinam degradation dynamics on top of this strong background it was necessary to start our experiments with very high concentrations of mecillinam. Luckily mecillinam is usually prepared in water, and therefore it was possible to directly add mecillinam powder to the

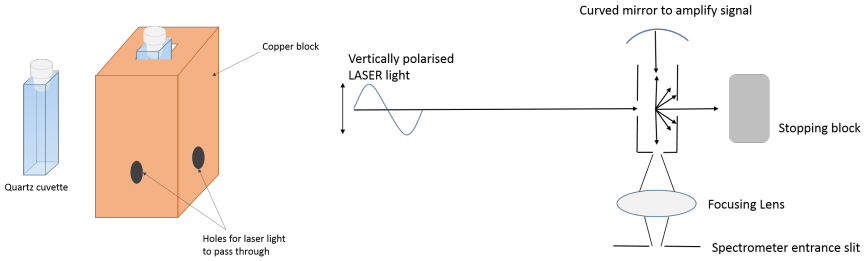

Figure 2.14: The Raman spectroscopy set-up. Left: A representation of the cuvette used to store the liquid sample, and the copper block used to regulate the temperature and block stray light. Right: A diagram of the light path used to obtain the Raman spectra of the sample within the copper block.

MOPSgluRDM at a starting concentration of 3 mg/ml (the typical stock solution concentration). MOPSgluRDM was either used at the standard pH 7.4 or at pH 6.5.

Initially spectra were measured for MOPSgluRDM media at both pH 7.4 and pH 6.5. The spectra for mecillinam in MOPSgluRDM were measured at various timepoints over several days. Media-only spectra were obtained as averages of three independent measurements, while one to two independent spectra were obtained at each timepoint with mecillinam in the media. The Raman spectra were obtained using a high contrast Coderg triple spectrometer set at a resolution between five and six wavenumbers across the recorded spectral region. The excitation source was an argon ion laser operating at 488 nm with plasma lines removed by a prism spectrometer to produce approximately 1W pure laser light though the cell. The sample cuvette was fitted into a copper block with 4 holes at right angles to let the beam through and allow right-angle Raman collection; Figure 2.14 shows a schematic of this set-up. The copper block was temperature controlled to better than 0.1°C with a Eurotherm controller in P.I.D. mode, and maintained at 37°C. To reduce the time taken per scan, allowing better time resolution, spectra were recorded only in the range 0-1800cm^{-1}.

Following data acquisition, difference spectra were obtained by subtracting the (averaged) MOPSgluRDM spectra for a given timepoint from those of the mecillinam-MOPSgluRDM samples at the same timepoint, using Origin. The resulting difference spectra were then cross-referenced with the standard mecillinam spectrum available in Biorad's KnowItAll software. Using peak height relative to the background, peaks were identified which showed clear decay over time. These peaks were assigned using Biorad's KnowItAll software, combined with a literature survey [41, 52, 56, 59, 63, 111, 123, 127, 158]. Two main peaks of interest were determined (see Figure 3.14): 1278 cm^{-1} (thought to be due to twisting of C-N-C [63], or twisting of the CH_2 group [127]) and 1450 cm^{-1} (linked to the CH_2 ring [127]). The peak at 1278 cm^{-1} is thought to be of the most interest as a database search of possible mecillinam degradation products demonstrated that these degradation products generally did not have a peak at 1278 cm^{-1}.

2.6 Whole genome sequencing

In some of our experiments, we suspected that genetic mutants, resistant to the antibiotic, might be emerging at long times (see Chapter 3). To investigate this, we used whole genome sequencing which is a powerful tool to detect mutations in the *E. coli* genome. Cell culture samples were taken from a 96-well plate after incubation for 24 hours with and without antibiotic. Susana Direito (School of Physics and Astronomy, University of Edinburgh) performed genomic DNA extraction using the MasterPure DNA Purification kit and an adapted protocol. Samples were sent to Edinburgh Genomics where the DNA sequencing was performed. Edinburgh Genomics used the Nextera XT sequencing library (a sequencing library is a collection of short DNA fragments with the same short sequences on the 5' and 3' ends [120]) to process the DNA samples into readable fragments (this is an enzymatic process). The DNA fragments were then sequenced using an Illumina HiSeq 4000 75PE. The sequence results were analysed by a bioinformatician (Dr. Alison Meynert, IGMM Bioinformatics Analysis Core Manager, MRC Institute of Genetics and Molecular Medicine kindly performed this analysis for us) and Dr. Bartlomiej Waclaw (School of Physics and Astronomy, University of Edinburgh) carried out a post-processing filtering step to determine the mutations with the highest incidence, and the highest probability of being significant.

In this analysis, single nucleotide or insertion-deletion mutations were identified by comparing the DNA sequence of interest with the DNA sequence of the control strain: any differences between the control DNA sequence and the sample DNA sequence may be mutations. The position of the mutation in the DNA sequence is used to identify which gene has been mutated. As there will be DNA strands from many cells in the sample, and not all cells will necessarily have the same mutations, the frequency of each mutation in the sample is the returned result. Genes with significantly frequent mutations were compared to known resistance gene mutations in the literature for each antibiotic. However a limitation of this gene sequencing method is its inability to identify certain deletions, due to the enzymatic fragmentation (as DNA material may be lost or subjected to faulty end-repair by the ligase [71]) and because the reads sample the genome in a random and independent manner there is a certain percentage of the genome which will not be sequenced (https://emea.illumina.com/content/dam/illumina-marketing/documents /products/technotes/technote_coverage_calculation.pdf).

Chapter 3

Initial characterisation of *E. coli* population dynamics in the presence of cell wall-targeting antibiotics

In this chapter we present a broad-scale investigation of the response of *E. coli* populations to several cell wall-targeting antibiotics. The focus here is on three antibiotics: fosfomycin, cefotaxime and mecillinam. We characterise the population dynamics of *E. coli* during growth in these antibiotics, noting "bumps" in optical density and cell population recovery at late times, which we term "regrowth". We also investigate how these phenomena depend on the growth medium. In these experiments we use inocula prepared using a non-steady state protocol (Chapter 2 Section 2.1.3). In subsequent chapters we will look at some of these phenomena in more detail, and with inocula that are pre-grown to steady state.

Three cell wall-targeting antibiotics were selected that target different stages of the cell wall synthesis process: fosfomycin (Fos.), mecillinam (Mec.) and cefotaxime (Ctx.). The hypothesis was that different growth dynamics might be observed depending on which stage of the cell wall synthesis pathway is inhibited.

3.1 Literature observations of population dynamics with cell wall-targeting antibiotics

Growth curves for *E. coli* in the presence of fosfomycin have been described in the literature: an example from the work of Kurabayashi et al. [76] is shown in Fig. 3.1. It is interesting to see that there is a "bump" in the optical density.

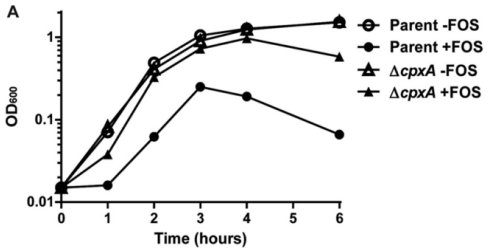

Figure 3.1: Growth curves for *E. coli* MG1655 (shown with circle markers) grown with and without fosfomycin (at a concentration of 0.78 μg/ml), found in Kurabayashi et al (2014) [76].

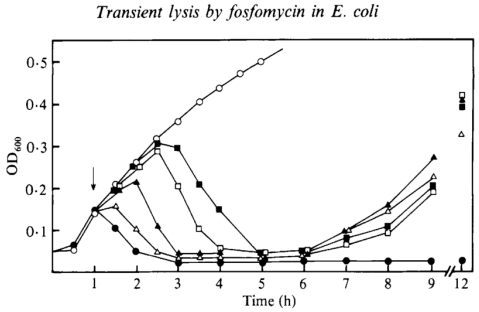

Figure 3.2: Effect of the addition of different concentrations of fosfomycin to cultures of *E. coli* 185 (circles) and *E. coli* 185(pOU900) (squares and triangles). The arrow indicates the addition of fosfomycin [79].

Growth curves over longer times were reported in Leon et al. [79] (Fig. 3.2). These curves also show bumps in the optical density although they do not look exactly the same as those in Figure 3.1, likely due to the use of different *E. coli* strains and different growth media. After 6 hours Leon et al. [79] observed "regrowth"; they found that this was not due to inactivation of the antibiotic but rather some phenotypic change in the bacteria. Along similar lines, Kurabayashi et al. [76] argue that it is physiologically beneficial for the bacteria to reversibly regulate fosfomycin resistance and that, specifically the CpxAR two-component system reversibly controls fosfomycin resistance - thus transient fosfomycin resistance can arise in the presence of fosfomycin [76] (as a side note, Leon et al. [79] also report a growth-rate dependence of the emergence of fosfomycin resistance).

Bumps in the optical density have also been observed for *E. coli* populations exposed to mecillinam (Figure 3.3). These bumps are believed to be due to cell lysis [7]. Similarly, a bump and regrowth have been observed for *E. coli* populations exposed to cefotaxime (Figure 3.4).

Based on this literature we might expect to see bumps, and potentially regrowth, in our population dynamics experiments for *E. coli* exposed to cell wall-targeting antibiotics.

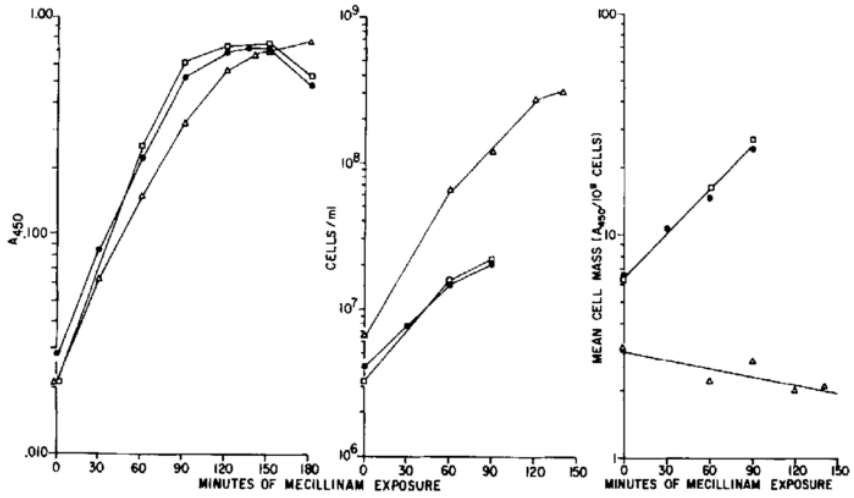

Figure 3.3: Figure 1 from Barbour et al. [7] showing absorbance at 450nm, cell count and mean cell mass for various *E. coli* strains during exposure to 10 μg/ml mecillinam in LB broth.

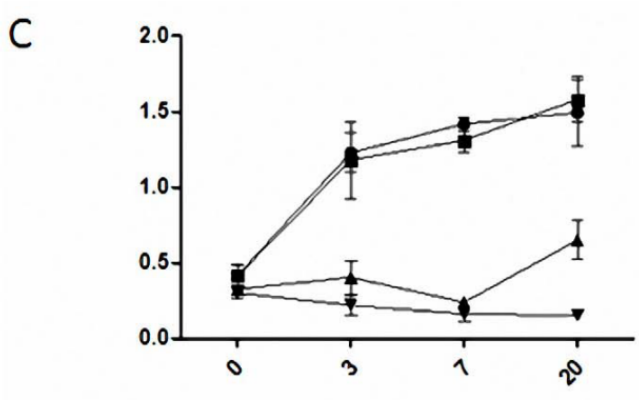

Figure 3.4: Panel C from Figure 3 from Molina-Quiroz et al. [92] showing optical density at 600nm with time (in hours) for *E. coli* exposed to 0.5μg/ml cefotaxime (black upwards triangles) in LB broth.

3.2 Initial growth curves in LB medium

Growth curves were initially measured in LB as this medium is widely used and *E. coli* is known to grow well in it, with doubling times of 20-25 minutes [119]. We used a 96-well plate and a plate reader (see methods Chapter 2) to measure multiple replicate growth curves, using a non-steady state inoculum. This inoculum is considered "non-steady state" as it was only diluted once after growing over night and as such it is likely that the population is composed of bacteria in different phases of growth.

Our plate reader growth curves for *E. coli* MG1655 growing in LB with various concentrations of the three antibiotics cefotaxime (Ctx.), fosfomycin (Fos.) and

(a) Cefotaxime

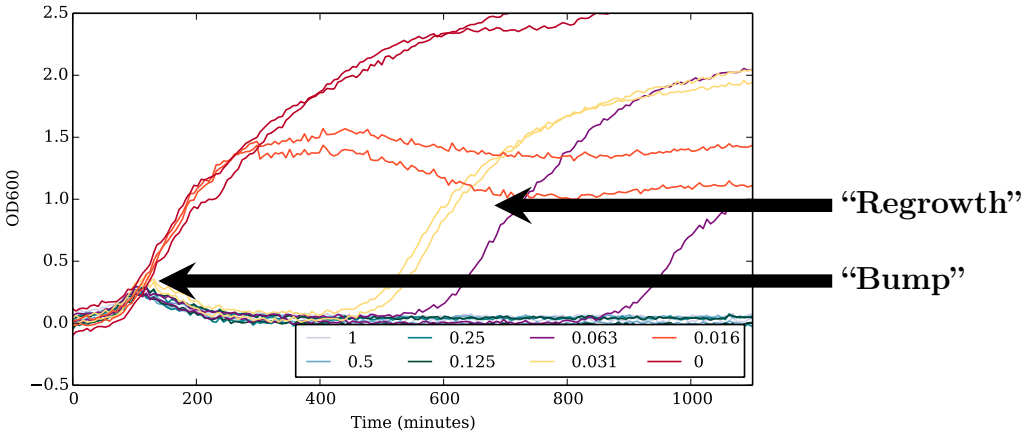

(b) Fosfomycin

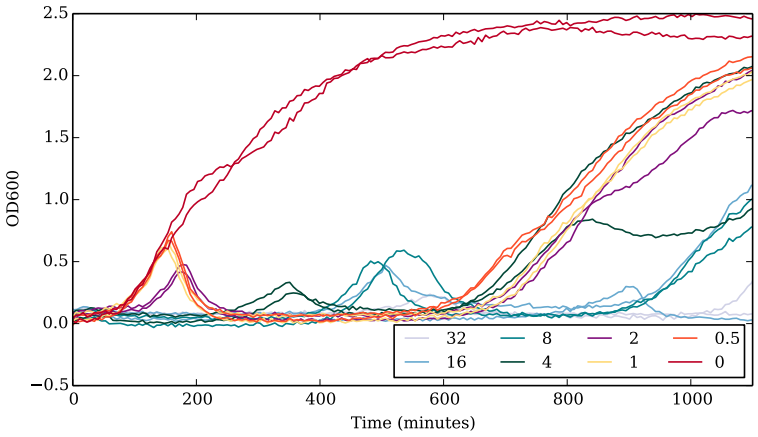

(c) Mecillinam

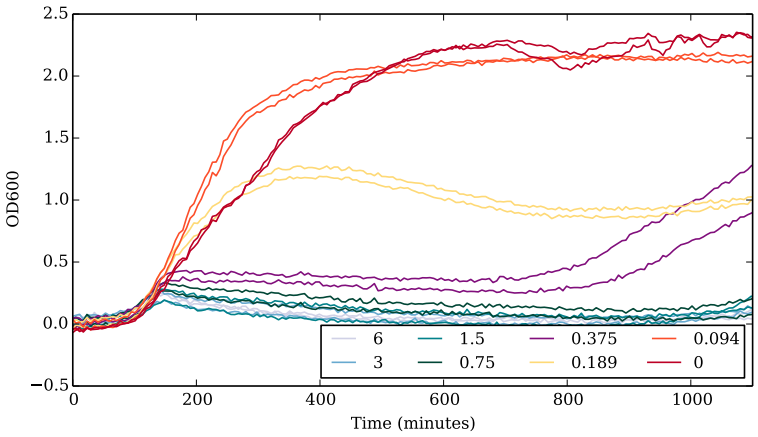

Figure 3.5: Plate reader growth curves (legends contain antibiotic concentrations in μg/ml) for (a) cefotaxime, (b) fosfomycin and (c) mecillinam in LB medium at 37°C. The starting inoculum size was $\sim 10^7$ CFU/ml.

mecillinam (Mec.) can be seen in Figure 3.5. In all three plots the red trace is for growth with no antibiotic i.e. typical *E. coli* growth in the plate reader. For the experiments with antibiotic, two distinctive features, the bump and the regrowth, are found to be common to all three antibiotics (Fig. 3.5). However, we also observe some differences among the three antibiotics.

For cefotaxime (Fig. 3.5a) at concentrations above a certain threshold, a clear bump in the optical density can be seen at around 100 minutes, occurring at the same time for all concentrations. At later times there appears to be population recovery ("regrowth") at sub-MIC concentrations, occurring later for higher concentrations.

Our results for fosfomycin can be seen in Fig. 3.5b. As for cefotaxime, there is a clear bump in the growth curve at a range of fosfomycin concentrations. The growth dynamics are clearly different however, as the bumps occur at different times for different fosfomycin concentrations. The bumps are also much more pronounced than those seen for cefotaxime, with the peak height showing a dependence on the antibiotic concentration. Compared to cefotaxime, there also appears to be a lot more regrowth of the population even at very high fosfomycin concentrations, with the majority of the regrowth appearing after 600 minutes.

Figure 3.5c shows our results for mecillinam. Mecillinam produces growth curves that are different again. Similarly to cefotaxime, we observe a bump above a certain mecillinam concentration which occurs at the same time for all concentrations; however the bump is much less pronounced than those observed for cefotaxime or fosfomycin. Making a comparison to the results of Barbour et al. [7] (Fig. 3.3) it is also interesting to note that, even though a much higher Mec. concentration was used in that work, the bump seems to occur in our experiments at roughly the same time (120-150 minutes). Regrowth is also observed at all concentrations, happening later the higher the antibiotic concentration.

These growth curves are quite different to those that have been reported for antibiotics with other targets (for example, ribosome-targeting antibiotics show a simple decrease in growth rate with increasing antibiotic concentration, with no bumps [48]). Moreover "bumps" and "regrowth" have been relatively little discussed in the literature, even though they are important for understanding the efficacy of cell wall-targeting antibiotics in treating a bacterial infection. These features could arise for several different reasons. The bump indicates an initial increase in optical density (OD) followed by lysis (bursting of the cells). Lysis results in debris which scatters the light less than intact cells, resulting in a decrease in OD. For mecillinam the gradual decrease in OD might suggest that growth is arrested i.e. cell division does not occur, but the non-dividing cells are somewhat stable, only lysing sporadically. In contrast, for fosfomycin, we could hypothesise that lysis is much more sudden, since the decrease in OD occurs sharply and at a well-defined time. An interesting question concerns why for Mec. and Ctx. the bump happens at the same time for all concentrations whereas the bump shifts in time with concentration for fosfomycin. Another factor that

needs to be considered is possible morphological changes of the cell induced by the antibiotics [7, 132]. Changes in cell shape could result in light being scattered differently, impacting on the observed optical density. This will be discussed in detail in Chapters 4 and 5.

The common phenomena of the bump and regrowth will now be investigated in more detail.

3.3 Understanding the bumps

3.3.1 Characterising the bumps: Inoculum effect

We wished to determine whether lysis (which causes the bump) is triggered at a fixed time, or at a fixed population density. We hypothesised that this could be determined by varying inoculum size, i.e. by exposing different initial bacterial inoculum sizes to the same antibiotic concentrations.

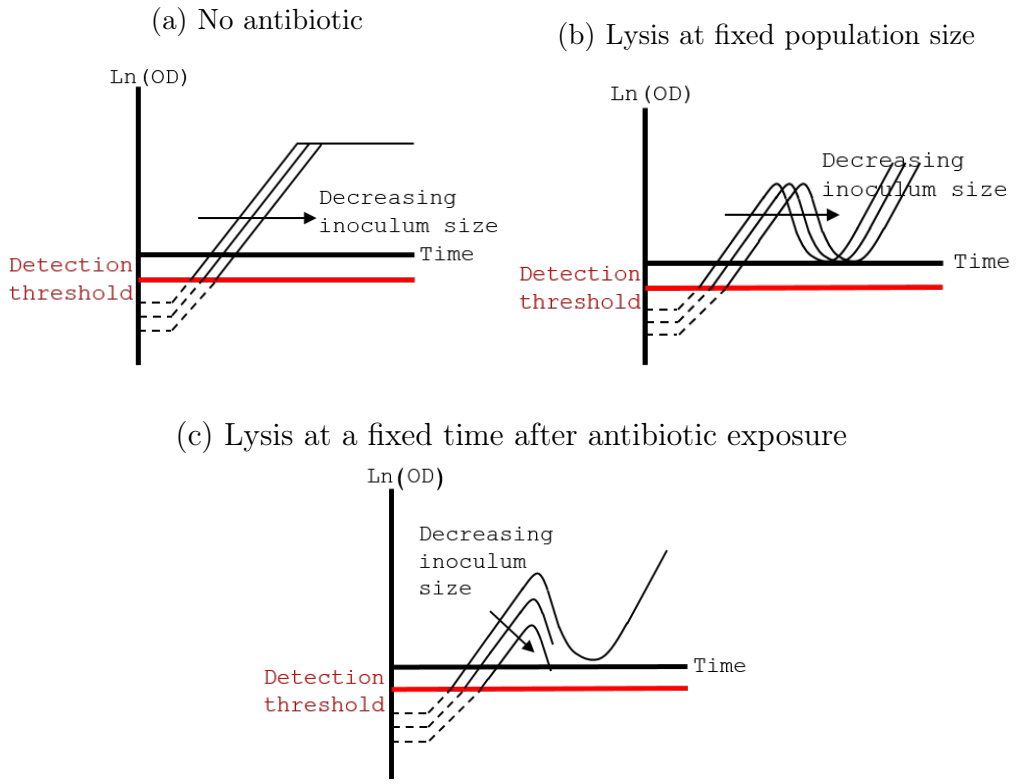

Figure 3.6: a) Hypothesised impact of inoculum size on a standard antibiotic-free growth curve. b) Impact that inoculum size is predicted to have on the bump dynamics if lysis occurs at a fixed critical population size. c) Impact that inoculum size is predicted to have on bump dynamics if lysis occurs at a fixed time after antibiotic exposure.

We had two simple hypotheses about how the dynamics of the bump would change with inoculum size. First, let us consider what is expected if the initial inoculum size was varied in the absence of antibiotics (Figure 3.6a, this has been verified experimentally). As the inoculum is decreased in size, the bacterial density will remain below the detection threshold of the plate reader for longer (if we assume that the lag phase of the bacterial population is independent of the inoculum size). This results in growth curves that appear shifted to later times but have the same gradient. Now let us suppose a cell wall-targeting antibiotic is present. Applying the same thought process to the bump dynamics leads to two potential scenarios, depending on the criteria for lysis onset. If lysis starts to occur at a fixed critical population size (which could depend on the antibiotic concentration) then the bump will be shifted to later times with decreasing inoculum size as in Fig. 3.6b. However if lysis occurs a fixed time after antibiotic exposure then the bump will occur at the same time, but will decrease in height with decreasing inoculum size as the bacterial density at the onset of lysis will decrease.

As can be seen in our experimental results (Fig. 3.7, where only some antibiotic concentrations are shown for clarity), we find that decreasing the initial inoculum size in fact has different effects depending on which antibiotic is present. In the presence of cefotaxime the bump decreases in height and disappears with decreasing inoculum size, Fig. 3.7a. This fits with the hypothesis that lysis starts at a fixed time after antibiotic exposure. In contrast, in the presence of fosfomycin, the bump is shifted to later times (Fig. 3.7b), fitting with the hypothesis that lysis starts to occur once a fixed critical population density has been reached. The situation with mecillinam is more subtle. Figure 3.7c shows that at mecillinam concentrations where growth is barely inhibited, decreasing the inoculum size increases the lag time until growth is detected by the plate reader, similar to the hypothesised scenario in Figure 3.6 when there is no antibiotic. However at higher mecillinam concentrations lowering the inoculum size to 10^5 cfu/ml leads to the emergence of a bump and regrowth pattern where there was previously uninhibited growth, and at the even lower inoculum size of 10^3 cfu/ml no growth is observed (until the regrowth). This cannot be explained by either of the suggested hypotheses. Instead we can conclude that mecillinam shows an "inoculum effect" in combination with lysis onset a fixed time after antibiotic exposure. The term inoculum effect is used to describe a scenario when an antibiotic has different inhibition capacity at different inoculum sizes [139]. In this case mecillinam becomes more inhibitive as the inoculum size decreases from 10^7 cfu/ml to 10^5 cfu/ml.

Broadly speaking our results show support for both lysis hypotheses. For fosfomycin, where the antibiotic target is in the cytoplasm, lysis appears to occur at a fixed population size. Meanwhile, for cefotaxime and mecillinam, where the antibiotic targets are PBPs, lysis appears to occur at a fixed time after exposure to the antibiotics, but with the complication that mecillinam also shows an inoculum effect.

(a) Cefotaxime

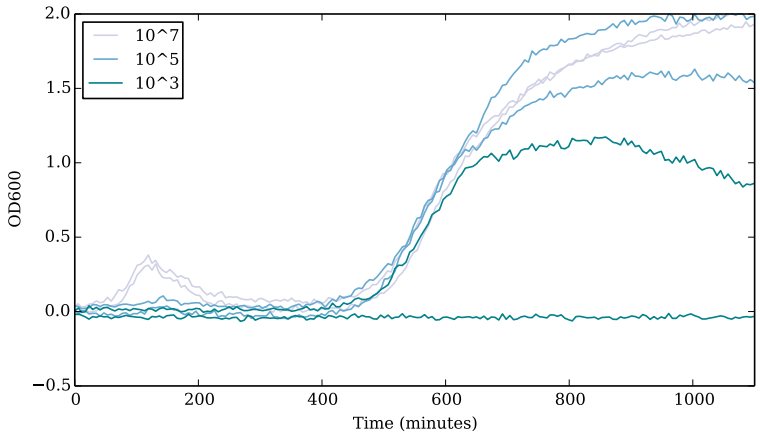

(b) Fosfomycin

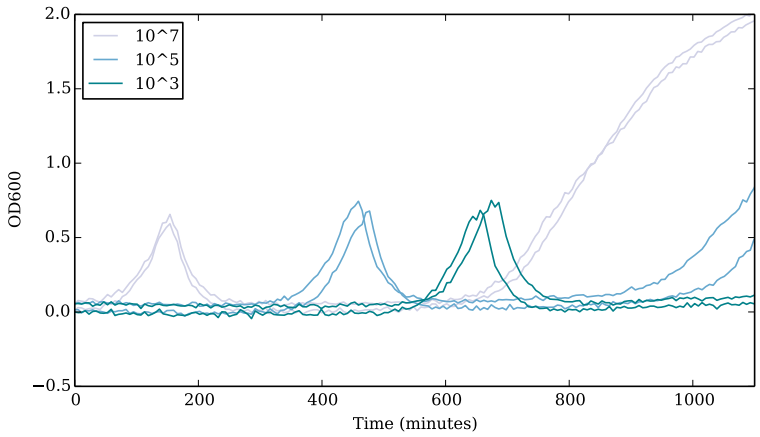

(c) Mecillinam

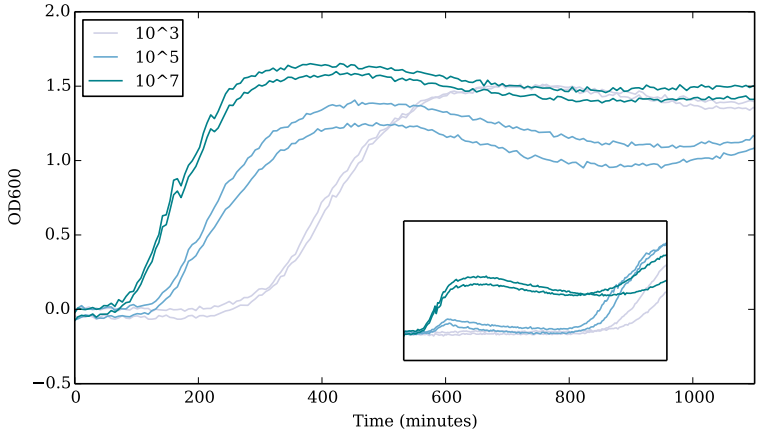

Figure 3.7: Growth curves at 1/8 MIC at different initial inoculum sizes of 10^7, 10^5 and 10^3 CFU/ml for cefotaxime (a), fosfomycin (b) and mecillinam (c). The inset of (c) shows the growth curves at 1/4 MIC mecillinam.

3.3.2 How the bump depends on growth medium

It is known that some antibiotics can be more or less effective depending on whether bacteria are growing quickly or slowly [22, 48, 134]. The "bump" can be regarded as an indicator of antibiotic efficacy (as it signals lysis). Therefore we repeated our experiments on a range of well-defined growth media to determine the impact of the growth medium on the bump dynamics.

Six different nutrient media were explored using MOPS (3-Morpholinopropane-1-sulfonic acid [95]) as a base (in order of increasing growth rate): MOPSglycerol, MOPSglucose, MOPSglycerol+casamino acids, MOPSglucose+casamino acids, MOPSglycerol Rich Defined Media (RDM) and MOPSglucose RDM (see Methods Ch. 2). These media give bacterial doubling times ranging from 25 to ∼170 minutes (Table 3.1). The growth curves for *E. coli* in the presence of fosfomycin, cefotaxime and mecillinam, for the rich and poor MOPSglucose variants (MOPSgluRDM and MOPSgluMIN respectively) can be found in Figure 3.8 and for the intermediate MOPSglucoseCAA and all MOPSglycerol variants in the Appendix (Figures B.5, B.6 and B.7).

To summarise broadly, the bumps that we saw in LB medium (Fig. 3.5) are still observed for all three antibiotics in the rich defined medium MOPSgluRDM (Figure 3.8), demonstrating that this 'growth then lysis' dynamic is associated with a fast growth rate rather than the specific growth medium. Similarly, the dynamics observed on the minimal MOPS defined media (Figure 3.8) correlate well with separate observations on M9 minimal growth medium (Appendix B.2). In Figure 3.8 we have rescaled time by the antibiotic-free doubling time; this makes it easier to compare and contrast the growth dynamics across different growth rates. For example, this rescaling allows us to see that, in the presence of cefotaxime, the bump occurs at approximately five antibiotic-free doublings in both MOPSgluRDM and MOPSgluMIN (Fig. 9.1a and 9.2a). This suggests that we can use the optical density at a set number of antibiotic-free doublings to compare the antibiotic effectiveness across different growth media.

To summarise the growth-medium dependence, the optical density after ten

Growth medium	Doubling time (minutes)
MOPSglycMIN	172 ± 15
MOPSgluMIN	63 ± 5
MOPSglycCAA	48 ± 1
MOPSgluCAA	40 ± 4
MOPSglycRDM	31 ± 3
MOPSgluRDM	25 ± 1

Table 3.1: Doubling times for the different MOPS growth media as measured using the plate reader optical density measurements.

(a) Cefotaxime in MOPSgluRDM.

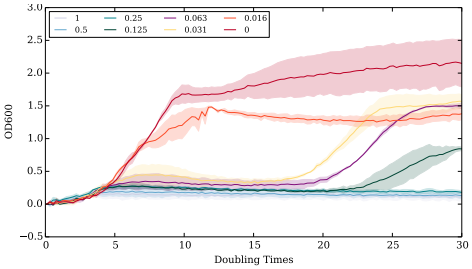

(b) Cefotaxime in MOPSgluMIN.

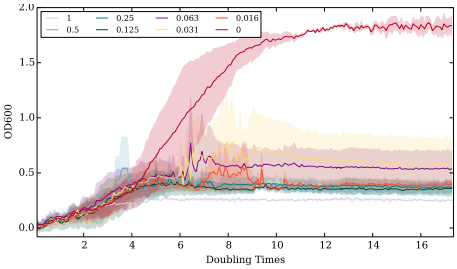

(c) Mecillinam in MOPSgluRDM.

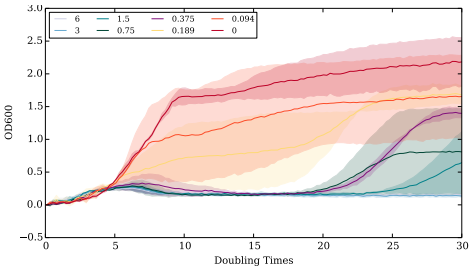

(d) Mecillinam in MOPSgluMIN.

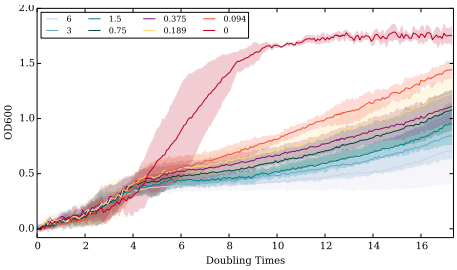

(e) Fosfomycin in MOPSgluRDM.

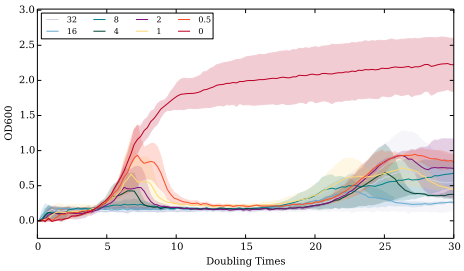

(f) Fosfomycin in MOPSgluMIN.

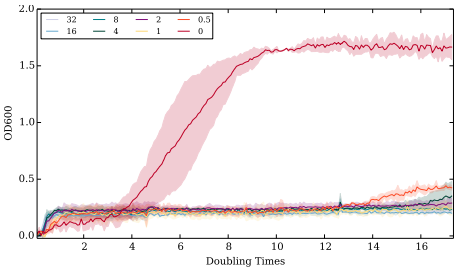

Figure 3.8: Rich and poor MOPSglucose variants with cefotaxime, fosfomycin and mecillinam. Time has been rescaled by the antibiotic-free doubling time to give the growth curves in terms of the number of antibiotic-free doublings. This enables better comparison between the rich and poor growth media.

antibiotic-free doubling times has been taken as a measure of the antibiotic effectiveness (Fig. 3.9). In Figure 3.9, poor growth media curves are shown in the blue spectrum whereas rich growth media curves are shown in the orange spectrum. The optical density at ten antibiotic-free doubling times turns out not to be a very good measure for the effectiveness of fosfomycin as all concentrations lead to a low optical density at this time, missing the bump behaviour that occurs earlier. The optical density at five antibiotic-free doubling times is thus also displayed for fosfomycin to clarify the growth-medium dependence. To further clarify the growth-medium dependence this data has also been plotted in an IC50-like manner (Figure 3.10). The IC50 is the half-maximal inhibitory concentration of the antibiotic and is generally represented as the concentration which leads to a 50% reduction in growth rate of the bacteria. In this case we normalised the optical density at six antibiotic-free doubling times (we used six in this case for increased consistency between the antibiotics) so that it was 1 in the absence

of antibiotic, and then found the antibiotic concentration that would result in a factor of 2 decrease, by linear interpolation, for each growth medium. This "IC50" is then plotted against the drug-free doubling times to indicate how the antibiotic effectiveness changes with growth rate (Figure 3.10).

Below we summarise the results for each antibiotic, combining observations from Figures 3.8, 3.9 and 3.10.

Fosfomycin is more inhibitive on poor media

Fosfomycin exhibits greater inhibition in poorer media (all bumps disappear in Figure 9.2e compared to Figure 9.1e). We also observe an interesting phenomenon that appears in the rich media (Fig. 9.1e) of a "double bump". The reason for this is unclear. Also note that the IC50 decreases with antibiotic-free doubling time in Fig. 3.10.

Mecillinam is more inhibitive on intermediate media

The general observation for mecillinam is that there is greater inhibition at faster growth rates (compare Fig. 9.1c and Fig. 9.2c). This is marked by the separation

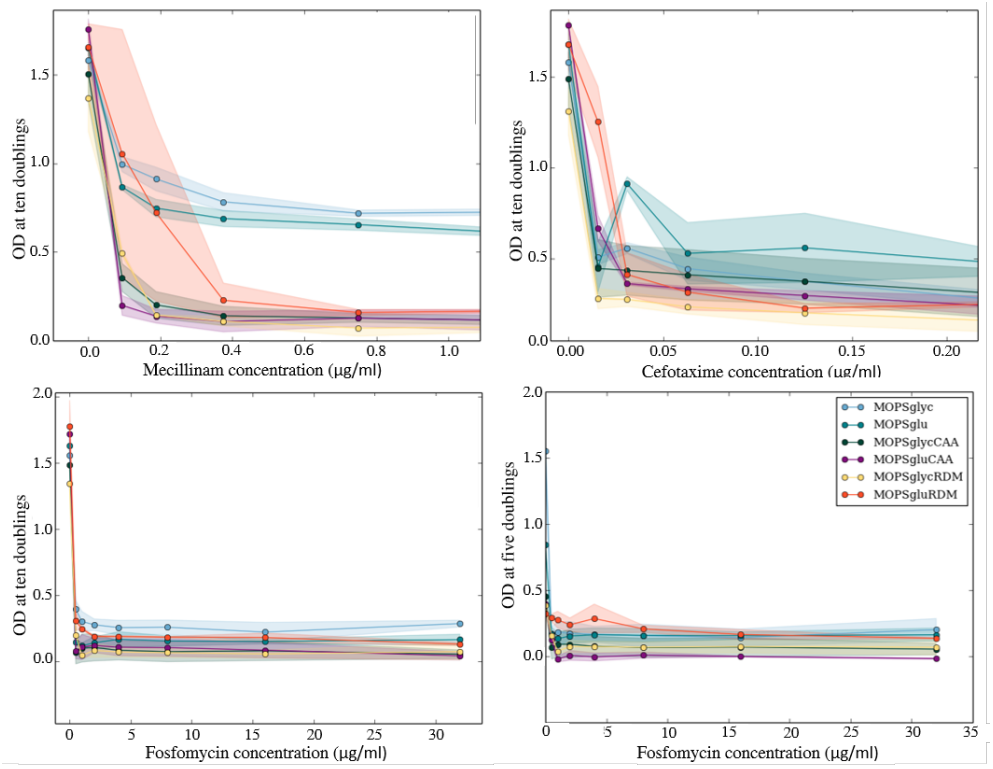

Figure 3.9: 'Inhibition' plots comparing the optical density at ten (or five) antibiotic-free doubling times for various concentrations of mecillinam (top left), cefotaxime (top right) and fosfomycin (bottom left: at ten antibiotic-free doubling times, bottom right: at five antibiotic-free doubling times) across the six different growth media (see legend).

Mecillinam: more inhibitive at intermediate doubling times

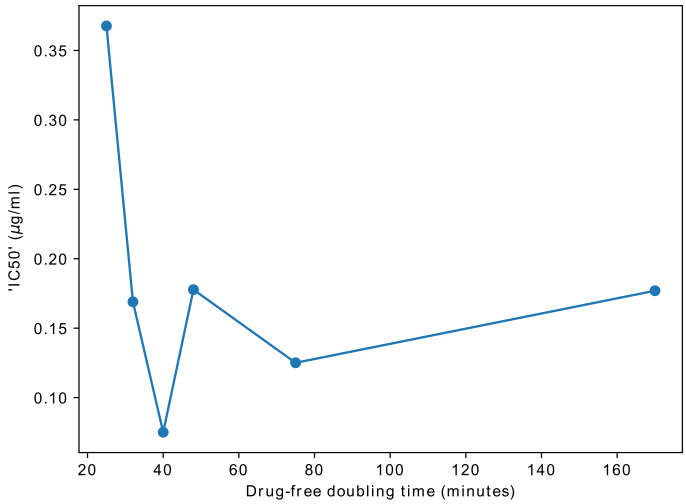

Cefotaxime: more inhibitive at long doubling times

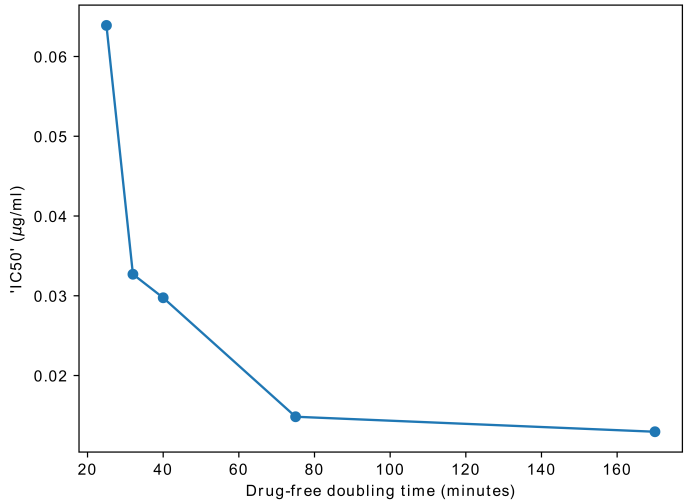

Fosfomycin: more inhibitive at long doubling times

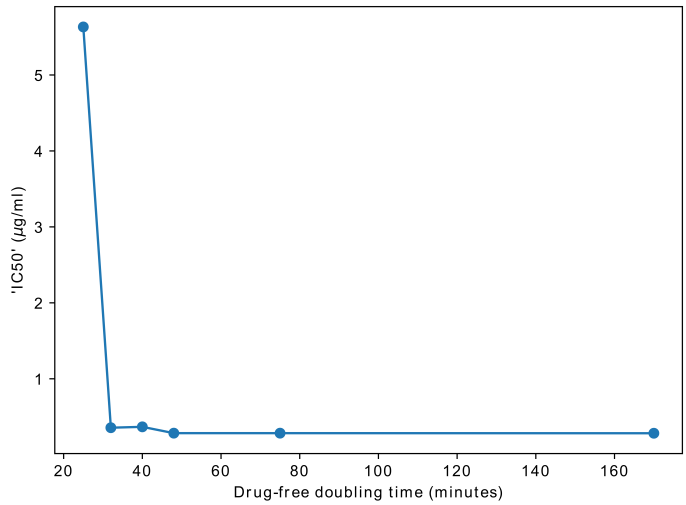

Figure 3.10: Alternative representation of the data in Figure 3.9 using a similar format to the IC50 but relative to OD at 6 drug-free doubling times rather than growth rate.

in the 'OD after ten drug-free doubling times' between MOPSgluMIN/MOPSglyc and the other media, particularly at the higher mecillinam concentrations (Figure 3.9). More subtly, in Figure 3.9 it can be seen that on the intermediate growth media (MOPSglycCAA, MOPSgluCAA and MOPSglycRDM) apparently greater inhibition is observed than on the richest growth medium MOPSgluRDM. This is presented more clearly in Figure 3.10, which suggests a possible non-monotonic dependence on growth medium.

Cefotaxime is more inhibitive on poor media

For cefotaxime, there appears to be little medium-dependence at high concentrations. However, at the lowest cefotaxime concentration of 0.016 μg/ml we observe greater inhibition in the poorer media compared to MOPSgluRDM (Figure 9.1a, Fig. 9.2a and Fig. 3.9). This increased inhibition at longer doubling times is clarified in Figure 3.10 where the IC50 decrease with antibiotic-free doubling time. Interestingly, this is the opposite scenario than observed for mecillinam.

These observed growth rate dependencies may be linked to the mechanism of action of the antibiotics. Mecillinam primarily inhibits the elongation mechanism of *E. coli*, whereas both cefotaxime and fosfomycin inhibit the division process in some way. One might then hypothesise that cell wall-targeting antibiotics that only inhibit the elongation machinery are more effective at faster growth rates, whereas antibiotics that inhibit the division machinery are more effective at slower growth rates. As will be discussed in later chapters, however, this situation turns out to be more complex.

3.4 Understanding "regrowth"

A striking characteristic of our growth curves is the "regrowth" of the bacterial population at long times (after 400 minutes). This could be important clinically as it suggests that apparently eliminated infections may be able to regrow. One explanation for the regrowth is that the antibiotic is simply degrading or being used up over the course of the experiment. Another possibility is that bacteria within these populations are becoming resistant to the antibiotic. This could be transient resistance (e.g. due to gene regulatory changes), or it could be genetic resistance (due to mutations) which will be maintained even when the antibiotic is removed. To investigate this in more detail we determined the properties of the bacterial population at the end of growth curve, by carrying out 're-inoculation' experiments, combined with whole genome sequencing (Section 3.4.1.1). Later we also tested directly for antibiotic degradation (Section 3.4.2).

3.4.1 Re-inoculation experiments

We hypothesised that if regrowth was due to a decrease in the effective antibiotic concentration then when the population that is present at the end of an experiment, is re-inoculated into fresh media (with antibiotic), then the population should be sensitive to the antibiotic and should reproduce its original growth curve for that antibiotic concentration. Alternatively, if regrowth is due to resistant mutants then the population at the end of the experiment will be resistant and growth curves upon re-introduction to the antibiotic should be more like wild-type growth curves with no antibiotic present. Furthermore, as resistance can be permanent or transient, allowing the population to grow for some time in the absence of antibiotic (LB only), prior to re-introduction to the antibiotic, should show if resistance is transient. For permanent resistance, growth curves upon re-introduction to the antibiotic should be similar regardless of how long the population has grown in LB only. However, if resistance is transient a reversion to antibiotic-sensitive growth is expected after longer periods of growth in LB only.

To test these ideas, we designed the following protocol. 100μl samples were extracted after 24 hours' growth in the plate reader, at a range of concentrations of mecillinam, fosfomycin and cefotaxime. These samples were diluted so that the inoculum size for the next "round" would be comparable to the initial

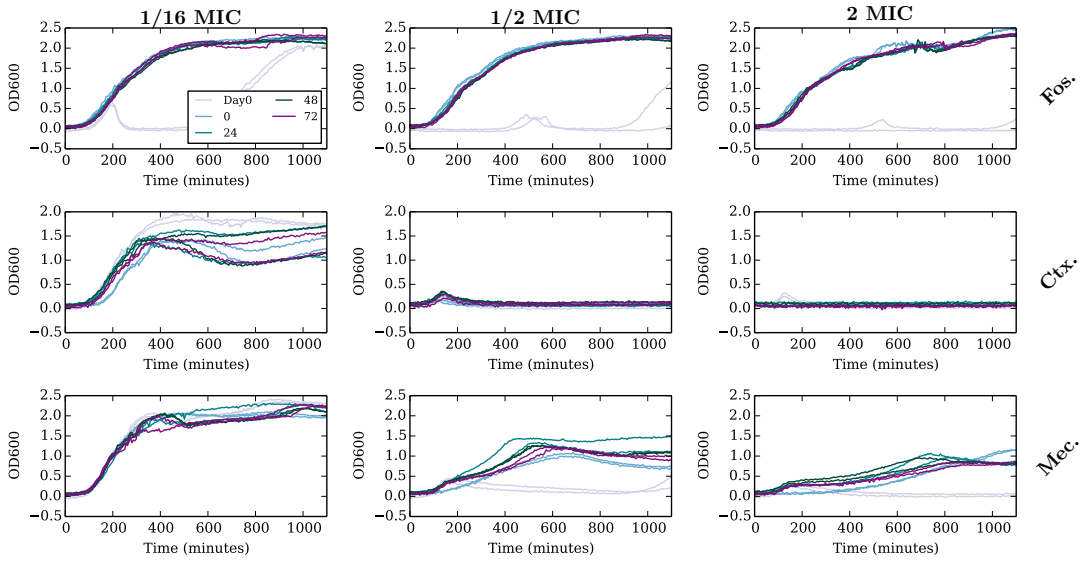

Figure 3.11: Growth when cultures are re-inoculated into the same antibiotic concentration as previously exposed to on Day 0, with breaks in LB of varying lengths, shown in hours in the legend i.e. the pink curves show growth at the indicated antibiotic concentration after a 72 hour break growing only in LB. Fosfomycin curves indicate the emergence of resistance. Cefotaxime curves indicate antibiotic degradation. Mecillinam curves seem to indicate a mixture of resistance and antibiotic degradation.

inoculum size. The samples were then either re-introduced to the same antibiotic concentration that they had grown in (for another 24 hours), or were inoculated in LB only. We defined a "break" as a period of 24 hours' growth in LB only. Multiple breaks were carried out, so some samples had up to 72 hours growing in LB before being re-introduced to the antibiotic. After each break the sample was diluted to achieve the desired inoculum size and re-inoculated. The purpose of the breaks in LB was to determine whether any resistance observed was transient or permanent.

This protocol resulted in a large number of growth curves. A select sample of these can be seen in Figure 3.11. Here, the first row shows experiments in the presence of fosfomycin, the second row cefotaxime and the third row mecillinam. The first column shows growth curves at 1/16 MIC for the respective antibiotics, the second column at 1/2 MIC and third column at 2xMIC. The grey growth curves are from the initial exposure to the antibiotic, while the other colours correspond to the different numbers of breaks: no break, one, two or three breaks.

The fosfomycin curves clearly indicate, at all three concentrations, that the population at the end of the initial regrowth has become long-term resistant to the antibiotic, as consistently wild-type growth is observed, regardless of the length of break in LB.

A very different outcome is observed with cefotaxime. Surprisingly, at the low concentration of cefotaxime, growth is observed after all the different LB break lengths but growth is reduced compared to that observed upon initial exposure to this concentration of Ctx. The intermediate cefotaxime concentration demonstrates the outcome expected when no resistance arises, i.e. similar, sensitive, growth is observed after each re-inoculation. At the high Ctx. concentration there were no viable cells left after Day 0 (as indicated by the lack of growth in the first LB break, not shown). Taken together, these results seem to suggest that regrowth in cefotaxime occurs due to a decrease in antibiotic concentration.

For mecillinam, we observe that at the lowest concentration used the antibiotic has negligible impact on the growth of *E. coli*. At the other Mec. concentrations the bacterial population grows better upon re-inoculation but growth is still hampered in comparison to growth without antibiotic. This may indicate a partially resistant population, perhaps due to a mixture of resistant and sensitive bacteria. Another explanation could be that the effective mecillinam concentration is decreasing (mecillinam is degrading) over the course of the initial 24 hours, and that resistance emerges at a lower effective mecillinam concentration, and so is only partially resistant when re-exposed to the initial mecillinam concentration.

3.4.1.1 Whole genome sequencing

To further understand the re-inoculation experiment we decided to sequence samples from 24 hour plate reader cultures with observed regrowth. Based on our interpretation of the re-inoculation experiments we did not expect to observe resistance in the cefotaxime regrowth, therefore we only used one cefotaxime sample. For fosfomycin and mecillinam the re-inoculation experiments suggest that resistance may be emerging and therefore two samples for each antibiotic were chosen.

The sample cultures sent for genome sequencing were collected from a 96-well plate after 24 hours of incubation with or without antibiotic in LB. The samples consisted of one control (from growth without antibiotic), two samples from growth with fosfomycin (0.5 and 0.25MIC), two samples from growth with mecillinam (1/16 and 2MIC) and one from growth with cefotaxime (0.25MIC). The results of the genome sequencing (method described in Chapter 2) are in the form of mutation frequencies (Table 3.2). As the samples are composed of mixed populations, it is likely that there are range of mutations present. The mutation frequency is determined by the number of reads that had the mutation relative to the total number of reads. If a mutation is causing the observed regrowth it is expected to occur at high frequency in the population, therefore the sequencing results were sifted to find the most abundant mutations. These mutation frequencies can be found in Table 3.2.

The green highlights in Table 3.2 indicate samples where high mutation frequencies were observed in genes which are known to contribute to resistance if mutated (based on literature reported resistance mutations for the relevant antibiotic [38, 132]). Blue highlights indicate samples with mutation frequencies that are high but for which no evidence was found in the literature linking these mutations to antibiotic resistance.

Resistance mutations detected for fosfomycin

At the higher fosfomycin concentration we detected a mutation in the *glpT* gene which encodes for the GlpT transporter. This is one of the transporters used by fosfomycin to enter the bacterium and reach its target in the cytoplasm [66]. We observed that this mutation is accompanied by a high incidence of mutation in the *paaX* gene. The *paaX* gene encodes for a transcriptional repressor that participates in transcriptional regulation of genes involved in the catabolism of

Condition	Gene Mutation Frequency													
	sdhA	yeaJ	rfbC	yjgL	stfE	paaX	glpT	yciH	pykF	wbbI	ptsI	ddlA	waaL	lysS
0.5MIC Fos.	0.1149		1.0		0.1449	0.4371	0.4320							
0.25MIC Fos.			0.3279					0.1111	0.3934	0.1071	1.0000			
0.25MIC Ctx.	0.1359	0.1096	1.0	0.1667										
2MIC Mec.			1.0		0.1429									0.9527
0.0625MIC Mec		0.1148	0.9828									0.1089	0.1111	

Table 3.2: Table of significant gene mutation frequencies, ignoring those that were present in the antibiotic-free control.

phenylacetic acid [39]. We hypothesise that this may be linked to a change in *E. coli* metabolism to avoid glucose uptake, since fosfomycin enters the cytoplasm via the same route as glucose [38]. At the lower fosfomycin concentration these mutations do not appear, and instead we observe mutations in the *ptsI* and *pykF* genes. Mutations in *ptsI* can reduce the expression of GlpT [66] therefore this mutation could also corresponds to reduced uptake of fosfomycin. Mutations in *pykF* have also been linked to reduced glucose uptake [122]. All in all our genome sequencing results agree with our interpretation of the re-inoculation experiment, that regrowth in the presence of fosfomycin is due to the emergence of genetic mutations. Interestingly, *uhpT*, a gene commonly associated with fosfomycin resistance when mutated [38, 66, 76], does not appear in our data.

Resistance mutation detected for mecillinam

The only significant mutation that we detected in our mecillinam samples is in the gene *lysS* (for the high concentration of mecillinam). This mutation does not appear in the work of Thulin et al. [132], who describe over thirty genes associated with mecillinam resistance [132]. However, the *lysS* gene is related to tRNA charging, and mutations in tRNA-related genes have been found to result in increased levels of ppGpp, which in turn confers resistance to mecillinam, as PBP2 is no longer required for growth under conditions of high ppGpp [29, 144]. From the literature we might have expected to see more resistance mutations [132]; however our observation of only a single resistance mutation is consistent with the partially inhibited growth observed in the re-inoculation experiment (Figure 3.11). Our conclusion is therefore that regrowth in mecillinam is only partially due to resistance, and may also be due to a decrease in the effective mecillinam concentration.

No resistance mutations detected for cefotaxime

We observed no significant gene mutations in our cefotaxime sample. This is consistent with the re-inoculation experiment which found no evidence for resistance in the presence of cefotaxime. Therefore regrowth in the presence of cefotaxime is hypothesised to arise solely due to a decrease in the effective cefotaxime concentration.

3.4.2 Antibiotic degradation

In several of our population dynamics experiments with mecillinam it was observed that the antibiotic stock tended to decrease in potency over time. This strongly suggested that mecillinam degrades easily and we hypothesised that this degradation could be contributing to the observed regrowth in the presence of mecillinam. To investigate this, we developed a "delay-time bioassay".

The delay-time bioassay measures antibiotic degradation rates by sequential bacterial inoculation of identically-prepared wells in a 96-well microplate, at

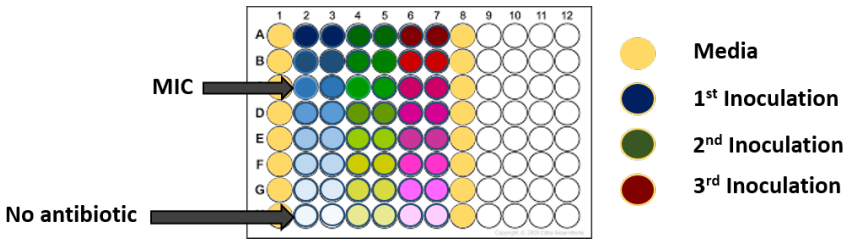

Figure 3.12: Diagram of a 96-well plate used in the delay-time assay. The first inoculation occurs immediately after the antibiotic is added to the plate, and thus can be assumed to experience the expected antibiotic concentrations. The second inoculation occurs 2 hours later, while the third inoculation occurs 4 hours after the first. If there is any degradation of the antibiotic then this will be reflected by an increased level of growth in the second and third inoculations.

regular time intervals. If an antibiotic is degrading over time we should observe a change in the growth dynamics between sequential inoculations. For example, if an antibiotic had a half-life of two hours, and an inoculate "A" is added two hours after the plate is filled with antibiotic, at what was initially a concentration of X μg/ml, inoculate "A" should exhibit the growth dynamics normally associated with a concentration of X/2 μg/ml.

More specifically, the delay-time bioassay is an adaptation of the protocol for measuring the MIC (Methods Chapter 2). A microplate was set up as in Fig. 3.12, with at least 6 columns of 190 μl antibiotic-supplemented growth medium per well. In these columns, the antibiotic concentration was diluted 2-fold in successive rows, and the bottom row contained no antibiotic. The starting concentration was set at four times the MIC as measured by ourselves (Table 2.1 in Chapter 2), therefore the third row was at the MIC. At least one additional column was prepared with growth medium only, as a control for contamination.

At the start of the experiment, the first 2 columns were inoculated with 10μl of a "starter" culture of *E. coli* RJA002, that had been prepared to be in the exponential phase of growth at OD$\sim$0.2. Following inoculation, the OD of the inoculated wells was $\sim$0.01 and the final volume was 200μl. The plate was incubated in the plate reader, with OD measurement, as described in Chapter 2 (37°C, 600rpm double orbital shaking). At the same time, the starter culture was diluted such that it was expected to again reach OD$\sim$0.2 after a period of 2 hours. After the plate and starter culture had been incubated for 2 hours, the plate was removed from the plate reader, the next 2 columns were inoculated from the starter culture, the starter culture was again diluted, and incubation of the microplate was continued. This process was repeated until all wells had been inoculated. The plate was then incubated in the plate reader, with OD measurement, for a further 16-18 hours.

Following data acquisition, OD measurements from each pair of replicate wells were averaged. Furthermore, as the optical density was measured continuously for each well from the start of the experiment, each set of data was time-shifted

by its inoculation time, so that the beginning of each growth curve corresponds to the addition of bacteria. The background optical density of the growth media was subtracted for each well, using each well's first data point as that well's background. This is feasible as the starting optical density of 0.01 is below the plate reader's detection threshold.

This results in a set of growth curves, corresponding to bacterial growth in media that had been pre-incubated for different lengths of time prior to inoculation. Figure 3.13 a) shows that we do indeed observe differences in the growth curves in the presence of mecillinam when there is no delay, compared to a two hour delay, prior to inoculation. In order to extract a half-life for the antibiotic, under these experimental conditions, it was necessary to quantify the observed differences in the growth curves. To achieve this quantification, we set a threshold OD value (OD_t) of 0.75 and recorded, for each growth curve, the time, T, taken to reach this threshold OD.

Plotting T versus $\log_2$(antibiotic concentration) allows us to directly compare the antibiotic effectiveness at the different inoculation times. If there is no antibiotic degradation then every growth experiment (from different inoculation times) should result in the same T versus $\log_2$(antibiotic concentration) curve. However, if there has been antibiotic degradation the T versus $\log_2$(antibiotic concentration) curve will shift in the positive x-direction as inoculation time increases. The antibiotic half-life is the inoculation delay required to shift the T versus $\log_2$(antibiotic concentration) curve by one unit to the right on the x-axis. An example of this analysis is shown in Figure 3.13 b), from which an

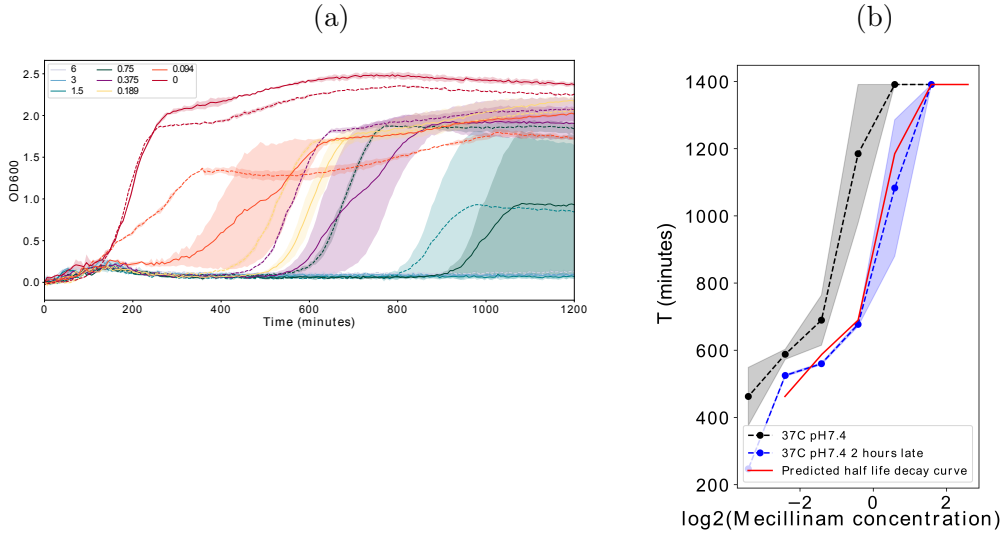

Figure 3.13: a) Growth dynamics of *E. coli* RJA002 in MOPSgluRDM pH 7.4, 37°C, under initial inoculation (solid lines) and two hour delayed inoculation (dashed lines). Initial antibiotic concentrations are displayed in the legend in μg/ml. b) The corresponding analysis which approximates a half-life of 2 hours. Shaded areas represent the standard deviation between replicates.

estimate of the antibiotic half-life can be obtained (2 hours in this case).

3.4.2.1 Mecillinam degradation

Using the delay-time bioassay with *E. coli* RJA002 growing in MOPSgluRDM (pH 7.4 and 37°C) we determined that the half-life of mecillinam was around 2 hours (Figure 3.13b).

The rapid degradation inferred from our delay-time bioassay was confirmed by direct measurement of mecillinam degradation using Raman spectroscopy in collaboration with Hugh Vass (University of Edinburgh). Raman spectra were measured for samples of mecillinam (at 3 mg/ml) in MOPSgluRDM, and for MOPSgluRDM alone, over a period of 60 hours (see Methods Ch. 2). Figure 3.14 shows part of the resulting subtracted spectra (shifted vertically for clarity). A peak at 1278 cm^{-1}, which is believed to arise due to the amidine link in the mecillinam molecule (see Fig. 1.12 and Methods), clearly disappears over time. This is consistent with evidence that the primary degradation pathway for mecillinam is via hydrolysis of the amidine bond [5]. Fitting an exponential decay function to the relative peak height at 1278 cm^{-1} as a function of time gives a half life of 1.3 ± 0.4 hours (Fig. 3.14), in agreement with the delay-time bioassay value of ~ 2 hours.

3.4.2.2 Increasing mecillinam stability

To perform bacterial growth experiments in the presence of mecillinam, one would like to find conditions under which mecillinam is more stable, while the bacterial growth rate is perturbed as little as possible. Decreasing pH is known to increase the stability of mecillinam in aqueous solution [5]. *E. coli* grows well only in the range pH 6.0 to 7.5 [109], and MOPS acts as a pH buffer in the range pH

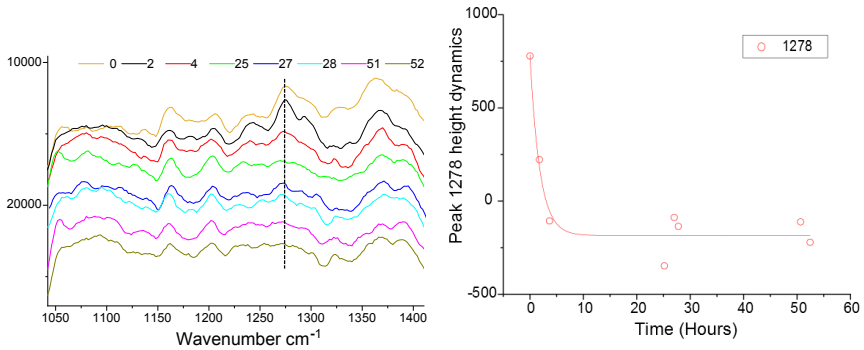

Figure 3.14: Left: Raman spectra from the region of interest between 1000 and 1400 wavenumbers from 0 to 52 hours for 3 mg/ml mecillinam in MOPSgluRDM at 37°C and pH 7.4. Right: Peak height dynamics at 1278 cm^{-1} fit with an exponential decay which gives a half life of 1.3 ± 0.4 hours.

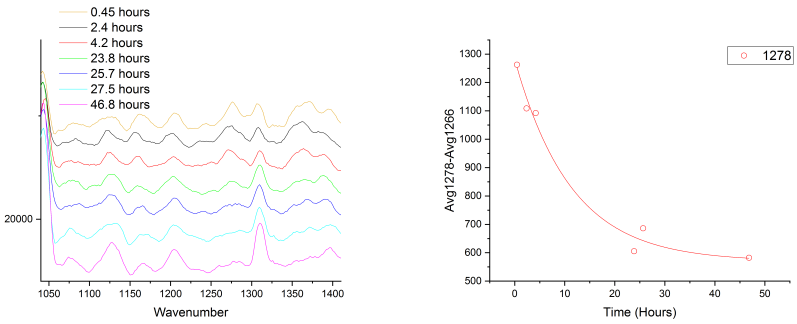

Figure 3.15: Left: Raman spectra from the region of interest between 1000 and 1400 wavenumbers from 0 to 52 hours for 3 mg/ml mecillinam in MOPSgluRDM at 37°C and pH 6.5. Right: Peak height dynamics at 1278 cm^{-1} fit with an exponential decay which gives a half life of 7.8 ± 3.1 hours.

6.2 to 8.0 [95]. Therefore we repeated our delay-time bioassay in MOPSgluRDM medium at the lower pH of 6.5. As expected, this led to an increase in half-life of mecillinam, to approximately 4 hours (Figure 3.16), which was confirmed by Raman spectroscopy (Figure 3.15). Since this is still rather short on the timescale of a typical bacterial growth experiment, we sought to further optimise the conditions by decreasing the temperature. Therefore we repeated the delay-time assay at 34°C, for pH 7.4 and pH 6.5. While a decrease in temperature to 34°C on its own did not significantly increase mecillinam stability (Figure B.8), combining the temperature decrease with a pH of 6.5 led to a mecillinam half-life of more than six hours, while still maintaining acceptable bacterial growth rate (Table 3.3). Decreasing the temperature to 30°C resulted in a significantly lower bacterial growth rate (Table 3.3) and was therefore not considered any further.

To conclude, regrowth in the presence of mecillinam is caused in part by a previously little remarked decay of mecillinam in bacterial growth medium (half-life of approximately two hours) in standard experimental conditions (media at pH 7.4 and 37°C). Regrowth appears later in growth media at pH 6.5 (Figure B.8, Appendix) (but still significantly within the timescale of a typical experiment).

Temperature (°C)	pH	Growth rate (/h)	Mecillinam half-life (h)
37	7.4	1.24 ± 0.20	2
37	6.5	1.18 ± 0.06	4
30	7.4	0.63 ± 0.23	N/A
34	7.4	1.43 ± 0.02	≥ 2
34	6.5	1.13 ± 0.22	> 6

Table 3.3: Growth rates in MOPSgluRDM at varying temperature and pH, measured by applying a linear fit to the log of the optical density measured in the plate reader (note the data for 34°C and pH 7.4 is from only two replicates). The corresponding half-life of mecillinam measured using the delay-time bioassay is also included.

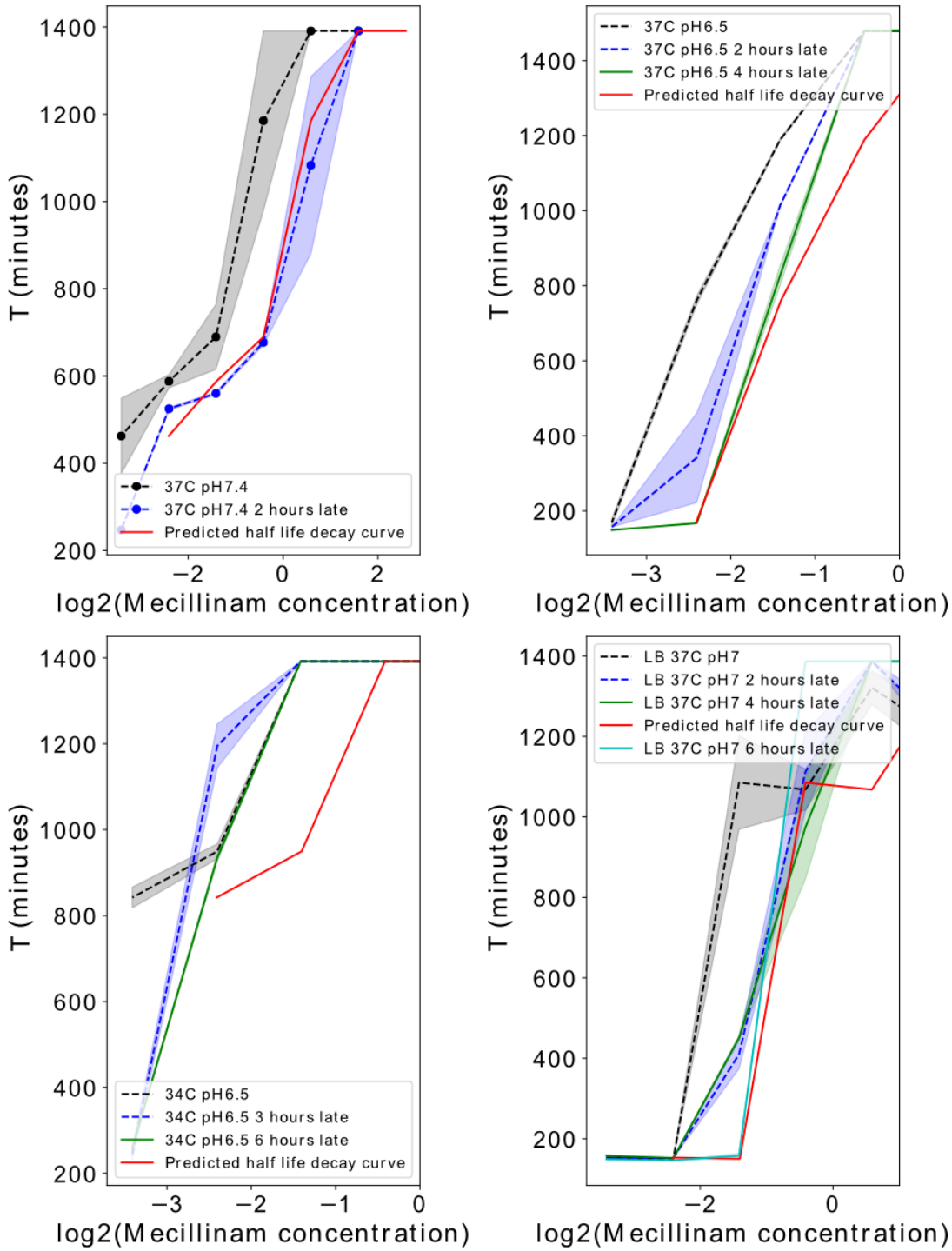

Figure 3.16: Summary of analysis results to approximate the half-life of mecillinam under different environment conditions. Top left: MOPSgluRDM at 37°C and pH 7.4, half-life of mecillinam is approximately 2 hours. Top right: MOPSgluRDM at 37°C and pH 6.5, half-life of mecillinam is approximately 4 hours. Bottom left: MOPSgluRDM at 34°C and pH 6.5, half-life of mecillinam is greater than 6 hours. Bottom right: LB at 37°C and pH 7, half-life of mecillinam is between 4 and 6 hours.

The best experimental condition for measuring population dynamics in the presence of mecillinam was determined to be 34 °C and pH 6.5.

3.4.2.3 Cefotaxime degradation

A delay-time bioassay was also performed to determine whether cefotaxime degradation was contributing to the regrowth observed. Only three cefotaxime concentrations result in regrowth (Figure 3.17, left panel) and thus the delay-time bioassay (Figure 3.17, right panel) focuses on this concentration region of interest. Degradation of cefotaxime appears to be concentration-dependent. We observe that the cefotaxime concentrations of 0.031 and 0.063μg/ml appear to have half-lives of around four hours, whereas the concentration of 0.125μg/ml appears to have a half-life greater than six hours.

From this delay-time bioassay we conclude that cefotaxime can have a short half-life of four hours in MOPSgluRDM at pH 7.4 and 37°C. Therefore previous observations of regrowth in LB are also likely to be due to the degradation of cefotaxime.

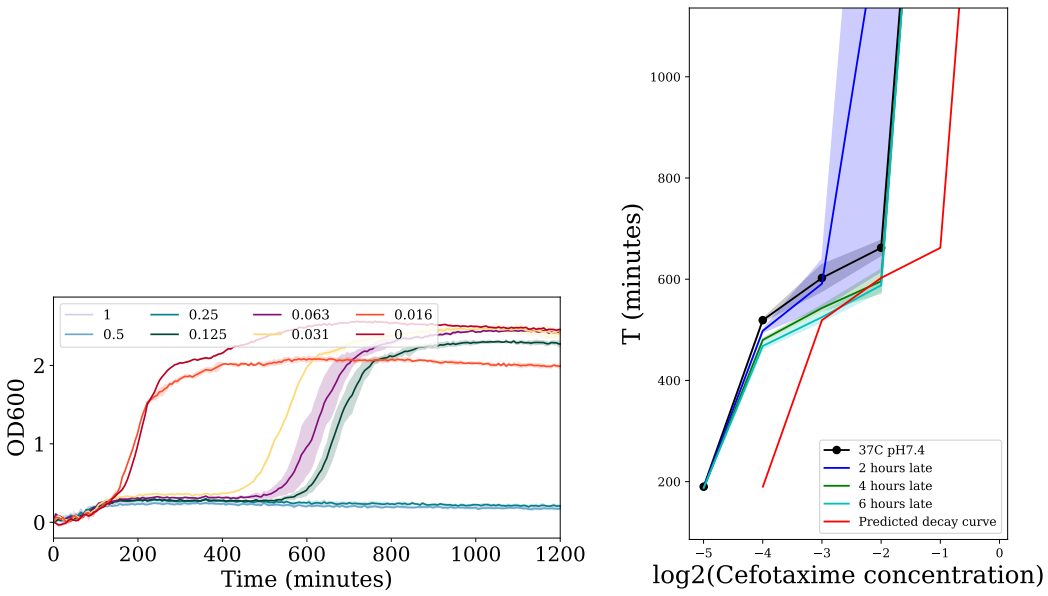

Figure 3.17: Left: Plate reader OD curve for *E. coli* RJA002 growing in the presence of cefotaxime in MOPSgluRDM at 37°C and pH 7.4. Only the intermediate concentrations (0.031μg/ml, 0.063μg/ml and 0.125μg/ml) are observed to result in regrowth. Right: Delay-time bioassay results for cefotaxime degradation in MOPSgluRDM at 37°C and pH 7.4, focusing on the intermediate concentrations (~ -4, -3 and -2).

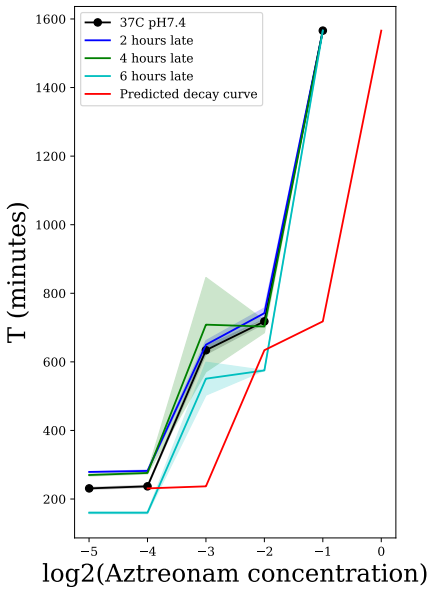

Figure 3.18: Delay-time bioassay results for aztreonam degradation in MOPSgluRDM at 37°C and pH 7.4. Aztreonam has a half-life of 6 or more hours in this growth medium.

3.4.2.4 Aztreonam degradation

Aztreonam is another antibiotic of interest that will be studied in this thesis, so it is important to know how stable aztreonam is in our experimental conditions. A delay-time bioassay was therefore performed in MOPSgluRDM at 37°C and pH 7.4. The results of this can be found in Figure 3.18, from which we conclude that aztreonam has a half-life of 6 or more hours, and can therefore be assumed to be stable in this growth medium.

3.5 Summary of our initial series of experiments

In this chapter we have discussed a series of experiments using non-steady state inocula (see methods Ch. 2) and plate reader optical density measurements. Using these experiments we explored the growth dynamics of *E. coli* in LB and MOPS media variants in the presence of fosfomycin, mecillinam and cefotaxime. The main outcomes from these experiments were as follows:

1. There are two key features of the OD growth curves in the presence of cell wall-targeting antibiotics: “bump” and “regrowth”.

2. The shape and dynamics of the bump change in different growth media, indicating growth-medium dependent antibiotic efficacy.

3. The shape of the bump appears to have some dependence on the mechanism of action of the antibiotic.

4. The regrowth can result from the emergence of resistant mutations on fosfomycin and mecillinam.

5. The regrowth observed in the presence of mecillinam and cefotaxime is also due to degradation of the antibiotic.

Due to observation 5, all of our subsequent experiments with mecillinam will be carried out at 34°C and pH 6.5 to minimise the impact of degradation on the observed results. Additionally, in our subsequent work we will continue to consider cell wall-targeting antibiotics with different mechanisms of action to further elucidate how the mechanism of action influences the population dynamics in different growth media. Furthermore, as the regrowth is generally due to either a genetic mutation or antibiotic degradation it will be ignored in the development of our mathematical model (Chapters 6 and 7) which will focus on the early time growth dynamics in the presence of cell wall-targeting antibiotics.

Chapter 4

Mecillinam: population dynamics and morphology

4.1 Introduction

Chapter 3 presented a broad overview of the population dynamics of *E. coli* in the presence of various cell wall-targeting antibiotics, revealing a dependence of the dynamics on the detailed mode of action of the antibiotic. However for so many antibiotics it was not feasible to achieve a deep understanding of the cellular mechanisms behind the population dynamics. To increase the depth of the study it was necessary to reduce the number of antibiotics investigated.

For this detailed study we focused on two antibiotics: mecillinam and aztreonam. These were chosen because they both bind specifically to a given molecular target. Mecillinam targets PBP2, a monofunctional transpeptidase, which is active during bacterial elongation [16], and aztreonam targets PBP3, also a monofunctional transpeptidase, which is active during cell septation [16]. This specificity of binding makes it easier to interpret our results in terms of molecular mechanisms and to build a mathematical model.

In this chapter the population dynamics of *E. coli* RJA002 growing in the presence of mecillinam are examined in detail, in parallel with the morphological changes observed using microscopy. All the experiments described used *E. coli* RJA002 prepared in the steady state growth condition (as described in Methods Chapter 2 Section 2.1.3) in MOPSglucose variants. *E. coli* RJA002, which has a YFP fluorescent tag, was used throughout to ensure consistency between the population dynamics experiments and the microscopy work.

The morphological changes due to mecillinam were carefully characterised using steady state *E. coli* RJA002 in both MOPSgluRDM and MOPSgluMIN. The main method for imaging the cells was phase contrast microscopy (as described in Chapter 2 Section 2.4.1); some further imaging of the mecillinam-treated

cells was performed using the MACS imaging protocol (described in Chapter 2 Section 2.4.2). The results of these two imaging protocols will be compared, to test the capability of the MACS to produce high-throughput data when the cell wall is potentially compromised. The results from the phase contrast microscopy will be used in conjunction with the mathematical model in later chapters, as the experimental conditions for this imaging protocol were more tightly controlled and more consistent with those of the population dynamics experiments.

In the literature mecillinam has been reported to result in a bump in the optical density due to cell lysis [7], and to produce round cell morphologies [126]. It is thought that these round morphologies arise because cell wall growth continues primarily via pole synthesis [144]. We will recover these observations in our own experiments, whilst building our own dataset for use with our mathematical model.

Experimental results for aztreonam will be presented in the next chapter.

4.2 Population dynamics

The population dynamics of *E. coli* RJA002 in the presence of mecillinam were measured in two different types of experiments. Firstly, we measured growth in small volumes (200μl) via optical density measurements in a plate reader. Secondly, we tracked growth in larger volumes (10 ml) in a shake flask with regular measurements of the optical density (using a spectrophotometer) and colony forming units (CFUs). The plate reader was used to measure the dynamics for a wide range of mecillinam concentrations over a 22-24 hour period. This allowed us to select two mecillinam concentrations of particular interest to use in our shake flask experiments. It was desirable to study fewer mecillinam concentrations with the shake flask as these experimental techniques (particularly CFU measurements) are more labour intensive. It was also desirable to corroborate the plate reader-observed dynamics using shake flask growth, as there are potential issues with growth in a 96-well plate due to the smaller volumes and potentially reduced oxygen transfer [32]. For the shake flask experiments, measurements of CFUs were included because optical density cannot differentiate easily between changes in cell size/shape versus changes in cell number. As lysis has been reported in the presence of mecillinam [7] it is necessary to count the colony forming units to have a quantitative measure of the number of viable cells in the population.

The various antibiotic-free growth rates and doubling times measured in the plate reader and shake flask experiments can be found in Table 4.1 for growth media at pH 6.5 and 34°C (as this condition was found to increase the stability of mecillinam, Section 3.4.2). For the rich media, the plate reader and shake flask doubling times agree well (Table 4.1). However, in the poor media (MOPSgluMIN) the plate reader measured doubling time is

Experimental method	Growth media	Growth rate (/h)	Doubling time (min)
Plate reader OD	MOPSgluRDM	1.52 ± 0.04	27 ± 1
Shake flask OD	MOPSgluRDM	1.42 ± 0.03	29 ± 1
Shake flask CFUs	MOPSgluRDM	1.71 ± 0.08	24 ± 1
Plate reader OD	MOPSgluMIN	0.62 ± 0.05	67 ± 5
Shake flask OD	MOPSgluMIN	0.75 ± 0.03	55 ± 2
Shake flast CFUs	MOPSgluMIN	0.71 ± 0.04	58 ± 3
Shake flask OD	MOPSgluCAA	0.93 ± 0.08	45 ± 4
Shake flask CFUs	MOPSgluCAA	1.09 ± 0.04	38 ± 1

Table 4.1: Growth rates and doubling times measured for *E. coli* RJA002 growing without antibiotic in different growth media in different experimental protocols. These experiments were performed at pH 6.5 and 34°C.

significantly longer than that measured with the shake flask OD (Table 4.1). From the CFU measurements we find faster doubling times in MOPSgluRDM and MOPSgluCAA, compared to the doubling time determined from the optical density. The opposite is observed in MOPSgluMIN (Table 4.1). The shake flask optical density growth rates will be used as the growth rate values in the mathematical model. Growth rates were calculated as described in Chapter 2 Section 2.2.1.3.

4.2.1 Population dynamics observed in the plate reader

Figure 4.1 shows the observed population dynamics in the presence of mecillinam for *E. coli* RJA002 in two growth media. Both the rich and poor growth media (MOPSgluRDM and MOPSgluMIN respectively) are at pH 6.5 and 34°C, a condition found to increase the stability of mecillinam to a half-life of approximately 6 hours (Chapter 3 Section 3.4.2.2).

We first observe that mecillinam is less inhibitive at all concentrations on the poor growth medium (MOPSgluMIN) compared to the rich growth medium (MOPSgluRDM) (Fig. 4.1). This agrees with the previously discussed literature (Chapter 1) suggesting that cell wall-targeting antibiotics are more inhibitive for faster growing bacteria. This also agrees with the preliminary results discussed in Chapter 3.

Additionally, Fig. 4.1 shows that for the rich growth condition there is very little change in the inhibitory dynamics as the mecillinam concentrations is increased above 0.189μg/ml. Similarly, on the poor growth medium all mecillinam concentrations tested produce remarkably similar population dynamics. Both these observations might suggest saturation of binding of mecillinam to PBP2.

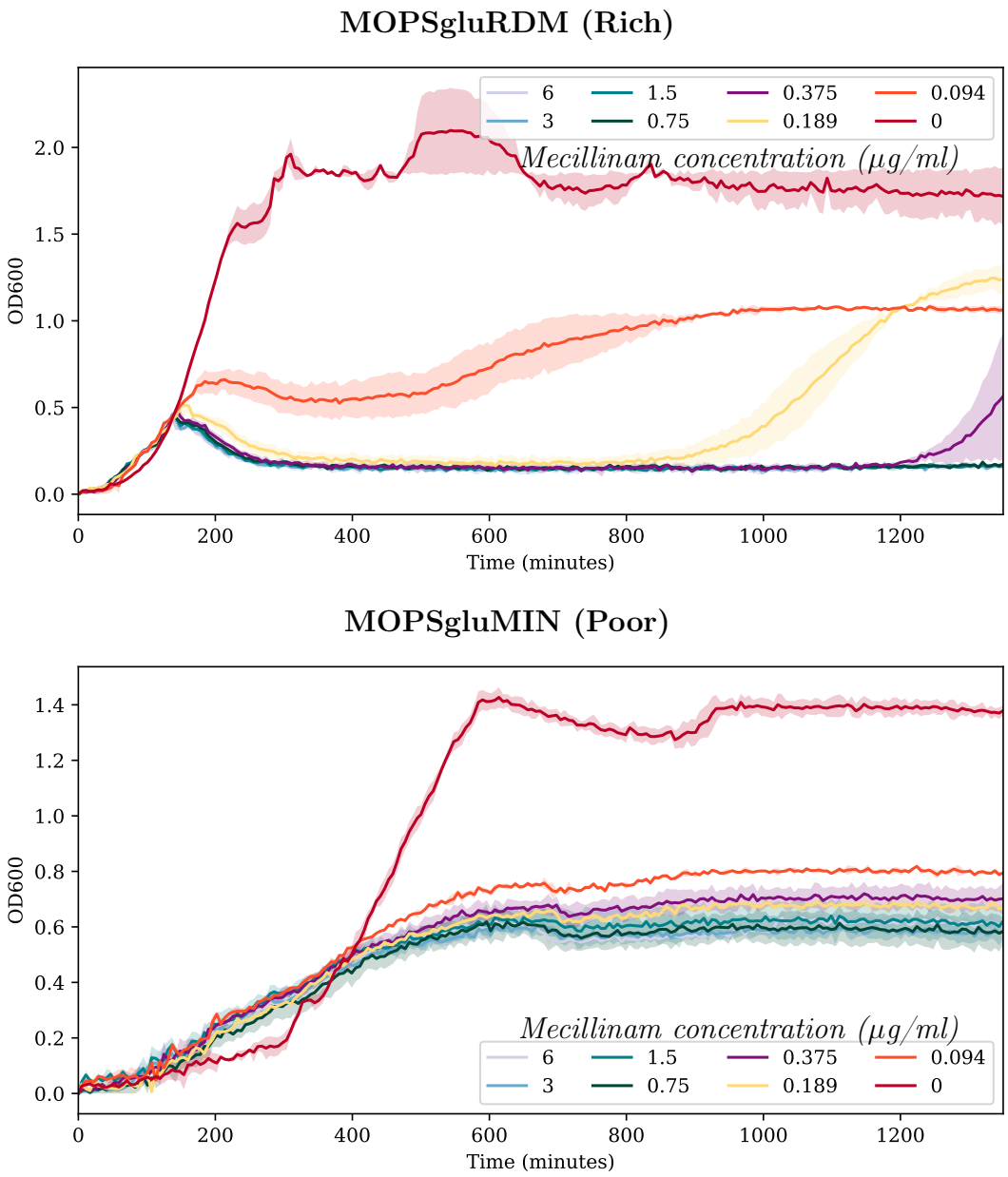

Figure 4.1: Averaged growth curves from two replicates from the plate reader at different mecillinam concentrations (listed in μg/ml in the legend) and in different MOPSglucose variants. Top: MOPSgluRDM. Bottom:MOPSgluMIN. The growth media were at pH 6.5 and 34°C. Errors bars are presented as shaded areas coloured according to the corresponding mecillinam concentration. These indicate the standard deviation between multiple wells of the same concentration.

4.2.2 Population dynamics observed via OD measurements in the shake flask

Growing bacteria in a shake flask, and thus in larger volumes than in the 96-well plate, was necessary to be able to directly compare optical density

measurements and colony forming units (CFUs). Guided by the plate reader observations, two mecillinam concentrations were considered. These were the lowest concentration (0.094μg/ml), which exhibited the most variance in outcome across the growth media in the plate reader, and the minimum inhibitory concentration (1.5μg/ml). These will be respectively referred to as the "low" and "high" mecillinam concentrations. For the shake flask experiments, three growth media were used: rich (MOPSgluRDM), poor (MOPSgluMIN) and an intermediate growth medium (MOPSgluCAA).

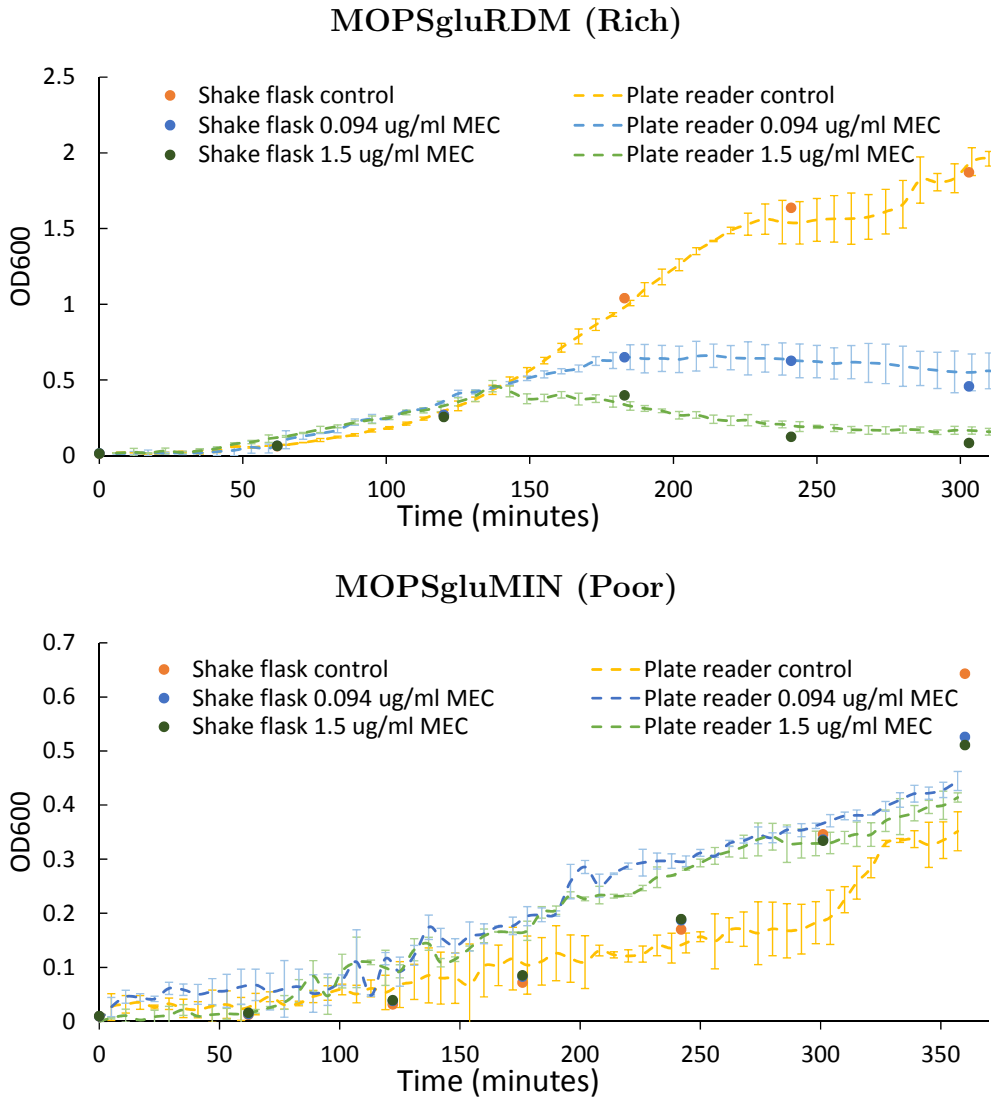

Figure 4.2: Direct comparison of the plate reader optical density measurements from 0 to 300 minutes (with no antibiotic, low and high mecillinam (MEC)) with the spectrophotometer readings from the shake flask experiment. Error bars represent the standard deviation of the plate reader OD measurements across replicate experiments. The spectrophotometer optical density readings are single measurements, with a reading error of ± 0.01: as such the error bars are not visible on this scale.

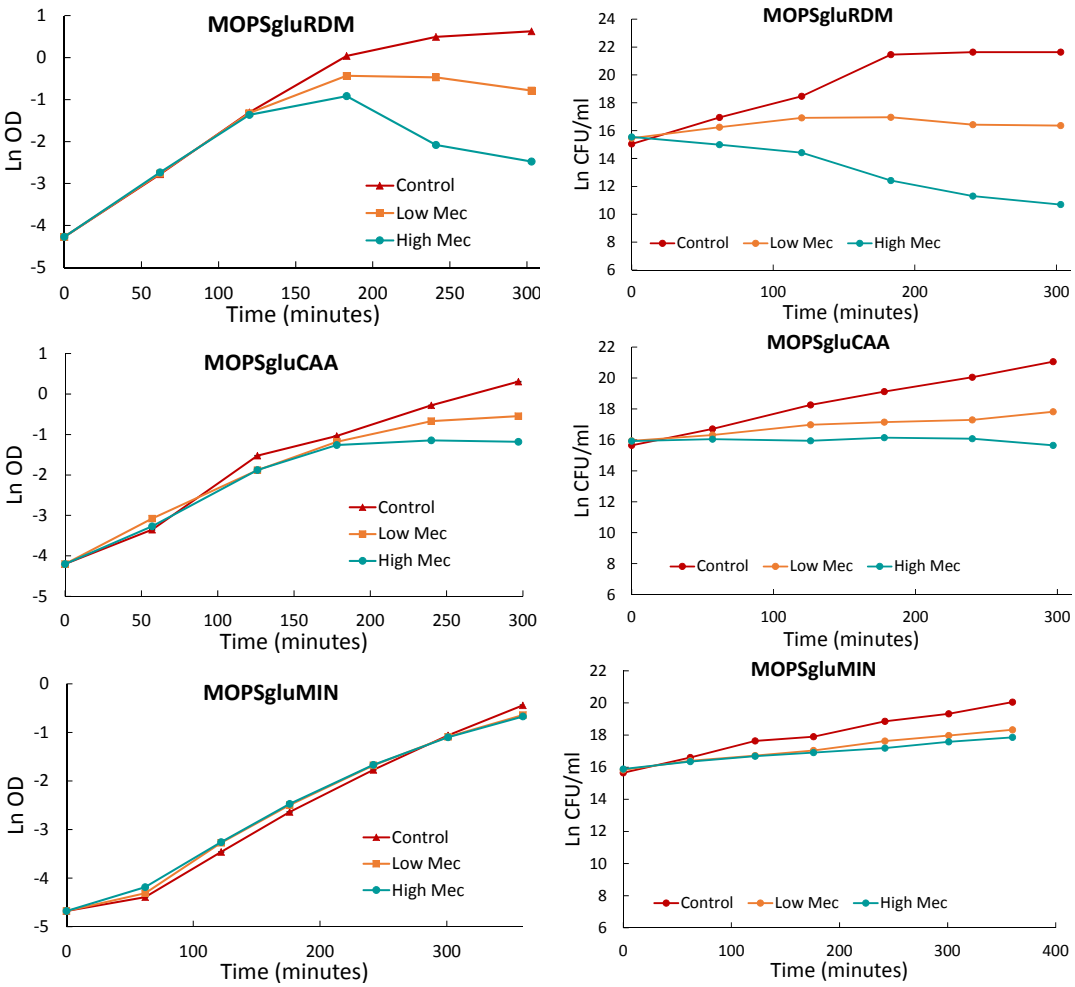

Figure 4.3: Left column: Growth curves from the spectrophotometer at low (0.094μg/ml) and high (1.5μg/ml) mecillinam concentrations and in different MOPSglucose variants: MOPSgluRDM (top), MOPSgluCAA (middle) MOSgluMIN (bottom). Right column: Growth curves from the colony forming units at low (0.094μg/ml) and high (1.5μg/ml) mecillinam concentrations and in different MOPSglucose variants: MOPSgluRDM (top), MOPSgluCAA (middle), MOPSgluMIN (bottom). The growth media were at pH 6.5 and 34°C.

The optical density measurements on the rich (MOPSgluRDM) and poor (MOPSgluMIN) media from the shake flask growth experiments were directly compared with the plate reader OD measurements (Figure 4.2). The MOPSgluRDM results agree quantitatively between plate reader and shake flask, while the MOPSgluMIN results differ somewhat. This difference in the MOPSgluMIN growth dynamics could be due to the ten minute difference in doubling time between the shake flask and plate reader (Table 4.1). Nevertheless, the same qualitative trends in the presence of mecillinam are observed, indicating that the key dynamics are not dependent on the culture volume and experimental set-up.

The complete shake flask OD results for mecillinam can be seen in Figure 4.3, left column. Consistent with our preliminary experiments (Chapter 3), we see that

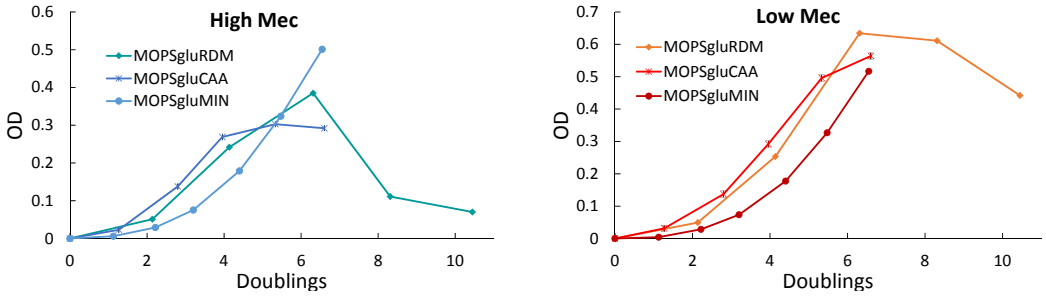

Figure 4.4: Plots directly comparing MOPSgluRDM, MOPSgluCAA and MOPSgluMIN with high mecillinam (left) and low mecillinam (right). The x-axis has been re-scaled to the number of antibiotic-free doublings for a better comparison (time divided by antibiotic-free doubling time). The growth media were at pH 6.5 and 34°C. Error bars are smaller than the markers.

in the shake flask experiments, the intermediate growth medium MOPSgluCAA apparently shows increased inhibition relative to both MOPSgluRDM and MOPSgluMIN. This is apparent when we plot results for all three media together, as in Figure 4.4. Note however that this conclusion will be modified when we come to discuss CFUs in Section 4.2.3.

4.2.3 Population dynamics observed via colony forming units in the shake flask

In an optical density measurement, growth is simply measured as an increase in light scattering, which is assumed to correlate with total biomass or total cell volume [146]. The optical density measurement can be affected by changes in cell morphology, and cannot distinguish between live and dead cells [87]. As our mathematical model will track the number of living cells it is necessary to also track the number of living cells experimentally by measuring colony forming units (see Methods Chapter for experimental details). During the shake flask experiments, samples were taken and plated following the CFU protocol (Chapter 2). As a result the optical density and colony forming units can be directly compared. The results of these CFU measurements can be found in Figure 4.3, right column.

Comparing the OD and CFU measurements from the shake flask experiments in MOPSgluMIN demonstrates that in this case the optical density is a good measure of the population dynamics (Fig. 4.3, bottom row). The OD and CFU results suggest the same conclusion, that *E. coli* growing in MOPSgluMIN at both low and high mecillinam concentrations continue to grow and divide, albeit at a reduced rate when compared to the antibiotic-free condition. Furthermore, the high mecillinam concentration is only marginally more inhibitive compared to the low mecillinam concentration.

In the MOPSgluCAA growth medium, at the low mecillinam concentration

(orange curve), the OD and CFU measurements both increase, but more slowly than in the antibiotic-free case (Fig. 4.3, middle row). In contrast, at the high mecillinam concentration (blue curve), the optical density increases and then plateaus whereas the CFUs remain pretty much flat. This increase in optical density, while the CFUs remain unchanged, suggests a morphological change in the bacteria i.e. that they become larger and therefore scatter more light. The relatively small change in the number of viable cells (CFUs) suggests that there is either no successful division occurring, or that cell division is balanced by cell death. At later times, beyond the scope of the shake flask experiments, we expect cell death to dominate, as suggested by the decrease in optical density observed in our plate reader experiments at late times (Figure B.6 - data not at pH6.5).

A similar outcome occurs for MOPSgluRDM. For low mecillinam (orange curve) the CFUs increase slightly before decreasing (Fig. 4.3, top right), while at high mecillinam (blue curve) the CFUs clearly decrease from the start. In contrast, the OD measurements for both high and low mecillinam increase first before decreasing (Fig. 4.3, top left). This would suggest a similar situation as for MOPSgluCAA: the cells are undergoing morphological changes (getting bigger at both low and high mecillinam) causing a larger increase in optical density than might be expected from the changes in viable cell number. For MOPSgluRDM it appears that cell death is dominating over cell division, as there is a slight decrease in CFU after 200 minutes at low mecillinam, and a significant decrease from the beginning at high mecillinam (Fig. 4.3).

The CFU data provides a different perspective on the growth-medium dependent action of mecillinam. As discussed previously, from the shake flask OD measurements it appeared that *E. coli* growing in MOPSgluCAA were most inhibited. The CFU measurements, however, suggest that cells growing in MOPSgluRDM are most inhibited by mecillinam, with a higher rate of cell death. Taken together we conclude that bacteria growing in the presence of mecillinam in MOPSgluRDM are getting bigger, and that this increase in size is correlated with cell death. Our data hints that this phenomenon also occurs for bacteria growing in the presence of mecillinam in MOPSgluCAA, but to a lesser extent. In contrast, our data suggests that bacteria exposed to mecillinam in MOPSgluMIN do not die, since growth measured by OD and CFU is still net positive.

4.2.4 Key data from population dynamics observations

Our conclusions so far regarding *E. coli* RJA002 population dynamics in the presence of mecillinam are as follows. Firstly, viable cell numbers, at either low or high mecillinam, decrease as the richness of the growth medium increases. Secondly, total biomass (which has been shown to correlate with OD [146]) appears to be minimised in MOPSgluCAA. Thirdly, inhibition saturates with increasing mecillinam concentration. Lastly, comparing the shake flask optical density and CFU measurements suggests that cells are undergoing morphological changes, becoming larger in rich media but not in poor media.

4.3 Dynamical changes in *E. coli* morphology

Next, we carefully examine the changes in morphology for *E. coli* growing in the presence of mecillinam, as the optical density and CFU measurements described in previous sections suggested that the bacteria were changing shape and/or size. *E. coli* cells were grown under the same low and high mecillinam conditions (in rich and poor growth media) as for the shake flask experiments and samples were extracted for phase contrast microscopy (performed by a postdoctoral researcher in the group, Sharareh Tavaddod). In this way we could be sure that the morphologies observed would correspond with the population dynamics previously discussed.

Initially we were concerned that phase contrast microscopy might not provide sufficient cell number statistics to determine the full distribution of cell morphologies. Therefore, some microscopy was performed with a microfluidic device ('MACS') which enables trapping of a large number of bacteria, to increase the sample size and improve the statistics (see Chapter 2 Section 2.4.2 for more details). MACS microscopy was used for *E. coli* RJA002 growing in MOPSgluRDM only. Ultimately it was decided that the MACS trapping protocol deformed the antibiotic-weakened bacteria significantly. This deformation of the morphology outweighed the benefit of increased sample size, so we focused on phase contrast microscopy for the majority of our study. Nevertheless the MACS data will be discussed in Section 4.3.2 as our work represented a novel application for MACS and the results were of some interest.

4.3.1 Phase contrast microscopy

Phase contrast microscopy was carried out as described in the Methods Chapter (Ch. 2), for *E. coli* RJA002 exposed to high (1.5μg/ml) mecillinam in MOPSgluRDM and MOPSgluMIN, at pH 6.5 and 34°C (as for the plate reader and shake flask experiments). These two growth media were chosen in order to cover the full range of growth dynamics whilst maximising the number of cells that could be imaged for each growth condition. We also measured some key antibiotic-free morphology data: the length and width of an average cell in a population growing

Growth media	Average length (μm)	Average width (μm)
MOPSgluRDM	5.2 ± 0.6	0.98 ± 0.06
MOPSgluMIN	2.8 ± 0.4	1.0 ± 0.04

Table 4.2: Average cell length and width (with the standard deviation as the error) measured for *E. coli* RJA002 growing without antibiotic in MOPSgluRDM and MOPSgluMIN using phase contrast microscopy. These experiments were performed at pH 6.5 and 34°C. $N = 76$ on MOPSgluRDM. $N = 181$ on MOPSgluMIN.

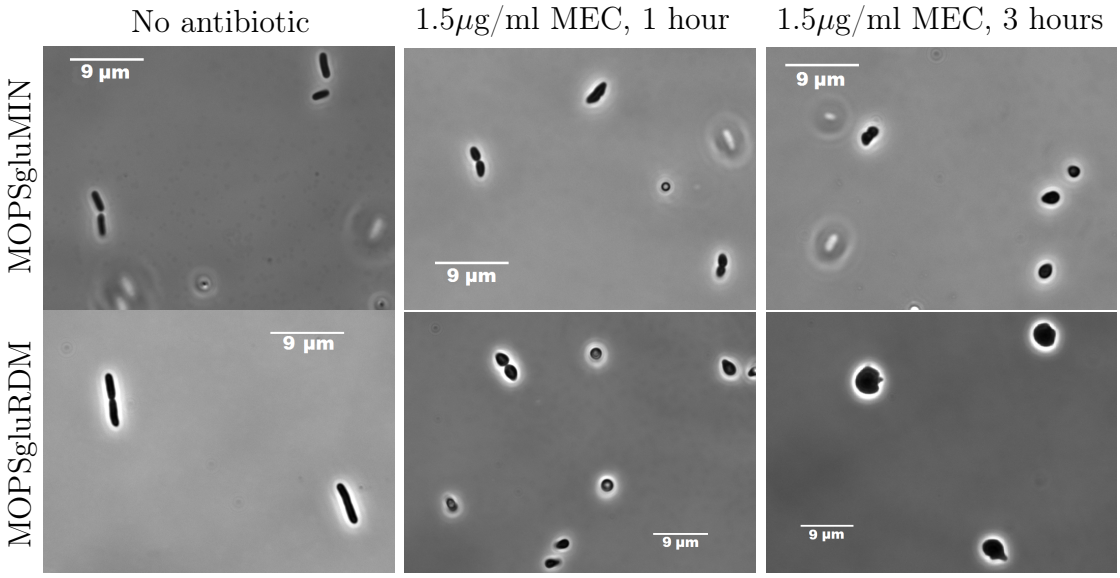

Figure 4.5: Some representative microscopy images in MOPSgluMIN (top row) and MOPSgluRDM (bottom row) with no antibiotic (first column), with mecillinam at 1.5μg/ml after one hour (2nd column) and after three hours (3rd column).

in MOPSgluRDM or MOPSgluMIN at pH 6.5 and 34°C. This information can be found in Table 4.2. These dimensions will be used in Chapter 6 to parameterise our mathematical model.

Figure 4.5 shows some example images of the cell morphology after exposure to 1.5μg/ml mecillinam in rich (bottom row) and poor (top row) growth media. It is clear that, consistent with the literature [46, 126, 137], *E. coli* responds to the inhibition of PBP2 by mecillinam by becoming ovoid, or spherical. It is important to note that these are unlikely to be "spheroplasts" (a widely reported consequence of cell wall-inhibiting antibiotics [43]) which have no cell wall and are osmotically unstable [30]. Spherical cells observed in the presence of mecillinam are thought to still have at least a partial cell wall, as they are more osmotically stable [44, 60, 137]. Dividing spherical cells result in butterfly-like morphologies, as can be seen in the three hour image with mecillinam in MOPSgluMIN (Fig. 4.5, top right).

Analysing our microscopy data in more detail, at 1.5μg/ml mecillinam in MOPSgluRDM we find that after sixty minutes the average length has decreased significantly (Figure 4.6) and the average width has increased significantly (Figure 4.6). The average length is then stable for the next couple of hours (Figure 4.6), before increasing at 240 minutes, and the average width continues to increase (Figure 4.6). This indicates that the cells quickly become fatter and shorter and thus spherical, before continuing to grow as increasingly larger spheres. Thus, even though mecillinam selectively inhibits the elongation machinery, we observe that division also ceases to occur [147]. Later, as cells become bigger and bigger spheres they apparently become increasingly unstable, eventually lysing.

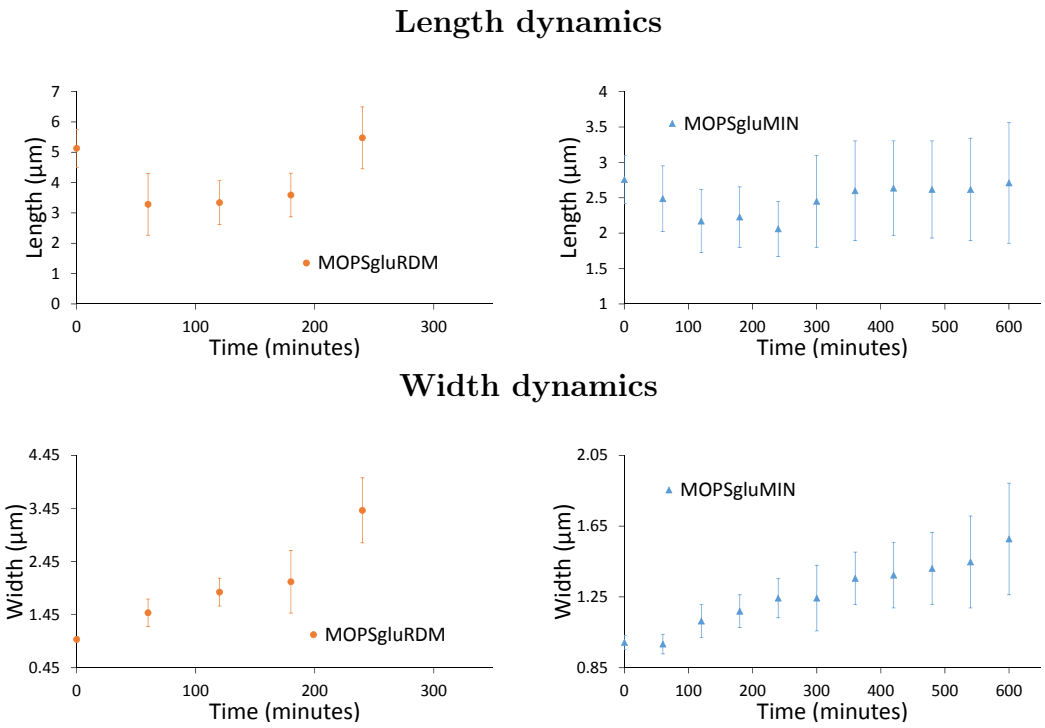

Figure 4.6: The average length and width dynamics for *E. coli* RJA002 growing in both MOPSgluRDM and MOPSgluMIN with a mecillinam concentration of 1.5μg/ml. The error bars are the standard deviations. Each datapoint is averaged over at least 75 bacteria. The sphere line indicates where length equals width.

In contrast, for cells growing in MOPSgluMIN in the presence of 1.5μg/ml mecillinam morphological changes appear to be much more gradual. In Figure 4.6 the length can be observed to decrease slowly over a four hour period before increasing slightly and stabilising after 300 minutes. Figure 4.6 shows that the cell width increases consistently over the same period. To summarise the data, Figure 4.7 shows a "morphology track" where length is plotted against width, and each marker is a different timepoint. Here, the large morphological changes in MOPSgluRDM can clearly be contrasted with the relatively small morphological changes in MOPSgluMIN.

4.3.2 High-throughput MACS microscopy

To achieve better cell number statistics, the MACS set-up was used in collaboration with Sebastían Jaramillo-Riveri and Meriem El-Karoui (SynthSys, Unversity of Edinburgh), to study the cell morphology statistics of the bacterial population over time at two mecillinam concentrations (low: 0.094μg/ml and high: 1.5μg/ml) in MOPSgluRDM at pH 7.4 and 37°C. A detailed description of the MACS protocol can be found in Chapter 2 Section 2.4.2. Briefly, MACS is a microfluidic device designed for high-resolution microscopy, where the bacteria flow through and are trapped in a channel.

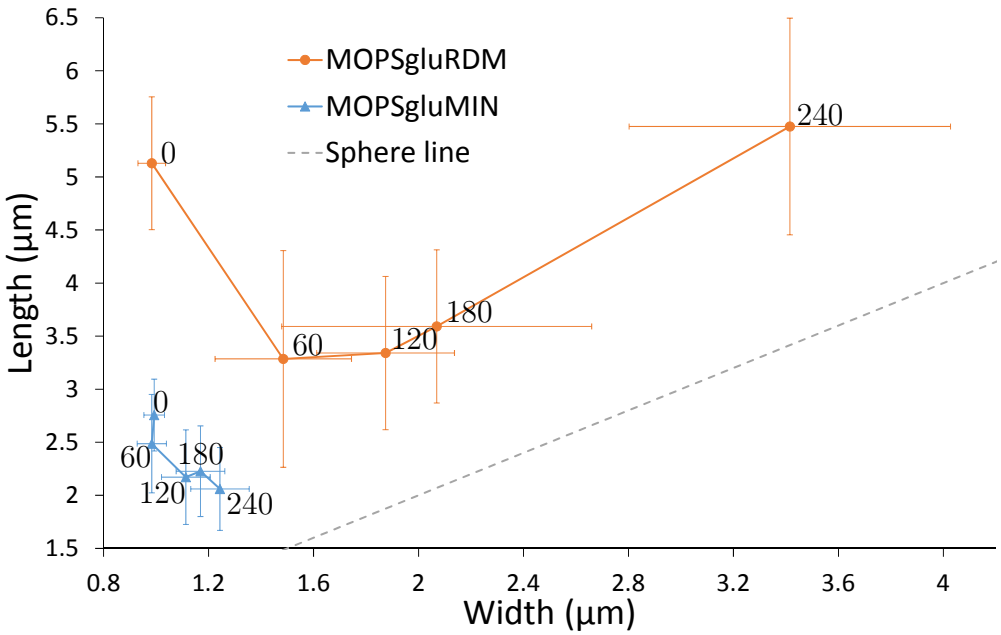

Figure 4.7: 'Morphology tracks': The average length and width dynamics for *E. coli* RJA002 growing in both MOPSgluRDM and MOPSgluMIN with a mecillinam concentration of 1.5μg/ml. The error bars are the standard deviations. Each datapoint corresponds to at least 75 bacteria. The numbers by the datapoints indicate the time, in minutes, after antibiotic exposure.

Figure 4.8 shows representative images taken after three hours in low and high mecillinam (MOPSgluRDM) for both MACS and phase contrast microscopy at pH 7.4 and 37°C. The phase contrast microscopy shows that spherical cells have developed at both mecillinam concentrations after three hours. We found that it was difficult to capture these spherical morphologies with MACS due to the trapping protocol. For the high mecillinam dataset the following trapping protocol was used: 1) flow on, pressure off 2) flow on, pressure on 3) flow off, pressure on (for more details see Chapter 2). This results in "strong" trapping and the mecillinam-treated cells become stretched in the flow direction (Figure 4.8, high mecillinam). We found that so as not to disrupt the spherical morphology one should instead use the following trapping protocol: 1) flow on, pressure off 2) flow on, pressure on i.e. the flow through the channel should be maintained throughout the imaging process. This results in "weak" trapping which is sufficient to trap the large spheres which have developed without damaging them (Figure 4.8, low mecillinam).

To present the data in an easier to compare format, the average lengths and widths for both mecillinam concentrations are plotted versus time in Figure 4.9, showing the MACS data alongside the phase contrast results. In these plots the zero minute datapoint is the average of the measured lengths and widths of bacteria growing without antibiotic. The width dynamics for the two experimental methods are found to be consistent: both low and high mecillinam can produce

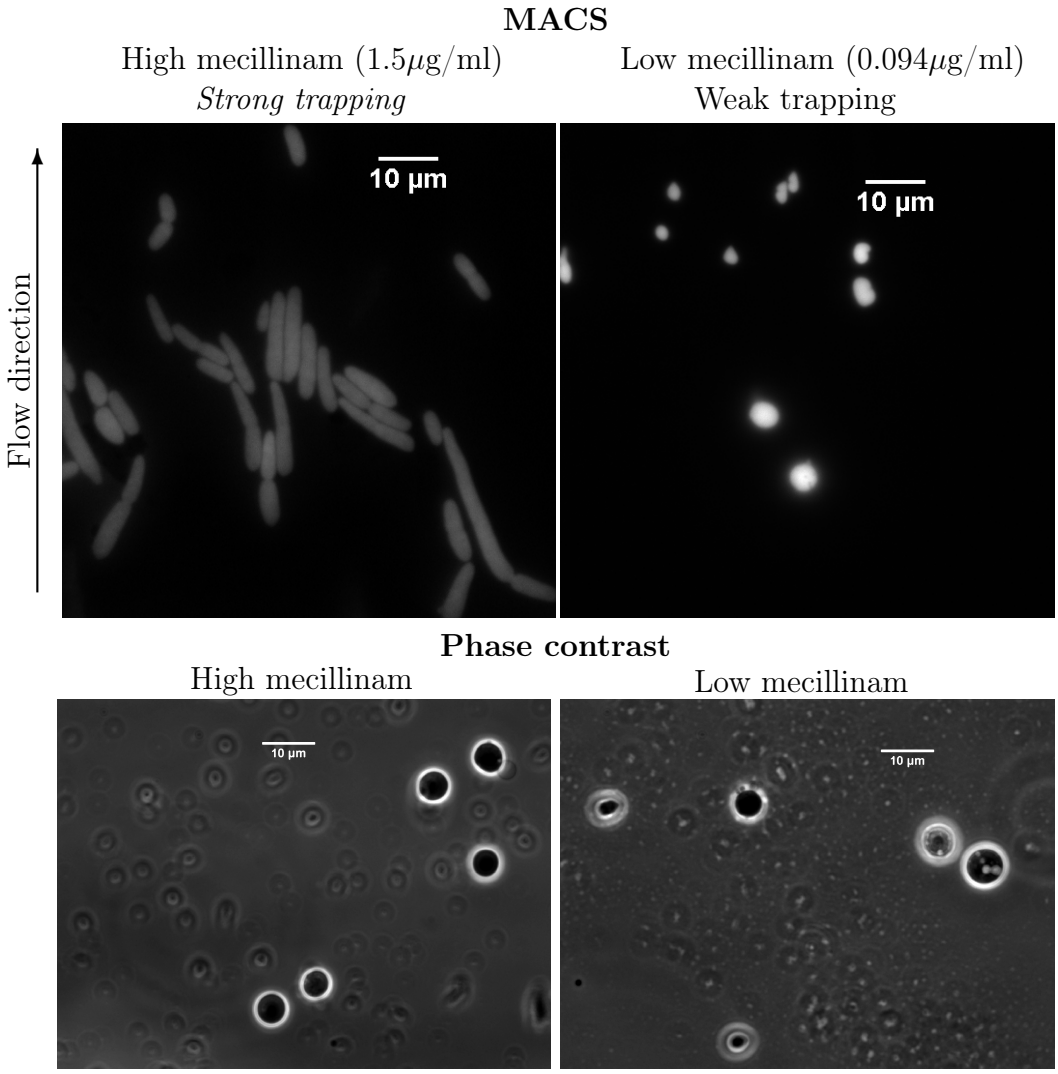

Figure 4.8: Example images from the MACS and phase contrast microscopy in MOPSgluRDM with high mecillinam (left) and low mecillinam (right) after approximately three hours in the presence of the antibiotic. Scale bar is 10μm.

an increase in cell width (Figure 4.9, top panel). However, the observed length dynamics are not consistent between the MACS and the phase contrast microscopy (Figure 4.9, bottom panel). The phase contrast results do not detect a significant change in length, and low and high mecillinam concentrations lead to the same average length at 180 minutes. The MACS data in contrast suggests a slight decrease in length at low mecillinam, but agrees with phase contrast regarding the length observed at 180 minutes. Meanwhile, as discussed, the cells appear to have been stretched by the MACS trapping protocol at high mecillinam, and as such the length appears to increase over time (Figure 4.9, bottom panel).

We conclude that the discrepancy in the cell length dynamics at high mecillinam between the phase contrast and MACS microscopy was due to the design of the microfluidic device protocol. Adapting the protocol to maintain flow throughout imaging for low mecillinam was more successful, with the length and width

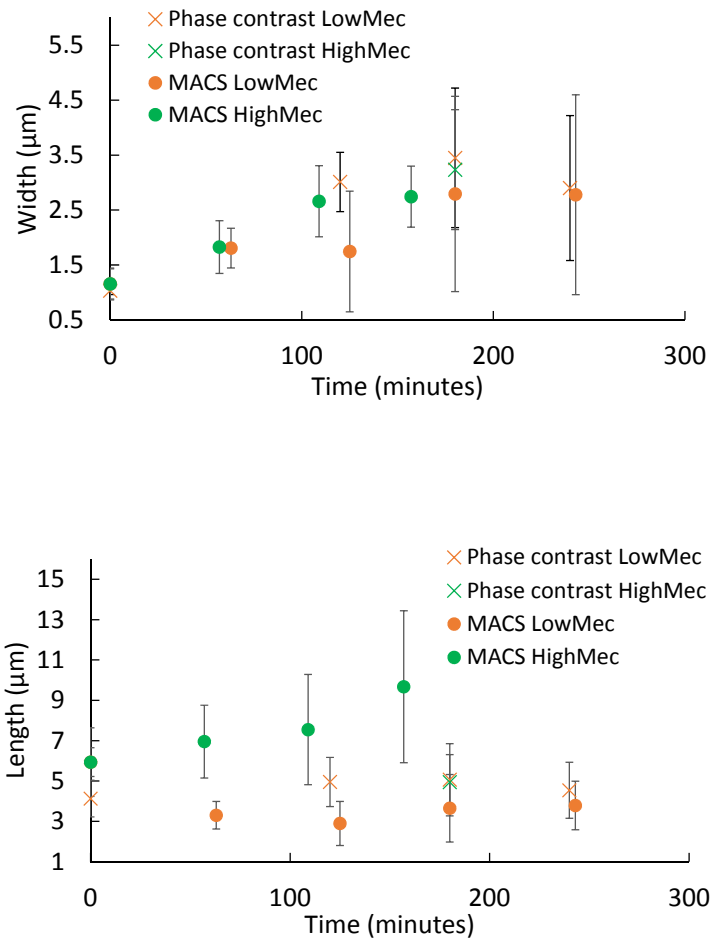

Figure 4.9: Average widths (top) and lengths (bottom) for *E. coli* RJA002 growing in MOPSgluRDM pH 7.4 at 37°C with low mecillinam (LowMec, 0.094μg/ml) and high mecillinam (HighMec, 1.5μg/ml).

dynamics at low mecillinam (Fig. 4.9) following the same trends as observed in the phase contrast: namely that the width increases continually and that the length decreases slightly before stabilising (Fig. 4.6 and Fig. 4.9).

To conclude, the MACS protocol did allow us to image 10-20 times more bacteria and we succeeded in imaging spherical morphologies using an adapted trapping protocol. However, the increase in cell size caused by the trapping mechanism and the uncertainty regarding the repeatability of cell deformation between time points and replicate experiments (the pressure is shut off when loading each sample onto the chip, and there is no guarantee that the same pressure will be applied when turned back on) meant that further MACS microscopy was not performed for this project. Thus our key conclusions will be drawn from phase contrast microscopy, combined with CFU and OD measurements.

4.3.3 Key morphology observations

The key length dynamics for *E. coli* in the presence of mecillinam can be summarised as follows. First there is an initial decrease in length in both MOPSgluRDM and MOPSgluMIN. Then after about four hours in MOPSgluRDM there is an increase in length as the bacteria become large spheres. After about four hours in MOPSgluMIN we instead observe a stabilisation of the average length.

The width dynamics in the presence of mecillinam can be described more simply: in both MOPSgluRDM and MOPSgluMIN the width is seen to grow continually at high mecillinam. This increase is more rapid in MOPSgluRDM than in MOPSgluMIN. Taken together, we get increasingly large spheres then lysis in MOPSgluRDM, but smaller spheres with division in MOPSgluMIN. We have also done phase contrast microscopy at pH 7.4 for low mecillinam on MOPSgluRDM which gives similar results.

Chapter 5

Aztreonam: population dynamics and morphology

5.1 Introduction

We also performed a detailed investigation into the *E. coli* dynamics in the presence of aztreonam. Aztreonam is interesting because it binds selectively to PBP3, a monotranspeptidase active in the divisome. As PBP3 is active during cell septation and division, and not during cell elongation (where mecillinam's target, PBP2, is active), it was hypothesised that aztreonam inhibition would lead to different growth dynamics compared to that of mecillinam.

In this chapter the population dynamics of *E. coli* RJA002 growing in the presence of aztreonam are examined in detail, in parallel with morphological changes observed using phase contrast microscopy. All the experiments used *E. coli* RJA002 prepared in the steady state growth condition (as described in Methods Chapter 2 Section 2.1.3) in MOPSglucose media variants at pH 7.4 and 37°C.

In the literature, aztreonam exposure has been reported to result in a slow rate of bacterial killing at concentrations where PBP3 is saturated (measured using CFU measurements), even though the corresponding optical density measurements still show apparent net growth [107, 114]. Aztreonam is also known to produce filamentous morphologies [3, 54].

5.2 Population dynamics

The population dynamics of *E. coli* RJA002 in the presence of aztreonam were measured using the same procedure as described for mecillinam (Chapter 4 Section 4.2), i.e. using both plate reader and shake flask experiments to measure

optical density and to count colony forming units.

The antibiotic-free growth rates and doubling times measured in the plate reader and shake flask experiments (at pH 7.4 and 37°C) can be found in Table 5.1. The shake flask optical density growth rates will be used as the growth rate values in the mathematical model in Chapter 6.

5.2.1 Population dynamics observed in the plate reader

In Chapter 3, it was found that aztreonam had a relatively long half-life of 6 or more hours in the MOPS media variants at pH 7.4 and a temperature of 37°C. We therefore used these conditions so that this work would be comparable with the majority of the literature. Growth curves for *E. coli* RJA002 in the presence of a range of aztreonam concentrations were observed for the three MOPS media variants: MOPSgluRDM, MOPSgluCAA and MOPSgluMIN, over long times in the plate reader.

A summary of the results is given in Figure 5.1. In MOPSgluRDM (Fig. 5.1, top panel) high concentrations of aztreonam ($> 0.0313\mu$g/ml) result in a small initial increase in optical density followed by a plateau. In MOPSgluCAA (Fig. 5.1, centre panel) a similar picture holds but the bacterial population reaches a higher optical density followed by a plateau with a slightly negative slope. Finally in MOPSgluMIN (Fig. 5.1, bottom panel) we again see an initial increase in optical density but compared to other media the population reaches an even higher optical density (~ 0.7) before undergoing a rather rapid decrease in OD, followed by a plateau with a slight negative slope. Figure 5.2, left panel, brings together these observations demonstrating that, at concentrations greater than 0.0313μg/ml, aztreonam becomes less inhibitive with decreasing growth rate (see Figure 5.2, left panel).

Experimental method	Growth media	Growth rate (/h)	Doubling time (min)
Plate reader OD	MOPSgluRDM	1.3 ± 0.04	32 ± 1
Shake flask OD	MOPSgluRDM	1.51 ± 0.06	28 ± 1
Shake flask CFUs	MOPSgluRDM	1.4 ± 0.2	30 ± 4
Plate reader OD	MOPSgluMIN	0.68 ± 0.02	61 ± 2
Shake flask OD	MOPSgluMIN	0.74 ± 0.03	56 ± 2
Shake flask CFUs	MOPSgluMIN	0.89 ± 0.05	47 ± 3
Shake flask OD	MOPSgluCAA	0.90 ± 0.09	46 ± 5
Shake flask CFUs	MOPSgluCAA	1.15 ± 0.08	36 ± 2

Table 5.1: Growth rates and doubling times measured for *E. coli* RJA002 growing without antibiotic in different growth media in different experimental protocols. These experiments were performed at pH 7.4 and 37°C.

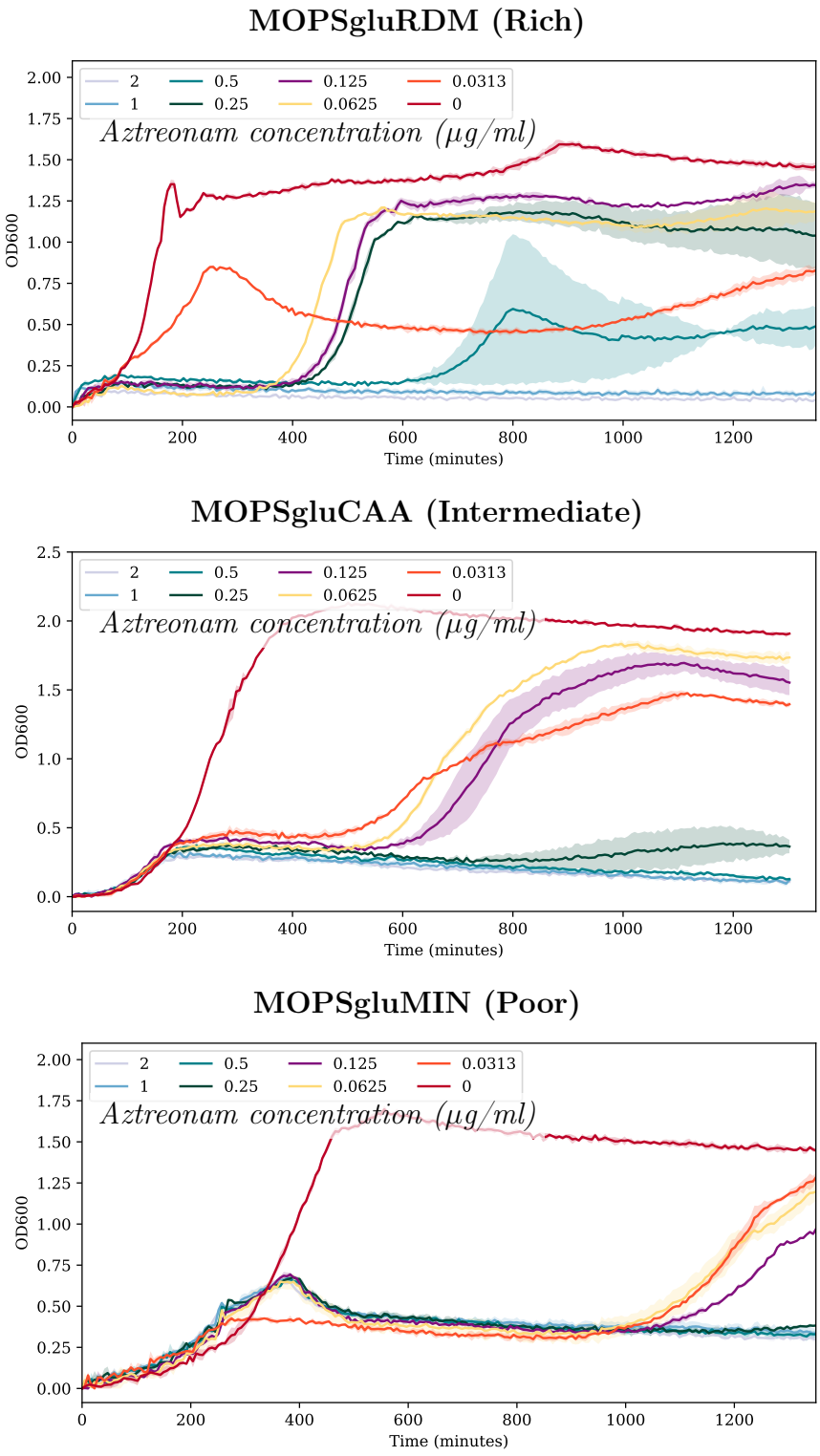

Figure 5.1: Averaged growth curves from the plate reader at different aztreonam concentrations (listed in μg/ml in the legend) and in different MOPSglucose variants (3-4 replicates). Top: MOPSgluRDM (data from undergraduate student Elizabeth Tatham (E.T.)). Middle: MOPSgluCAA. Bottom: MOPSgluMIN (data from E.T.). The experiments were performed at pH 7.4 and 37°C. Error bars are presented as shaded areas coloured according to the corresponding aztreonam concentration. This error is calculated as the standard deviation between the replicate wells of the same concentration.

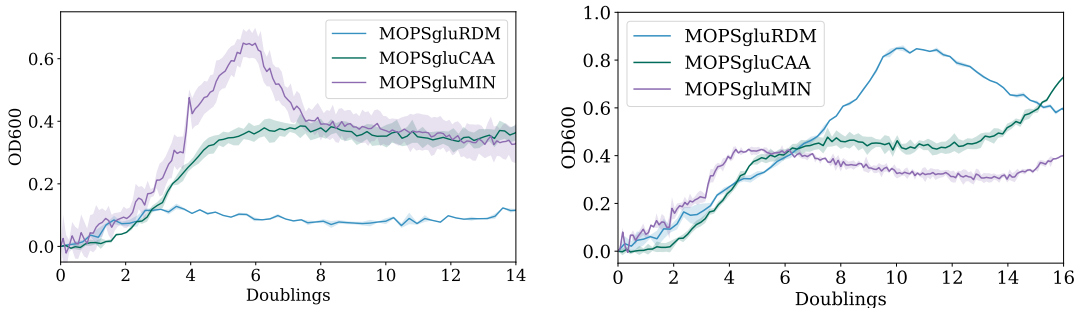

Figure 5.2: Contrasting the level of growth achieved between the three growth media: MOPSgluRDM, MOPSgluCAA and MOPSgluMIN at the aztreonam concentrations of 0.0625μg/ml (left) and 0.0313μg/ml (right). The x-axis has units of 'doublings' which is the time since antibiotic exposure divided by the antibiotic-free doubling time. This makes it easier to compare the different levels of inhibition across the three media.

Curiously, a contrasting growth medium dependence is observed for the lowest aztreonam concentration of 0.0313μg/ml (Figure 5.2, right panel). At this concentration significant growth is observed in MOPSgluRDM while less growth is observed in MOPSgluCAA, and even lower growth in MOPSgluMIN. Thus, this very low aztreonam concentration is more effective at inhibiting slow-growing *E. coli* (see Figure 5.2, right panel). Capturing this concentration-dependent change in the growth-medium dependence will present a challenge for the mathematical model to be developed in Chapters 6 and 7.

An interesting observation, from Figure 5.1, is that, for each growth medium, all aztreonam concentrations higher than 0.0313μg/ml result in apparently identical early-time growth curves, suggesting saturation of PBP3 by aztreonam.

5.2.2 Population dynamics observed in the shake flask

Growing bacteria in a shake flask, and thus in larger volumes than permitted in a 96-well plate, was necessary to be able to directly compare optical density, colony forming units and microscopy results. In these experiments only two aztreonam concentrations were considered: the lowest concentration from the plate reader experiments, 0.0313μg/ml, and the minimum inhibitory concentration, 0.5μg/ml. These will be respectively referred to as the "low" and "high" aztreonam concentrations.

The results of the shake flask experiment agree well with those from the plate reader, as can be seen in Figure 5.3. The situation is very similar to that discussed for mecillinam (Ch. 4 Section 4.2.2), where the MOPSgluRDM data across the two experiments agree very well whilst there is greater discrepancy between the plate reader and shake flask experiments for MOPSgluMIN. This could be due to a difference in the antibiotic-free doubling time between plate reader and shake

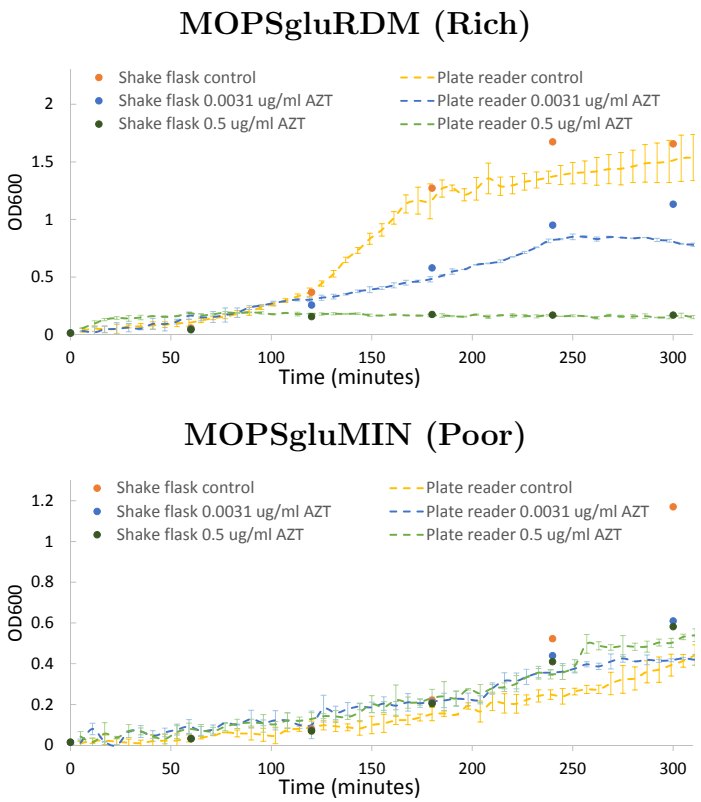

Figure 5.3: Direct comparison of the plate reader optical density measurements from 0 to 300 minutes (with no antibiotic and, low and high aztreonam (AZT)), with the shake flask optical density readings. Error bars represent the standard deviation of the plate reader optical density measurements across replicate experiments. The shake flask readings are single measurements, with a reading error of ± 0.01: as such the error bars are not visible on this scale.

flask. For MOPSgluRDM the plate reader doubling time is 32 minutes, while the shake flask doubling time is 26 minutes. For MOPSgluMIN the plate reader doubling time is 61 minutes, while the shake flask doubling time is 56 minutes. Therefore antibiotic-free growth is consistently slightly slower in the plate reader (as suggested in the literature [87]) but the impact of this is more pronounced on the minimal media. If the x-axis is scaled by the antibiotic-free doubling time we observe that the growth medium-dependent growth dynamics are the same in both the plate reader and the shake flask experiments (Fig. 5.4).

In the shake flask, as in the plate reader, the high aztreonam concentration becomes less inhibitive as the growth rate decreases from MOPSgluRDM to MOPSgluMIN (Figure 5.5, left panel). For the low aztreonam concentration (Figure 5.5, right panel) the shake flask dynamics appear to be growth medium-independent, at least on the relatively short timescale of these experiments (the plate reader results, Fig. 5.2, suggest there may be growth medium-dependence for later times).

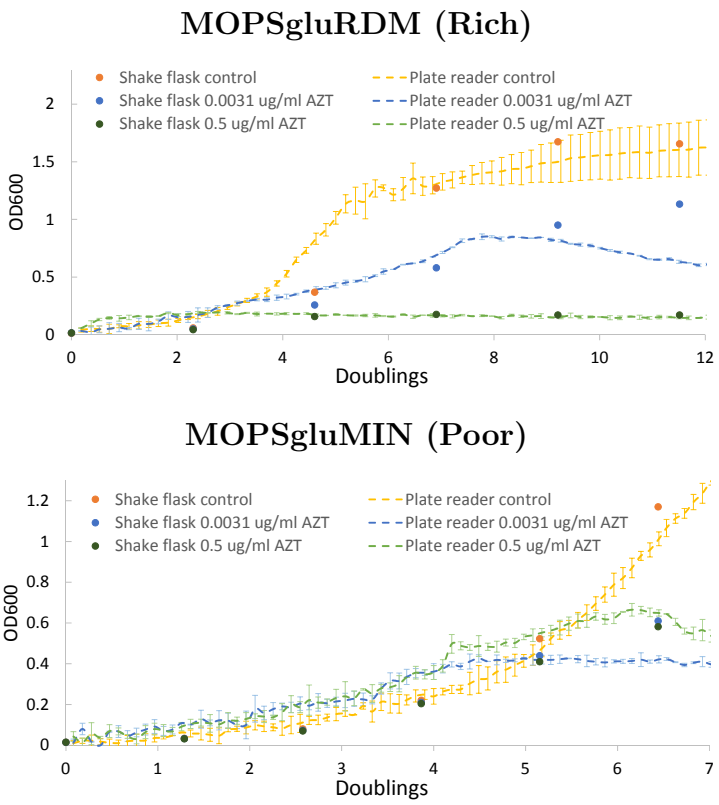

Figure 5.4: Direct comparison of the plate reader optical density measurements from 0 to 300 minutes (with no antibiotic and, low and high aztreonam (AZT)), with the shake flask optical density readings. Time was scaled by the measured antibiotic-free doubling times to give the number of antibiotic-free doublings. Error bars represent the standard deviation of the plate reader optical density measurements across replicate experiments. The shake flask readings are single measurements, with a reading error of ± 0.01: as such the error bars are not visible on this scale.

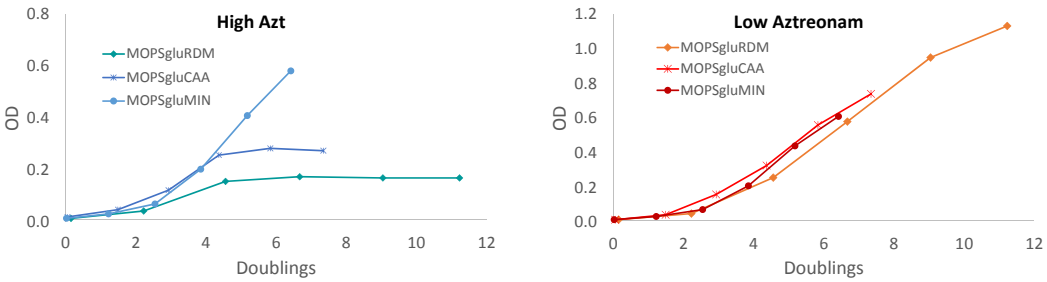

Figure 5.5: Growth curves from the spectrophotometer at low (0.0313μg/ml) and high (0.5μg/ml) aztreonam concentrations and in different MOPSglucose variants. Plots directly comparing the three media with high aztreonam (left) and low aztreonam (right). Here the x-axis has been scaled to the number of antibiotic free doublings (time since antibiotic exposure divided by antibiotic-free doubling time) for a clearer comparison of the level of inhibition.

5.2.3 Population dynamics observed via colony forming units

As for mecillinam in Chapter 4 we took samples from the shake flask experiments and measured the viable cell count via CFUs (according to the method in Chapter 2). The CFU dynamics for the three growth media can be seen in Figure 5.6, right panel. Focusing first on the results for the high aztreonam concentration, we see that in MOPSgluRDM, *E. coli* RJA002 undergo significant cell death. The CFU dynamics for *E. coli* RJA002 growing in MOPSgluCAA (Fig. 5.6, middle panel) follow the same pattern as in MOPSgluRDM, although with a lower rate of cell death at high aztreonam than in MOPSgluRDM. In MOPSgluMIN the rate of cell death at high aztreonam is again reduced

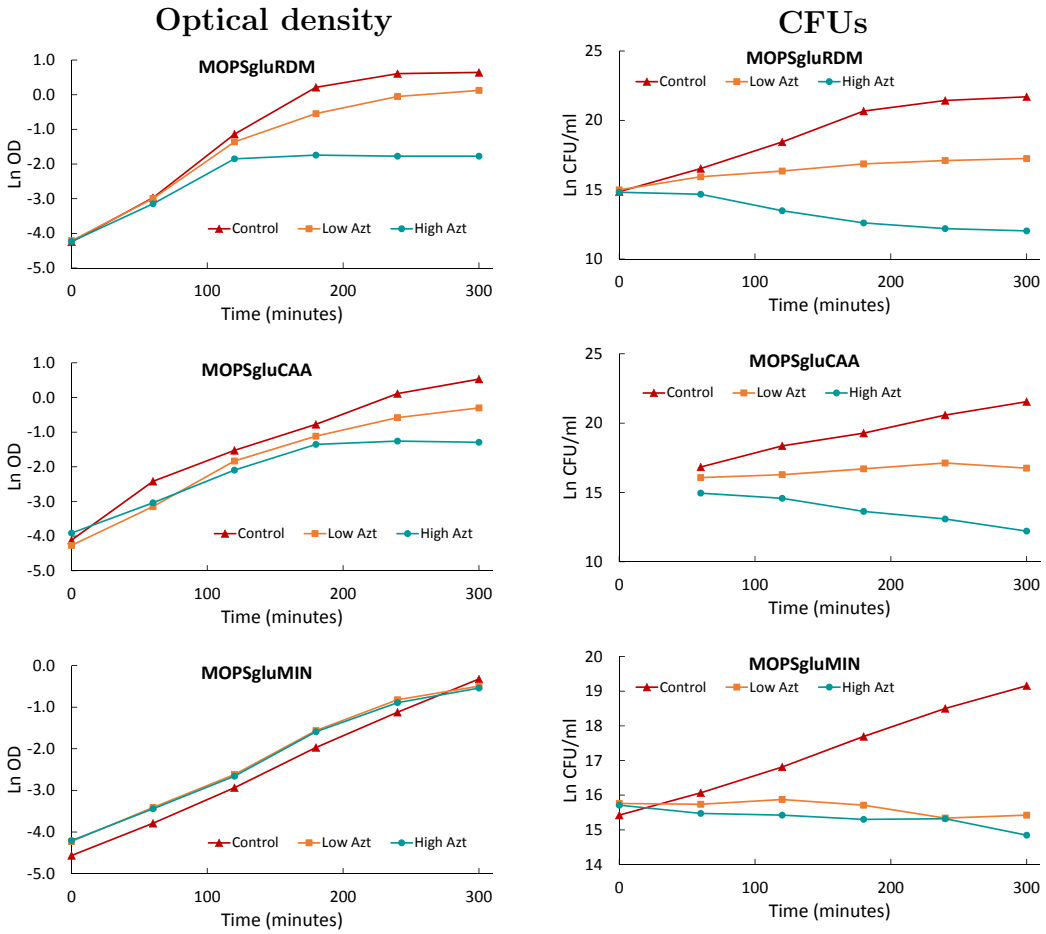

Figure 5.6: Left column: Growth curves from the spectrophotometer at low (0.0313μg/ml) and high (0.5μg/ml) aztreonam concentrations and in different MOPSglucose variants: MOPSgluRDM (top), MOPSgluCAA (middle) MOPSgluMIN (bottom). Right column: Growth curves from the colony forming units at low (0.0313μg/ml) and high (0.5μg/ml) aztreonam concentrations and in different MOPSglucose variants: MOPSgluRDM (top), MOPSgluCAA (middle), MOPSgluMIN (bottom). The growth media were at pH 7.4 and 37°C.

relative to that observed in MOPSgluCAA and MOPSgluRDM (Fig. 5.6, right column). This agrees with the previous observation (from the optical density measurements) that the high aztreonam concentration is more effective at inhibiting growth in richer growth media.

For the low aztreonam concentration, in MOPSgluRDM a slight increase in viable cell number is observed, indicating that there are still successful division events occurring (Figure 5.6, right panel). Once again MOPSgluCAA results in similar growth to that observed in MOPSgluRDM. The growth dynamics of *E. coli* RJA002 in MOPSgluMIN at low aztreonam display a similar degree of cell death to the high aztreonam condition (Figure 5.6, right panel). Thus, as observed from the optical density measurements (Fig. 5.1, Fig. 5.6), the degree of inhibition for the low aztreonam concentration increases as the growth rate decreases, as seen by a transition from a positive slope with MOPSgluRDM to a negative slope with MOPSgluMIN in the CFUs (Fig. 5.6).

Comparing the CFU results with our optical density measurements (Figure 5.6 left vs right columns), the discrepancy between the CFU and OD dynamics is highlighted. Namely, the decrease in CFU in all media at high aztreonam while the OD increases before plateauing suggests changes in the cell morphology. For low aztreonam, the same discrepancy is seen on MOPSgluMIN but on the other growth media both the optical density and CFUs indicate growth.

5.2.4 Summary of population dynamics observations

The growth dynamics at low and high aztreonam concentrations were found to be consistent between the plate reader and shake flask experiments. Curiously, the high aztreonam concentration becomes more inhibitive as the growth medium becomes richer, while the low aztreonam concentration becomes more inhibitive as the growth medium becomes poorer. Furthermore the discrepancy between the optical density and CFU results suggests a significant morphological change at high aztreonam in all media, and also in low aztreonam in MOPSgluMIN.

5.3 Morphology dynamics: phase contrast microscopy

Morphology changes for *E. coli* RJA002 in the presence of aztreonam were studied using phase contrast microscopy (using the method described in Chapter 2), the imaging was done by Sharareh Tavaddod and I performed the image analysis. To ensure enough bacteria were imaged across the rich (MOPSgluRDM) and poor (MOPSgluMIN) growth media only one aztreonam concentration was studied. The concentration chosen was that of "high aztreonam" used in the previous sections: 0.5μg/ml. For comparison, Table 5.2 gives the length and width of

Growth media	Average length (μm)	Average width (μm)
MOPSgluRDM	3.9 ± 0.7	0.95 ± 0.06
MOPSgluMIN	3.0 ± 0.6	0.89 ± 0.06

Table 5.2: Average cell length and width measured for *E. coli* RJA002 growing without antibiotic in MOPSgluRDM and MOPSgluMIN using phase contrast microscopy. These experiments were performed at pH 7.4 and 37°C. $N = 203$ on MOPSgluRDM. $N = 259$ on MOPSgluMIN.

an average cell in a population growing in MOPSgluRDM or MOPSgluMIN at pH 7.4 and 37°C in the absence of antibiotic.

Some representative images of the cell morphology, in the absence and presence of high aztreonam in the rich and poor growth media, can be seen in Figure 5.7. Looking from left to right along the top row of Figure 5.7 it can be clearly seen that the cells in MOPSgluMIN become much longer after growing in the presence of the high aztreonam concentration for four hours. In contrast, bacteria in MOPSgluRDM (Figure 5.7, bottom row) elongate less but appear to undergo a change in the cytoplasmic content, showing dark spots instead of a homogeneous texture (Fig. 5.8). Variation in the density of the cytoplasmic content has previously been linked to the bactericidal activity of beta-lactam antibiotics [10, 135], therefore this could indicate lack of cell viability in MOPSgluRDM in the presence of high aztreonam.

At the high aztreonam concentration it was observed that the antibiotic was less inhibitive on MOPSgluMIN relative to MOPSgluRDM (Figure 5.6). It is therefore

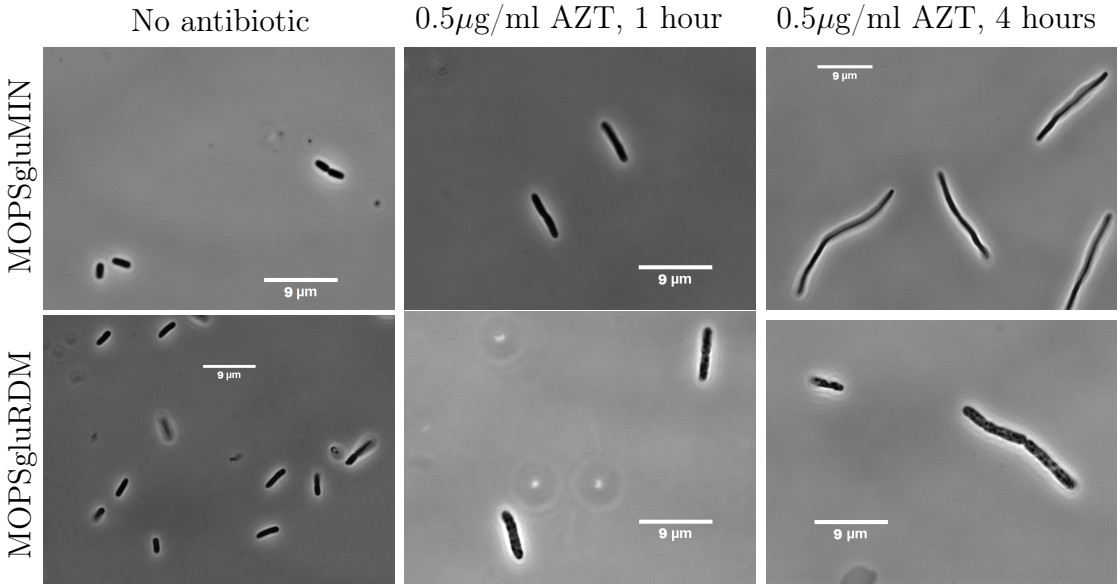

Figure 5.7: Some representative microscopy images in MOPSgluMIN (top row) and MOPSgluRDM (bottom row) with no antibiotic (first column), with aztreonam at 0.5μg/ml after one hour (2nd column) and after four hours (3rd column). Scale bars are 9μm.

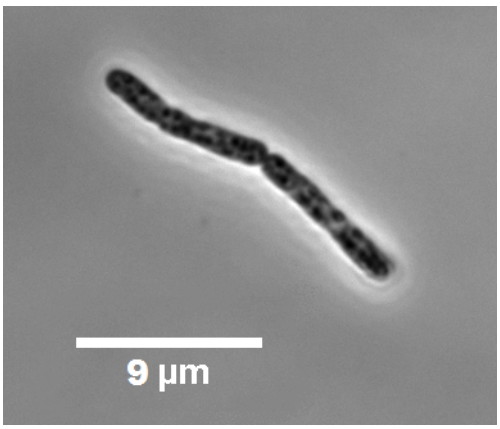

Figure 5.8: A zoomed-in version of the image in Figure 5.7 of a cell with changes in the cytoplasmic content after growing in MOPSgluRDM with 0.5μg/ml aztreonam, for four hours.

interesting to see from the phase contrast microscopy that it is in MOPSgluMIN where significant filamentation occurs. Figure 5.9 quantifies the filamentation in MOPSgluMIN: the average length increases from $3.0 \pm 0.6\mu$m in the absence of aztreonam to $18 \pm 8\mu$m after four hours in the presence of high aztreonam. In contrast a relatively small increase in cell length is observed in MOPSgluRDM, from $3.8 \pm 0.8\mu$m in the absence of aztreonam to $7 \pm 4\mu$m after four hours in the presence of high aztreonam (Fig. 5.9).

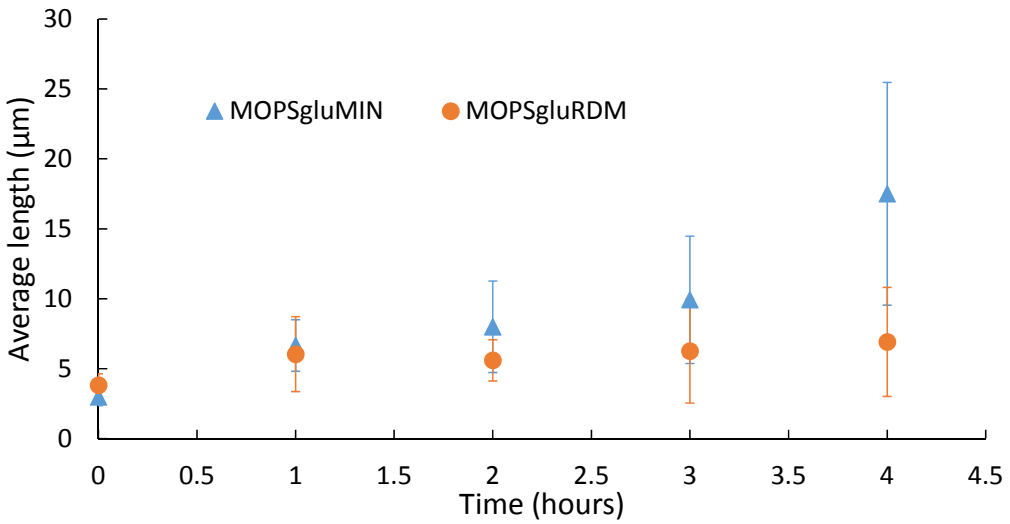

Figure 5.9: The average length dynamics for *E. coli* RJA002 growing in both MOPSgluRDM and MOPSgluMIN with an aztreonam concentration of 0.5μg/ml. The error bars are the standard deviations. Each datapoint is the result from at least 50 bacteria.

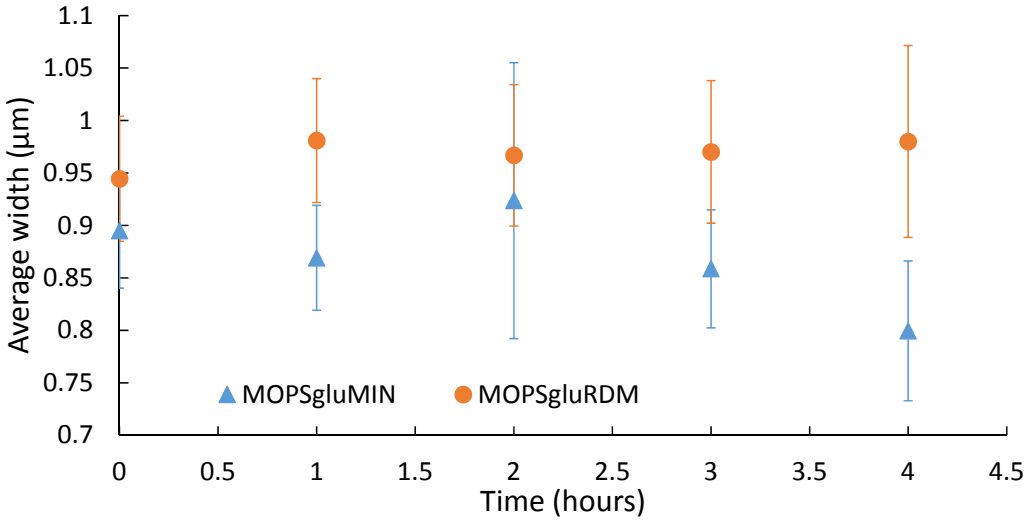

Figure 5.10: The average width dynamics for *E. coli* RJA002 growing in both MOPSgluRDM and MOPSgluMIN with an aztreonam concentration of 0.5μg/ml. The error bars are the standard deviations. Each datapoint is the result of analysing at least 50 bacteria.

The corresponding measurements of cell width, shown in Figure 5.10, indicate that there is no significant increase in width in either MOPSgluRDM or MOPSgluMIN. In fact, in MOPSgluMIN it appears that there is in fact a decrease in width from three hours onwards. This decrease in average width could be related to local changes in width along the filaments (Figure 5.11) which may occur because septal rings form but do not fully constrict when PBP3 is inhibited [25, 150].

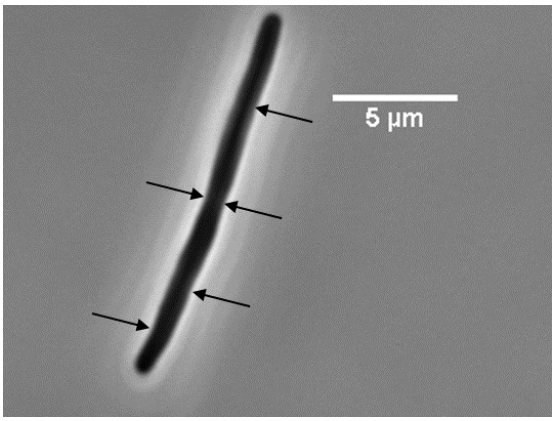

Figure 5.11: An *E. coli* RJA002 filament after 4 hours growth in MOPSgluMIN with 0.5μg/ml aztreonam. Variability in the filament width is indicated by the arrows.

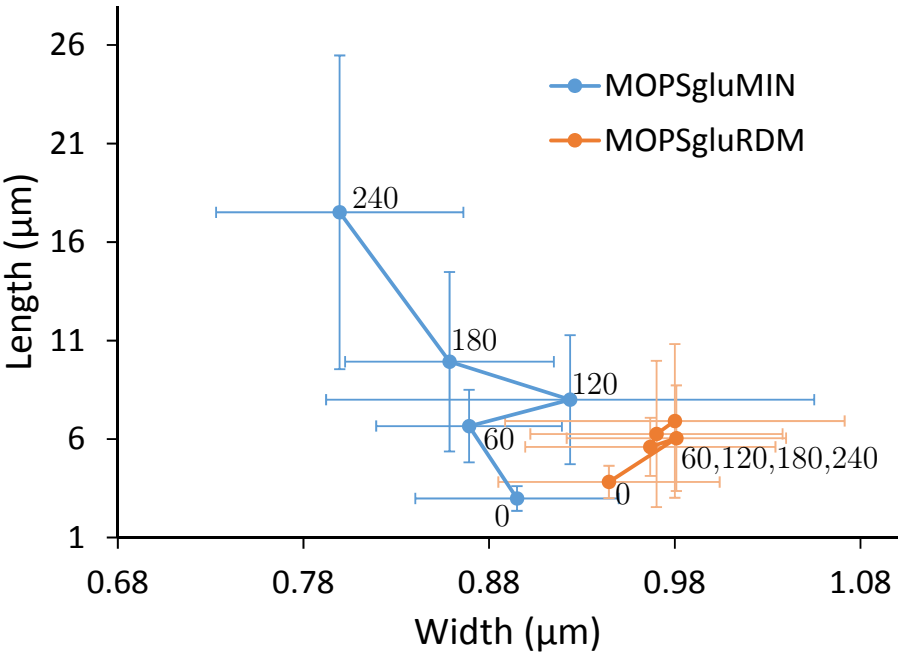

Figure 5.12: "Morphology tracks": The average length and width dynamics for *E. coli* RJA002 growing in both MOPSgluRDM and MOPSgluMIN with an aztreonam concentration of 0.5μg/ml. The error bars are the standard deviations. Each datapoint is the result of measuring at least 50 bacteria and represents a different timepoint: 0, 60, 120, 180 and 240 minutes (going roughly upwards).

These results suggest that when aztreonam inhibits *E. coli*'s division machinery this has a significant impact on the cell length for slow-growing cells. Interestingly, this filamentation seems to be associated with survival: there was little change in the MOPSgluMIN CFUs at high aztreonam, while there was a significant decrease in CFUS in MOPSgluRDM where we do not see much filamentation (Figure 5.6). A possible link between filamentation and increased survival under stressful environments has been suggested in the literature [65]. This is a key hypothesis that will be explored further with the mathematical model in Chapter 8.

Figure 5.12 summarises our morphology data, showing the average length versus average width for *E. coli* cells in both MOPSgluRDM and MOPSgluMIN, in the presence of aztreonam as a "morphology track". This plot clearly highlights the difference in the degree of filamentation between the two media.

5.3.1 Key data from morphology dynamics observations

The cell length dynamics in the presence of high aztreonam can be summarised as follows. In MOPSgluRDM *E. coli* RJA002 approximately double in length within the first hour and then remain around this length for the remainder of

the four hour experimental period. In MOPSgluMIN filamentation is observed, in which cell length increases continually, reaching lengths almost ten times the antibiotic-free average after four hours in high aztreonam.

The bacterial cell width in the presence of high aztreonam does not change as much as the length. In MOPSgluRDM the width increases slightly within the first hour and then remains stable for the remaining measurement time. In MOPSgluMIN the width appears to be fairly constant for the first three hours before decreasing slightly. Collating the morphology dynamics with the CFU data leads to the hypothesis (to be discussed in Chapters 7 and 8) that if a cell enters the filamentation regime (as in MOPSgluMIN) this leads to a reduced rate of cell death.

Chapter 6

Mathematical model: development

6.1 Introduction

The current state of the literature on modelling bacterial cell wall synthesis and its response to antibiotics was discussed in Chapter 1. To summarise, previous work can be grouped into three types of mathematical models which either focus on population dynamics, cell structure or cell physiology. Very few models link cell physiology to population dynamics [48]. In this chapter, I develop a mathematical model which aims to link the intracellular dynamics of cell wall-targeting antibiotics binding to their targets (cell physiology) to changes in cell morphology (cell structure), and in population dynamics. I will also implement different models for the triggering of cell division with the aim of testing which of these are compatible with the results of my experiments.

6.1.1 Linking cell physiology, cell morphology and population dynamics

To achieve a model that links antibiotic mechanism of action with population dynamics via cell morphology it is necessary to coarse-grain the biochemistry - otherwise the number of parameters would be immense. In our model, the biochemistry is coarse-grained in two ways. Firstly, the intracellular biosynthesis of peptidoglycan precursors is not modelled explicitly. Rather, it is assumed that peptidoglycan precursors are simply created at rate S, ignoring the multitude of individual enzymes involved in peptidoglycan biosynthesis, and the chain of different precursor molecules. Secondly, the penicillin binding proteins (PBPs) which are active at the periplasmic/cytoplasmic interface (synthesising peptidoglycan from precursors and controlling peptidoglycan incorporation) are

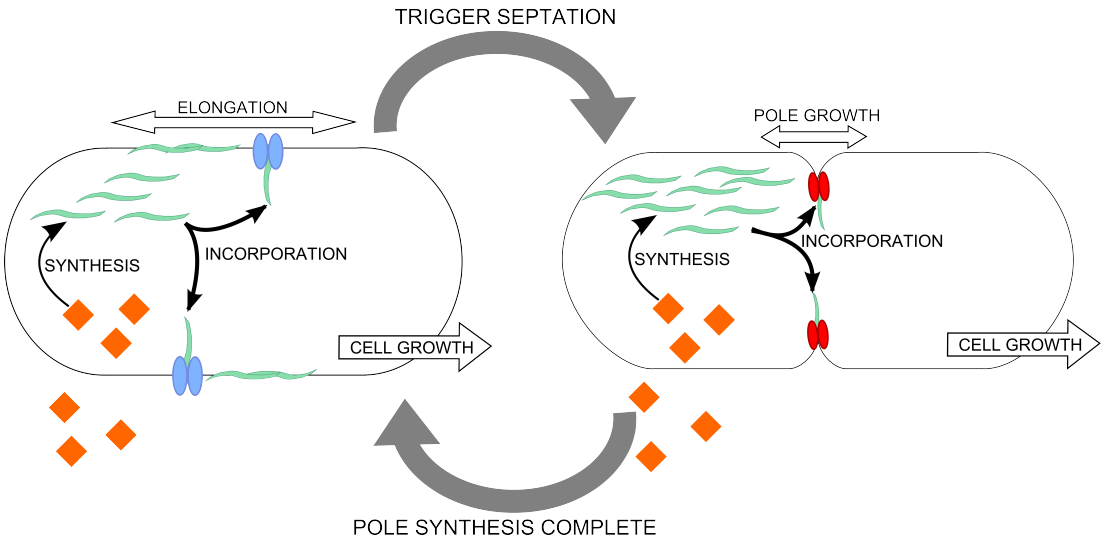

Figure 6.1: Schematic of the mathematical model demonstrating the elongation and pole synthesis processes. Orange diamonds represent nutrients (not modelled explicitly). Green fragments represent peptidoglycan precursors. Blue ellipses represent elongasomes. Red ellipses represent divisomes.

considered simply as two enzyme complexes. One of these enzyme complexes performs elongation (the elongasome) and the other performs division (the divisome) [16]. There are assumed to be a number of each of these complexes per cell. In reality, the nature of the enzyme complexes that are present in the bacterial cell wall is more complex, and remains up for debate [33, 138].

In the model, this coarse-grained representation of the biochemistry is linked to the cell morphology via the surface area and volume. Harris and Theriot [51] have emphasised the importance of the ratio of surface area to volume for bacterial growth (Chapter 1 Section 1.2.3.5). Here, we make the assumption that surface area growth is governed only by the incorporation of new peptidoglycan into the cell wall, ignoring any contributions of phospholipid membrane synthesis or hydrolysis (removal) of peptidoglycan. Volume growth is assumed to be independent of the surface area, and to be exponential in time, as in other models [6, 21, 128]. Furthermore, the density of peptidoglycan is assumed to be constant [156], although this assumption may not hold for growth in the presence of antibiotic.

The cell morphology is then linked to the population dynamics via cell division, which requires the formation of new poles. We will also include lysis in the presence of antibiotics, which may be morphology-dependent.

6.2 The Model

The model follows the protocol presented schematically in Figure 6.1 and described in Figure 6.2. The rate of volume growth, λ, is a model input, based on the antibiotic-free growth rate in our experiments, and represents the nutrient conditions. Peptidoglycan precursors are assumed to be continually synthesised. The model alternates between two phases. In the elongation phase the cylindrical surface area increases (Fig. 6.3). The model exits the elongation regime if a trigger for new pole formation (septation) is reached and the bacteria are not "too fat". If these conditions are met then the pole formation phase begins. Here, elongation stops and only the hemispherical pole surface area is increased (Fig. 6.3). Once enough hemispherical surface area has been made to cover the new poles, the bacterium is assumed to divide and the model returns to the elongation regime (note that we track only one daughter cell). Volume growth occurs continually throughout these cycles of elongation and pole formation (Figure 6.2).

6.2.1 Model set-up

6.2.1.1 Precursor synthesis

As already described, the model coarse-grains the biosynthesis of peptidoglycan precursors into one synthesis reaction. The synthesis rate S of precursors is assumed to be proportional to the cell volume V and a baseline synthesis rate (proportionality constant) s, and to have an additional dependence on the growth

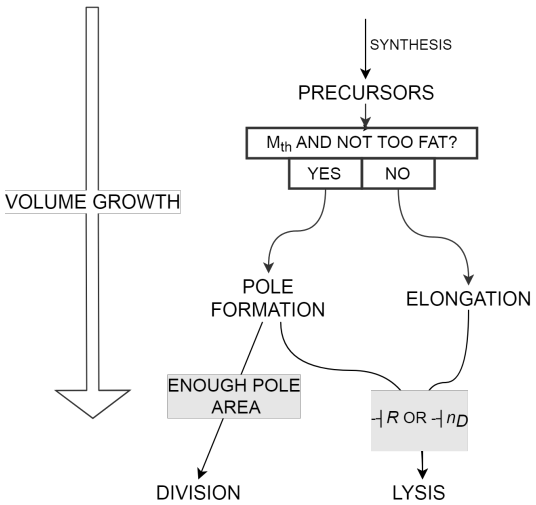

Figure 6.2: Flow chart describing the implementation of the model using the precursor threshold (M_{th}) paradigm for triggering pole formation/synthesis.

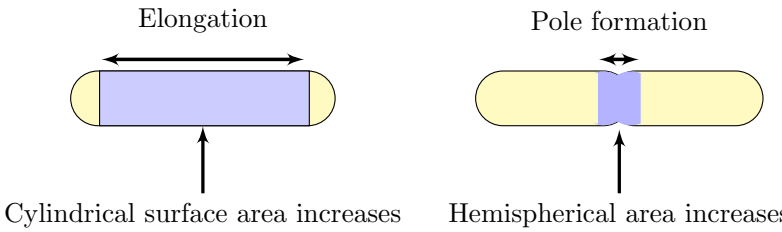

Figure 6.3: Schematic showing the different regions of surface area growth (blue area) during elongation (left) and pole formation (right).

rate λ:

$$S(t) = sV(t)\left(1 + \frac{\lambda}{\lambda_m}\right) \tag{6.1}$$

The term in brackets in Eq. 6.1 accounts for the change in relative abundance of cell wall synthesis enzymes at different growth rates. As discussed in Chapter 1, Li et al. [82] demonstrate that the synthesis rate of cell wall biosynthesis enzymes has a positive dependence on the growth rate. In our model we qualitatively capture this growth rate dependence by considering the most common fold-change in synthesis rate of cell wall synthesis enzymes, as measured by Li et al. [82] between MOPSgluRDM and MOPSgluMIN. As our model coarsegrains the entire biosynthesis process into one equation we hypothesised that it would be most appropriate if the growth rate dependence captured the fold-change experienced by the majority of the synthesis enzymes. This was 2-3 fold between MOPSgluMIN and MOPSgluRDM. Consequently we considered that an equation with a growth rate dependence that could vary between 1 and 2 would be sufficient to qualitatively capture the dynamics (it is not unreasonable to have a non-zero

Variable	Definition	Units
S	total precursor synthesis rate	$\times 10^6$ molecules/h
V	cell volume	μm^3
λ	growth rate	/h
s	baseline synthesis rate	$\times 10^6$ molecules/h/μm^3
λ_m	maximal growth rate ($r_{max}\kappa_t$)	/h
M	total number of precursors	$\times 10^6$ molecules
M_0	number of precursors in the initial cell	$\times 10^6$ molecules
q_E/q_D	incorporation rate for elongation/division	$\times 10^6$ disaccharides/h
A_c/A_p	cylindrical/pole surface area	μm^2
ρ_0	peptidoglycan density	$\times 10^6$ disaccharides/μm^2
R	baseline elongation incorporation rate	$\times 10^6$ disaccharides/h
I	baseline septation incorporation rate	$\times 10^6$ disaccharides/h
n_E	number of elongasomes	n/a
n_D	number of divisomes	n/a
K_m	Michaelis constant for incorporation dynamics	$\times 10^6$ molecules/ μm^3

Table 6.1: Summary table of the model variables and their definitions.

synthesis rate as the growth rate approaches zero [35]). Furthermore as there is a theoretical limit on how fast *E. coli* can grow [118], we include the $1/\lambda_m$ (where λ_m is the theoretical maximum growth rate) in order to also impose an upper limit on the synthesis rate. The value of λ_m was set somewhat arbitrarily and should perhaps be set as a fit parameter instead. In this way we qualitatively capture the observed growth rate dependence in Li et al. [82], however this is not necessarily the most optimum method for capturing the growth rate dependence.

In equation 6.1 the baseline synthesis rate (s) is one of the fitting parameters of the model, and it is presumed to be constant for a given temperature and pH, and independent of the growth media composition. As the baseline synthesis rate is based on the concentration of synthesis enzymes, it is necessary to include a dependence on the volume, V, so that S becomes the absolute synthesis rate.

The number of precursors M, is set to be M_0 in the initial cell (see Table 6.2 for value range). M increases due to synthesis and decreases due to the incorporation of precursors into the growing cell wall. Incorporation is assumed to happen at rate q_E during elongation and q_D during division, thus in general:

$$\frac{\mathrm{d}M(t)}{\mathrm{d}t} = S(t) - q_x(t)/7 \tag{6.2}$$

In Eq. 6.2 q_x has units of 10^6 disaccharides per hour, whereas $\frac{\mathrm{d}M}{\mathrm{d}t}$ and S have units of precursors per hour. Based on Vollmer and Bertsche [147], the average precursor strand is 21 disaccharide units long, and every third disaccharide is crosslinked, so incorporating one precursor strand corresponds to crosslinking/incorporating 7 disaccharides on average. The factor of 7 is therefore used as a conversion factor between number of precursor strands and number of crosslinked disaccharides.

6.2.1.2 Precursor incorporation

The incorporation of precursors into the cell wall increases the surface area (A_c or A_p for cylindrical or pole area, respectively) of the cell, according to:

$$\frac{\mathrm{d}A_x}{\mathrm{d}t} = \frac{q_x(t)}{\rho} \tag{6.3}$$

where the disaccharide incorporation rate, q_x, is scaled by the peptidoglycan density ρ, in units of $\times 10^6$ disaccharides/μm^2 (see Table 6.2 for literature estimates), which is assumed to be constant. The incorporation rate is a measure of the rate at which disaccharides are actively crosslinked into the existing peptidoglcyan, if no crosslinking occurred the surface area would not be able to increase in a structurally sound fashion.

The incorporation rate functions q_x are assumed to be proportional to a baseline incorporation rate, R for elongation and I for pole formation, the total volume V

and the abundance of the relevant enzyme machinery: the number of elongasomes (n_E) for elongation and the number of divisomes (n_D) for pole formation. They also depend non-linearly on the number of precursors M. For elongation, the incorporation rate has the form:

$$q_E = Rn_E \left(\frac{1}{1 + \frac{K_m V(t)}{M(t)}} \right) V(t)/\bar{V} \tag{6.4}$$

Here $\bar{V}$ is the average volume expected for the fixed growth rate λ, calculated from Schaechter's growth law [142], and being employed as a normalisation to maintain the equation dimensions. In this way the surface area grows at a rate proportional to volume as discussed in Harris and Theriot [51]. Our reasoning behind this volume dependence is that the production of elongasomes is limited by the cytoplasmic volume available for protein synthesis. Relaxing this assumption would potentially also require relaxing either of the constant volume growth, or constant peptidoglycan density assumptions. Meanwhile, for pole formation, the incorporation rate is:

$$q_D = In_D \left(\frac{1}{1 + \frac{K_m V(t)}{M(t)}} \right) \tag{6.5}$$

The parameters n_E and n_D will be fit, taking account of literature estimates [28] (Table 6.2). For simplicity it is assumed that $R = I$ in the absence of antibiotic - this is also a fit parameter (taking account of literature estimates, Table 6.2). K_m is the Michaelis constant and is another one of the fitting parameters for the model.

$$Rn_E \left(\frac{\frac{M(t)}{V(t)}}{\frac{M(t)}{V(t)} + K_m} \right) = k_{cat}[E] \frac{[S]}{[S] + K_m} \tag{6.6}$$

As we show in Equation 6.6, the non-linear core of the incorporation rate equations is an adaptation of the classic reaction rate equation for an enzyme of concentration $[E]$ with catalytic rate k_{cat} and binding constant K_m acting on a substrate of concentration $[S]$ [36]. Here, the catalytic rate, k_{cat} is substituted with R, the enzyme concentration $[E]$ is substituted with n_E and the substrate concentration $[S]$ is replaced with $\frac{M(t)}{V(t)}$, the concentration of precursors. This has been rearranged in equations 6.4 and 6.5 in order to simplify the fraction.

6.2.1.3 Volume and surface area growth

As previously mentioned, volume growth is assumed to be independent of surface area growth, and to be exponential, since the bacteria are in steady state growth before the antibiotic is added:

$$\frac{\mathrm{d}V(t)}{\mathrm{d}t} = V\lambda \tag{6.7}$$

Parameter	Literature Value(s)	Reference
r_{max}	65.8 μM	Scott el al 2010 [118]
κ_t	0.06 $\mu M^{-1}h^{-1}$	Scott et al 2010 [118]
R	$\sim 0.018 \times 10^6$disaccharides/h	Lee, Tropini et al 2014 [78]
n_E	1 - 150 complexes	The range of PBP2 molecules at different growth rates [28]
n_D	1 - 150 complexes	The range of PBP3 molecules at different growth rates [28]
ρ	50 disaccharides/μm^2	Lower bound: 1 disaccharide $\approx$ $0.02\mu m^2$ [78]
	0.2×10^6 disaccharides/μm^2	Upper bound: 1 disaccharide $\approx 6 \times 10^{-6} \mu m^2$ [147]
M_0	$0.5 - 30 \times 10^6$ mol.	Wientjes et al [151]

Table 6.2: Literature values for some of the key model parameters. These were used to constrain the phase space.

where λ is the experimentally measured population growth rate in the absence of antibiotic.

The model is initialised with new-born cells which firstly grow by elongation via $\frac{dV}{dt}$ and $\frac{dA_c}{dt}$ (Equations 6.7 and 6.3 with Eq. 6.4). Once the condition to start pole formation is met, volume growth continues, but elongation stops and pole growth commences with $\frac{dA_p}{dt}$ (Equation 6.3 with Eq. 6.5). When sufficient pole surface area has been made for the new poles, division occurs; the number of cells is doubled while volume, cylindrical surface area, pole surface area, and the number of precursors are halved. This process is visualised in Figure 6.2. In this way a population of identical cells grows exponentially and deterministically in the absence of antibiotic, with a growth rate equal to λ if the volume and surface area growth are balanced correctly by fitting the s, R, K_m and M_0 parameters.

6.2.1.4 Lysis rates

The model at this stage can describe the population dynamics in the absence of antibiotics, as well as the cell morphology in the presence and absence of antibiotics (representing the effect of antibiotic by a change in R, I, n_E or n_D). However the model cannot predict the effect of antibiotic on the number of viable bacteria as no lysis (cell death) rates have been introduced. The aim of the model is to successfully replicate the population dynamics experimentally measured for *E. coli* growing in the presence of mecillinam and aztreonam (Chapters 4 and 5), therefore it is necessary to include cell lysis in the model.

Mecillinam and aztreonam exposure result in very different population dynamics (Figures 4.3 and 5.6). Therefore we hypothesised that the different modes of

inhibition (i.e. inhibiting elongation versus division) induce different types of lysis. When elongation is inhibited (mecillinam, simulated by decreasing R), the corresponding lysis rate (L_E) is assumed to be proportional to the number of elongasomes (n_E), the change in the incorporation rate ($R_0 - R$) and the ratio of initial surface area to volume $(SA/V)_0$ to current SA/V (which acts a measure of how stretched the cell wall has become).

$$L_E = \phi_E n_E \left(R_0 - R\right) \frac{(SA/V)_0}{SA/V} \tag{6.8}$$

The dependence on n_E and $R_0 - R$ is based on the concept of out-of-control elongasomes. Within the elongasome there is a balance between transpeptidase, glycotransferase and hydrolase reactions [16]. By decreasing the incorporation rate this balance is upset and a toxic cycle can occur, which leads to lysis [16]. The surface area to volume ratio term is based on the hypothesis that as the bacteria become larger and larger spheres the cell wall becomes unstable, and the rate of lysis therefore increases. The lysis rate constant of proportionality ϕ_E is another parameter that will need to be set.

Meanwhile, when division is inhibited (aztreonam, simulated by decreasing n_D), the corresponding lysis rate is assumed to have two options: a filament-associated component or a non-filament associated component. This assumption arises from the observed population dynamics (Figure 5.6), where filaments lyse more slowly than non-filamenting bacteria exposed to the same aztreonam concentration. We assume that $L_D = L_D^{filament}$ or $L_D = L_D^{non-filament}$ i.e. that there are two distinct lysis regimes with no combination of the lysis rate options. The filament-associated option is assumed to be proportional to the fractional increase in length $\left(\left(l - l_0\right)/l_0\right)$, and to be active throughout elongation:

$$L_D^{filament} = \psi_D \left(l - l_0\right)/l_0 \tag{6.9}$$

This is controlled by the parameter ψ_D. We suppose that filaments are unsustainable as they get longer based on observations in the literature that filaments eventually lyse [18, 45].

The non-filamenting option is assumed to result due to out-of-control divisomes as fast lysis has been observed with division inhibitors when the cell is unable to prevent hydrolase activity, despite the lack of incorporation [18]. This faster non-filament lysis is controlled by the constant of proportionality ϕ_D. $L_D^{non-filament}$ is assumed to be proportional to the incorporation rate (I) and the change in the number of divisomes ($n_{D0} - n_D$) (in the same manner as for mecillinam-related lysis), and only active during pole formation:

$$L_D^{non-filament} = \phi_D I \left(n_{D0} - n_D\right) \tag{6.10}$$

The development of the lysis rate equations generates additional parameters that

require fitting: ϕ_E, ϕ_D, ψ_D. This will be described in Chapter 7.

6.2.2 Division criteria

The trigger for *E. coli* cell division is a topic of intense debate in the literature [6, 51, 128, 148]. In this model I have implemented three division models to test which are capable of capturing the observed experimental dynamics. We use the term "division model" to describe the criterion that the mathematical model uses to transition from the elongation regime to the pole formation regime.

Our first division model is the "Precursor Threshold" model, which is based on a suggestion by Harris and Theriot [51]. In this model pole formation is initiated once a threshold number of precursors (M_{th}) is reached. In our model this threshold number was assumed to be twice the initial precursor number, M_0, plus the number of precursors theoretically required to form new poles i.e. $A_p \times \rho$. In other words, the cell triggers division once it has built up enough precursors to carry out division.

Our second division model is the well-discussed "Adder Model" [128], which was proposed based on single-cell measurements of bacterial growth [128]. In the adder model a constant volume (or length) is added between birth and division. The molecular mechanism underlying this is not known. To simulate the adder model in our mathematical model framework, it was hypothesised that if there is a constant volume added between birth and division, then there must also be a constant volume (Δ) added between birth and new pole initiation. Thus the model tracks the volume added during each elongation cycle and initiates pole formation once a threshold volume added value Δ is reached. In fact, as discussed in Chapter 8, we find that the precursor threshold and adder models behave very similarly, although with some key differences.

Thirdly, a "Timer Model" based on the Cooper-Helmstetter division model [20] (discussed in Chapter 1) was implemented. This model tracks the time elapsed from birth and at a set time (in proportion to the expected length of the cell cycle, t_p) new pole initiation is triggered.

6.2.3 Fatness threshold

Regardless of the division model implemented, our model imposes the condition that if cells are too fat then division cannot be initialised. This assumption is based on the observation that division is inhibited if the cellular levels of FtsZ are decreased below a critical level, preventing formation of the septal ring [85, 149]. This suggests that a critical density of FtsZ around the cell circumference is needed for division. Therefore we suggest that if the cell width becomes too large, then the FtsZ ring will be unable to form.

In our model the threshold radius (r_{th}) at which division is no longer possible is a fit parameter, guided by assuming a minimum density of divisomes (x) around the septal ring. This can be described with the following equation:

$$r_{th} = xn_D \tag{6.11}$$

An initial estimate for r_{th} was determined based on antibiotic-free literature values for the number of divisomes at different growth rates [28], and our microscopy measurements for the cell width at comparable growth rates. We approximate the number of divisomes using the number of PBP3 molecules and so compared the number of PBP3 molecules in minimal and rich media (63 ± 12 and 132 ± 17, respectively [28]), with average *E. coli* radii at comparable growth rates measured in our microscopy experiments ($0.45 \pm 0.03\mu$m and $0.47 \pm 0.03\mu$m, respectively).

Comparing $\frac{n_D}{r}$ across the two growth rates gives rise to the observation that the average cell radius $< 0.008\times$ the average number of PBP3 molecules, under antibiotic-free conditions. Therefore,

$$r_{th} = 0.008n_D \tag{6.12}$$

was used as an initial estimate for what we term the "fatness threshold" in the absence of antibiotic. This will be fit more carefully in Chapter 7. 0.008 can be viewed as the hypothetical maximum distance, in microns, covered per divisome required for successful division. As we shall see, this fatness threshold is important for the cell morphology dynamics in the presence of antibiotics. In fact, this turns out to be much more important than the choice of division model.

6.2.4 Determining the cell length and width

It is necessary to know the length and width (or radius) of the simulated cells for two reasons: to implement the fatness threshold on division, and secondly to directly compare model output with our microscopy data. The model does not track these dimensions explicitly, but they can be determined from the surface area and volume if a spherocylinder geometry is assumed (e.g. Fig. 6.3).

Taking the cylindrical portion of the cell to have length l and radius r, the hemispherical ends have the same radius r. Therefore the total volume can be written as the sum of the cylindrical and spherical volumes:

$$V = \pi r^2 l + \frac{4}{3}\pi r^3 \tag{6.13}$$

The cylindrical surface area (A_c) is related to length and radius by:

$$l = \frac{A_c}{2\pi r} \tag{6.14}$$

Combining equations 6.13 and 6.14, a polynomial in terms of the radius can be derived with the (known) volume and cylindrical surface area as coefficients:

$$\frac{8}{3}\pi r^3 + A_c r - 2V = 0 \tag{6.15}$$

In the simulations, this is solved using the Python numpy.roots function to determine the radius, which can then be used to find the length according to Eq. 6.14.

From our experimental results (Chapter 4) (and the literature) it is clear that bacteria exposed to the action of mecillinam will end up having a spherical geometry. For cells growing as spheres, rather than spherocylinders, we need a different geometrical description. The model copes with the transition from spherocylinder to sphere by assuming that there is some minimal cylindrical length (l_{th}) at which the bacterium re-models its peptidoglycan network to a spherical geometry: the "sphere threshold". This minimal cylindrical length is assumed to depend on the radius according to:

$$l_{th} = xr \tag{6.16}$$

where x is a fraction. A dependence on the radius is included as it is assumed that if the bacterial cells are becoming fatter, then they will become more likely to transition to a spherical morphology. The value of x will be discussed in detail in Chapter 7. Once the cylindrical length hits this threshold and the cylindrical length is set to zero, the bacterium is considered a sphere and its radius is determined from the cell volume, according to:

$$r = \sqrt[3]{\frac{3V}{4\pi}} \tag{6.17}$$

Once the bacteria have become spherical it is assumed that they cannot return to the spherocylinder geometry.

6.3 Parameterising the model in the absence of antibiotics

Now that the foundations of our mathematical model have been laid out, it is necessary to parameterise the model. First, suitable parameters have to be found for antibiotic-free growth. These parameters are the baseline synthesis rate s, the baseline incorporation rate $R = I$, the Michaelis constant K_m, the number of elongasomes n_E, the number of divisomes n_D and the initial number of precursor molecules M_0. We will use our experimental data for the antibiotic-free bacterial morphology to determine the best parameter values at different growth rates. It should be noted that most of the parameter fitting was performed using the precursor threshold division model.

6.3.1 Constraining the parameter space

As previously noted, the model in the absence of antibiotic has a relatively large number of parameters (6-8 depending on the division model): the peptidoglycan density (ρ), the baseline synthesis rate (s) of PG precursors, the Michaelis constant for precursor-enzyme dynamics (K_m), the incorporation rate of PG precursors into the cell wall during elongation and pole formation ($R = I$), the initial number of precursor molecules (M_0), the number of elongasomes (n_E), the number of divisomes (n_D), the constant volume added (Δ) for the adder division model and the time to initiate pole formation (t_p) for the timer division model. Nevertheless, it is possible to determine these using only the antibiotic-free experimental data. If we consider the peptidoglycan density to be fixed, the precursor threshold division model has six fit parameters and there are nine constraints. These constraints will now be discussed in more detail.

For the four experimental growth conditions (MOPSgluRDM pH 7.4, MOPSgluRDM pH 6.5, MOPSgluMIN pH7.4 and MOPSgluMIN pH 6.5) we have measured average cell morphology (length and width) in the absence of antibiotic. The MOPSgluRDM and MOPSgluMIN pH 6.5 growth conditions were used to study the population dynamics and morphology of *E. coli* growing in the presence of mecillinam, while the MOPSgluRDM and MOPSgluMIN pH 7.4 growth conditions were used to study the impact of aztreonam. Having four experimental conditions provided us with four antibiotic-free growth rates and the corresponding average lengths and widths of *E. coli* growing at these growth rates. For each growth rate the model has to return an average length and width, within the experimental error, and maintain stable steady-state growth. Thus there are three constraints per growth rate.

Further constraints on the parameter values arise from their expected growth rate dependence. Chemical reaction rates are known to be affected by pH and temperature [110], hence s, $R = I$ and K_m are expected to change between the pH 6.5 and pH 7.4 conditions; however if the pH and temperature are constant, these fundamental enzymatic properties should not be affected by the growth medium. Therefore the baseline synthesis rate s, baseline incorporation rate $R = I$ and the Michaelis constant K_m are assumed to be growth medium independent, but pH dependence is allowed. This means that the two growth media at pH 6.5 are assumed to have the same s, $R = I$ and K_m values, and the two growth media at pH 7.4 will have the same s, $R = I$ and K_m values, but these may be different from those at pH 6.5.

Meanwhile the number of elongasomes n_E and the number of divisomes n_D are assumed to have a positive growth rate dependence. The growth rate dependence of the number of elongasomes and divisomes is based on the observation that there are more of every PBP in fast growing *E. coli* than in slow growing *E. coli* [28]. Furthermore, the number of initial precursors M_0 is hypothesised to have little, or a slight negative, dependence on growth rate based on measurements of the precursor pools for *E. coli* in different growth media [88]. This means that the n_E

and n_D values for the MOPSgluRDM condition are required to be greater than (or equal to) those for the corresponding MOPSgluMIN condition and the M_0 values should be approximately equal , while sharing the same s, R and K_m. Thus there are six additional constraints based on the expected growth rate dependence.

The parameter space searched is defined in Table 6.3. The ranges for ρ, n_E, n_D, R and M_0 were constrained using the literature [28, 78, 88, 151]. The ranges for s and K_m were determined by preliminary simulations, as such s and K_m were the only truly free parameters in the fitting routine. For each condition the parameter set which satisfied the constraints and produced a cell morphology closest to the measured average values was chosen. Only a small proportion of the theoretically possible parameter space was searched. In particular only one possible peptidoglycan density has been considered: $\rho = 0.1 \times 10^6$ disaccharides/μm^2 [151].

6.3.2 Finding the best fit parameters

The parameter search was performed in a "brute-force" way by systematically scanning, in a grid-like fashion, all possible parameter combinations within the range defined by Table 6.3 and following the protocol described in Figure 6.4. For each growth condition, the growth rate, a sensible birth volume and birth surface area are set from the experimental data. The model is then run with each possible parameter set for 20 simulation hours. This simulation length was chosen because we expect that a sensible parameter set should reach steady state growth by 10-12 divisions.

Each parameter set was scored based on its predicted steady-state cell dimensions. The steady state cell length ($\bar{l}$) and radius ($\bar{r}$) were calculated by averaging over fifty measurements taken over the final 250 simulation minutes. For a parameter set to be deemed acceptable, the steady state radii had to be within the

Parameter	Range searched
ρ	0.1×10^6 disaccharides/μm^2 [151]
n_E & n_D MOPSgluRDM	75 - 160 enzyme complexes [28]
n_E & n_D MOPSgluMIN	10 -100 enzyme complexes [28]
s	(0.1 - 2.0) $\times 10^6$ molecules/h/μm^3
K_m	(0.01 - 1.0) $\times 10^6$ molecules/ μm^3
$R = I$	(0.009 - 0.018) $\times 10^6$disaccharides/h [78]
M_0	(0.5 - 6.0) $\times 10^6$ molecules [88]

Table 6.3: Final parameter ranges used in the parameter space search. These ranges were guided by literature values (if possible) and then refined via wider, exploratory, space searches which determined that these ranges were more likely to contain the ideal solutions.

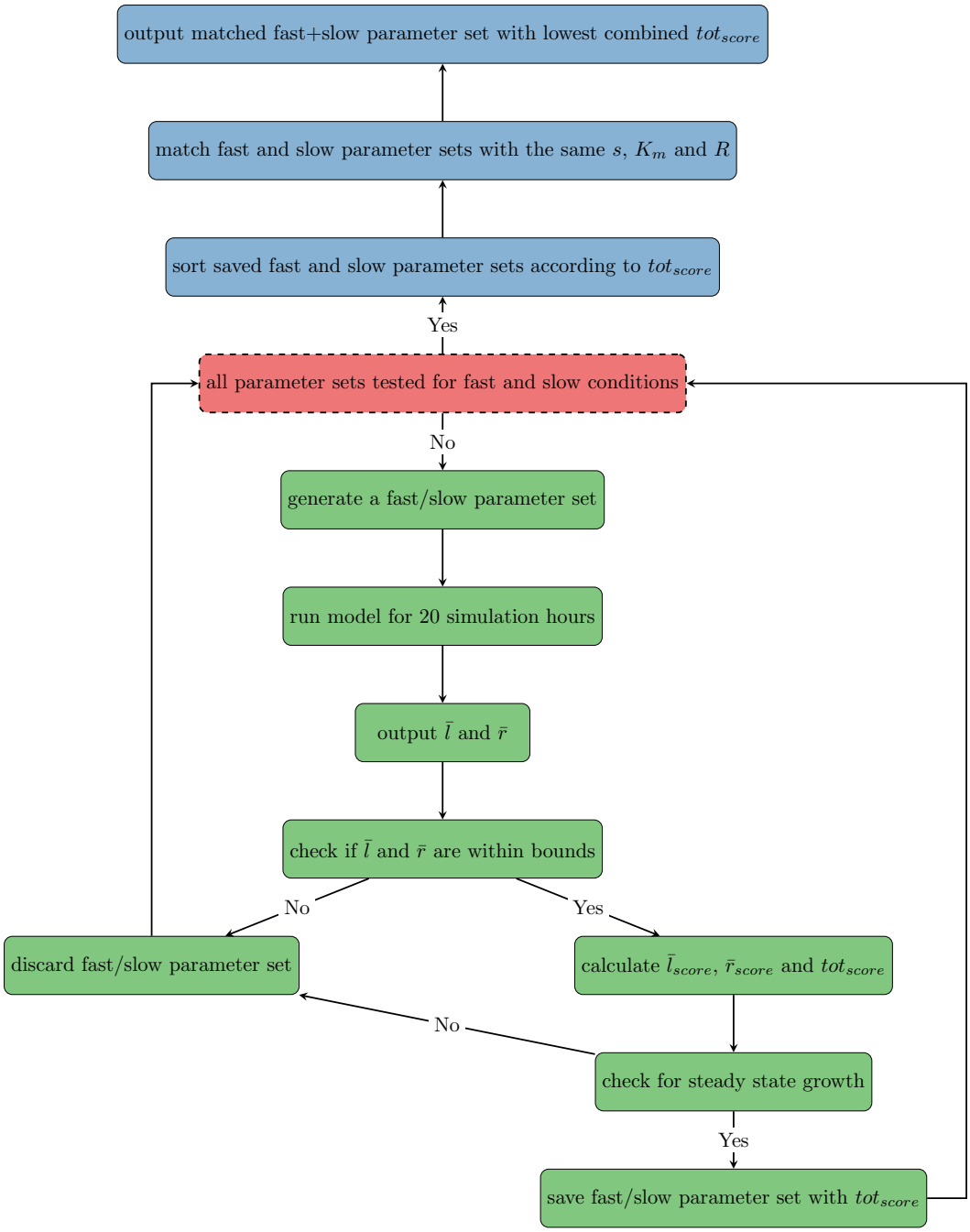

Figure 6.4: Flow diagram demonstrating the process of finding the best fit parameter sets according to the cell morphology. Fast and slow parameter sets are searched in parallel, and only brought together to check the growth-rate dependent constraints once all possible fast and slow parameter sets have been tested.

experimental cell radii and their standard deviations. Cell lengths were allowed to vary significantly over a cell cycle therefore the steady state lengths were allowed to be within 30% of the experimental cell length and its standard deviation. If a parameter set produced an average radius and length within the acceptable limits, a "goodness of fit" score was assigned to that parameter set. This score has two components, l_{score} and r_{score}, corresponding to the lengths and widths:

$$\begin{aligned} l_{score} &= |\bar{l}_{exp} - \bar{l}| \\ r_{score} &= |\bar{r}_{exp} - \bar{r}| \\ tot_{score} &= \frac{l_{score}}{10} + r_{score} \end{aligned} \tag{6.18}$$

The "goodness of fit" score (tot_{score}) is the sum of the deviation between the average model radius and the average experimental radius, and one tenth of the deviation between the average model length and the average experimental length (Eq. 6.18). The length component of the score is scaled by ten because the cell length is generally about a factor of ten larger than the radius. This ensures that variations in length and radius contribute approximately equally to the total score. A low score therefore signifies a model parameter set that produces dimensions close to the average experimental cell. A chi-squared test would be a good, and perhaps more standard, method for measuring the goodness of fit. The main advantage of chi-squared would be that it takes the experimetnal distribution into account (not just the averages as was used in tot_{score}). As such it would measure whether the distribution of lengths and widths over a simulated cell cycle is consistent with the experimentally measured distribution.

Having done this, the next stage was to group together parameter sets for the fast and slow growth conditions, which were under the same pH and temperature conditions. As discussed previously, it is assumed that cells growing at the same temperature and pH will have the same baseline synthesis rate of precursors (s), the same baseline incorporation rate ($R = I$) and the same K_m, thus fast and slow parameter sets were paired according to s, R and K_m and the fast and slow scores added together to give the total "goodness of fit" score for that pair. The best

Growth condition	ρ_0	s	K_m	$R = I$	n_E	n_D	M_0	Δ (μm^3)	t_p (hr)
pH 6.5 34°C fast	0.1	1.9	0.1	0.009	120	160	3.3	1.28	0.288
pH 6.5 34°C slow	0.1	1.9	0.1	0.009	20	100	2.8	0.7	0.8040
pH 7.4 37°C fast	0.1	1.4	0.3	0.0113	120	180	1.5	0.655	n/a
pH 7.4 37°C slow	0.1	1.4	0.3	0.0113	20	75	1.8	0.4	n/a

Table 6.4: Best fit parameters for the two pH conditions and in both rich and poor growth conditions.

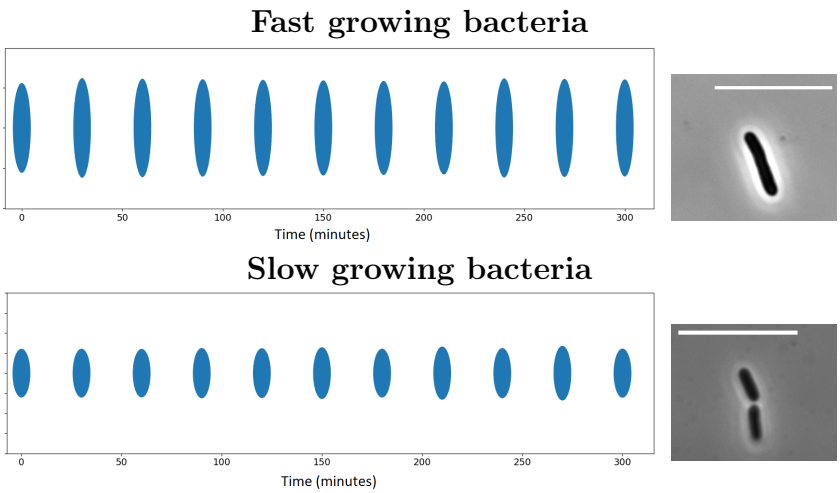

Figure 6.5: An ellipse representation of the good parameter set for MOPSgluRDM and MOPSgluMIN pH 6.5 and 34°C. The average lengths and widths are used to plot ellipses over time. This kind of figure can be used to visualise the morphology predictions of the model. Representative experimental images are shown alongside, the scale bar is 9μm.

parameter set pair for that pH and temperature is then the combination with the lowest total score. Having the fast and slow growing cells in two pH/temperature conditions provided enough experimental data to enable the model to be fit purely to antibiotic free morphology data, thus freeing up the antibiotic data to act as a test of the model's capacity for prediction and for fitting the lysis rates. This pairing process is described in the blue zone of Figure 6.4.

The resulting "best" parameters are listed in Table 6.4, and a representation of the morphology output for the best fit to the pH 6.5 and 34°C data can be found in Figure 6.5. From these best-fit parameter values it is possible to determine that under normal growth conditions M/V is on the order of 20-30 times greater than K_m, and therefore M is saturating the need for cell wall insertion. Furthermore, examining the range of parameter sets with good scores it is possible to conclude that there is no dependence on M_0 (within an appropriate range).

An illustration of how changing s and K_m can result in good or very bad "goodness of fit" scores can be found in Figure 6.6. The s and K_m values used for illustration in Figure 6.6 were chosen based on the phase space slice visualised in Figure 6.7. In Figure 6.7 the output of combined rich and poor parameter sets at different s and K_m (and for fixed n_E, n_D, M_0 and $R = I$) is represented. Filled circles indicate parameter sets which satisfied all the constraints, and are coloured according to the total score. Black diamonds represent parameter sets which broke all constraints. Other markers indicate which constraint was broken for that parameter set. Orange stars indicate that fast growing cells were too fat, while blue crosses indicate that poor growing cells were too fat. Open circles indicate that steady state growth was not achieved, with the colour indicating the corresponding growth rate: black for slow growing cells, green for fast growing

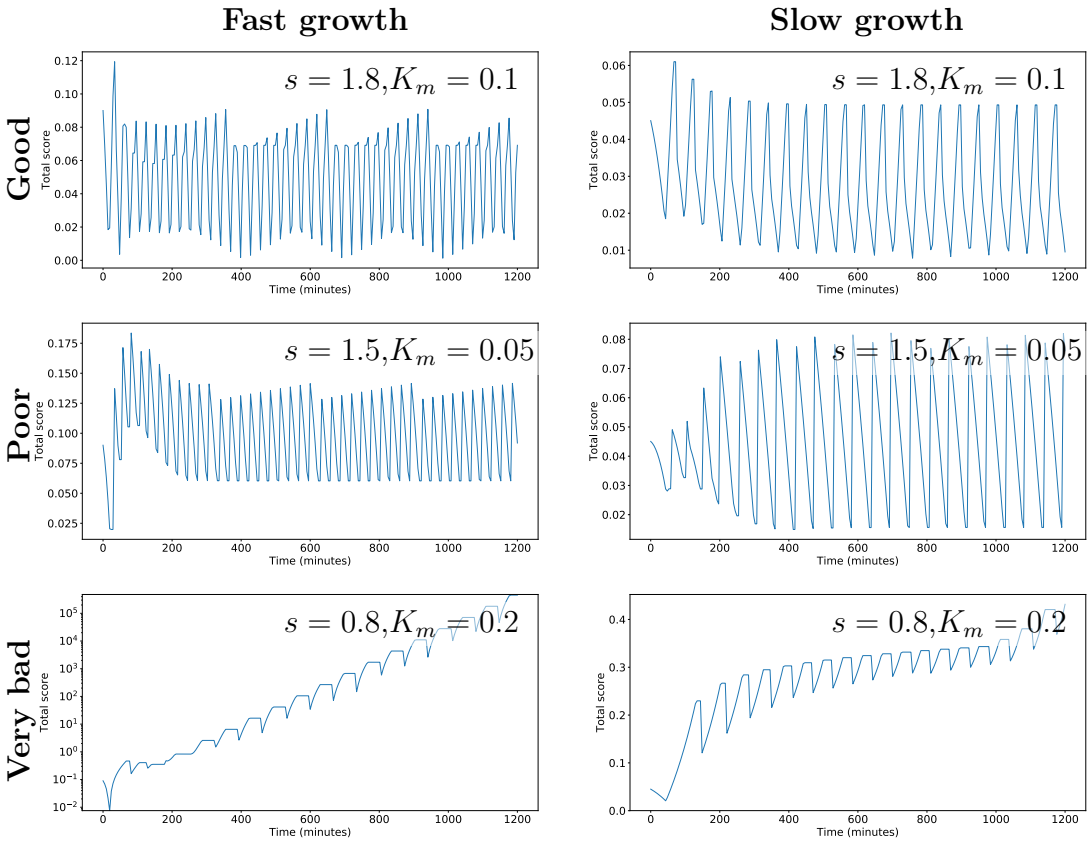

Figure 6.6: Trajectories of the total score ("goodness of fit") with time in simulations with good, poor and very bad s and K_m pairs for both fast and slow growth conditions. Here n_E, n_D, M_0 and R were kept constant using the values found in Table 6.4 for the pH 6.5 34°C condition.

cells, and red if neither growth rate achieved steady state growth. Cells being too long, but not too fat, were not observed and are therefore not indicated.

There are some limitations to this method of parameter space search. In particular, the space was discretised somewhat arbitrarily and searches stopped when reasonable parameter sets were found. It is probable that there are other valid parameter sets with equally good, or better, fits which were not found here. This method is also computationally inefficient. However, as explored in Chapter 8 the fits turn out to be good enough to reproduce other experimental observations relating to the population dynamics and morphology of bacteria in the presence of various cell wall-targeting antibiotics.

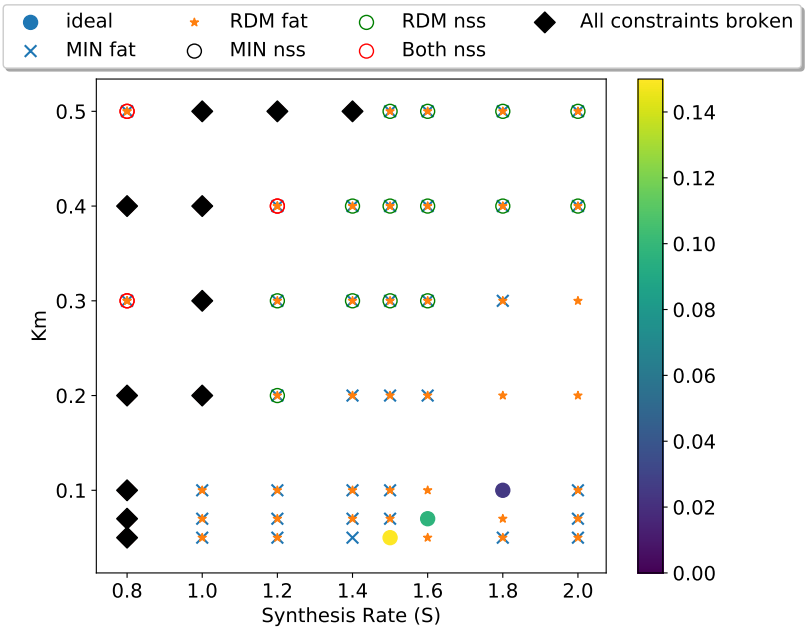

Figure 6.7: A slice of the parameter phase space with n_E, n_D, M_0 and R fixed at the values found in Table 6.4 for the pH 6.5 34°C condition demonstrating how the size and steady state constraints reduce the space of viable parameter sets.

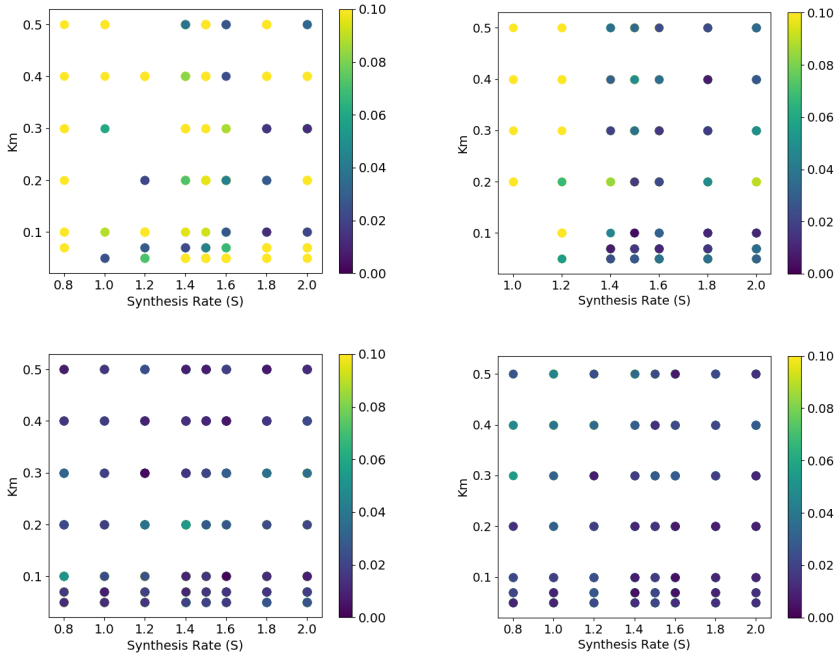

Figure 6.8: Phase space diagrams for the s and K_m space when using the precursor threshold division model in the parameter search. Top left: pH 6.5 34°C fast, top right: pH 7.4 37°C fast, bottom left: pH 6.5 34°C slow, top right: pH 7.4 37°C slow. The colour represents the "goodness of fit" score.

6.4 Observations about the model

Following the development and antibiotic-free parameterisation of the model, several observations can already be made.

- Cell morphology on slow media is less sensitive to the choice of parameters. This is shown in Figure 6.8. From our parameter space search we can generate a visual representation of the s and K_m space, where the colour of each (s, K_m) point indicates the lowest "goodness of fit" score that was found at that s and K_m by varying all the other parameters (s and K_m are used to visualise the parameter space as the same ranges were searched for all growth conditions). Figure 6.8 shows a higher prevalence of low-scoring parameter sets for the slow growth conditions. This might suggest that slow-growing *E. coli* are generally more robust to biochemical perturbations.
- The timer division model does not work with this model construction as a steady state is never reached. This is demonstrated in Figure 6.9, where we observe a decreasing birth volume contrasted with the relative stable birth volumes found in the precursor threshold and adder division models. Due to this the timer model will not be significantly discussed in the following chapters.

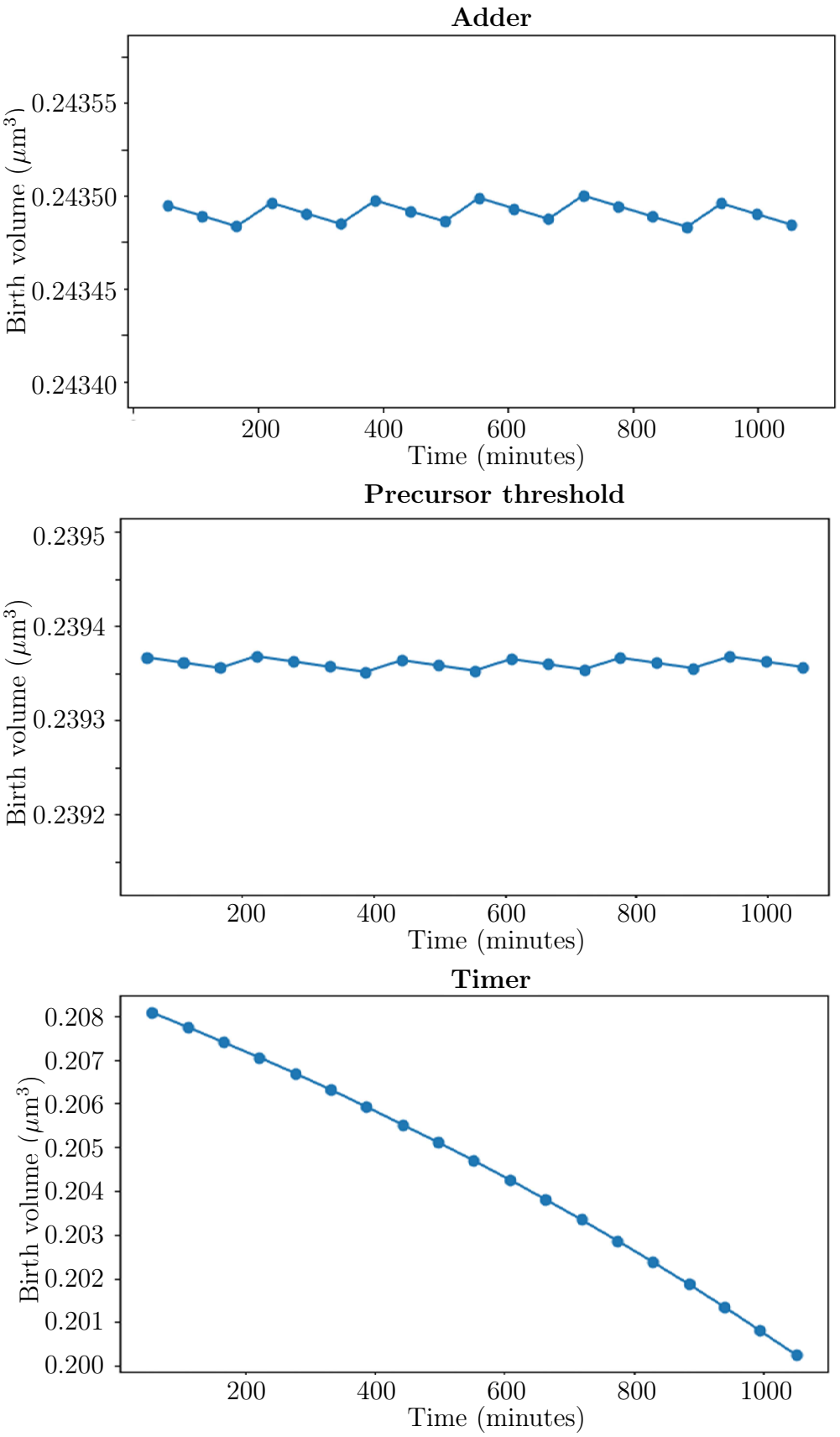

Figure 6.9: Birth volume dynamics in the model using the parameters listed in Table 6.4 for the pH 6.5 condition and the three division models. Top: Adder. Middle: Precursor threshold. Bottom: Timer.

Chapter 7

Mathematical model: fitting the antibiotic parameters

Here we complete the development of our mathematical model introduced in Chapter 6, by determining the parameters related to antibiotic action. We will start by fitting the model to mecillinam data and then move on to aztreonam. These two antibiotics have been shown experimentally (Chapters 4 and 5) to exhibit very different behaviour.

The parameters that we need to fit include the "inhibition levels" (values of R or n_D/n_{D0}, for mecillinam and aztreonam respectively) which correspond to the high and low antibiotic concentrations used in the experiments. We also need to fit the lysis rates: ϕ_E for mecillinam, and ϕ_D and ψ_D for aztreonam (to reproduce the cell number dynamics). The "fatness threshold" (the radius at which pole formation is no longer attempted) and the "sphere threshold" (the length at which a cell is considered to turn into a sphere) also need to be fit.

These fits will be performed with the precursor division model, for fast growing bacteria for both mecillinam and aztreonam. These fits will be tested by applying them to the remaining experimental datasets in Chapter 8, where the adder division model will also be compared.

In all cases, the remaining parameters n_E, s, K_m, R_0, n_{D0} and M_0 are fixed at the values that were established in Chapter 6 using the antibiotic-free data (Table 6.4), where it was determined that M is saturating the need for cell wall insertion under normal growth conditions. R_0 and n_{D0} are the antibiotic-free incorporation rate and divisome number.

7.1 Simulation protocol

The typical simulation protocol for modelling the addition of antibiotic to bacteria growing in the steady state was as follows. The simulation was started with no antibiotic and allowed to stabilise to steady state growth. Since the model generally took 10 or 11 divisions in both fast and slow growth conditions to reach the steady state (defined by stable length and width dynamics), "antibiotic challenge" was only applied after at least 12 divisions. Once 12 divisions had been completed the relevant parameter was decreased to mimic antibiotic action e.g. the precursor incorporation rate during elongation, R, for mecillinam.

The protocol as currently described would always add the "antibiotic" at the beginning of a cell cycle i.e. to the newborn cell after the twelfth division. However, in the experiments the bacterial population is composed of cells at different stages of the cell cycle when the antibiotic is added. We decided that to best mimic the experiments we should also add the antibiotic at different points in the cell cycle. This was achieved by running multiple simulations, applying the "antibiotic" at different points in the cell cycle (10%, 20%, 30% , 40%, 50%, 60%, 70%, 80%, 90% and 95% of the way through a theoretical cell cycle were used). The length of a cell cycle was assumed to be the doubling time ($\ln 2/\lambda$) determined by the fixed model growth rate (λ).

The outputs (e.g. cell length, cell width, cell number) from the multiple simulations, where "antibiotic" was applied at different points in the cell cycle, were then averaged, taking account of the age distribution in a steady-state population. The theoretical distribution of cell ages during exponential growth is [20]:

$$f(\alpha) = \ln(2)2^{1-\alpha} \tag{7.1}$$

This captures the phenomenon that in a population of exponentially growing bacteria, we expect to see twice as many newborn bacteria as dividing bacteria: $f(0) = 1.386$ while $f(0.9) = 0.743$. Averages were computed according to:

$$\sum_j f(\alpha_j) A_j \tag{7.2}$$

where A_j is the simulation output for simulation j in which antibiotic was added after fraction α_j of the cell cycle.

7.2 Parameter fits for mecillinam

As mecillinam inhibits the transpeptidase PBP2 (which incorporates new precursors during elongation), the action of mecillinam is modelled by decreasing the elongation incorporation rate, R. We therefore need to establish which values of R correspond to the high and low mecillinam concentrations used in our

experiments. This was done by fitting our simulation results for cell morphology (without lysis), to the experimental morphology dynamics in the presence of high mecillinam.

Once an inhibition level ($R < R_0$) was found which fits the experimental morphology dynamics for the high mecillinam concentration at the fast growth rate, this inhibition level was used to fit the lysis rate (ϕ_E) in order to reproduce the corresponding cell number dynamics.

7.2.1 Fitting process for mecillinam morphology dynamics

The parameter R (elongation incorporation rate) was varied over a series of simulations, and the resulting length and width dynamics extracted using the previously described simulation protocol (Section 7.1). These length and width dynamics are presented as "morphology tracks", alongside the experimental morphology track (Chapter 4 Section 4.3.1), for high mecillinam in MOPS-

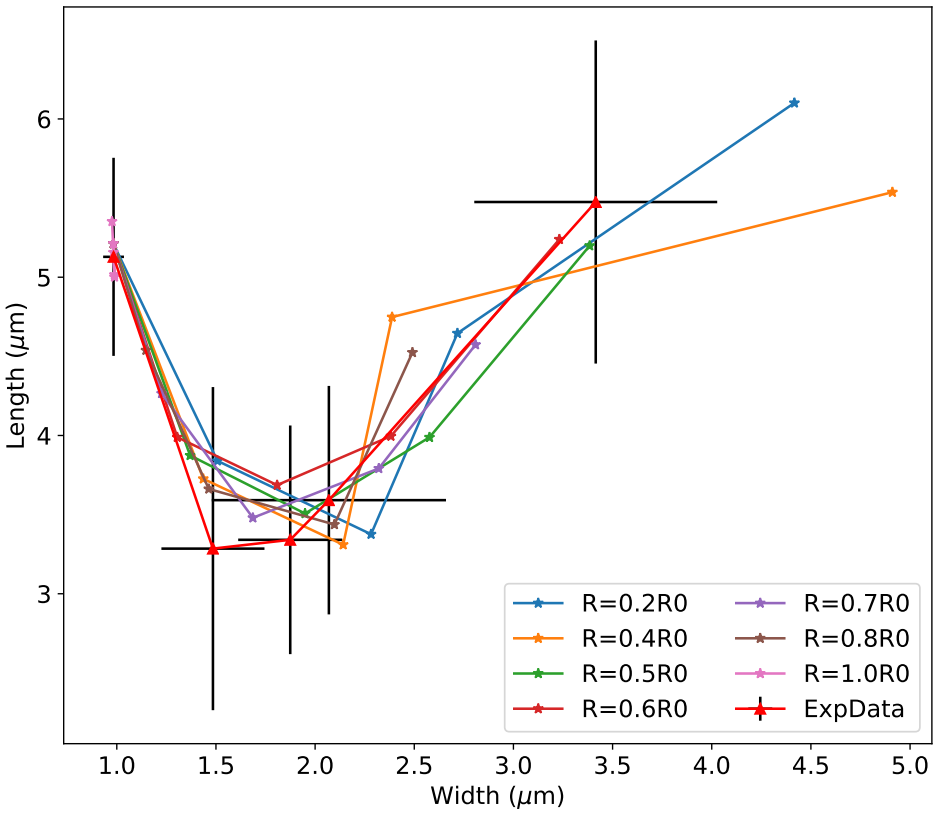

Figure 7.1: Simulated morphology tracks for fast growing bacteria at various values of R, compared to the experimental morphology track for *E. coli* RJA002 growing in MOPSgluRDM, exposed to high mecillinam. Each marker corresponds to a single timepoint: 0, 60, 120, 180, and 240 minutes from the addition of mecillinam, going roughly from left to right.

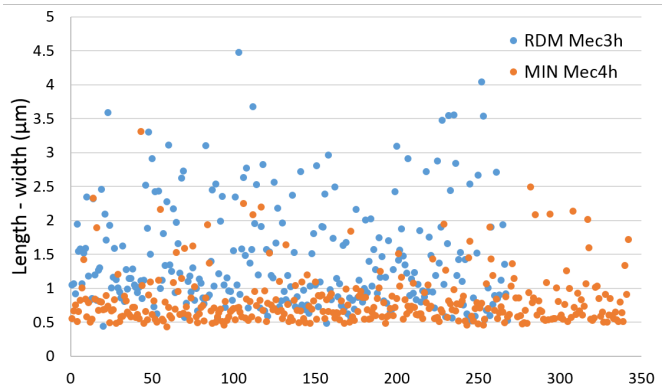

Figure 7.2: Experimental data with high mecillinam in MOPSgluRDM after 3 hours (RDM Mec3h) and in MOPSgluMIN after 4 hours (MIN Mec4h). Looking at the distribution of the width subtracted from the cell length indicates a highly conserved limit of around 0.5μm. This strongly suggests that there are no true spheres observed experimentally, with cells instead exhibiting a prolate spheroid geometry.

gluRDM, in Figure 7.1. It should be noted that experimentally no cells become perfect spheres, instead reaching a prolate spheroid morphology (Figure 7.2). I hypothesise that this arises due to the immutable nature of the old poles which results in a non-removable length component, and thus the length is always greater than the width. However, extracting the length and width of a prolate spheroid from the surface area and volume is non-trivial and as such for our qualitative model we instead consider the cells as perfect spheres. This results in the model containing a mixed population of spherical, and non-spherical cells depending on when in the cell cycle the antibiotic is applied (Figure D.1)

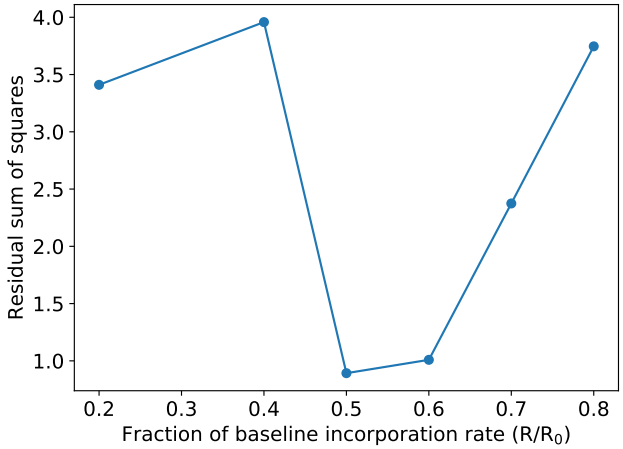

Figure 7.3: The residual sum of squares between simulated and experimental data, at different simulated incorporation rates (R) relative to the baseline incorporation rate (R_0) for fast growing cells. The minimum at $R = 0.5R_0$ indicates that this value of R best approximates the morphology dynamics at high mecillinam in MOPSgluRDM.

The experimental and simulated morphology tracks are compared by calculating the sum of the square distance between equivalent time points (Figure 7.3). The inhibition level that gives the least square distance is assumed to best correspond to the high mecillinam concentration. A chi-squared test would be a potential improvement upon this fitting method as discussed in Section 6.3.2. Thus, based on Figure 7.3, $R = 0.5R_0$ (where R_0 is the elongation incorporation rate in the absence of antibiotic) is the inhibition level that makes the best prediction for the morphology dynamics of fast growing *E. coli* at high mecillinam.

7.2.2 Sphere and fatness thresholds

It was additionally realised that two components of the mathematical model played a key role in controlling the geometry under mecillinam-like inhibition, for fast growing cells. Adjusting these components generally lead to incorrect morphology but in an illuminating way.

The first component to consider is the "spherical threshold" i.e. the point at which the bacterial cell is defined in the model to have changed its geometry from a spherocylinder to a sphere. Once this threshold is passed Eq. 6.17 is used rather than Eq. 6.15 to calculate the geometry. This is described in terms of the cylindrical length at the point of transition (l_{th}) and the radius (r): $l_{th} \leq xr$, where x is a positive real number.

The impact of the spherical threshold on fast growing cells is as follows. If the value of x is very low, e.g. 0.01, the model assumes that the cylindrical length has to be negligible before the bacterium is considered as a sphere. Such a low value of x results in non-biological morphology under mecillinam-like inhibition: after 200 minutes the cell width decreases during elongation, and the cell length increases considerably (see Figure 7.4 top panel for example width and length dynamics). As such dynamics are not observed experimentally this suggests a flaw in the model, and in the model's assumptions. It is possible that the assumptions of constant volume increase and constant peptidoglycan denisty are no longer valid when mecillinam is present. However, the model also assumes a spherocylindrical geometry, and as our microscopy data clearly shows a deviation from spherocylinders in the presence of mecillinam, I chose to relax this assumption as a starting point. Ideally, the model would transition from a spherocylinder to a prolate spheroid. However, as previously described, determining the semi-major axes of a prolate spheroid from the surface area and volume is non-trival, therefore I decided to approximate this behaviour with spherical geometries. This leads to the requirement that a cell transitions to a sphere before the non-biological dynamics manifest, therefore it was hypothesised that the value of x should be larger. In reality, a larger value of x might correspond to the bacterium actively adjusting its morphology towards that of a sphere, as a spherocylinder shape starts to become unsustainable. It is also very likely that the peptidoglycan denisty is changing under this condition, and a potential improvement of the model would be to allow the peptidoglycan density to change.

$l_{th} = 0.01r$ **: too small spherical threshold gives filamentation.**

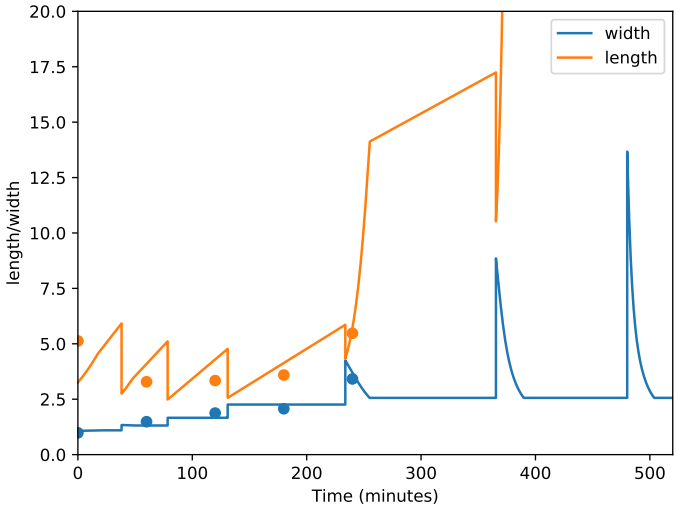

$l_{th} = r$ **: becomes spherical too quickly**

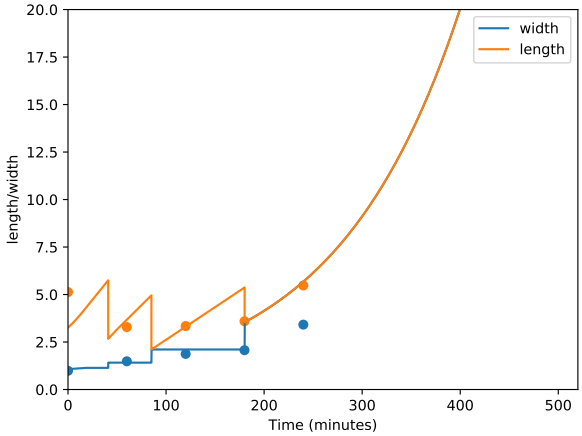

Figure 7.4: The length and width dynamics in the model for $R = 0.5R_0$ with a spherical threshold of $l_{th} = 0.01r$ (top) or $l_{th} = r$ (bottom). The markers represent the experimental results for the average width and average length for *E. coli* in the presence of 1.5μg/ml mecillinam. For a small value of l_{th} (top) the key observation is that from around 300 minutes the width decreases during elongation, and the cell length becomes exceedingly long, which does not correspond with the experimental observations. For a large value of l_{th} (bottom), the key observation is that cells grow too quickly as spheres leading to a poor fit to the experimental data at 180 and 240 minutes.

If the sphere threshold x is too high (e.g. $x = 1$), this also leads to qualitatively incorrect results. In particular this leads to the production of spheres at earlier times, which grow very quickly ("runaway spheres"), leading to a poor fit to the experimental data at three and four hours (Figure 7.4, bottom panel). The sphere threshold was set to 0.6 in the end.

$l_{th} = 0.6r$ **and** $r_{th} = 0.007n_D$**: spheres emerge too quickly**

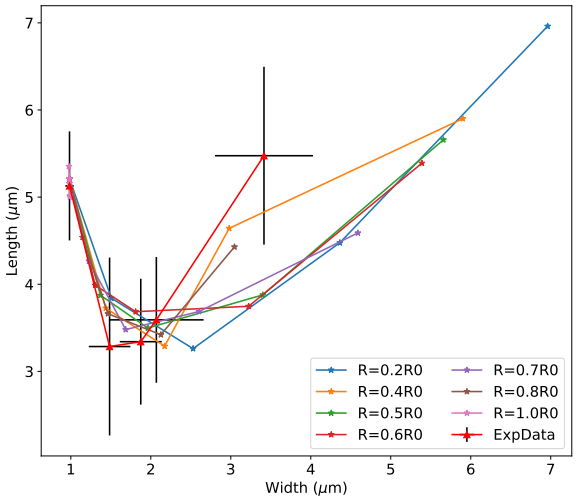

$l_{th} = 0.6r$ **and** $r_{th} = 0.008n_D$**: biologically sound dynamics at all** R

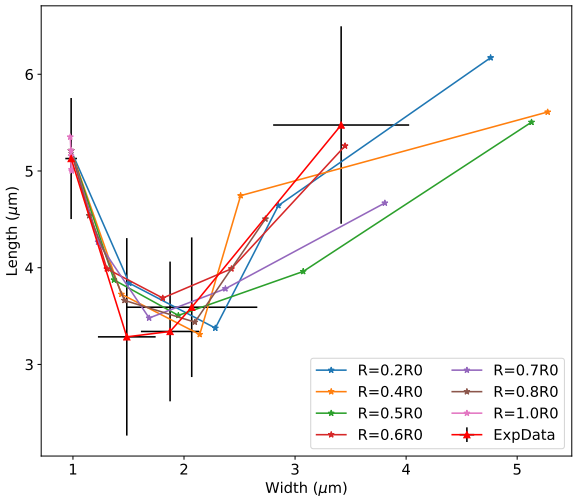

$l_{th} = 0.6r$ **and** $r_{th} = 0.009n_D$**: biologically sound dynamics at all** R

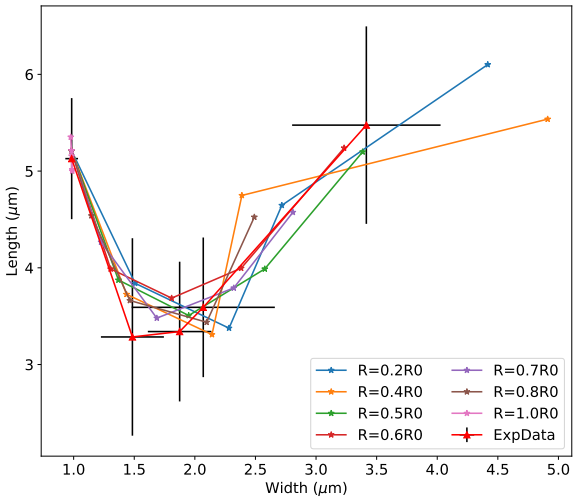

Figure 7.5: Results from the precursor division model with different fatness thresholds for fast (rich media) growing cells.

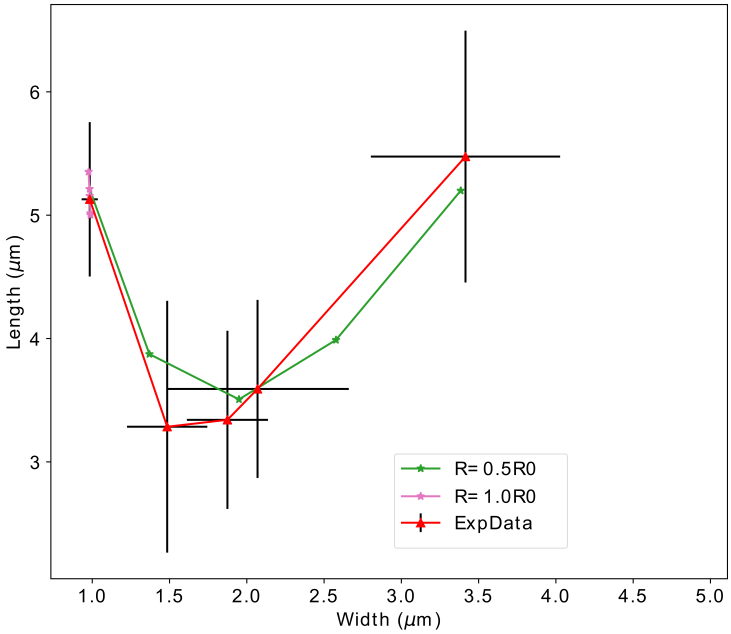

Figure 7.6: Length and width dynamics. A comparison between experimental and simulated results using the precursor division model in the rich growth conditions under mecillinam-like inhibition ($R = 0.5R_0$). The values in the legend indicate the inhibition level. Each marker corresponds to a single timepoint: 0, 60, 120, 180, and 240 minutes from the addition of mecillinam, going roughly from left to right.

The other component of the model to consider is the "fatness threshold" i.e. the radius at which the bacterial cell becomes too fat to divide. The fatness threshold (r_{th}) depends on the number of divisomes (n_D) and the hypothetical distance a divisome has to cover for successful division (x).

$$r_{th} = xn_D \tag{7.3}$$

If the fatness threshold is too small (e.g. $r_{th} = 0.007n_D$), the model produces runaway spheres (Figure 7.5, top panel) in a similar manner as when the spherical threshold is too high. These aberrant morphologies can be avoided by increasing the fatness threshold to $r_{th} = 0.008n_D$, which gives a reasonably good fit to the experimental data (Figure 7.5, middle panel); an even better fit can be achieved with a fatness threshold of $r_{th} = 0.009n_D$ (Figure 7.5, bottom panel).

To summarise, we found that to best fit the experimental data our mathematical model should have a sphere threshold of $l_{th} = 0.6r$ and a fatness threshold of $r_{th} = 0.009n_D$. Further work could be done exploring the impact of these thresholds.

7.2.3 Best fit morphology dynamics in detail

Table 7.1 (at the end of this chapter) combined with Table 6.4, summarise the best fit parameters for mecillinam. Figure 7.6 shows the resulting morphology dynamics, comparing model output to experiments, for 1.5μg/ml mecillinam and $R = 0.5R_0$. With our mathematical model we can successfully capture:

- the decrease in length, and increase in width after 60 minutes exposure to high mecillinam.
- the stabilisation of the length while the width continues to increase at 120 and 180 minutes.
- the significant increase in width and the increase in length at 240 minutes.

7.2.4 Lysis rates: fitting population dynamics in the presence of mecillinam

Our next task is to set the constant in the lysis rate equation (ϕ_E, Eq. 6.8 in Section 6.2.1.4). As R has units of $\times 10^6$ disaccharides/h and the lysis rate (L_E) has units of /h, ϕ_E has units of $\times 10^{-6}$ disaccharides. Setting ϕ_E was done by fitting to the CFU results at high mecillinam using the parameters that had already been determined and $R = 0.5R_0$. The cell number dynamics were modelled using the same simulation protocol as described in Section 7.1. The simulation was initialised with a number of cells close to the initial number of colony forming units in the experiments (Chapter 4), to allow direct comparison. Only a small range of values were tested for ϕ_E (1.0 to 1.5 $\times 10^{-6}$ disaccharides)

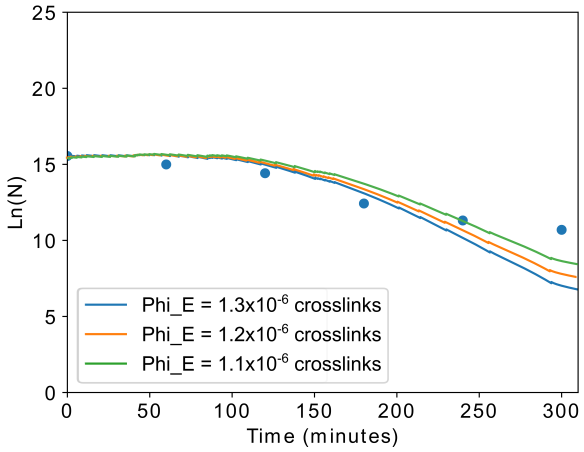

Figure 7.7: A demonstration of how changing the lysis rate constant, ϕ_E impacts the fit of the simulation output (solid lines) to the experimental data (filled circles) for growth in MOPSgluRDM with high mecillinam (1.5μg/ml)

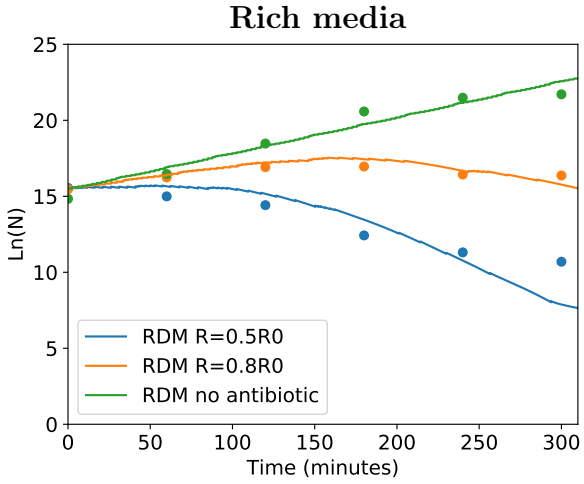

Figure 7.8: Solid lines: The log cell number dynamics in the model at high ($R = 0.5R_0$) and low ($R = 0.8R_0$) mecillinam like inhibition for fast growing bacteria using the precursor division model, for $\phi_E = 1.2 \times 10^{-6}$ disaccharides. Filled circles: The experimental data for colony forming units in the presence of high (1.5μg/ml Mec.) and low (0.094μg/ml Mec.) for both fast and slow growing cells.

as the aim was to recover the general dynamics rather than to obtain an exact fit (see Figure 7.7 to see the impact of small changes to ϕ_E).

From this search $\phi_E = 1.2 \times 10^{-6}$ disaccharides was chosen as the best fit value. Figure 7.8, blue line, shows the model output for the cell number dynamics in the presence of a high concentration of mecillinam in rich media, using this value of ϕ_E. The model captures the population dynamics well at early times, however there is some significant deviation from the experimental results after 240 mintutes.

7.2.4.1 Value of R corresponding to low mecillinam

Assuming that the lysis rate (ϕ_E) is independent of mecillinam concentration we can now determine the level of inhibition (value of R) that corresponds to the low mecillinam concentration (0.094μg/ml). To this end the incorporation rate R was changed by increments of 0.1 and the value of R that best fit the CFU dynamics, for low mecillinam, in the rich media chosen (Figure 7.9). This value was $R = 0.8R_0$ (Figure 7.8, orange line and Figure 7.9).

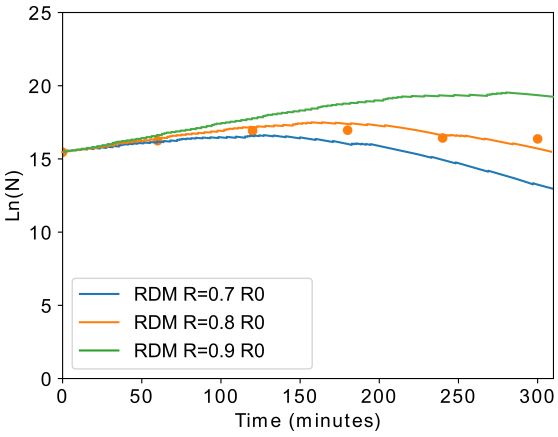

Figure 7.9: A demonstration of how changing the value of the incorporation rate, R, using the precursor division model, impacts the fit of the simulation output (solid lines) to the experimental data (filled circles) for growth in MOPSgluRDM with low mecillinam (0.094μg/ml). The other simulation parameters are as in Tables 6.4 and 7.1.

7.3 Parameter fits for aztreonam

Our model also needs to simulate the action of the antibiotic aztreonam, which inhibits division. To do this we need to fit four more parameters, corresponding to the inhibition levels for high and low aztreonam, and the two rates of aztreonam-induced lysis (Section 6.2.1.4). Using the same protocol as for mecillinam, we performed fits to the morphology using the rich media data.

Because experiments involving aztreonam were performed at pH 7.4 and 37°C (not pH 6.5 and 34 °C as for mecillinam), we use the parameters for pH 7.4 in Table 6.4 (Chapter 6).

Aztreonam is known to inhibit cell division by binding to the divisome protein PBP3. This could be implemented in the model, in principle, by either decreasing the pole formation incorporation rate (I) or by decreasing the number of divisomes (n_D). However, within this model, decreasing the pole formation incorporation rate does not result in filamentation whereas decreasing the number of divisomes does (Figure 7.14).

As filamentation is a key morphological change we want to capture when modelling the inhibitory action of aztreonam we define the level of inhibition as the fraction of uninhibited divisomes relative to the antibiotic-free number of divisomes: ${}^{n_D}/_{n_{D0}}$. Using the precursor threshold division model we determined the value of ${}^{n_D}/_{n_{D0}}$ which produced the correct length dynamics for bacteria growing in the rich medium in the presence of high aztreonam. This inhibition level, determined for high aztreonam, was then used to fit the lysis rate constants (ϕ_D and ψ_D) to reproduce the cell number dynamics in both rich and poor media (both growth media are required to constrain the two constants).

We then determined the value of ${}^{n_D}/_{n_{D0}}$ corresponding to the low aztreonam concentration by fitting to the CFU dynamics at low aztreonam on the rich media.

7.3.1 Best fit morphology dynamics for fast growing bacteria in high aztreonam

Figure 7.10 shows model morphology tracks, for decreasing values of n_D for fast growing bacteria. While the model clearly does not capture the correct width dynamics in the presence of high aztreonam (Figure 7.10, top panel) we can still find a best fit inhibition level which reproduces the length dynamics (Figure 7.10, bottom panel). From the length-only dynamics in Figure 7.10, bottom panel, ${}^{n_D}/_{n_{D0}} = 0.5$ was chosen as the best fit value.

7.3.2 Fitting the lysis rates for aztreonam-like inhibition

Using the same protocol as for mecillinam, the constants in the lysis rate equation (ϕ_D and ψ_D) were set by comparing the cell number dynamics at high aztreonam ($n_D = 0.5n_{D0}$), with the experimental CFU data for 0.5μg/ml. To recap, ψ_D is the rate constant for lysis due to excessive cell length and has units of $/h$ as it scales the fractional change in length (which is dimensionless) and the lysis rate has units of $/h$. Meanwhile ϕ_D is the rate constant for divisome-mediated lysis (due to out of control hydrolase action) and has units of $\times 10^{-6}$ disaccharides, in the same manner as ϕ_E. On rich media, bacteria inhibited by high aztreonam ($n_D = 0.5n_{D0}$) do not develop as filaments, therefore the population dynamics are hypothesised to depend only on ϕ_D. Therefore ϕ_D is fit by comparing the predicted cell number dynamics at $n_D = 0.5n_{D0}$ for fast-growing cells, with the experimental CFU data for *E. coli* growing in MOPSgluRDM at high aztreonam (Figure 7.11). A value of $\phi_D = 2.1 \times 10^{-6}$ disaccharides was found to give the best fit.

On poor media, aztreonam does cause filamentation. Therefore, setting ϕ_D to 2.1×10^{-6} disaccharides and $n_D = 0.5n_{D0}$, we fit ψ_D by examining the population dynamics of slow-growing bacteria (Figure 7.12). This lead to a best fit value of $\psi_D = 0.007$ h^{-1}. To summarise, $\phi_D = 2.1 \times 10^{-6}$ disaccharides, and $\psi_D = 0.007$ h^{-1} were found to give reasonable fits for high aztreonam in the rich and poor media.

7.3.2.1 Value of n_D corresponding to low aztreonam

Finally, we also need to find the level of inhibition in the model which corresponds to the low aztreonam concentration used in the experiments. This was obtained by fitting the CFU data for fast-growing bacteria at low aztreonam, assuming that

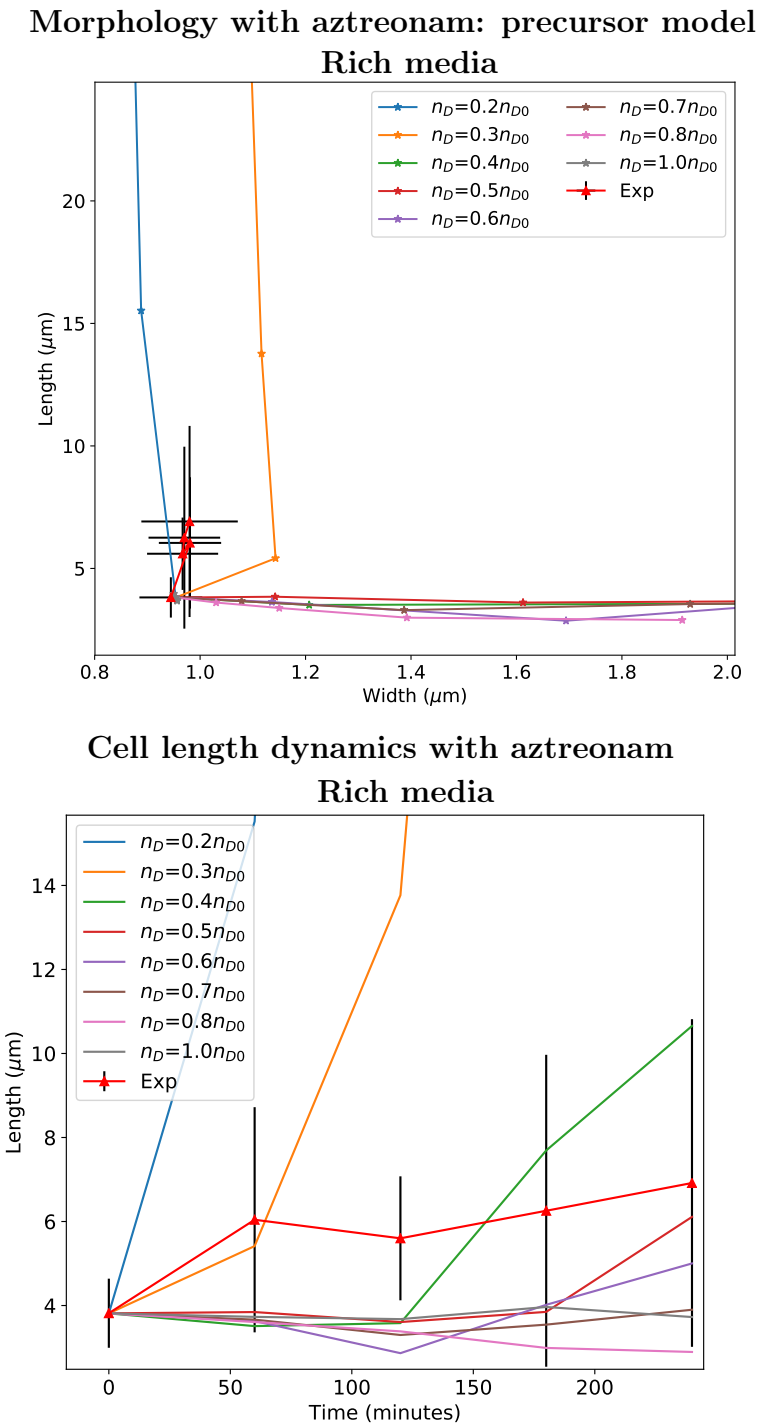

Figure 7.10: Length and width dynamics. A comparison between experimental (Exp, red triangles) and simulated values (no markers) in rich growth conditions under 0.5μg/ml aztreonam or aztreonam-like inhibition. The values in the legend indicate the fraction of active divisomes ($^{n_D}/_{n_{D0}}$). Each marker corresponds to a single timepoint: 0, 60, 120, 180 and 240 minutes going roughly from bottom to top. Other simulation parameters are as in Tables 6.4 and 7.1.

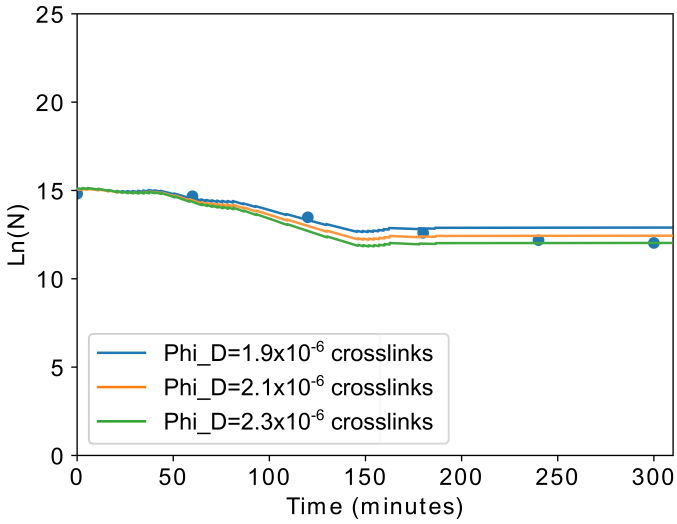

Figure 7.11: The impact of varying ϕ_D on the fit to the high aztreonam (0.5μg/ml) using the inhibition level $n_D = 0.5n_{D0}$ for fast growing *E. coli*. $\phi_D = 2.1 \times 10^{-6}$ disaccharides was chosen as the best fit. Other simulation parameters are as in Tables 6.4 and 7.1.

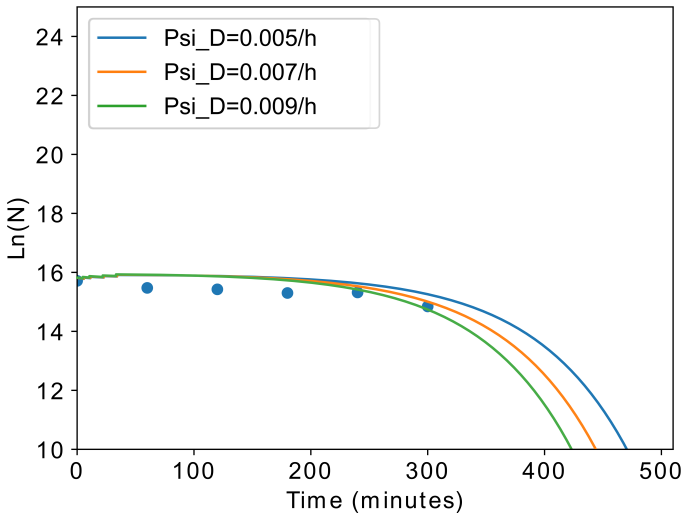

Figure 7.12: The impact of varying ψ_D on the fit to the high aztreonam (0.5μg/ml) data using the inhibition level $n_D = 0.5n_{D0}$ for slow growing *E. coli* on poor media. $\psi_D = 0.007/h$ was chosen as the best fit. Other simulation parameters are as in Tables 6.4 and 7.1.

the lysis rate constants ϕ_D and ψ_D were independent of aztreonam concentration. This fit is illustrated in Figure 7.13. $n_D = 0.8n_{D0}$ was found to be a good fit to the low aztreonam experimental CFU data for the fast growing cells (Figure 7.13).

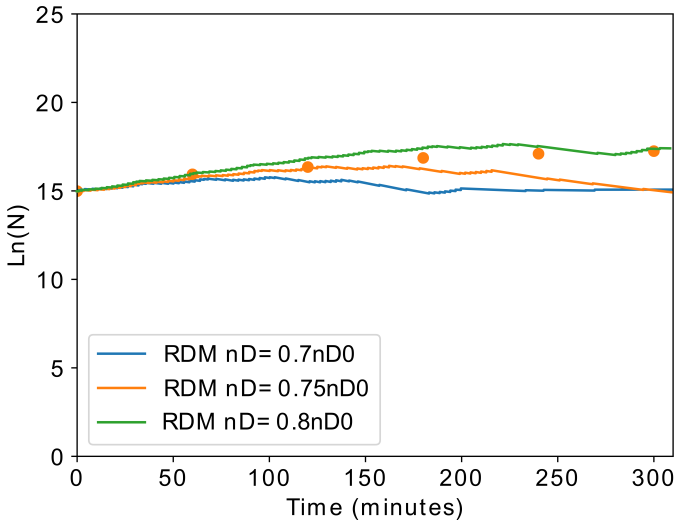

Figure 7.13: Fitting n_D to the experimental CFU results for fast growing *E. coli* in the presence of low aztreonam (0.0313μg/ml) on rich media. $n_D = 0.8n_{D0}$ was chosen as the best fit to low aztreonam. Other simulation parameters are as in Tables 6.4 and 7.1.

7.4 Discussion

A summary of the antibiotic related parameter fits for mecillinam and aztreonam can be found in Table 7.1, along with the experimental data that was used for the fitting. The remaining experimental datasets will be used to test the model in the next chapter.

From the parameter fitting process, and by visualising the length and width dynamics with an ellipse plot (Figure 7.14), various observations can be made:

- Whether we model mecillinam by changing the incorporation rate during elongation (R), or the number of elongasomes (n_E) makes no discernible difference (Figure 7.14). This suggests that the downstream impact of inhibiting elongation is key rather than whether we decrease the number of elongasomes or their activity, similar to the "lethal malfunctioning" described in Cho et al. [16].
- Sphere formation during elongation inhibition arises due to a combination of the inhibited elongation machinery and the non-inhibited division machinery. As cells become fatter to decrease the surface area to volume ratio, and hence cope with the reduced elongation rate, they then spend more time in pole formation to produce sufficient peptidoglycan to cover the increased pole area ($\sim r^3$). The possibilty of concurrent elongation and division will be discussed in Section 8.2.1.1.
- Inhibition of division results in filamentation (as we see experimentally for

aztreonam) only if the number of divisomes (n_D) is inhibited. Reducing the divisome incorporation rate (I) alone does not result in filamentation (Figure 7.14), as in the model filamentation arises from the assumption/hypothesis that a bacterial cell requires a minimum number of divisomes per micron to begin pole formation: the "fatness threshold".

Strikingly, an estimate of the fatness threshold using literature data agrees with the best fit value found using the mecillinam morphology tracks. Using the observation from Pisabarro et al. [107] that filamentation arises at inhibition of 60% of the PBP3, combined with the data from Dougherty et al. [28] for the number of PBP3 molecules (approximately 60) at the same doubling time (approximately 54 minutes, estimated from Figure 2 [107]), we can approximate that filamentation arises when there remain around 25 active PBP3 molecules. Combining this with the typical radius of *E. coli* at this doubling time ($\sim 0.3\mu$m [113]) gives a fatness threshold of $r_{th} \simeq 0.01 n_D$, remarkably close to our best fit of $r_{th} = 0.009 n_D$

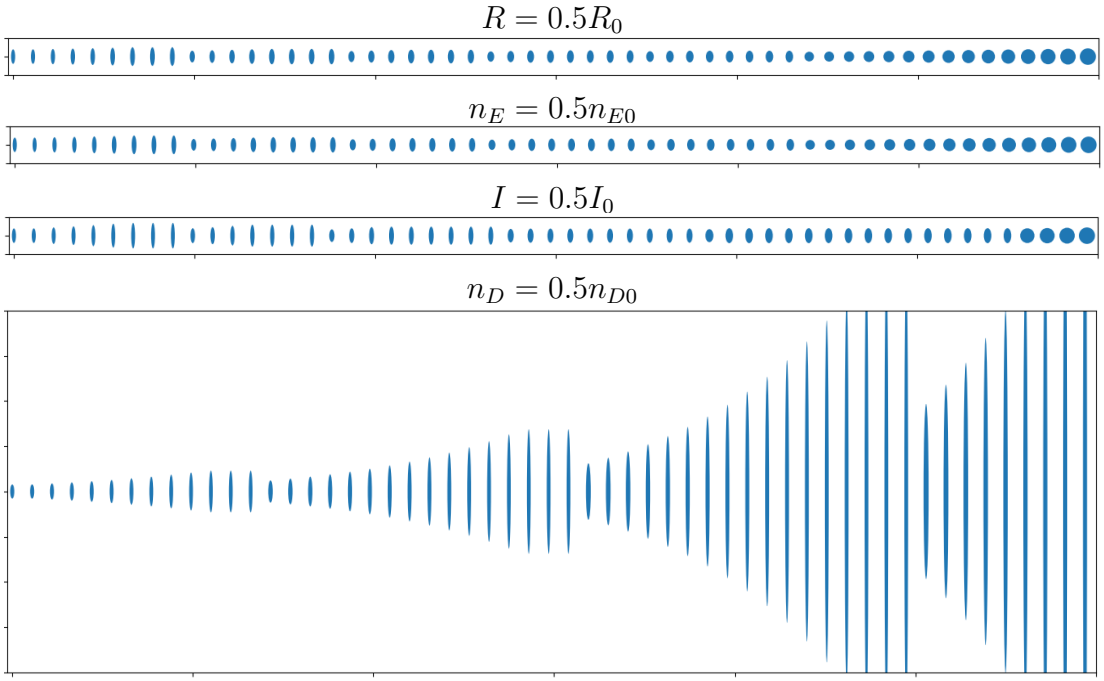

Figure 7.14: The impact of inhibiting either R, n_E, I or n_D visualised by plotting ellipses based on the cell length and width. Both axes have arbitrary units. The time between ellipses is approximately five minutes.

MECILLINAM	Parameters	Experiments used
High inhibition	$R = 0.5R_0$	RDM high Mec. morphology
Low inhibition	$R = 0.8R_0$	RDM low Mec. CFUs
Lysis rate	$\phi_E = 1.2 \times 10^{-6}$ disaccharidess	RDM high Mec. CFUs
Sphere threshold	$l_{th} = 0.6r$	RDM high Mec. morphology
Fatness threshold	$r_{th} = 0.009n_D$	RDM high Mec. morphology
AZTREONAM	Parameters	Experiments used
High inhibition	$n_D = 0.5n_{D0}$	RDM high Azt. morphology
Low inhibition	$n_D = 0.8n_{D0}$	RDM low Azt. CFUs
Lysis rates	$\phi_D = 2.1 \times 10^{-6}$ disaccharides, $\psi_D = 0.007$ h^{-1}	RDM and MIN high Azt. CFUs
Sphere threshold	$l_{th} = 0.6r$	RDM high Mec. morphology
Fatness threshold	$r_{th} = 0.009n_D$	RDM high Mec. morphology

Table 7.1: Best fit parameters for mecillinam-like and aztreonam-like inhibition in the model.

Chapter 8

Mathematical model: results and predictions

In Chapters 6 and 7 we have found the values of all the parameters of our model, by fitting to a subset of our experimental data (Tables 6.4 and 7.1). In this chapter, we recap the model's performance for the data it has been fitted to, and thoroughly test its capabilities by comparing its predictions with the remaining experimental data, to which it has not been fitted. We will start with the precursor threshold division model, and later discuss the differences (or lack thereof) with the adder division model at the end of the chapter.

8.1 Mecillinam

Using the parameters that were fitted for fast growing bacteria in the previous chapter (Table 7.1), the model predictions for bacteria in poor media (MOPSgluMIN) and intermediate media (MOPSgluCAA) exposed to low and high mecillinam can now be tested. For completeness, we also include the model fits for the fast growth media (MOPSgluRDM).

8.1.1 Morphology predictions

Starting with cell morphology, Figure 8.1 shows the model fit for MOPSgluRDM and the model predictions for MOPSgluMIN, for 1.5μg/ml mecillinam. For the minimal medium, the model successfully captures the transition to shorter, and fatter (but not spherical) bacteria in the presence of high mecillinam, although it does not capture the exact morphology dynamics, with the cell width predicted to become larger than observed experimentally and the cell length not decreasing as significantly as in the experiments. The relatively poor prediction for the

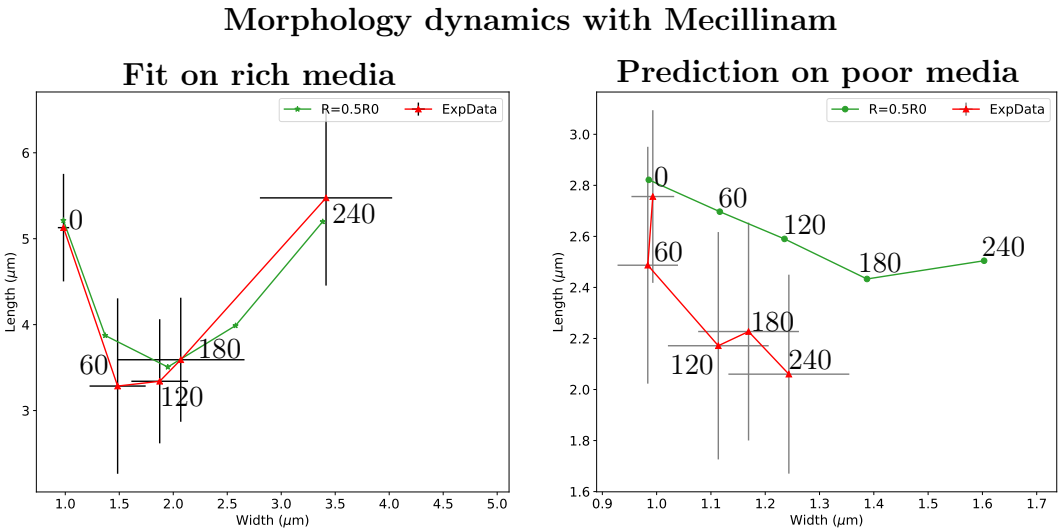

Figure 8.1: Length and width dynamics. A comparison between experimental and simulated results using the precursor division mode under mecillinam-like inhibition ($R = 0.5R_0$ in simulations; 1.5μg/ml in experiments). Each marker corresponds to a single timepoint: 0, 60, 120, 180, and 240 minutes from the addition of mecillinam, going roughly from left to right. Model parameters as in Tables 6.4 and 7.1.

minimal media morphology dynamics could be due to the inhibition level chosen. For example, in Figure 7.3, Section 7.2.1, $R = 0.6R_0$ was also a relatively good fit for the morphology dynamics in rich media. Using this lower inhibition level improves the prediction for the morphology dynamics on minimal media (see Appendix Figure D.2).

As an alternative way to visualise the model output, we use "ellipse" trajectories, as in Figure 8.2. In these plots the average length and width predicted by the model at thirty minute intervals are depicted by an ellipse of that length and width. Figure 8.2 makes it very clear that in the presence of high mecillinam, slow growing bacteria are predicted to turn into small, dividing "lemons", while fast growing bacteria get fatter, and shorter, eventually turning into large spheres/lemons. The transition to the more spherical morphology on the rich media occurs around 180 minutes.[1]

8.1.1.1 Low mecillinam morphology predictions for fast and slow growing bacteria

The model also allows us to predict the cell morphology dynamics at low mecillinam, 0.094μg/ml ($R = 0.8R_0$) (Figure 8.3), where we do not yet have

[1]The ellipse trajectories for the alternative fit, $R = 0.6R_0$ are also interesting to consider as they more clearly demonstrate a spherical morphology on the rich media at 300 minutes, rather than large lemons (Appendix Figure D.3). To truly distinguish which value of R is a better fit on rich media, more microscopy data at later times ($\geq$ 300 minutes) would be necessary.

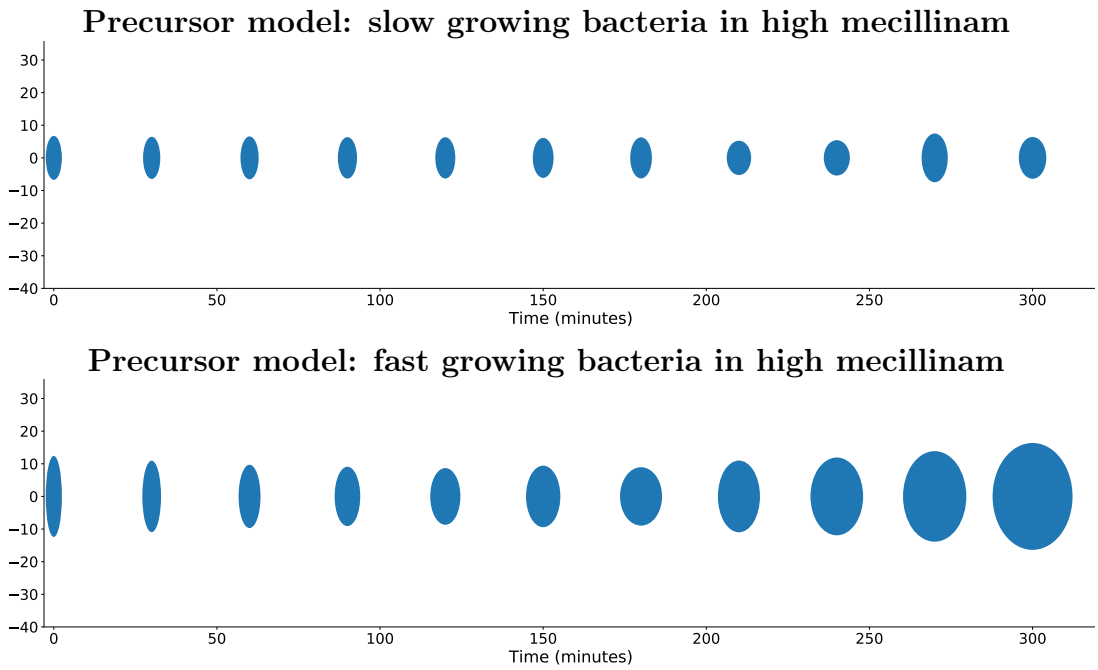

Figure 8.2: Ellipse trajectories generated by the model, based on the average length and width every thirty simulation minutes for $R = 0.5R_0$. Parameters as in Tables 6.4 and 7.1. The ellipse dimensions have arbitrary units.

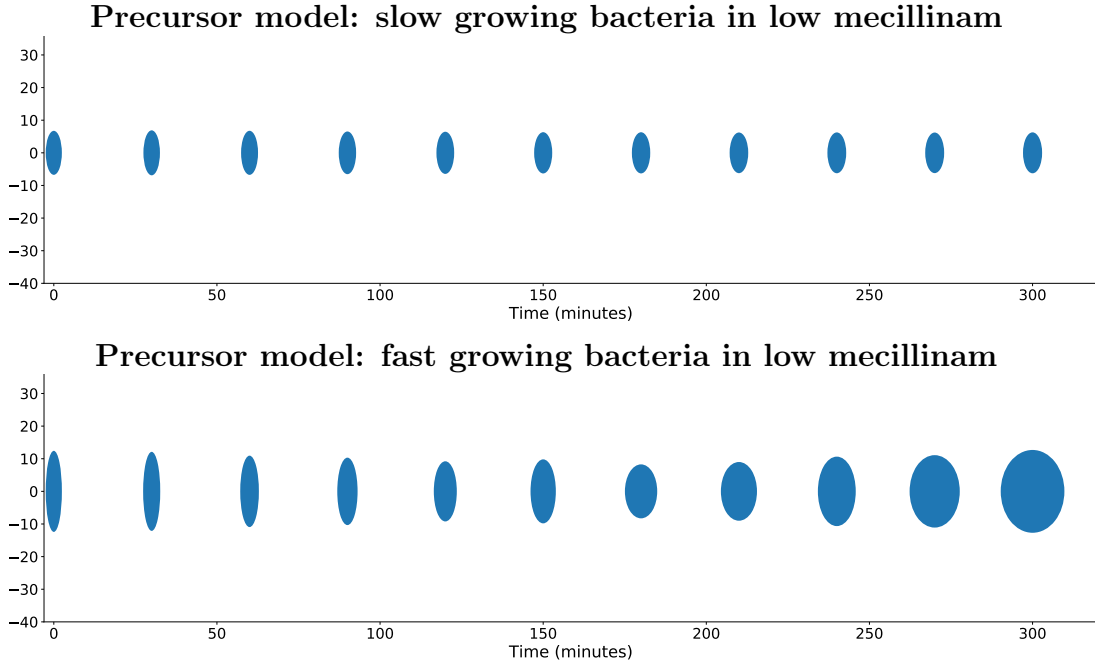

Figure 8.3: The predicted ellipse trajectories generated by the model for low mecillinam based on the average length and width every thirty simulation minutes ($R = 0.8R_0$). Parameters as in Tables 6.4 and 7.1. The ellipse dimensions have arbitrary units.

experimental data. The ellipse trajectories in Figure 8.3 show that the prediction for slow growing cells exposed to low levels of mecillinam is that they will become slightly fatter but not significantly shorter, and will continue to divide. Meanwhile fast growing bacteria are predicted to become significantly shorter and fatter, again reaching a large lemon morphology. Further work would be needed to test this prediction experimentally.

8.1.2 Predicted population dynamics for slow growing cells in the presence of mecillinam

Figure 8.4 (left) recaps the model fit for the CFU data on rich media. The model can also be used to predict the CFU dynamics of slow growing bacteria in the presence of mecillinam. In these simulations the model was initialised with a number of cells close to the initial experimental number of colony forming units (Chapter 4) for direct comparison. The predicted population dynamics can be found in Figure 8.4 (right).

Our mathematical model successfully predicts that slow growing bacterial populations will continue to grow in the presence of both low and high mecillinam, although at a reduced rate (Figure 8.4). The model is also correct in predicting that high mecillinam is only slightly more inhibitive than low mecillinam for slow growing bacteria at early time. These successful predictions suggest that our hypothesis that the inhibition level and lysis rate are independent of growth rate is correct, at least for the MOPS-based growth media used here. However, as for high mecillinam in the rich media, there is a significant deviation between the model prediction and experimental results in poor media at later times.

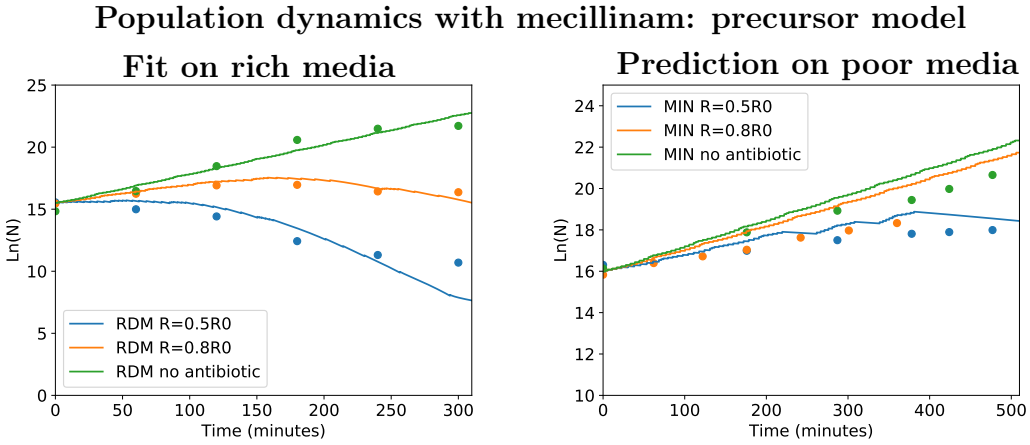

Figure 8.4: Solid lines: The log cell number dynamics from the model at high ($R = 0.5R_0$) and low ($R = 0.8R_0$) mecillinam like inhibition for cells growing on rich and poor media. Filled circles: The experimental data for colony forming units in the presence of high (1.5μg/ml Mec.) and low (0.094μg/ml Mec.) for slow growing cells in MOPSgluMIN and fast growing cells in MOPSgluRDM. Model parameters as in Tables 6.4 and 7.1.

8.1.3 Predicting the population dynamics in MOPSgluCAA

Up to this point we have only discussed model results for bacteria growing in rich and poor growth media, but we also have experimental data for an intermediate growth medium (MOPSgluCAA). The model was tested to see if it could recover the intermediate growth medium dynamics, without a full parameter search being performed at the intermediate growth rate.

To test the model for the MOPSgluCAA condition, values for those parameters which vary between fast and slow growing cells had to be approximated. These parameters are the numbers of elongasomes and divisomes (n_E and n_D), the starting number of precursors (M_0) and the starting cell dimensions (and the volume added (Δ) for the adder model, see Section 6.2.2). All these parameters (for cell dimensions, length and radius) were assumed to have a linear dependence on growth rate, and hence interpolated using the values for rich and poor media (see Table 8.1). The other parameters were as in Tables 6.4 and 7.1.

Figure 8.5 shows that the model produces results in remarkably good agreement with the experimental CFU results for MOPSgluCAA. The model correctly predicts a decreasing observed growth rate with increasing inhibition, to a similar extent as observed experimentally. The only aspect of the dynamics that the model does not capture is the slight population decrease at high mecillinam after 250 minutes (this only happens after 350 minutes in the model, Figure 8.6). This could be due to an incorrect estimate from the linear interpolation e.g. for the number of elongasomes. Further work could include microscopy for this growth medium to find the antibiotic-free cell morphology and check the "goodness-of-fit" of the estimated parameters.

Putting together the model results for the three growth media (Figure 8.6) demonstrates that the model successfully captures the growth-medium dependent dynamics of *E. coli* exposed to mecillinam. To briefly recap, the key features of the experimentally-observed growth-medium dependent dynamics were that: (i) inhibition increases as the richness of the growth medium increases, and (ii) decreasing cell numbers (lysis) were predominantly observed in MOPSgluRDM. Both of these features are captured by the model.

Growth condition	n_E	n_D	M_0	Δ (μm^3)	V_0	A_{c0}	A_{p0}
pH 6.5 34°C rich	120	160	3.3	1.28	2.6085	8.043	3.2685
pH 6.5 34°C inter.	42	113	2.9	0.82	1.603	4.108	3.2685
pH 6.5 34°C poor	20	100	2.8	0.71	1.314	2.974	3.2685

Table 8.1: Simulation parameters for the rich, intermediate and poor growth conditions at pH 6.5 34°C which are assumed to vary with growth rate. The intermediate parameter values are interpolated from the rich and poor values.

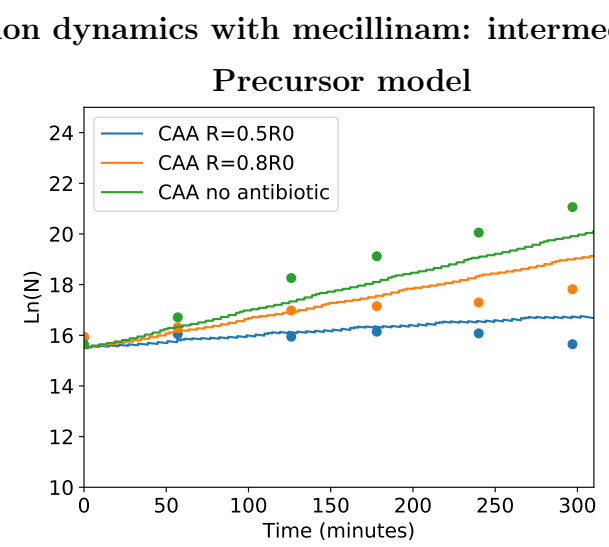

Figure 8.5: Solid lines: The log cell number dynamics from the model for high ($R = 0.5R_0$) and low ($R = 0.8R_0$) mecillinam-like inhibition for intermediate growth medium (MOPSgluCAA). Filled circles: The experimental data for colony forming units in the presence of high (1.5μg/ml Mec.) and low (0.094μg/ml Mec.) for cells growing in MOPSgluCAA. Model parameters as in Tables 6.4, 7.1 and 8.1.

To summarise, the model performs well in reproducing the morphology and population dynamics of bacteria growing in three growth media and at low and high concentrations of mecillinam. This suggests that a model which focuses on the surface area and volume growth dynamics of an individual cell can be sufficient to capture non-trivial individual cell and population level phenomena related to the inhibition of *E. coli* by cell wall-targeting antibiotics, such as mecillinam. Nevertheless, the systematic deviation between the experimental results and the model dynamics at later times suggests that there could be something lacking in the model.

8.2 Aztreonam

For aztreonam, the model parameters were fitted using the morphology track in MOPSgluRDM, the CFU dynamics at low and high aztreonam in MOPSgluRDM and the CFU dynamics at high aztreonam in MOPSgluMIN. The remaining experimental data (which was not used in the fitting process) can be used to test the model. This consists of: the morphology track for slow growing bacteria (MOPSgluMIN) in the presence of high aztreonam; the CFU dynamics for slow growing bacteria in the presence of low aztreonam; and the CFU dynamics at both high and low aztreonam for bacteria in the intermediate growth medium MOPSgluCAA.

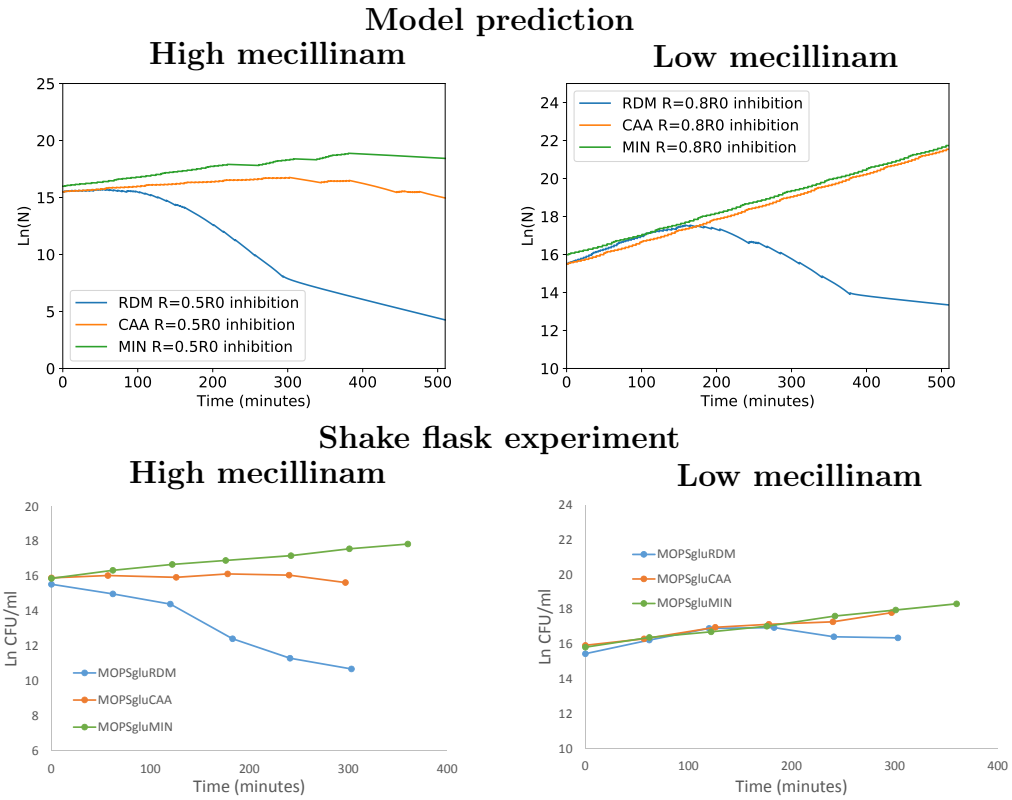

Figure 8.6: Comparison between model and experimental data for cell number dynamics in three different growth conditions: rich, intermediate and poor, for high (left) and low (right) mecillinam concentrations.

8.2.1 Morphology tracks

Figure 8.7 (left) shows the model fit for the morphology data for fast-growing *E. coli* in the presence of high aztreonam (0.5μg/ml) (see Section 7.3). Figure 8.7 (right) shows the corresponding model prediction for slow-growing bacteria in the presence of high aztreonam. The prediction of the model is that slow-growing bacteria will get slightly thinner, and significant longer, in the presence of high aztreonam. This agrees very well with the experimental observation, although the simulated bacteria do reach much longer cell lengths after three hours than observed experimentally.

To summarise, the model successfully captures filamentation on poor media, but not rich media, in the presence of high aztreonam.

8.2.1.1 Improving the aztreonam morphology tracks

In our model cells generally become fatter if there is an imbalance between the surface area and volume growth (since fat cells have a smaller surface area to volume ratio). I hypothesised that the model predicted fatter, fast-growing

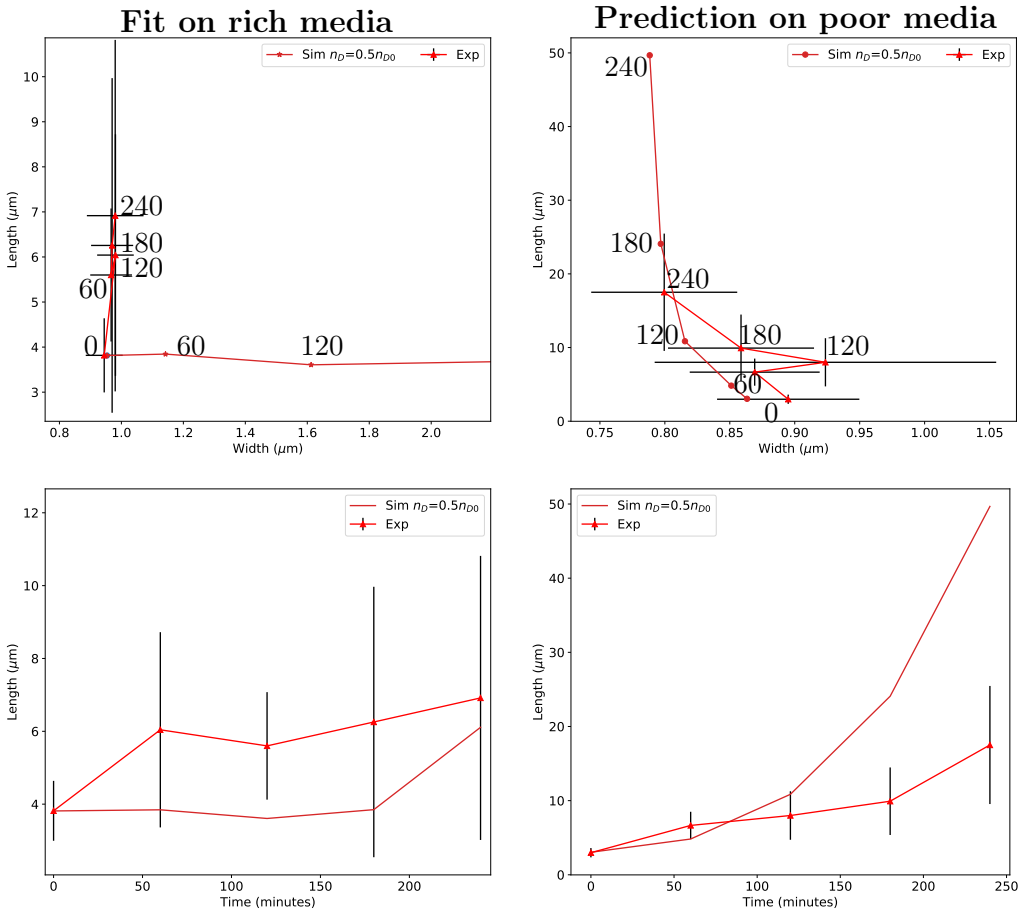

Figure 8.7: Length and width dynamics. A comparison between experimental and simulated results (using the parameters in Tables 6.4 and 7.1), under high aztreonam-like inhibition. Top: Morphology tracks where each marker corresponds to a single timepoint: 0, 60, 120, 180 and 240 minutes, going roughly from bottom to top. Bottom: The dynamics of the average length with time at high aztreonam.

bacteria than observed experimentally, under aztreonam challenge, because pole formation was slowed down due to the reduced number of divisomes. Under conditions where pole formation can still be attempted (as the fatness threshold has not been reached), the model then spends more time in pole formation, due to the reduced rate of peptidoglycan incorporation, in order to make sufficient surface area to cover the new poles. During this time volume growth continues uninhibited, while surface area growth is hampered. Therefore an imbalance occurs between surface area and volume growth during pole formation. This can lead the model to incorrectly predict sphere formation at high aztreonam for fast-growing bacteria (Figure 8.9).

Sphere formation is not observed experimentally at high aztreonam for fast-growing *E. coli*; instead we observe no change in width, and a doubling of the

Growth condition	ρ	S	K_M	$R = I$	n_E	n_D	M_0	Δ (μm^3)
pH 7.4 37°C rich	0.1	1.6	0.3	0.009	120	160	1.5	0.76
pH 7.4 37°C inter.	0.1	1.6	0.3	0.009	41	81	1.66	0.47
pH 7.4 37°C poor	0.1	1.6	0.3	0.009	20	60	1.7	0.4

Table 8.2: New simulation parameter values for the case where elongation is included during pole formation: for the rich, intermediate and poor growth conditions at pH 7.4 37°C. The intermediate parameter values are interpolated from the rich and poor values.

average cell length. In the model, one can correct the aberrant sphere formation by allowing some elongation to continue during pole formation. This restores the balance between surface area and volume growth. There is some evidence that elongation does continue (at a reduced rate) during pole formation in the literature [21, 25]. To examine this possibility a trial model was implemented where elongation continues during pole formation, but at a 40% slower rate (chosen arbitrarily).

A test run including elongation during pole formation, and using the parameters in Table 6.4 resulted in a very poor fit to the antibiotic-free experimental morphology for both fast and slow growing bacteria (Figure D.8, Appendix). Therefore to correct this, a parameter phase space search was performed, as

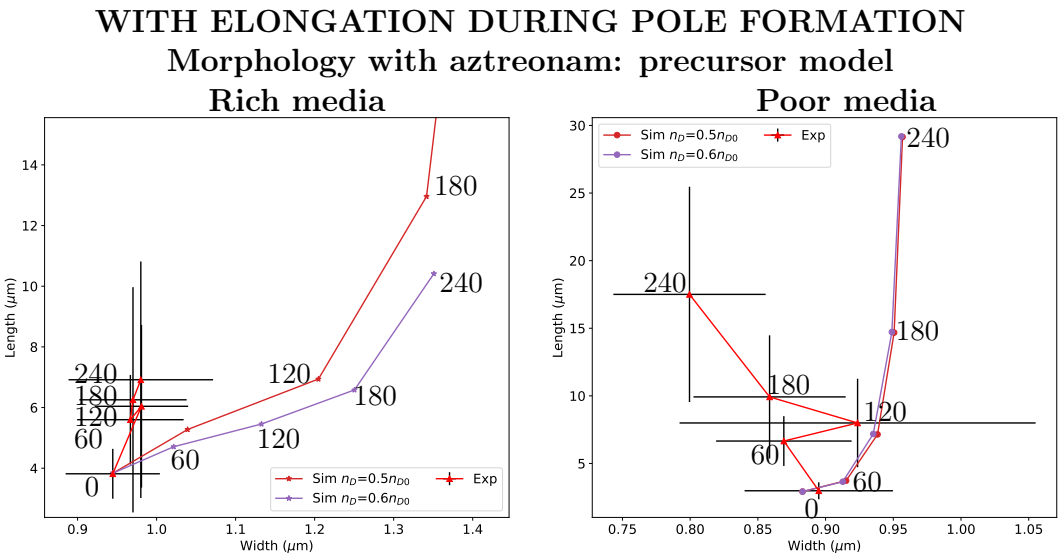

Figure 8.8: Length and width dynamics with elongation during pole formation. A comparison between experimental and simulated values in rich (left) and poor (right) growth conditions under aztreonam-like inhibition. The previous best fit inhibition level $n_D = 0.5n_{D0}$ is displayed alongside the new best fit inhibition level of $n_D = 0.6n_{D0}$. Each marker corresponds to a single timepoint: 0, 60, 120, 180 (and 240 for minimal media) minutes going roughly from bottom to top.

previously described (Ch. 6) using the antibiotic-free data only, to determine new best fit parameter values. The resulting parameter values for this model implementation can be found in Table 8.2, and the resulting morphology tracks are shown in Figure 8.8. The main difference between this parameter set, and the one found with no elongation during pole formation (Table 6.4) is that the synthesis rate has increased, while the incorporation rate and number of divisomes have decreased.

Figure 8.8 (left) shows that including elongation during pole formation, and re-parameterising, leads to a great improvement in the morphology fit for cells in rich media. The cells no longer become exceedingly fat but instead undergo a doubling of the cell length, as we see in the experiments.

On poor media (Figure 8.8, right), including elongation during pole formation results in a slight increase in the width of the filamenting cells, while the length dynamics now become more consistent with the experimental observations. Filamentation is now observed at all inhibition levels for slow-growing bacteria (Figure 8.20 contains a plot at a wide range of inhibition levels).

Without elongation during pole formation $n_D = 0.5n_{D0}$ was chosen as the best fit inhibition level for high aztreonam. Figure 8.8 shows that, with elongation during pole formation $n_D = 0.6n_{D0}$, could be a better choice.

As previously described, we can also visualise the morphology data with ellipse plots. These help to highlight the impact of including elongation during pole formation on the predicted morphologies in the presence of high aztreonam for slow and fast growing bacteria (Figure 8.9). For slow growing cells it can be seen that the filaments develop more gradually with elongation during pole formation. For fast growing cells, filamentation is observed with the inclusion of elongation during pole formation, whereas spheres are incorrectly predicted if elongation during pole formation is omitted.

Precursor division model

Slow growing bacteria in high aztreonam: no elongation during PF

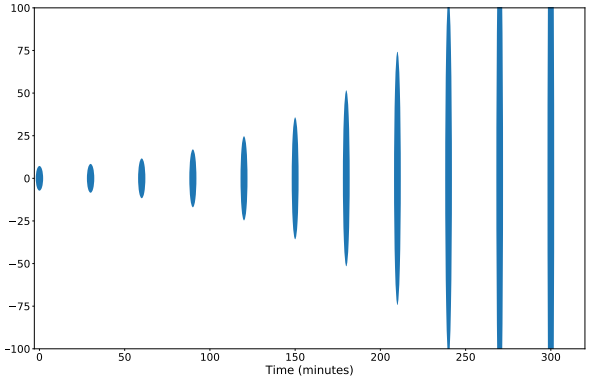

Slow growing bacteria in high aztreonam with elongation during PF

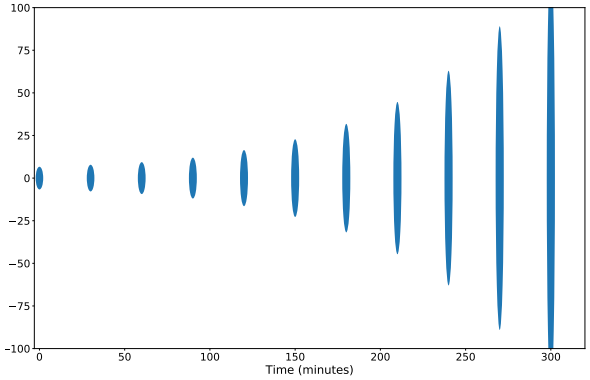

Fast growing bacteria in high aztreonam: no elongation during PF

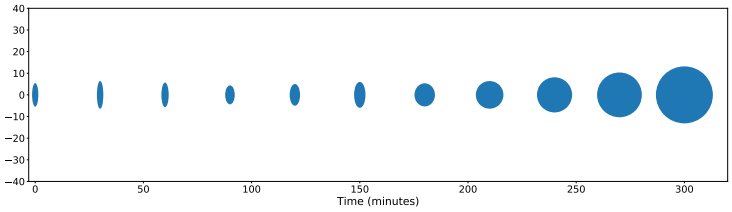

Fast growing bacteria in high aztreonam with elongation during PF

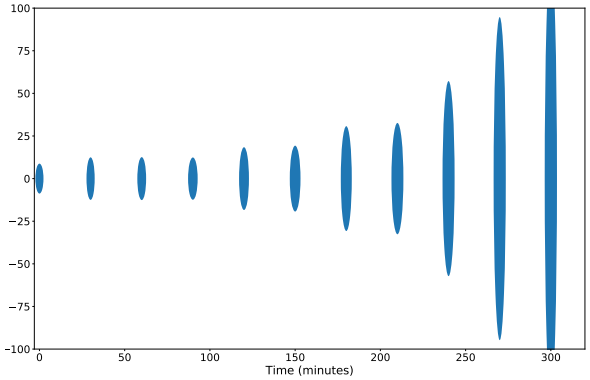

Figure 8.9: Ellipse trajectories generated from the model, based on the average length and width every thirty simulation minutes for $n_D = 0.5n_{D0}$. Parameters as in Tables 7.1, 6.4 and 8.2. Here we compare the impact of having elongation during pole formation (PF) or not. The ellipse dimensions have arbitrary units.

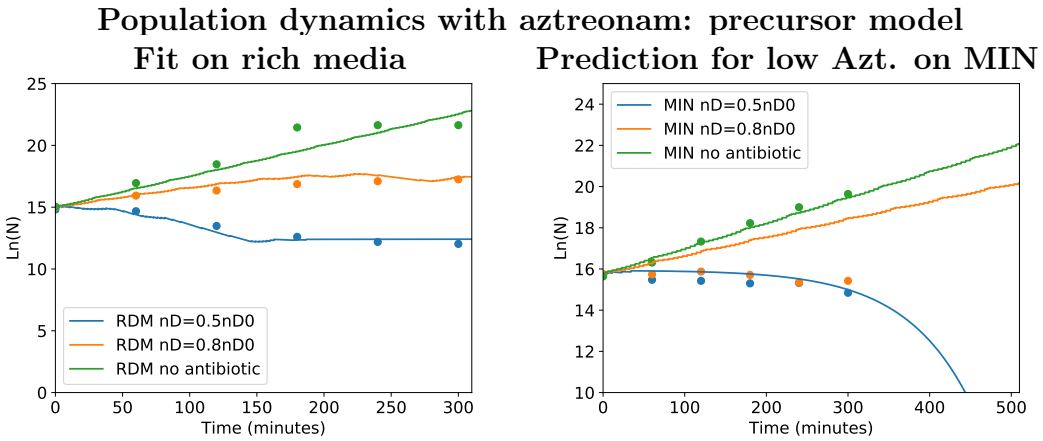

Figure 8.10: Population dynamics in the presence of aztreonam. Solid lines: The log cell number dynamics from the model, with no elongation during pole formation, at high ($n_D = 0.5n_{D0}$) and low ($n_D = 0.8n_{D0}$) aztreonam-like inhibition for both fast growing (left) and slow growing (right) cells. Filled circles: The experimental data for colony forming units in the presence of high (0.5μg/ml Azt.) and low (0.0313μg/ml Azt.) for both fast and slow growing cells. Model parameters as in Tables 7.1 and 6.4.

8.2.2 Population dynamics in the presence of aztreonam

8.2.2.1 Without elongation during pole formation

Figure 8.10 shows the model results for the population dynamics, in the absence of elongation during pole formation. For fast-growing bacteria the model fits well for both high and low aztreonam. However, for slow-growing bacteria, the model fit is good at high aztreonam but the model predicts growth at low aztreonam whereas in fact the population should decrease.

8.2.2.2 With elongation during pole formation

As better morphology dynamics were found when elongation was included during pole formation, the population dynamics predictions were also tested for this implementation of the model. However as the best fit morphology for fast growing bacteria is now at the inhibition level of $n_D = 0.6n_{D0}$, we have to fit new values for the lysis rate constants and the inhibition level for low aztreonam. As before, the lysis rate constant ϕ_D was fit using the CFU data for fast-growing cells in high aztreonam ($\phi_D = 2.3 \times 10^{-6}$ disaccharides) and ψ_D was fit using the CFU data for slow-growing cells in low aztreonam ($\psi_D = 0.011\text{h}^{-1}$) (see Appendix Figure D.9). The new inhibition level for low aztreonam was found to be $n_D = 0.75n_{D0}$ (see Appendix Figure D.9). The model prediction for low aztreonam for slow-growing bacteria is compared with the experimental CFU data in Figure 8.11 (right), while the fit on rich media is shown in Fig. 8.11 (left). The model is now successful in

AZTREONAM	Parameters	Experiments used in fitting
High inhibition	$n_D = 0.6n_{D0}$	RDM high Azt. morphology
Low inhibition	$n_D = 0.75n_{D0}$	RDM low Azt. CFUs
Lysis rates	$\phi_D = 2.3 \times 10^{-6}$ disaccharides, $\psi_D = 0.011\text{h}^{-1}$	RDM and MIN high Azt. CFUs

Table 8.3: New simulation parameter values for the case where elongation is included during pole formation. The experimental data used in the fitting process is also detailed.

capturing the decreasing population of slow-growing bacteria with low aztreonam (compare to Figure 8.10, right (orange line), in the absence of elongation during pole formation.

To summarise, aztreonam shows growth-medium dependent inhibition in the following way. At high aztreonam, fast-growing bacteria are more inhibited than slow-growing bacteria. In contrast, at low aztreonam, fast-growing bacteria are less inhibited than slow-growing bacteria. Our model captures this behaviour, and suggests that this growth-medium dependent inhibition stems from the different numbers of divisomes that are required to grow at different growth rates in the absence of the antibiotic. Specifically, in our model, more divisomes are needed for antibiotic-free growth on rich media to ensure that surface area growth continues to match volume growth, and therefore maintain a rod-shaped bacterium. In the

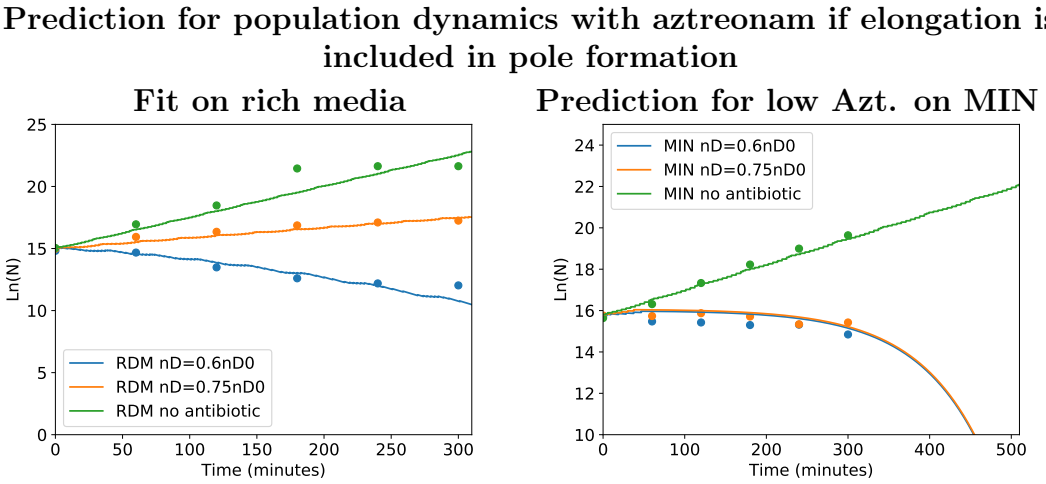

Figure 8.11: Population dynamics in the presence of aztreonam. Solid lines: The log cell number dynamics from the model, with elongation during pole formation, at high ($n_D = 0.6n_{D0}$) and low ($n_D = 0.75n_{D0}$) aztreonam-like inhibition for both fast growing (left) and slow growing (right) cells. Filled circles: The experimental data for colony forming units in the presence of high (0.5μg/ml Azt.) and low (0.0313μg/ml Azt.) for both fast and slow growing cells. Model parameters as in Tables 8.2 and 8.3

presence of aztreonam, the interplay between the number of active divisomes, filamentation and lysis leads to three possible population dynamics outcomes. In the first scenario few divisomes are inhibited, and cells can continue to divide at a rate higher than the lysis rate (e.g. rich media, low aztreonam). In the second scenario, a significant proportion of divisomes are inhibited but pole formation is still attempted. Here, cells continue to divide but at a rate lower than the lysis rate leading to a net loss of CFUs (e.g. rich media, high aztreonam). In the third scenario, enough divisomes are inhibited that pole formation can no longer be attempted (due to the fatness threshold) resulting in non-dividing filamentous cells which have a low lysis rate at early times (e.g. poor media, high and low aztreonam). This leads to the observed growth-medium dependence because cells growing on the poor medium have fewer divisomes in the absence of antibiotic and therefore reach the third, filamenting, scenario even at low aztreonam, whereas the fast growing cells still have sufficient, uninhibited divisomes to continue dividing (scenario 1).

8.2.3 Further predictions for population dynamics with aztreonam

8.2.3.1 MOPSgluCAA

We also have experimental data for bacteria exposed to aztreonam in an intermediate medium (MOPSgluCAA). The model predictions for aztreonam-like inhibition can therefore be tested for these intermediate growth dynamics. As in section 8.1.3, we use interpolation to estimate the parameter values for the MOPSgluCAA growth medium, both with and without elongation during pole formation (Table 8.4).

Figure 8.12 shows that the mathematical model performs similarly with and

No elongation	n_E	n_D	M_0	Δ (μm^3)	V_0	A_{c0}	A_{p0}
pH 7.4 37°C rich	120	180	1.5	0.95	1.474	4.351	2.799
pH 7.4 37°C inter.	41	97	1.7	0.67	1.067	3.029	2.556
pH 7.4 37°C poor	20	75	1.8	0.73	0.969	2.698	2.4885
With elongation	n_E	n_D	M_0	Δ (μm^3)	V_0	A_{c0}	A_{p0}
pH 7.4 37°C rich	120	160	1.5	0.76	1.474	4.351	2.799
pH 7.4 37°C inter.	41	81	1.66	0.47	1.067	3.029	2.556
pH 7.4 37°C poor	20	60	1.7	0.4	0.969	2.698	2.4885

Table 8.4: Growth-medium dependent simulation parameters for the rich, intermediate and poor growth conditions at pH 7.4 37°C. The intermediate parameter values are interpolated from the rich and poor values.

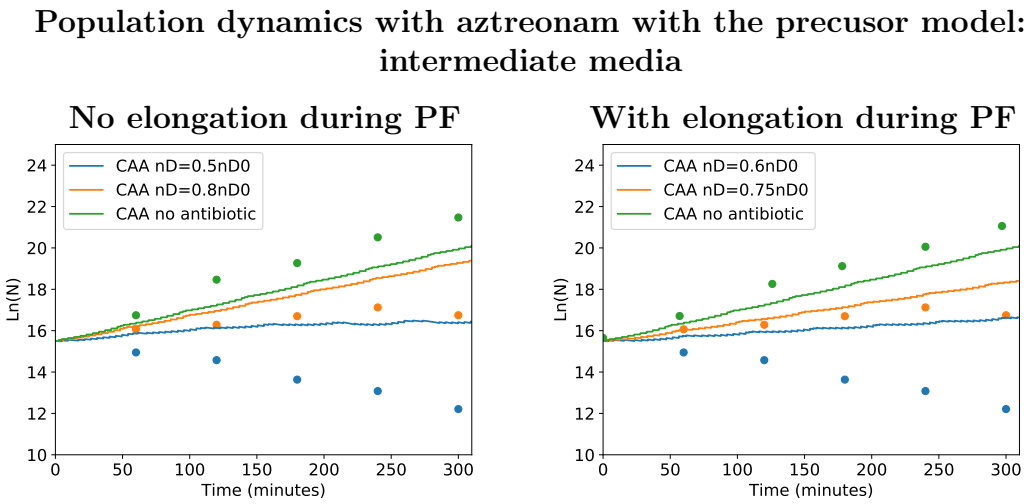

Figure 8.12: Solid lines: The log cell number dynamics from the model at high and low aztreonam-like inhibition for the intermediate growth medium. Parameters with no elongation during pole formation as in Tables 6.4, 7.1 and 8.4. Parameters with elongation during pole formation as in Tables 8.2, 8.3 and 8.4. Filled circles: The experimental data for colony forming units in the presence of high (0.5μg/ml Azt.) and low (0.0313μg/ml Azt.) for cells growing in MOPSgluCAA.

without elongation during pole formation for aztreonam in MOPSgluCAA. The model successfully predicts positive population growth observed with low aztreonam, performing better with elongation during pole formation, but

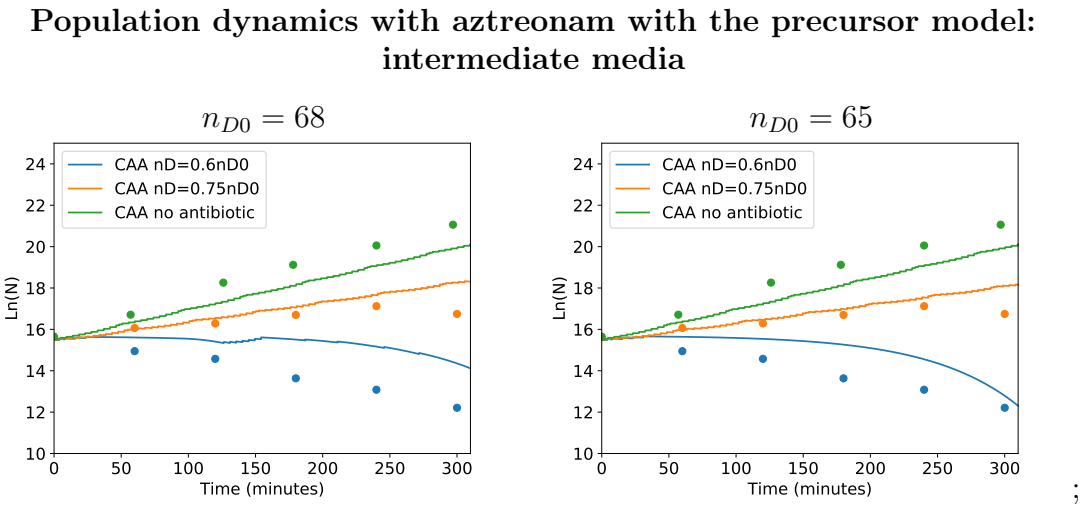

;

Figure 8.13: Solid lines: The log cell number dynamics in the model at high ($n_D = 0.6n_{D0}$) and low ($n_D = 0.75n_{D0}$) aztreonam-like inhibition for intermediate growth-rate cells with different n_{D0} values. Other parameters as in Tables 8.2 and 8.3. Filled circles: The experimental data for colony forming units in the presence of high (0.5μg/ml Azt.) and low (0.0313μg/ml Azt.) for cells growing in MOPSgluCAA.

gives an incorrect prediction for the high aztreonam dynamics; specifically the model predicts slight positive population growth whereas population decline was observed experimentally. This may be due to the linear interpolation of the parameter values. For example, if the number of divisomes (with elongation) is reduced from 81 to 68 or 65 a better prediction results for the MOPSgluCAA data (Figure 8.13).

8.2.3.2 Growth-medium dependent inhibition

We can now assess overall whether the model gives the correct predictions for growth-medium dependent inhibition by aztreonam. Figure 8.14 compares the model results (with elongation during pole formation, and $n_{D0} = 65$ at intermediate growth rate) for aztreonam on three media, with the experimental results. The growth-medium dependent inhibition predictions are very good. The model captures the low aztreonam behaviour well (Figure 8.14, right), in particular the similar dynamics observed for MOPSgluRDM and MOPSgluCAA. The high aztreonam predictions (Figure 8.14, left) are also good, apart from the result for MOPSgluCAA that was discussed above. Strikingly, the model successfully captures the reversal of the growth-medium dependence for low

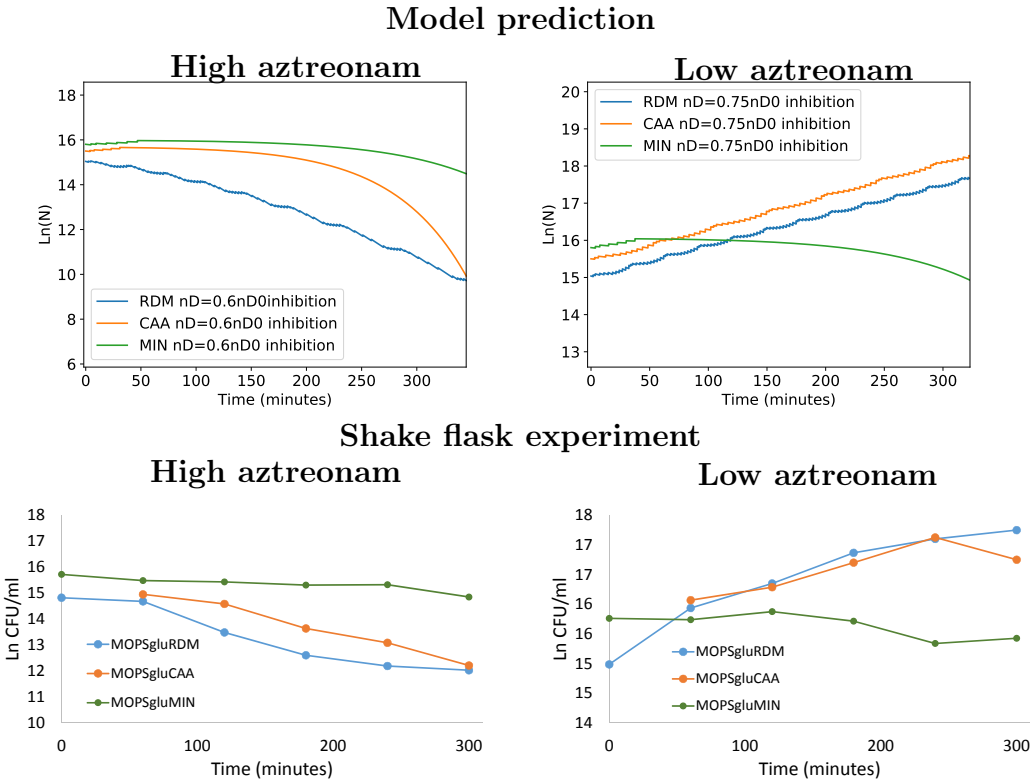

Figure 8.14: Comparison between cell number dynamics in three different growth conditions: rich, intermediate and poor, in a high (0.5μg/ml) aztreonam-like inhibition (left) and a low (0.0313μg/ml) aztreonam like-inhibition (right).

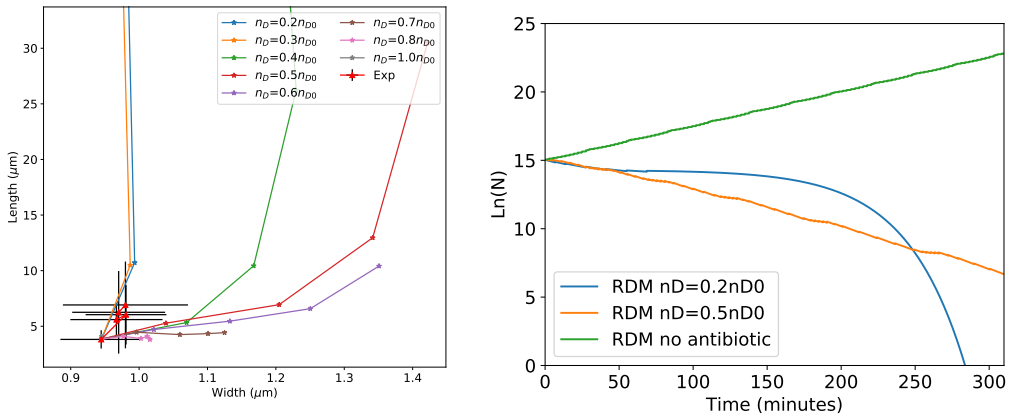

Figure 8.15: Left: The predicted morphology tracks from the model for fast-growing bacteria at a range of aztreonam-like inhibition levels. Filaments are predicted at inhibition levels greater than $n_D = 0.6n_{D0}$. Right: The predicted population dynamics from the model for fast growing cells at inhibition levels of $n_D = 0.2n_{D0}$ and $n_D = 0.5n_{D0}$, both of which are predicted to give filaments.

aztreonam - i.e. for low aztreonam, in contrast to other conditions, inhibition is strongest for slow-growing cells.

8.2.3.3 Long filaments on rich media

In our microscopy experiments with high aztreonam, long filaments were observed in the poor media (lengths of around 20μm) while in rich media filaments were not observed, although the cell length was observed to approximately double (lengths of around 8μm) (Chapter 5). The model makes an interesting prediction that longer filaments are expected to emerge on rich media, at higher concentrations of aztreonam. For example, Figure 8.15 (left) shows that filaments are predicted on rich media for inhibition levels greater than $n_D = 0.6n_{D0}$.

The model further predicts that the filaments that form at $n_D = 0.5n_{D0}$ become fatter as well as longer, while those at a higher inhibition level $n_D = 0.2n_{D0}$, simply become longer (Figure 8.15, left). We hypothesised that these different filament dynamics would also result in different predictions for the population dynamics, and so examined this with the model (Figure 8.15, right). Indeed, for high inhibition, $n_D = 0.2n_{D0}$, on rich media, the model predicts population dynamics similar to that previously observed on poor media (Figures 8.11, right and 8.15, right), i.e. there is no cell division. A somewhat lower level of inhibition ($n_D = 0.5n_{D0}$) appears to produce cells which can still divide while also becoming filamentous. This means that the population alternates between the two lysis regimes, that due to out-of-control divisomes and that due to the unstable increase in length (Figure 8.15, right, visible in the alternating gradients). This leads to the interesting prediction that the intermediate inhibition level of $n_D = 0.5n_{D0}$ gives a higher lysis rate compared to the higher inhibition level of $n_D = 0.2n_{D0}$

(Figure 8.15, right), at early times.

If these predictions are true, they could have clinical implications for the use of aztreonam against infections. Firstly, filamentous *E. coli* can subvert the innate immune response [65], so it could be hypothesised that using a very high aztreonam concentration that results in long filaments might make it more difficult to clear an infection. Secondly, the model predicts that there is a range of intermediate aztreonam concentrations where the lysis rate is greater than that predicted at very high aztreonam concentrations. As an antibiotic may not be at the site of interest for more than a couple of hours [94], the model predicts that it could be quicker to clear an infection using an intermediate aztreonam concentration than using a high concentration.

8.3 The adder division model

As previously discussed (see Chapter 6), we have also implemented the adder division model in our simulations. We were interested to see if the adder model would give significantly different predictions to the precursor model. It turns out that the adder and the precursor division models generally give very similar predictions, with only subtle differences that would be very difficult to differentiate between experimentally.

We will now discuss some of these subtle differences between the division models. The complete set of results for the adder division model can be found in the Appendix.

8.3.1 Mecillinam

The adder division model predicts slightly different morphology dynamics at high mecillinam for fast growing bacteria, compared to the precursor threshold division model (Figure 8.16, bottom). For the adder division model, the transition to a spherical morphology happens slightly earlier than it does in the precursor division model. This can be explained by looking at the length and width dynamics in more detail (Figure 8.17). Figure 8.17 highlights that when mecillinam inhibition is applied (midway through the cell cycle in this example) the division models give different predictions.

Specifically, the precursor threshold division model predicts that cells become elongating lemons after the third division event, before a spherical morphology is reached, when high mecillinam is applied (Figure 8.17). In contrast, the adder model predicts a transition directly to a spherical morphology after four division events. This happens because the fatness threshold has not yet been reached when the precursor model first transitions to the lemon morphology. This could potentially be due to cells reaching the criteria for pole formation earlier in the

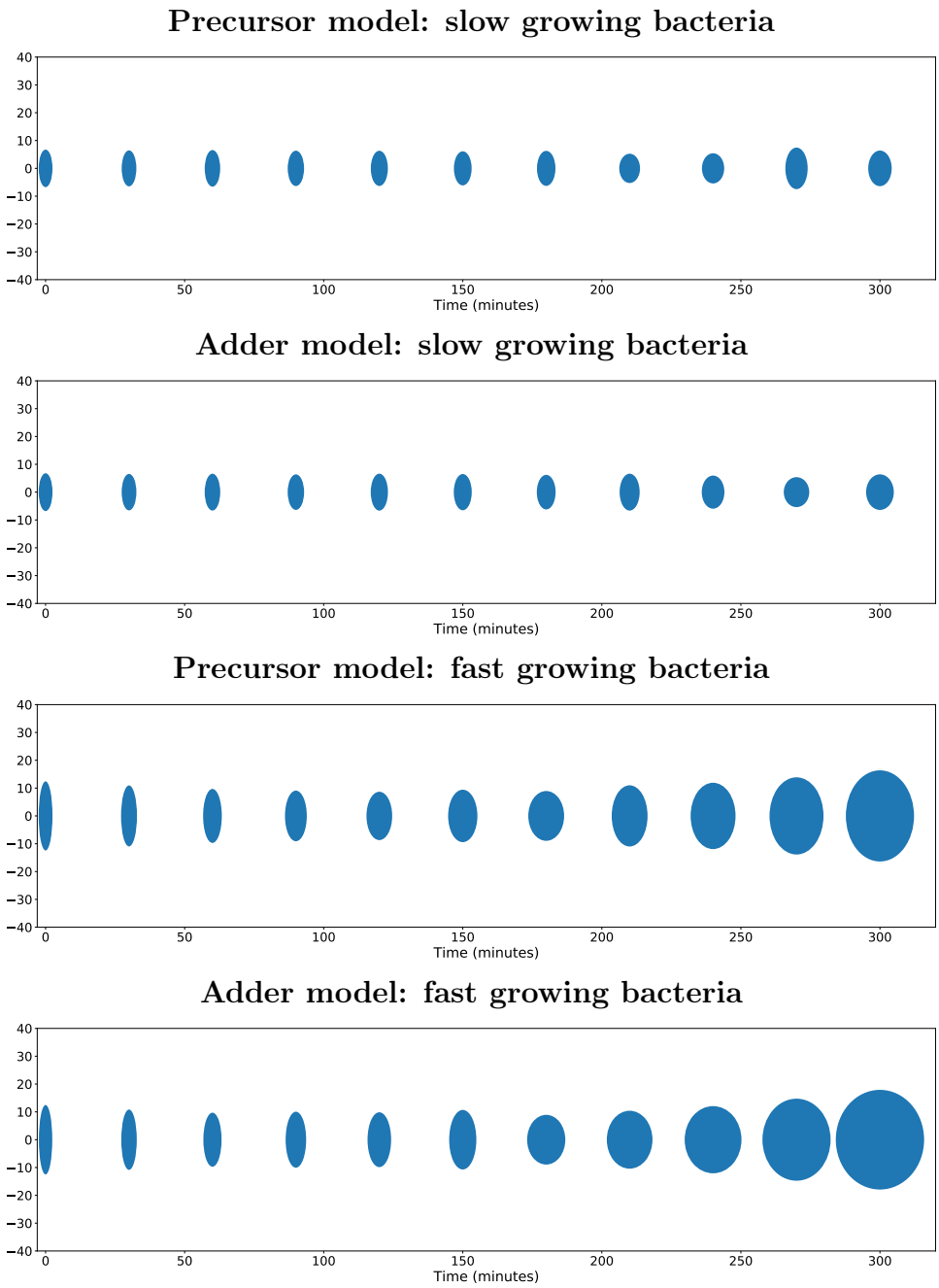

Figure 8.16: Ellipse trajectories generated by the model, based on the average length and width every thirty simulation minutes for $R = 0.5R_0$. Parameters as in Tables 7.1 and 6.4. The adder model predicts more spherical morphologies while the precursor model predicts lemon morphologies.

precursor threshold model (before getting too fat), perhaps due to a build-up of precursors. These different predictions are consistent regardless of when in the cell cycle the mecillinam inhibition is applied. The length and width dynamics when mecillinam inhibition is applied at either the beginning or the end of the cell cycle can be found in the Appendix Figure D.10.

The adder model also gives slightly different morphology tracks under mecillinam-like inhibition for slow-growing bacteria (Figure 8.18). The main difference between the precursor and adder division models is that the adder model tends to predict an increase in length after 180 minutes, at low and high inhibition levels, whereas the precursor model predicts a continuous decrease in length. These predictions could be tested experimentally by performing microscopy with *E. coli*

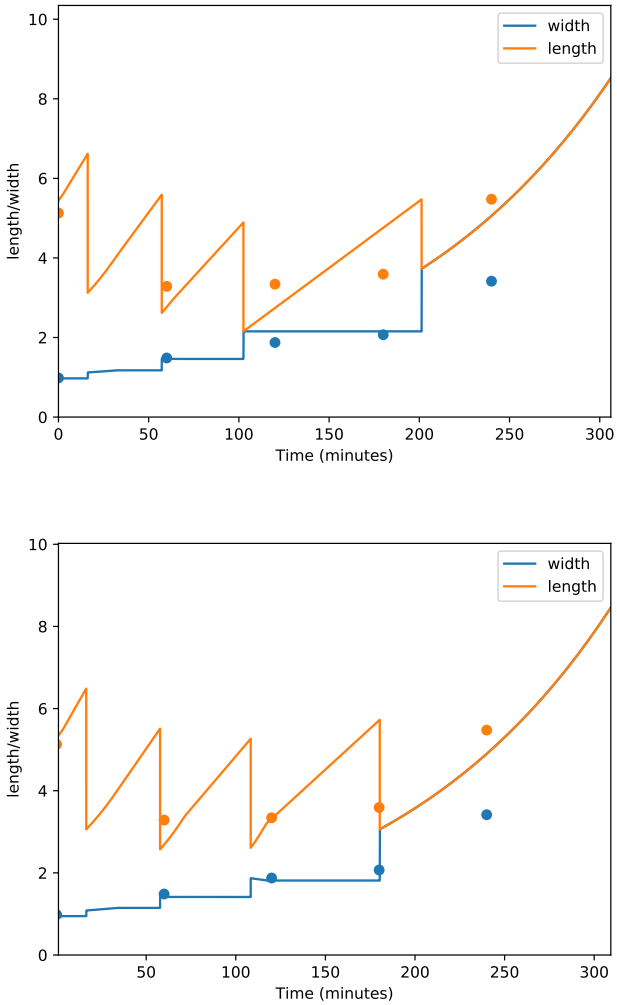

Figure 8.17: The length and width dynamics generated by the precursor and adder models for fast growing bacteria, when high mecillinam inhibition is applied halfway through the cell cycle. Parameters as in Tables 7.1 and 6.4. The bacteria become spherical when the length and width become equal i.e. when $\frac{length}{width} = 1$. Markers represent the experimental data at high mecillinam in MOPSgluRDM.

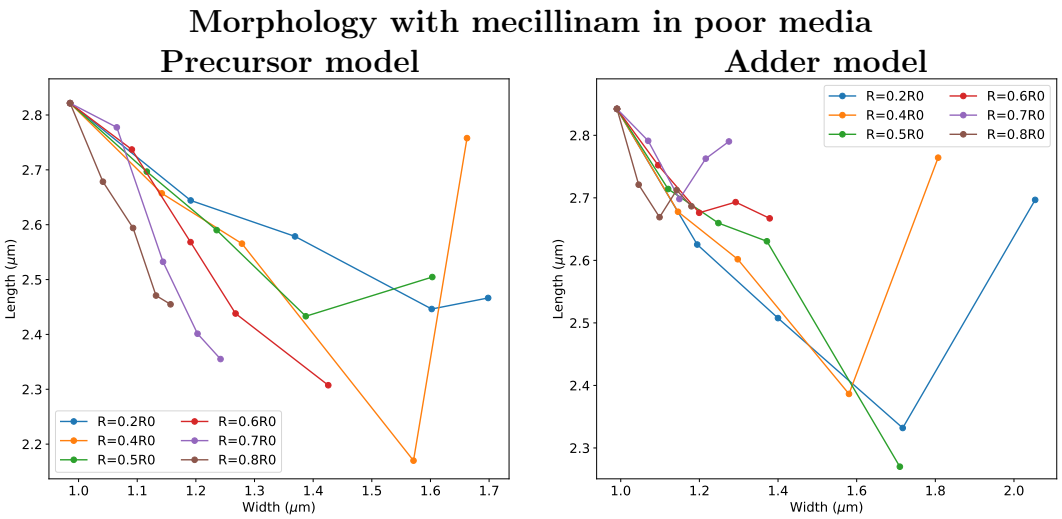

Figure 8.18: Length and width dynamics. A comparison between simulated results using the precursor and adder division models in poor growth conditions under mecillinam-like inhibition. The values in the legend indicate the inhibition level. Each marker corresponds to a single timepoint: 0, 60, 120, 180, and 240 minutes from the addition of mecillinam, going roughly from left to right. Parameters as in Tables 7.1 and 6.4. The adder model predicts an increase in length after 180 minutes

growing in poor media at a wider range of mecillinam concentrations.

We observe very little difference between the adder and precursor division models in terms of their population dynamics predictions. The only difference of note occurs on rich media for $R = 0.5R_0$ i.e. high mecillinam. In this case, as discussed, division stops at about 200 minutes in the precursor division model, but not until about 250 minutes in the adder model (see Appendix Figure D.4). However this does not make a significant difference to the log of the cell number.

8.3.2 Aztreonam

For aztreonam, the only significant difference between the predictions of the adder and precursor division models occurs at inhibition levels $n_D = 0.4n_{D0}$ and below (i.e. at higher aztreonam concentrations than used experimentally) for cells growing in rich media (Figure 8.19, right). Figure 8.19 shows that for the adder division model, cells become less fat at these inhibition levels with filaments observed at $n_D = 0.4n_{D0}$, whereas the precursor model predicts much fatter cells and no filaments at $n_D = 0.4n_{D0}$. This difference between the division models can be explained as follows. If cells do not filament on rich media ($n_D > 0.3n_{D0}$), they spend more time in pole formation, gradually getting fatter. As the exact timing of pole formation and the length of time spent in pole formation can vary slightly between the adder and precursor division models, the models predict slightly different cell widths.

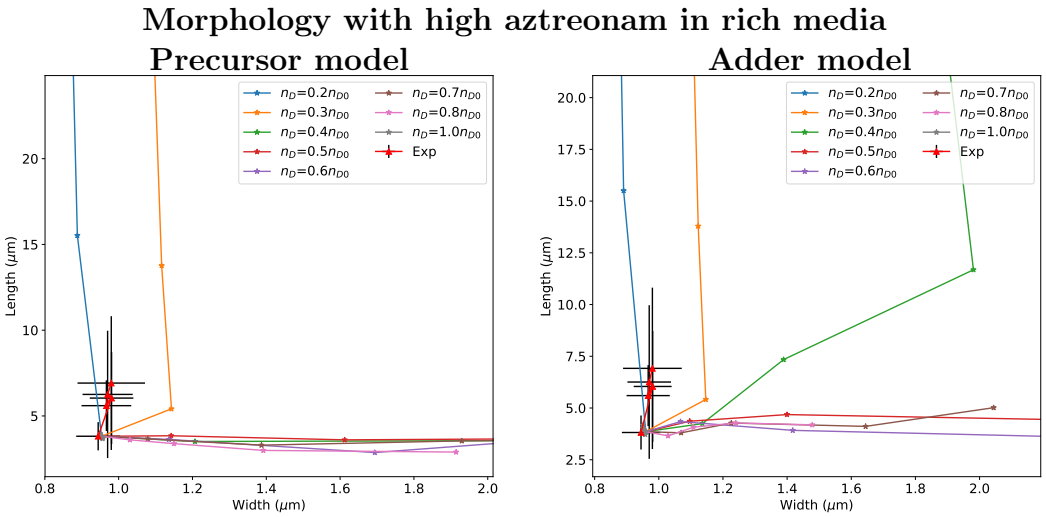

Figure 8.19: Length and width dynamics. A comparison between the simulated results using the precursor and adder division models, in rich growth conditions under high aztreonam-like inhibition. The values in the legend indicate the fraction of divisomes still active despite the inhibition. Each marker corresponds to a single timepoint: 0, 60, 120, 180 and 240 minutes, going roughly from bottom to top. Parameters as in Tables 6.4 and 7.1.

When elongation is included during pole formation we again see increased filamentation with the adder model in rich media (Figure 8.20, top) compared to the precursor model. No difference is observed between the adder and precursor division models on the poor media (Figure 8.20, bottom).

Despite the increased filamentation predicted by the adder model, there is no significant difference in the population dynamics of bacteria in the presence of aztreonam using either the adder or precursor division model for the concentrations of aztreonam used in our experiments (see Figure D.7). To conclude, from these predictions it not possible to differentiate between the adder and precursor division models when exposing the bacteria to aztreonam.

8.4 Summary

In summary, the model makes qualitatively, and largely quantitatively, correct predictions for the morphology at high mecillinam in MOPSgluMIN, and for the CFU dynamics in MOPSgluMIN and MOPSgluCAA, at both low and high mecillinam. The model is able to capture the non-trivial growth-medium dependence of inhibition that we observe experimentally, although long term dynamics are not always captured correctly. For aztreonam, the model is able to correctly predict long filaments on MOPSgluMIN, and short (fatter) filaments on MOPSgluRDM, at high aztreonam concentration, however it predicted positive population growth on MOPSgluMIN with low aztreonam, whereas we observe

slight negative growth experimentally. We found that improved morphology predictions could be achieved if elongation was allowed to continue at a reduced rate during the pole formation phase of the cell cycle. This then led to correct predictions for the CFU dynamics at low and high aztreonam in all three growth media i.e. low aztreonam is most inhibitive on the poor medium and high aztreonam is most inhibitive on the rich medium.

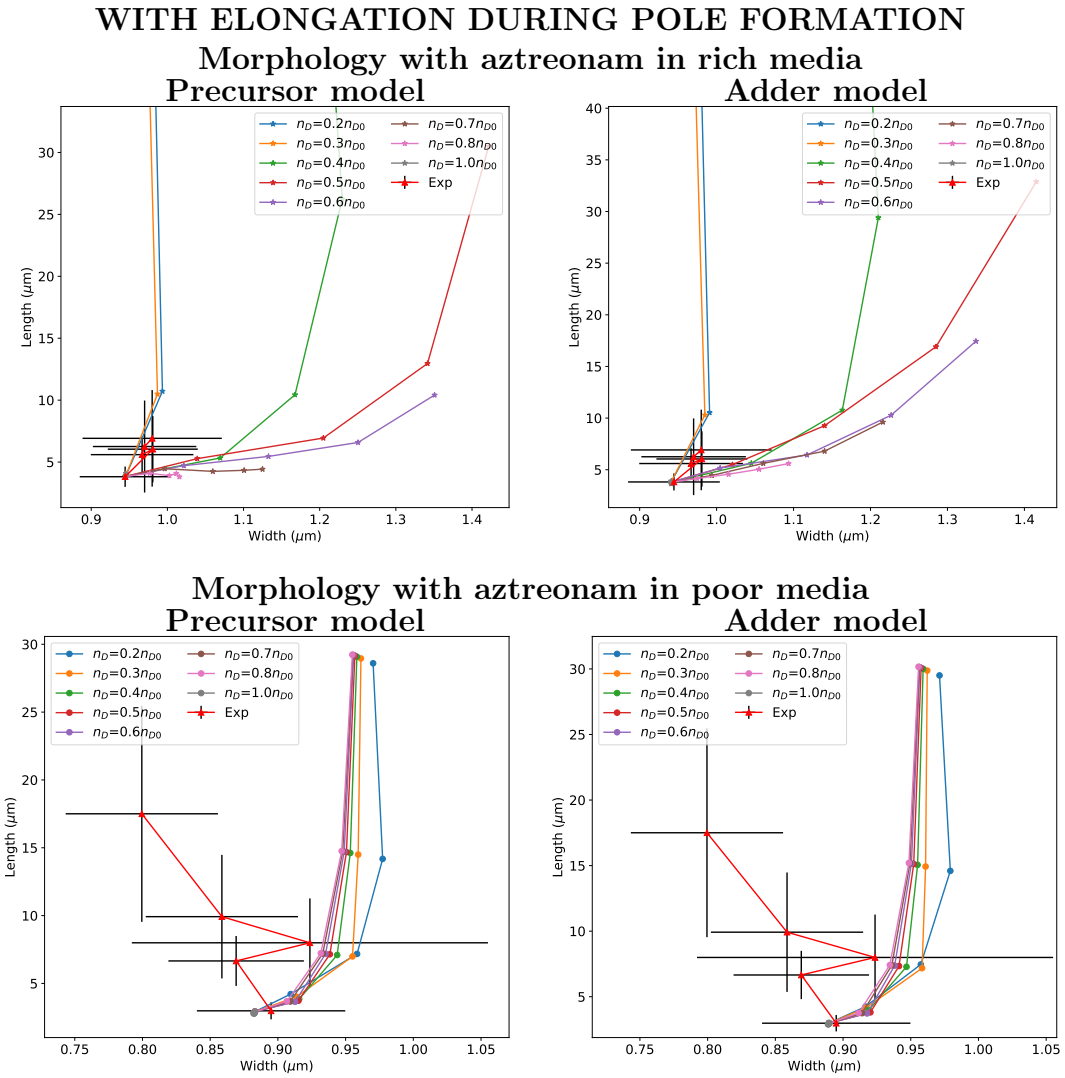

Figure 8.20: Length and width dynamics with elongation during pole formation. A comparison between simulated results in rich (top) and poor (bottom) growth conditions under aztreonam-like inhibition, and with the precursor (left) or adder (right) division models. The values in the legend indicate the fraction of divisomes still active despite the inhibition. Each marker corresponds to a single timepoint: 0, 60, 120, 180 and 240 minutes going roughly from bottom to top. Parameters as in Tables 8.2 and 8.3

Chapter 9

Expanding the project to more antibiotics

This thesis has so far discussed the population and morphology dynamics of *E. coli* in the presence of mecillinam and aztreonam in detail (Chapters 4 and 5), as well as giving an overview of the population dynamics of *E. coli* in the presence of cefotaxime and fosfomycin (Chapter 3). In this chapter we will compare experimental population dynamics results for two more antimicrobials, along with those for the four antibiotics already discussed. Additionally, we will present some microscopy results for cefotaxime and fosfomycin, along with some preliminary model results for fosfomycin-like inhibition.

9.1 Population dynamics with other cell wall-targeting antimicrobials

Plate reader experiments in poor media (MOPSgluMIN) and rich media (MOPSgluRDM) were used to observe the population dynamics of *E. coli* RJA002 in the presence of two more antimicrobial compounds: the antibiotic ampicillin and the antimicrobial compound A22. These results will be compared directly with the results observed in the presence of mecillinam, aztreonam, fosfomycin and cefotaxime.

Ampicillin primarily targets the endopeptidases PBP4, PBP7 and PBP8 (as discussed in Chapter 1, endopeptidases cleave the covalent bonds in the PG network to open space for new material [98]), although at higher concentrations it can target all major PBPs [72, 75, 115]. Thus ampicillin can be considered to inhibit both elongation and division. In contrast, A22 has a very specific target: MreB. As discussed in Chapter 1, MreB is a bacterial actin-like cytoskeletal filament that associates with the elongasome to produce *E. coli*'s characteristic rod-shape [117]. During elongation MreB forms dynamic filaments that rotate

Antimicrobial	Target
mecillinam	PBP2 (elongasome) [33]
aztreonam	PBP3 (divisome) [107]
fosfomycin	MurA (precursor synthesis) [38]
cefotaxime	PBP3 (PBP1a/PBP1b at high concentrations) [72]
ampicillin	PBP4, PBP7, PBP8 [72]
A22	MreB (elongation) [141]

Table 9.1: Summary table of the antimicrobials used and their key targets.

around the long axis of the cell [131]. MreB can be considered to be a key component of the elongasome [112] and therefore A22 can be considered to target elongation. The primary targets for all six antimicrobials that will be discussed here are listed in Table 9.1.

Based on the targets of the antimicrobials we can make some hypotheses regarding their expected effect on *E. coli*'s population dynamics. As A22 solely inhibits elongation, it might be expected to have similar effects as mecillinam. As ampicillin can inhibit both elongation and division it may have similar effects as fosfomycin, which effectively inhibits both elongation and division by preventing the production of precursors. Lastly as cefotaxime primarily inhibits PBP3 it is expected to result in similar effects as aztreonam.

9.1.1 The six antimicrobials on rich media

Plate reader results for the six antimicrobials acting on *E. coli* RJA002 growing in MOPSgluRDM can be found in Figure 9.1, in this figure all media are at pH 7.4 and 37°C apart from the mecillinam case where the more stable environmental conditions of pH 6.5 and 34°C were used. As hypothesised, cefotaxime (Fig. 9.1a) and aztreonam (Fig. 9.1b) display very similar looking growth curves, with a small increase in optical density followed by a plateau at all antibiotic concentrations. Furthermore mecillinam (Fig. 9.1c) and A22 (Fig. 9.1d) also give similar results, with a significant bump in optical density at most concentrations. From these plate reader observations we hypothesise that antimicrobials that primarily inhibit division (cefotaxime and aztreonam) result in a plateau phenotype for cells in MOPSgluRDM, while antimicrobials that primarily inhibit elongation (mecillinam and A22) result in a bump phenotype.

As mentioned, fosfomycin and ampicillin effectively inhibit both elongation and division, although in different ways. However, their effects on the plate reader-observed growth curves are very different. Ampicillin (Fig. 9.1f) results in a plateau phenotype (perhaps suggesting from previous observations that it may be inhibiting division more than elongation). Fosfomycin (Fig. 9.1e) results in a mixed phenotype. For concentrations below 4μg/ml a bump phenotype is observed, with a curious double peak at the lowest concentrations. However

(a) Cefotaxime in MOPSgluRDM.

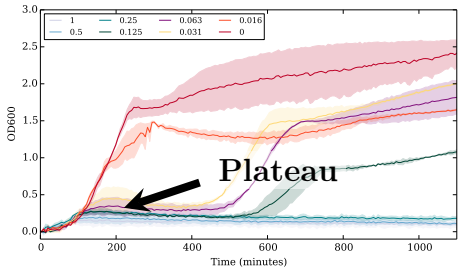

(b) Aztreonam in MOPSgluRDM.

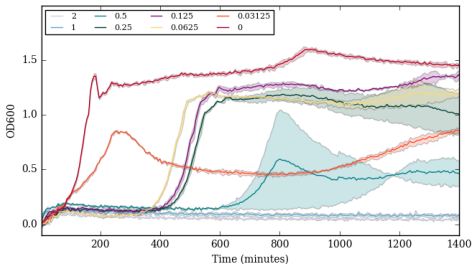

(c) Mecillinam in MOPSgluRDM.

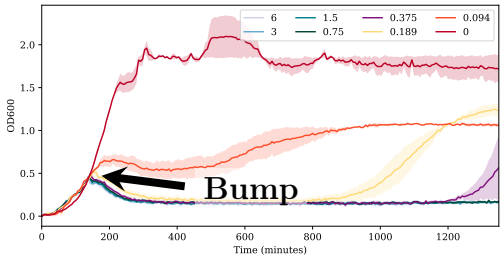

(d) A22 in MOPSgluRDM.

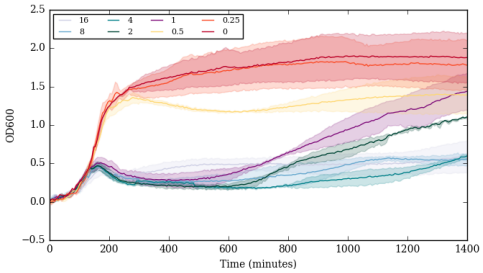

(e) Fosfomycin in MOPSgluRDM.

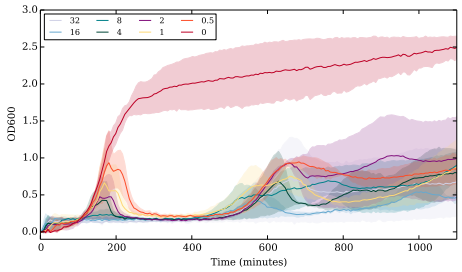

(f) Ampicillin in MOPSgluRDM.

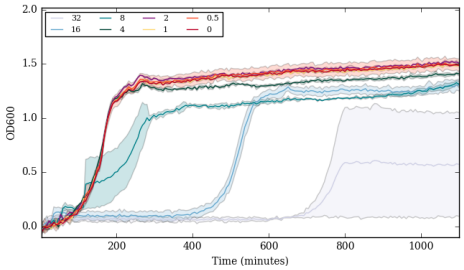

Figure 9.1: Plate reader optical density curves for *E. coli* growing in MOPSgluRDM at pH 7.4 and 37°C with six different antimicrobials, apart from the mecillinam data which was at pH 6.5 and 34°C.

at higher concentrations, above 8μg/ml, a plateau phenotype is observed. This might perhaps suggest that elongation is more inhibited at the lower concentrations (potentially resulting in spherical morphologies), and division is more inhibited at the higher fosfomycin concentrations (potentially resulting in filament morphologies).

9.1.2 The six antimicrobials on poor media

The plate reader results for the six antimicrobials in MOPSgluMIN are displayed in Figure 9.2. Unlike on MOPSgluRDM, cefotaxime (Fig. 9.2a) and aztreonam (Fig 9.2b), which both target division, display different growth curves on MOPSgluMIN. Cefotaxime results in a plateau phenotype at all concentrations. Conversely, aztreonam results in a bump followed by a plateau at all concentrations except the lowest (0.03125μg/ml), which simply plateaus.

(a) Cefotaxime in MOPSgluMIN.

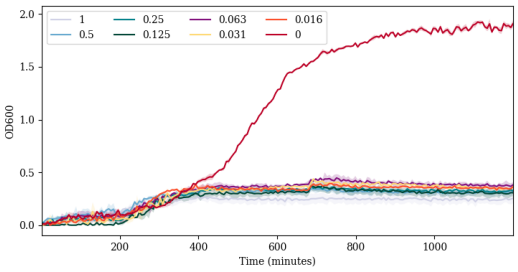

(b) Aztreonam in MOPSgluMIN.

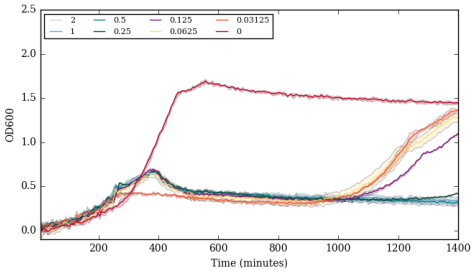

(c) Mecillinam in MOPSgluMIN.

(d) A22 in MOPSgluMIN.

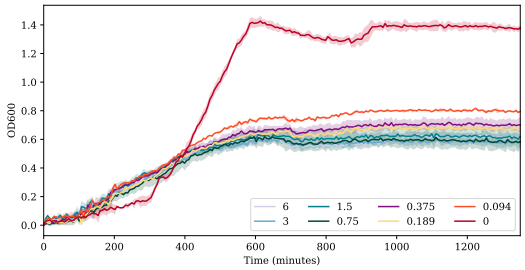

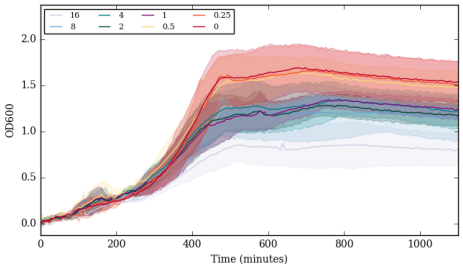

(e) Fosfomycin in MOPSgluMIN.

(f) Ampicillin in MOPSgluMIN.

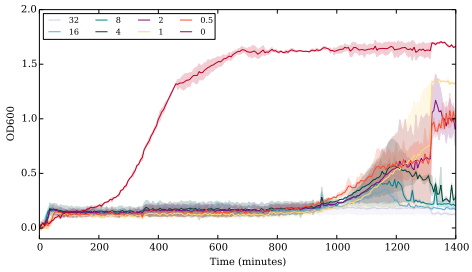

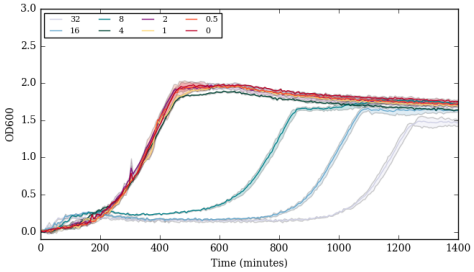

Figure 9.2: Plate reader optical density curves for *E. coli* growing in MOPSgluMIN at pH 7.4 and 37°C with six different antimicrobials, apart from the mecillinam data which was at pH 6.5 and 34°C.

For mecillinam (Fig. 9.2c) and A22 (Fig. 9.2d) the growth curves on poor media are similar, with both of the antimicrobials displaying weak growth inhibition on this medium. Furthermore our results for fosfomycin (Fig. 9.2e) and ampicillin (Fig. 9.2f) are similar in MOPSgluMIN, with both these antibiotics now resulting in a plateau phenotype.

9.1.3 Comparing population dynamics on rich and poor media

In Chapter 3 we discussed the growth medium dependence of the population dynamics of cefotaxime, fosfomycin and mecillinam as measured via optical density in a plate reader. There we concluded that cefotaxime and fosfomycin were more inhibitive on poor media, while mecillinam was apparently more

inhibitive on intermediate media (but still more inhibitive on rich media than poor media). As A22 apparently displays similar results to mecillinam in both rich and poor growth media this could suggest that antimicrobials that primarily target elongation are generally less inhibitive for slower growing bacteria.

For the antimicrobials targeting division, or both division and elongation, the growth medium dependence is less obvious. While fosfomycin is clearly more inhibitive on MOPSgluMIN, inhibition by ampicillin on MOPSgluMIN is not much different to that in MOPSgluRDM. Furthermore, while cefotaxime is more inhibitive on MOPSgluMIN, most aztreonam concentrations appear to be less inhibitive on MOPSgluMIN with only the lowest concentration becoming more inhibited on the poor media.

9.1.4 Conclusions regarding the six antimicrobials

Comparing the six antimicrobials across rich and poor media, for experiments using the plate reader, our results can be summarised as follows. For antimicrobials that primarily inhibit division a plateau phenotype is observed in the optical density measurements. Based on our results for aztreonam (Chapter 5), we hypothesise that this plateau phenotype may be related to the emergence of a filamentous morphology. As such, future microscopy experiments with cefotaxime, ampicillin and high concentrations of fosfomycin may reveal filamenting bacteria. This hypothesis agrees with literature observations that cefotaxime results in filamentation of bacteria [45, 69], as does ampicillin [47]. Furthermore, for *E. coli* in the presence of cefotaxime above the MIC, Kjeldsen et al. [69] observed elongated cells at 2 hours after inoculation and then no further growth. This is similar to what we observed for high aztreonam in rich media (Ch. 5 Sec. 5.3), further suggesting that the similar population dynamics for cefotaxime and aztreonam in rich media correlate to similar morphology dynamics.

Meanwhile for antimicrobials that primarily inhibit elongation a bump phenotype is observed in our optical density measurements. Based on our results for mecillinam (Chapter 4) we hypothesise that a bump phenotype corresponds to the development of spherical cells followed by lysis. Therefore future microscopy with A22 and low fosfomycin concentrations may reveal spherical morphologies. This hypothesis is also consistent with the literature observations that A22 results in lemon morphologies [42, 58] and that fosfomycin results in fatter (and longer) *E. coli* cells (Figure 9.7) [51].

9.2 Microscopy with cefotaxime and fosfomycin

To test the hypotheses that cefotaxime should produce filaments and fosfomycin should produce spherical morphologies some preliminary phase contrast microscopy was carried out. These experiments were done in rich LB media using *E. coli* MG1655.

9.2.1 Cefotaxime

Following the protocol in Chapter 2 for our plate reader experiments, samples were removed every hour, from a 96-well plate, to be studied using microscopy. To achieve this the plate reader was stopped every 60 minutes and $3-5$ μl samples taken from a selection of wells. This allowed us to directly correlate the observed morphologies with the plate reader optical density measurements. Samples from a range of cefotaxime concentrations were chosen and imaging was done with a 60x objective.

Interestingly, after one hour of exposure to a high concentration (1μg/ml) of cefotaxime, primarily spherical cells are observed while after two hours filaments were seen to have arisen (Figure 9.4). The spherical cells that we see in the first hour after exposure to cefotaxime are unexpected, and to our knowledge have not been described in the literature.

We also observe some spherical cells at all concentrations after three hours. These may be spheroplasts [45, 154] which form due to turgor pressure pushing the inner and outer membranes out through defects in the cell wall. We believe these are spheroplasts as spheroplasts have previously been reported to emerge after exposure to cefotaxime [45, 154].

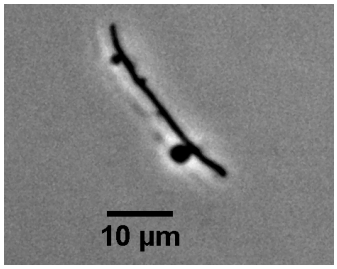

Figure 9.3: An example of a several bulges forming on a filament after 3 hours in 1 μg/ml cefotaxime at 60x magnification.

Some of our images for cefotaxime also show bulge formation (e.g. at 1 μg/ml Ctx. after 3 hours (Fig. 9.3)). This also has parallels in the literature in Yao et al. [154].

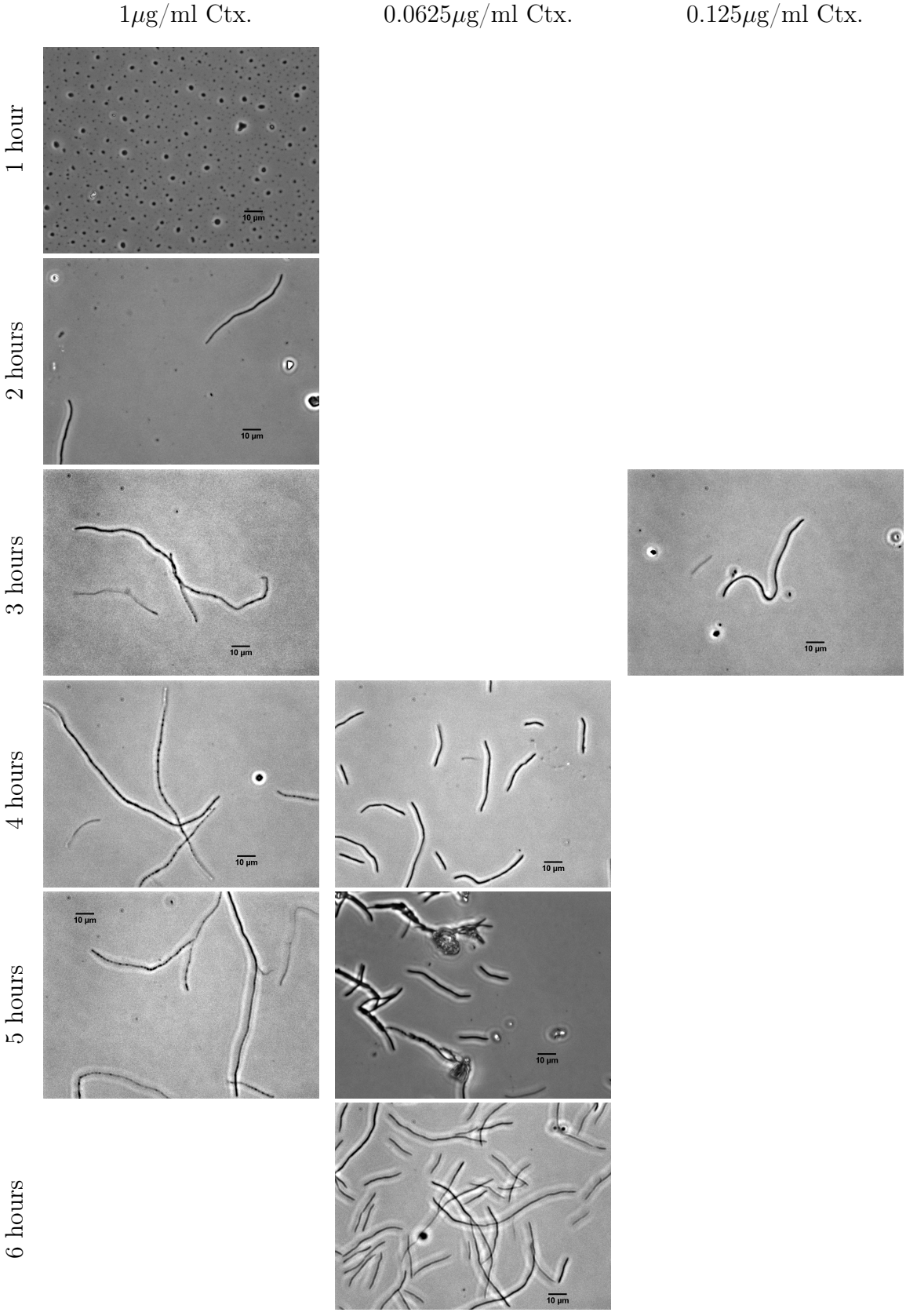

Figure 9.4: Microscopy images corresponding to 1 hour timepoints in the first 6 hours of *E. coli* MG1655 growth at cefotaxime concentrations of 1, 0.125 and 0.0625μg/ml in LB. Scale bars are 10μm.

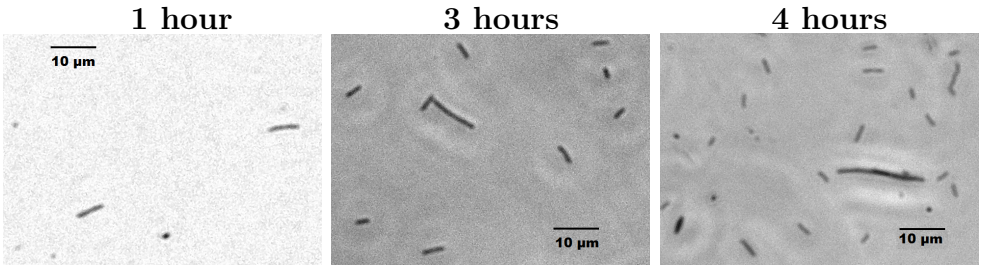

Figure 9.5: *E. coli* MG1655 imaged in LB with 0.5μg/ml fosfomycin at 1, 3 and 4 hours using a 60x objective.

9.2.2 Fosfomycin

Microscopy of *E. coli* exposed to various fosfomycin concentrations was carried out in parallel with growth in the plate reader, using the same protocol as described in Section 9.2.1. The resulting images can be seen in Fig. 9.8, and some higher resolution examples in Figure 9.5.

At the high fosfomycin concentrations (8 and 32μg/ml) *E. coli* MG1655 are observed to turn into small, spherical cells which do not appear to grow much over time. In the presence of the low fosfomycin concentration (0.5μg/ml), small filaments are seen to appear, and these increase in both length and width after 3 hours of exposure to the antibiotic (Figure 9.6).

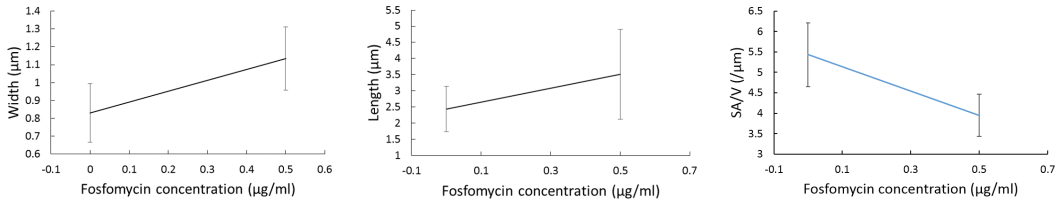

Figure 9.6: The experimental average widths (left), lengths (centre) and SA/V (right) after three hours growth at 0μg/ml and 0.5μg/ml fosfomycin. $N = 39$ at 0μg/ml. $N = 54$ at 0.5μg/ml. Error bars show standard error of the mean.

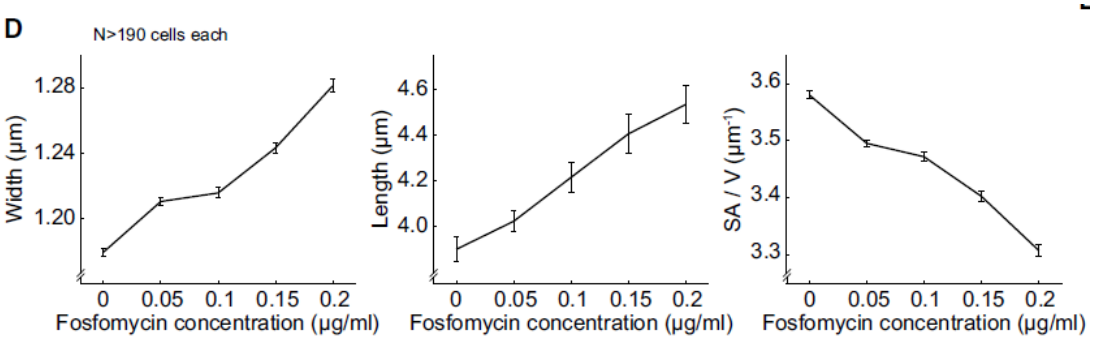

Figure 9.7: Panel D from Figure 2 of Harris and Theriot [51] demonstrating the change in width and length of *E. coli* MG1655 in LB after three hours with different fosfomycin concentrations.

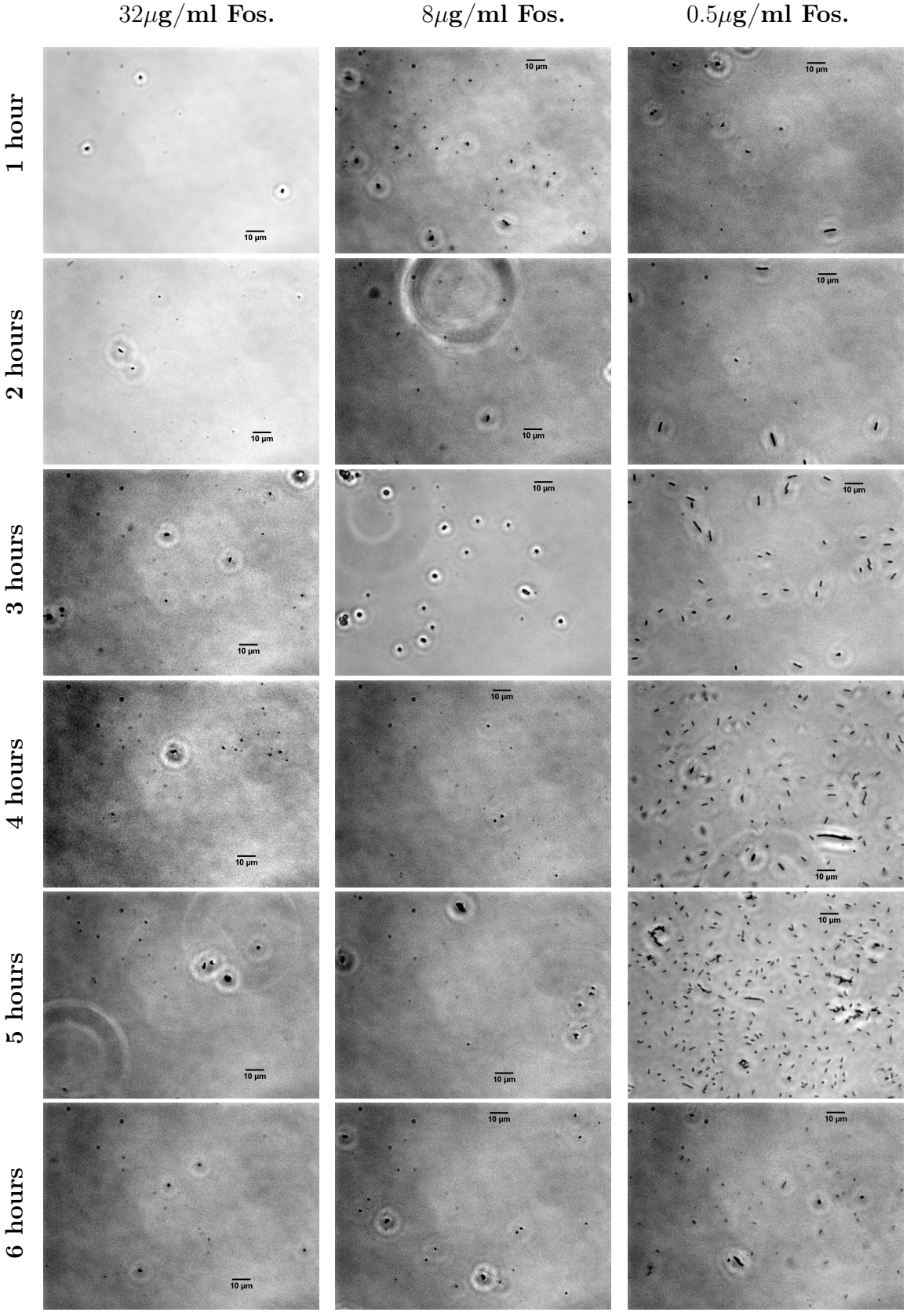

Figure 9.8: Microscopy images corresponding to 1 hour timepoints in the first 6 hours of *E. coli* MG1655 growth in LB for select fosfomycin concentrations: 32μg/ml, 8μg/ml and 0.5μg/ml. Scale bars are 10μm.

As previously mentioned, Harris and Theriot [51] also observed that *E. coli* cells become slightly larger in the presence of fosfomycin in LB, while maintaining a rod shape (an excerpt from Figure 2 of [51] is shown in Figure 9.7). Our antibiotic-free bacteria are slightly smaller than those in Harris and Theriot [51], however correcting for this and applying a linear projection on the data in Harris and Theriot [51] to a fosfomycin concentration of 0.5μg/ml yields good agreement. Our measured average width after 3 hours at 0.5μg/ml Fos. is $1.14\pm0.18\mu$m while the projection from the Harris and Theriot data gives a width of $1.06 \pm 0.17\mu$m. Similarly the average length we measured after 3 hours at 0.5μg/ml Fos. is $3.5 \pm 1.4\mu$m, and the projection gives a length of $4.1 \pm 0.7\mu$m.

Interestingly, these morphology dynamics are the opposite of what we hypothesised in Section 9.1.3 based on the optical density curves. The OD curves showed a bump at low fosfomycin and a plateau at high fosfomycin, thus we hypothesised that elongation was inhibited at low fosfomycin (suggesting likely spherical morphologies) while division was more inhibited at high fosfomycin (suggesting likely filaments). However our microscopy data demonstrates that in fact filaments form at low fosfomycin, and small spherical morphologies form at high fosfomycin.

9.3 Modelling fosfomycin morphology dynamics

Figure 9.6 shows that, after three hours of exposure to 0.5μg/ml fosfomycin, cell length and width increase relative to growth in the absence of antibiotic. These "fat filaments" were observed at the low fosfomycin concentration, while small spherical cells were observed at fosfomycin concentration at the MIC and above. The model was tested to see if it could recover this behaviour.

Fosfomycin can be mimicked by decreasing the synthesis rate of precursors in our

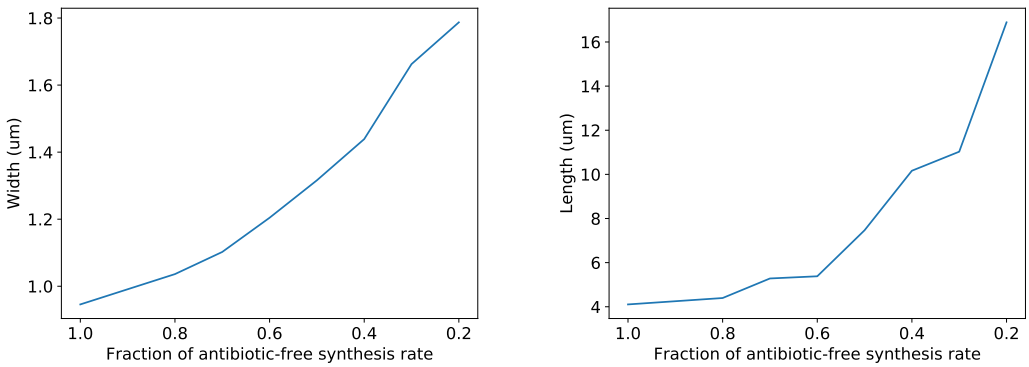

Figure 9.9: Simulation output for average width (left) and length (right) after three hours at various synthesis rates $S = xS_0$, where S_0 is the antibiotic-free synthesis rate. Parameters taken from Tables 7.1 and 8.2.

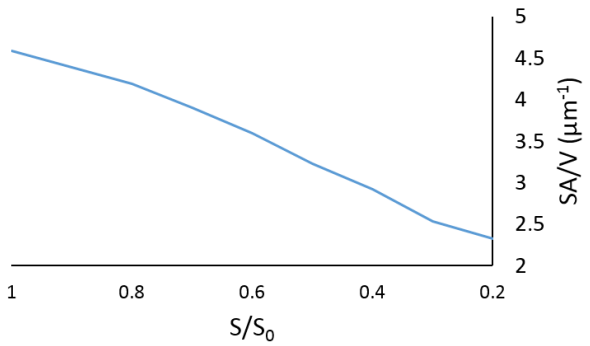

Figure 9.10: Predicted SA/V after 3 hours at decreasing synthesis rates, reproducing fosfomycin-like dynamics. Results of model simulations using parameters from Table 6.4.

mathematical model. Simulations were carried out as discussed previously (Ch 7 Section 7.1) at a range of synthesis rates, and the morphology assessed. The parameter values for pH 7.4, 37°C were used (see Table 6.4).

Figure 9.9 shows that the morphology dynamics were successfully captured in the model. The cell width and length after three hours of fosfomycin exposure increase with decreasing synthesis rate (mimicking increasing fosfomycin concentration) (Figure 9.9), and the surface area to volume ratio decreases with increasing inhibition (Figure 9.10) as we see in our experimental data (Figure 9.6) at the low (filament-forming) 0.5μg/ml fosfomycin, and as reported by Harris and Theriot [51]. The model successfully predicts small fat filaments at low levels of fosfomycin-like inhibition but, as can be seen in Figure 9.9, at high inhibition levels the model predicts longer and fatter filaments, not the small spheres we observed experimentally (Figure 9.8). This could be due to the lack of lysis in the simulations. This preliminary result is nevertheless encouraging, since it suggests that the model has the potential to be used for a wide range of cell wall-targeting antibiotics.

Chapter 10

Ideas for further work

10.1 Short term future work

To verify some of the model's predictions it would be useful to carry out more microscopy on the intermediate growth medium MOPSgluCAA, for mecillinam and aztreonam. This would allow us to verify if the quality of predictions for the CFU dynamics (using linear interpolation for the parameter values), correspond to the quality of the morphology predictions, by also comparing the morphology tracks. In particular, as the linear interpolation for the number of divisomes did not capture the correct CFU dynamics in the presence of high aztreonam, having more microscopy data would allow us to perform a fit to the antibiotic-free morphology and compare the predicted parameter values with those hypothesised from the linear interpolation. It would also be interesting to see if this antibiotic-free fit is able to recover the observed CFU dynamics at high aztreonam in MOPSgluCAA. Furthermore, having fits to the antibiotic-free morphology in MOPSgluCAA (and potentially other media variants) would allow us to determine the growth medium dependence of these parameters.

It would also be useful to have more experimental data with fosfomycin e.g. microscopy and CFUs in MOPS media variants rather than LB. Higher resolution microscopy in MOPS media would allow us to better quantify the morphology dynamics of *E. coli* in the presence of fosfomycin, and better compare to the model results. Furthermore, having CFU data would allow us to determine the lysis rates when precursor synthesis is blocked. This would allow us to test whether the experimental observation at high fosfomycin concentration is better predicted by the model when lysis is included.

10.2 Long term future work

10.2.1 Extending our work with the current antibiotics

In order to be able to make more predictions from the model it would be necessary to determine in more detail the relationship between the experimental antibiotic concentration and the inhibition level in the model. In order to determine this relationship it would be necessary to perform experiments, and fit the morphology dynamics, for a wider range of antibiotic concentrations.

Furthermore, the model currently assumes instantaneous diffusion of the antibiotics to their cellular target. This is not necessarily the case: e.g. cefotaxime is thought to take up to 2 hours to reach a sufficient concentration in the periplasm to be fully active [69]. Thus the model may make better predictions if the diffusion rates of the antibiotics are taken into account.

The model could also be extended to include the evolution of antibiotic resistance and thus recover the expected regrowth dynamics at later times, where the regrowth is caused by evolution. It would additionally be interesting to explore how well the model performs in scenarios when the antibiotic concentration is not constant. For example, one might wonder whether the model can recover normal growth once the antibiotic pressure has been removed, despite lacking the explicit inclusion of hydrolases/remodelling enzymes. It could also be interesting to know if the model can be adapted for resistant mutants, e.g. with modified PBPs.

10.2.2 Antibiotic combinations

Another interesting area that our model could be applied to is that of antibiotic combinations. Combination therapies are currently being used to improve antibiotic efficacy in the clinic, and can reduce the emergence of resistance [14]. It is necessary to study antibiotic combinations carefully as the combined impact is not always more effective at clearing the bacterial population. Furthermore, it is experimentally expensive to study antibiotic combinations in detail and only possible due to advances in automation [8].

Antibiotic combinations can result in synergy or antagonism. Synergy occurs with antibiotic combinations when less of each antibiotic is required to have the same level of inhibition, whilst antagonism occurs when the antibiotics are less effective when used in combination [14]. The class of antibiotic can often be used to guess if synergy or antagonism is expected, e.g. aminoglycosides and cell wall-targeting drugs are known to be synergistic [155].

It would be useful to have a mathematical model that can predict which combinations of cell wall-targeting antibiotics are likely to be synergistic or antagonistic. We believe that our model can help with this, and we have

	32Fos	16Fos	8Fos	4Fos	2Fos	Fos
3Mec	0.198	0.24	0.29	0.328	0.33	0.33
1.5Mec	0.186	0.23	0.354	0.396	0.44	0.5
0.75Mec	0.192	0.241	0.468	0.355	0.29	0.3
0.375Mec	0.185	0.755	0.392	0.265	0.27	0.25
0.188Mec	0.191	0.298	0.403	0.273	0.275	0.24
0.094Mec	0.189	0.323	0.314	0.254	0.27	0.26

Figure 10.1: Heat map for cell growth (represented as optical density) at five antibiotic-free doublings in the presence of both fosfomycin and mecillinam.

performed a small amount of preliminary work in this direction.

10.2.2.1 Population dynamics with fosfomycin in conjunction with mecillinam

In order to test the model's capabilities for antibiotic combinations we carried out a pilot "checkerboard assay" experiment for combinations of fosfomycin and mecillinam in MOPSgluRDM (this was performed in collaboration with E.T.). The protocol is as described in [77, 97] and involves carefully pipetting antibiotic solutions into the wells such that one antibiotic has a concentration gradient vertically and the other horizontally (Figure 10.1). The results for fosfomycin with mecillinam can be found in Figure 10.1, represented as a heatmap where the colour is indicative of the optical density reached after five antibiotic-free doubling times. From analysis of the growth rates in this experiment we conclude that the combination of fosfomycin and mecillinam is generally more inhibitive than either antibiotic on its own i.e. synergistic (see Figure E.1 in Appendix). Based on this statement one might expect the heat map in Figure 10.1 to have a gradient from green in the bottom right corner, to red in the top left corner. However, while the top left corner is indeed red, the bottom corner is in fact more orange and there is a green band across the diagonal. This means that higher optical densities are being reached at higher concentrations of the antibiotics, despite the synergism between them. We were interested to see if the model could explain this phenomenon.

10.2.2.2 Testing the model for fosfomycin and mecillinam synergy

The model can also be used to predict the population dynamics in combinations of mecillinam and fosfomycin in rich media. The model was set up using parameters in Tables 7.1 and 8.2 and the synthesis rate and elongation incorporation rate varied simultaneously. In order to be able to directly compare between the experiments and the simulation the number of cells after five antibiotic-free doubling times was extracted from the model. It has previously been shown

R1\S1	0.1	0.2	0.3	0.4	0.5	0.7	0.9
0.1	1	1	2	2	4	4	4
0.3	1	2	2	4	4	8	8
0.5	2	2	4	4	4	8	16
0.7	2	4	4	8	8	16	16

R1\S1	0.1	0.2	0.3	0.4	0.5	0.7	0.9
0.1	70.582	70.592	70.59226	70.60228	70.60228	70.61231	70.61231
0.3	70.59225	70.602	70.60228	70.60228	70.61231	70.62233	70.62233
0.5	70.592	70.602	70.61231	70.61231	70.61231	70.62233	70.62233
0.7	70.592	70.60228	70.61231	70.61231	70.62233	70.62233	70.63236

R1\S1	0.1	0.2	0.3	0.4	0.5	0.7	0.9
0.1	0.023666	0.026421	0.078839	0.06459	0.233595	0.162175	0.13716
0.3	0.01724	0.066948	0.058248	0.187521	0.172009	0.549743	0.408619
0.5	0.05071	0.041951	0.151127	0.137586	0.131886	0.397478	1.373695
0.7	0.023281	0.094967	0.093353	0.33194	0.30282	1.148304	0.99131

Figure 10.2: Predicted heat maps for cell growth at five doublings in the presence of both fosfomycin-like ($S1$) and mecillinam-like ($R1$) inhibition. The top grid on the left is the number of cells output from the model and the top grid on the right is the number of cells multipled by the volume to approximate biomass. The bottom grid is the number of cells divided by the surface area to give some approximation to the optical density

that the turbidity of a bacterial population that experiences shape changes, scales with $1/r^2$ [73]. Therefore to approximate optical density the number of cells at five antibiotic-free doubling times was divided by the surface area. These two interpretations of the model output can be seen in Figure 10.2 (Note that there is no lysis in this version of the model). By scaling the number of cells with the surface area, some of the non-monotonic behaviour observed experimentally can also be observed when R (the incorporation rate) is decreased at a range of synthesis rates. This suggests that the model indeed has potential for application to antibiotic combinations. Scaling the number of cells by the volume to approximate total biomass results in a similar heat-map as for the number of cells only, with no non-monotonic behaviour. This could be due to the lack of lysis in this model implementation, or perhaps the observation that optical density scales with total biomass no longer holds when bacteria experience large changes in cell width, as suggested in [73].

10.3 Conclusions

In this thesis we have presented a comprehensive experimental data set covering the morphology and population dynamics of *E. coli* in a range of growth media and with a range of cell wall-targeting antibiotics. Using our experimental results for mecillinam and aztreonam, and literature estimates, we have successfully constructed a mathematical model that can predict the morphology and CFU dynamics of *E. coli* in different growth media, by considering the mechanism of action of the antibiotic. This mathematical model makes a range of assumptions, and coarse-grains many of the cellular processes, while still successfully capturing the growth medium dependent inhibition of both mecillinam and aztreonam.

One of the core assumptions of our model was that cell wall expansion was carried out by elongasome and divisome enzyme complexes. During the course of this thesis, continuing work in the field has determined that the elongation machinery is more complex than a simple elongasome complex,

with evidence for multiple autonomous systems. It appears that aPBPs (bi-functional transpeptidase/glycotransferase enzymes) carry out elongation activity independently of the rod complex (i.e. PBP2, RodA MreC etc.) [26]. Furthermore it has been shown that in *B. subtilis* the rod-complex and aPBPs have inverse effects on cell width [26]. This could be relevant for future refinement of our model.

Some of the other key assumptions of the model were that peptidoglycan density remained constant, that lysis rates had a linear dependency on the fractional change imposed by the antibiotic on enzyme activity or enzyme number (e.g. in R for mecillinam), that there is some relation between lysis and the changes in morphology (e.g. becoming large spheres or long filaments), that the peptidoglycan precursor incorporation rate scaled with the volumem, that there exists some kind of fatness threshold, as well as a sphere threshold. Most of these assumptions arose in order to make the model fit the data. Possible refinements of the model could lie in removing, or relaxing, these assumptions. Potentially most importantly, relaxing the assumption of constant peptidoglycan density may remove the need for a sphere threshold. This could also allow the development of a more abstract model. For example, we believe similar results would be found in a model which only explicitly modelled the volume and surface area growth, but which had a fatness threshold. This in theory would still result in the key model predictions for lysing, spherical cells under the action of mecillinam, short lysing filaments in rich media under the action of aztreonam and long, relatively stable filaments in poor media under the action of aztreonam. Such a simplification of the model would allow us to more fully explore the phase space.

Another limitation of the model is that it deals with average behaviour i.e. does not account for cell to cell variation. As the aim of the model was to reproduce population level dynamics, this is a reasonable approximation. Nevertheless, cell to cell variation and heterogeneity, as well as potential stochastic effects (e.g. efficacy of antibiotics against individuals may depend on stochastic variation in gene expression e.g. in the formation of persister cells [70]), are likely to impact on the population dynamics observed experimentally. The model could be adapted to draw parameter values from various distributions e.g. number of elongasomes, lysis rates. In this way, by running many versions of the model it may be possible to recover any dynamics which arise due to variation in the population.

Our key result for mecillinam is that the antibiotic is less inhibitive on poor media as the bacteria can continue to divide as small spheres, whilst on rich media the spheres become too large and lyse (due to the fatness threshold). For aztreonam, our key result is that at low concentrations the poor medium is more inhibitive due the formation of filaments, whilst the rich medium is more inhibitive at higher concentrations due to malfunctioning divisomes. The aztreonam results are also dependent on the presence of the fatness threshold which has proven to be the most significant feature of the model. How, and if, such a fatness threshold is present in *E. coli* requires more careful experimental work.

In the model we also tested three models for the triggering of division: timer, adder and precursor threshold. We found that the timer model did not result in steady state growth in this simulation set-up. Little difference was observed between the adder and precursor threshold models. More work could be done to examine differences between the division models; for example, all the parameter fitting was performed with the precursor threshold model, and it would be interesting to see if the same parameter values emerge as best fits if the adder division model were to be used instead.

Overall the model has been very successful and has a lot of potential for extension in the current area, as well as application to new antibiotics, combination of antibiotics, and antibiotic resistant mutants.

10.3.1 Novelty with respect to other models in the literature

While other models exist that look at the relationship between bacterial cell morphology and population dynamics in the presence of cell wall-targeting antibiotics [124], we believe that our model is the first to successfully link cell wall biosynthesis, the antibiotic mechanism of action, changes in morphology and population dynamics. Furthermore the model is capable of making predictions for various cell wall-targeting antibiotics, with different mechanisms of action.

The complexity of cell wall synthesis (even in this coarse-grained form) results in a model which does not nicely collapse onto a universal result like that in Greulich et al. [48] for ribosome-targeting antibiotics. However, there is potential to take elements of the model and abstract them a little to get interesting analytical results. Nevertheless our model makes some broad conclusions. Firstly, we found that the fatness threshold was a crucial component for achieving the expected morphology dynamics in the presence of both mecillinam and aztreonam. Our fit for the fatness threshold ($r_{th} = 0.009 n_D$) was also found to agree with an estimate derived from literature data ($r_{th} \simeq 0.01 n_D$, Chapter 7). Additionally, it was observed that the mode of inhibition of elongation is not significant, but rather the downstream impact of the morphological changes which results in the lytic activities of the antibiotics. Overall this model, while it could be refined further, has made a decisive step towards increasing our understanding of the mechanisms leading to the population dynamics of *E. coli* in the presence of cell wall-targeting antibiotics.

Appendix A

Papers in preparation

- Cell wall model paper - I am currently drafting a manuscript which will include both experimental and modelling results.
- Morphology paper - I am also expecting to have a shorter paper focusing on the cell morphology results.
- Mecillinam degradation paper - I am also drafting a short note detailing our observations of antibiotic degradation under experimental conditions.

Appendix B

Early experiments

B.1 Population dynamics in 50ml tubes with mecillinam in LB and M9 variants

We see qualitatively similar growth curves for mecillinam when using test tubes instead of the plate reader Figure B.1, compared to Figure 3.5. This is re-assuring as it suggests that the increased growth at low Mec. concentrations are not dependent on the method used for measuring optical density. For this trial of growth in the shaker using tubes rather than using the microplate and plate reader, cultures were grown to exponential phase for 3 hours before inoculation into the final tubes. In the first trial the media for the final tubes was not pre-warmed to 37°C - this explains the slight lag seen in all three growth conditions. Despite this lag, we still recover very similar growth dynamics to those observed in the plate reader (Figure 3.5).

B.2 *E. coli* population dynamics in M9 media variants

B.2.1 Fosfomycin Summary

These observations are based on Figure B.2.

- In M9 minimal + glucose there are no bumps, no lysis is seen to occur. There appears to be normal growth up to some critical antibiotic threshold, which corresponds to the MIC.
- In M9 + casamino acids bumps start to appear, but they do not always

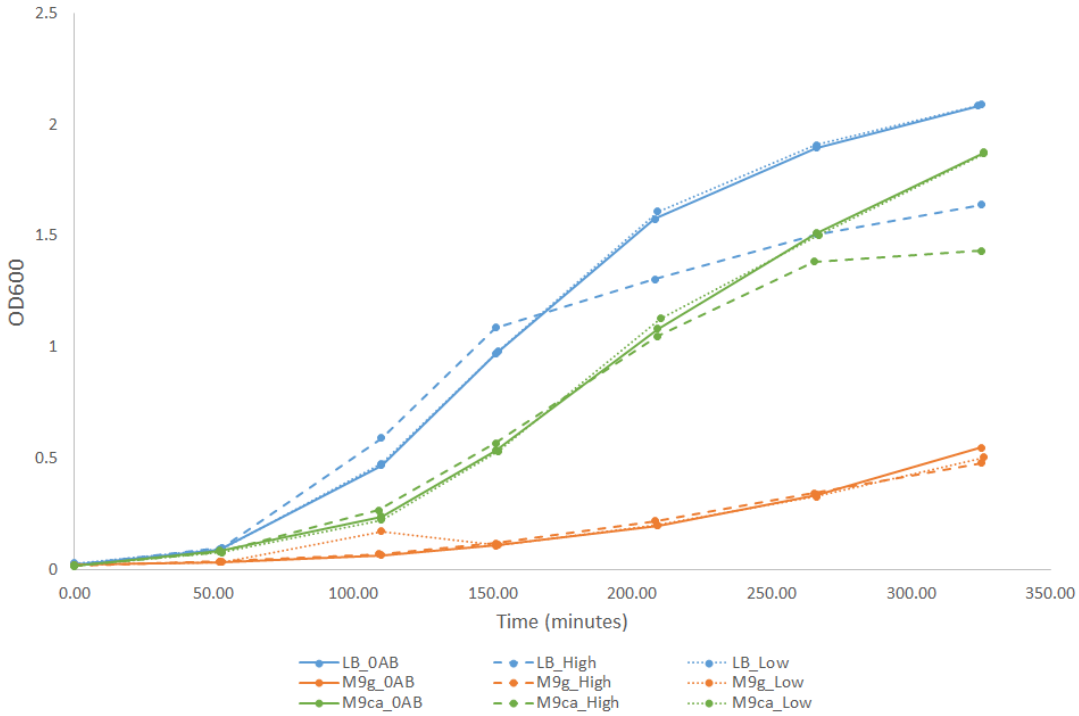

Figure B.1: Growth curves for MG1655 in 50 ml tubes in the shaker at 37C/200rpm in 3 different media (LB, M9 glucose and M9 glucose with casamino acids) and at 2 different mecillinam concentrations: high - 0.3μg/ml and low - 0.0096μg/ml, alongside growth in the absence of antibiotic.

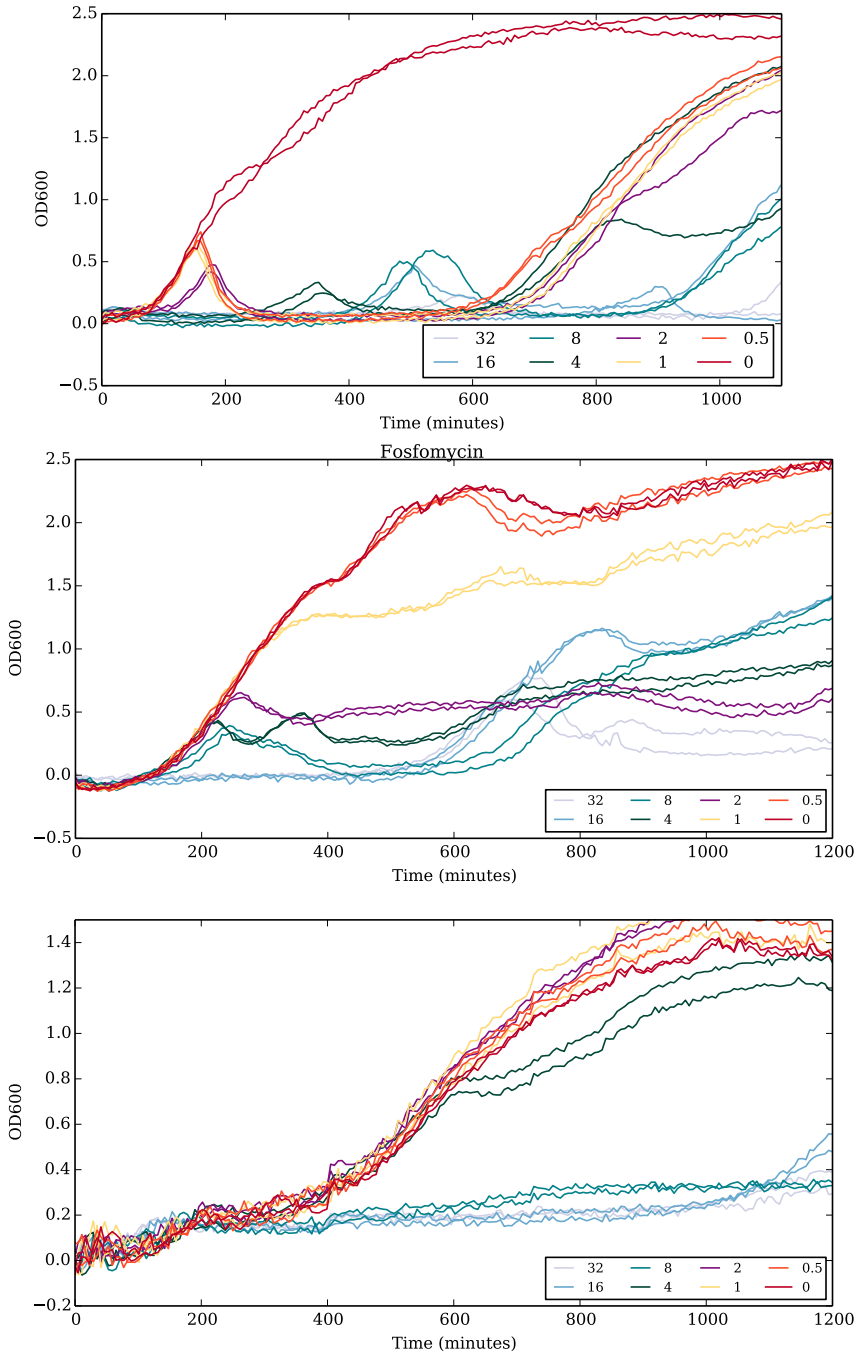

Figure B.2: Growth curves for MG1655 at varying concentrations of fosfomycin (indicated in the legend with units of μg/ml) in three different growth media: LB (top), M9 glucose + CAA (middle) and M9 glucose (bottom)

collapse to near background OD. The shifts of the bumps with fosfomycin concentration are less pronounced.

- In LB bumps decrease to background levels of OD and the bumps shift with fosfomycin concentration.

FOS IS MORE INHIBITING IN RICHER MEDIA

B.2.2 Cefotaxime Summary

These observations are based on Figure B.3.

- In M9 minimal + glucose there are no bumps, but all antibiotic concentrations inhibit growth.
- In M9 + casamino acids there are bumps but with slower lysis than in LB, generally the antibiotic is more inhibitive compared to growth in LB but there are similar levels of regrowth.
- In LB bumps appear at the same time and height for all concentrations and characteristic regrowth is observed.

CTX IS LESS INHIBITING IN RICHER MEDIA

B.2.3 Mecillinam Summary

These observations are based on Figure B.4

- inhibition seems to increase during growth in M9 + casamino acids compared to LB.
- no enhanced growth at low Mec. concentrations on M9 + casamino acids compared to growth on LB and M9 + glucose.
- on M9 + glucose see relatively less inhibition compared to growth in LB.

MEC IS MOST INHIBITING IN INTERMEDIATE MEDIA

B.3 MOPS variants - supplementary curves

B.4 Supplementary curves from the delay-time bioassay

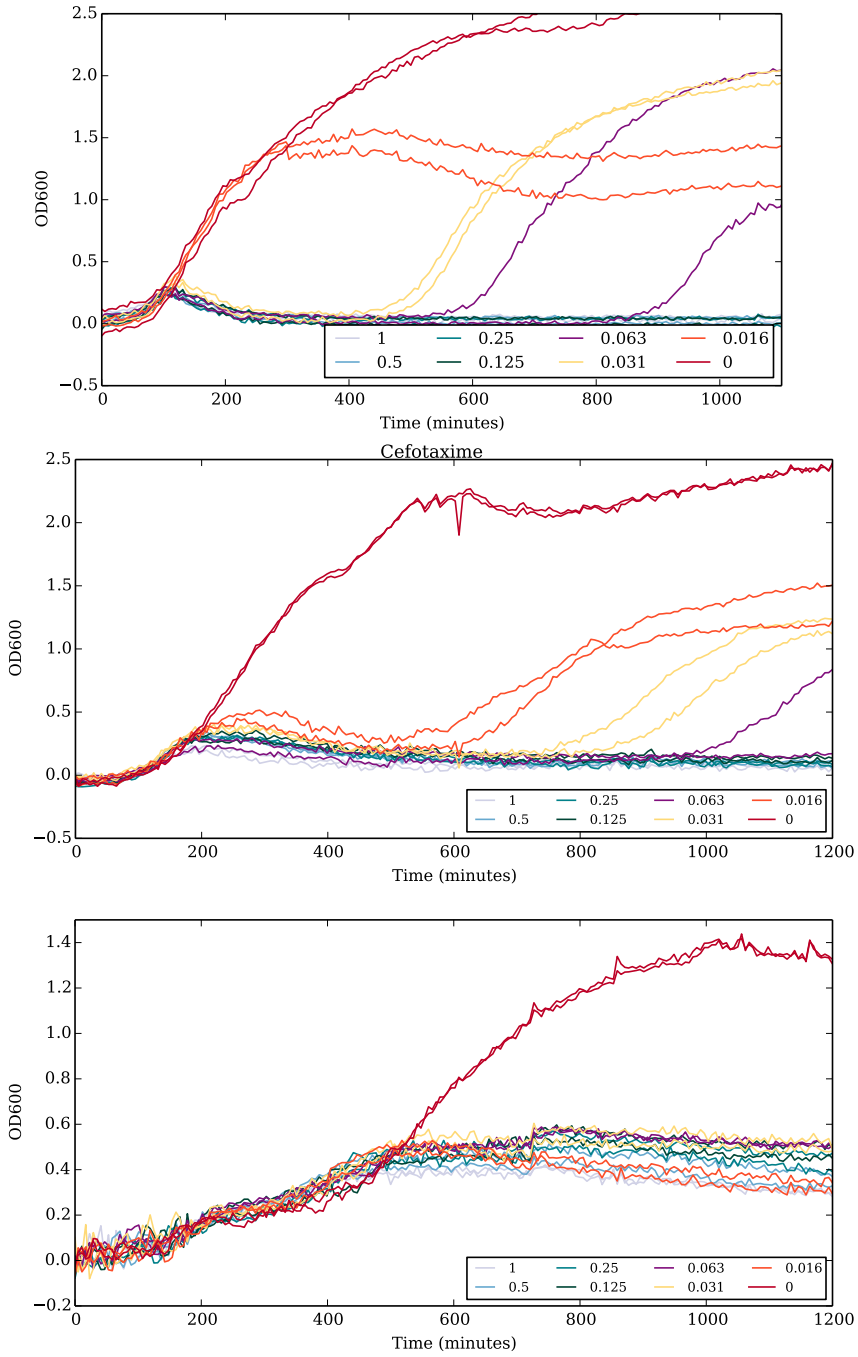

Figure B.3: Growth curves for MG1655 at varying concentrations of cefotaxime (indicated in the legend with units of μg/ml) in three different growth media: LB (top), M9 glucose + CAA (middle) and M9 glucose (bottom)

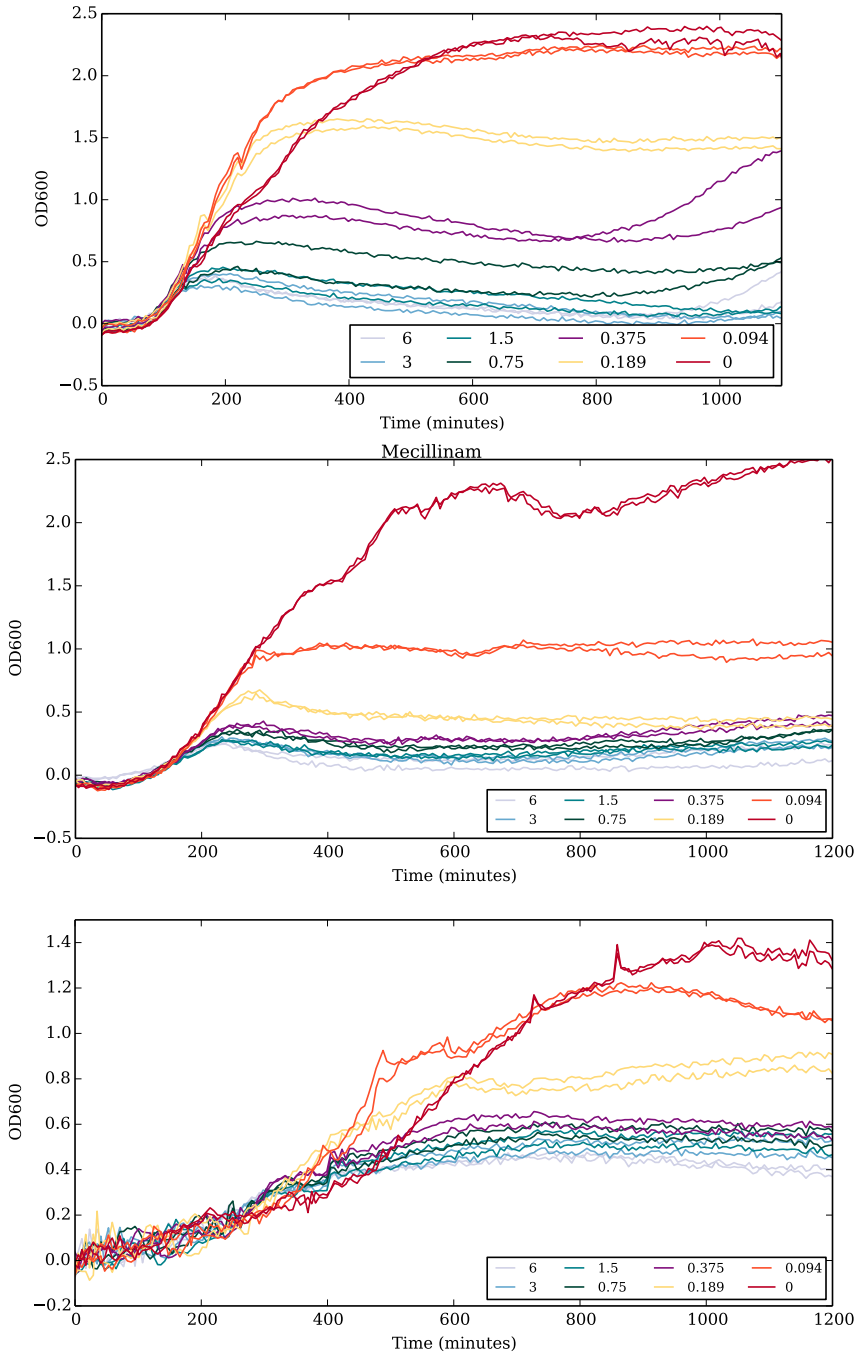

Figure B.4: Growth curves for MG1655 at varying concentrations of mecillinam (indicated in the legend with units of μg/ml) in three different growth media: LB (top), M9 glucose + CAA (middle) and M9 glucose (bottom)

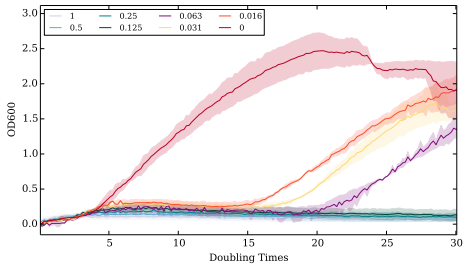

(a) Cefotaxime in MOPSglycRDM.

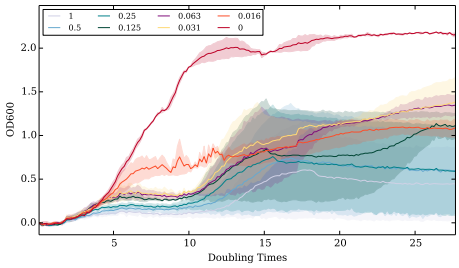

(b) Cefotaxime in MOPSgluCAA.

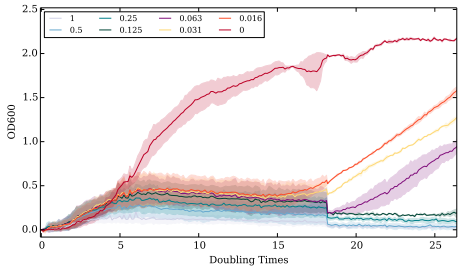

(c) Cefotaxime in MOPSglycCAA.

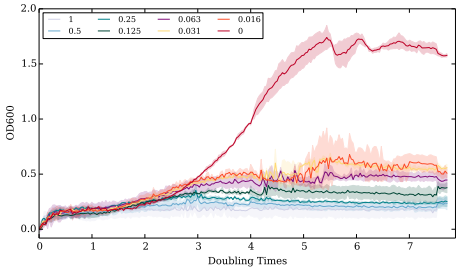

(d) Cefotaxime in MOPSglycMIN.

Figure B.5: Supplementary figure: Comparing the efficacy of cefotaxime across MOPS media variants at pH 7.4, 37°C.

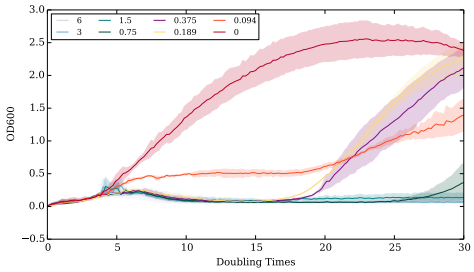

(a) Mecillinam in MOPSglycRDM.

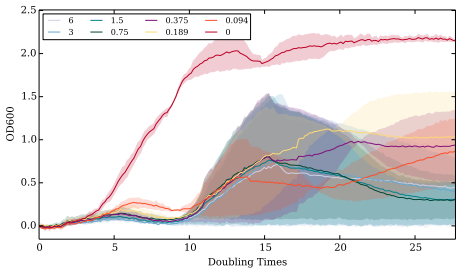

(b) Mecillinam in MOPSgluCAA.

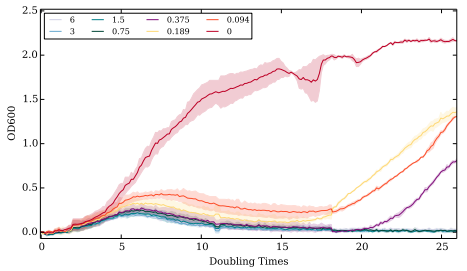

(c) Mecillinam in MOPSglycCAA.

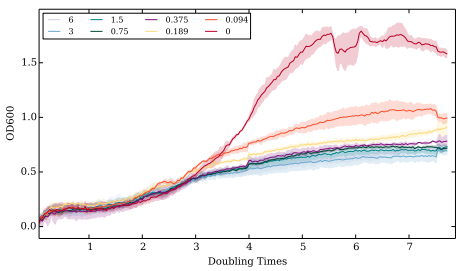

(d) Mecillinam in MOPSglycMIN.

Figure B.6: Supplementary figure: Comparing the efficacy of mecillinam across MOPS media variants at pH 7.4, 37°C.

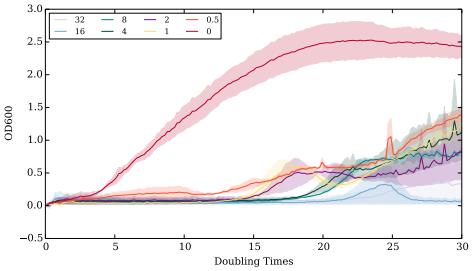

(a) Fosfomycin in MOPSglycRDM.

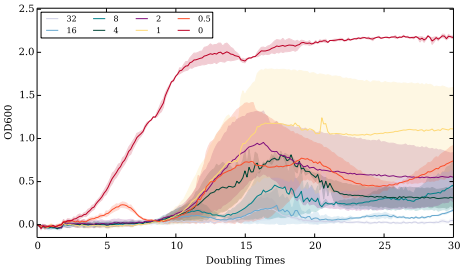

(b) Fosfomycin in MOPSgluCAA.

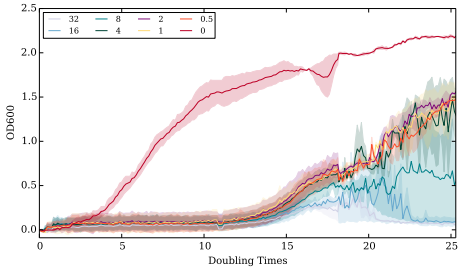

(c) Fosfomycin in MOPSglycCAA.

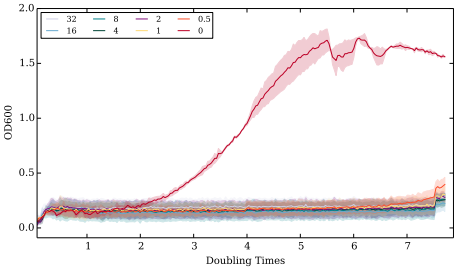

(d) Fosfomycin in MOPSglycMIN.

Figure B.7: Supplementary figure: Comparing the efficacy of fosfomycin across MOPS media variants at pH 7.4, 37°C.

LB media at 37°C and pH 7: no delay versus 2 hours delay

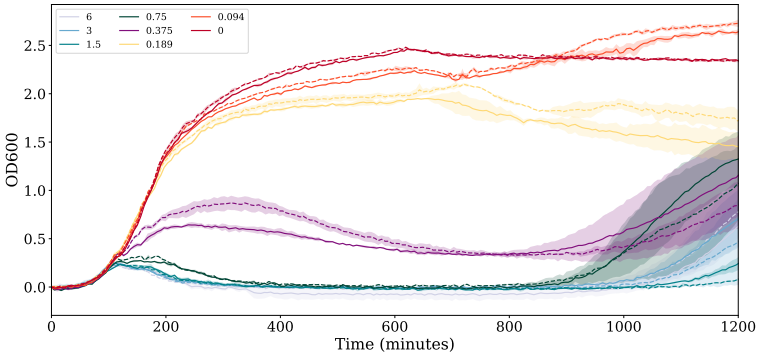

MOPSgluRDM at 37°C and pH 7.4: no delay versus 2 hours delay

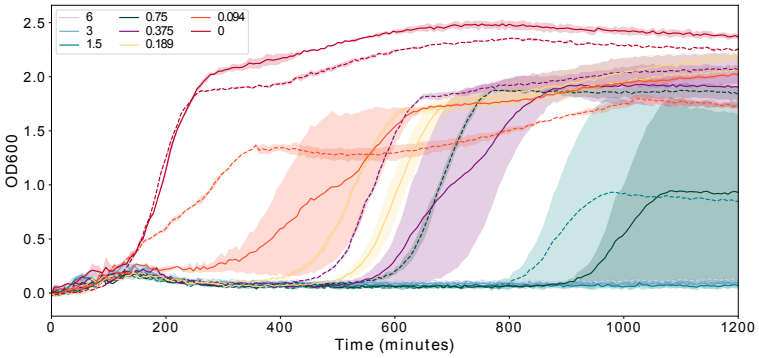

MOPSgluRDM at 37°C and pH 6.5: no delay versus 2 hours delay

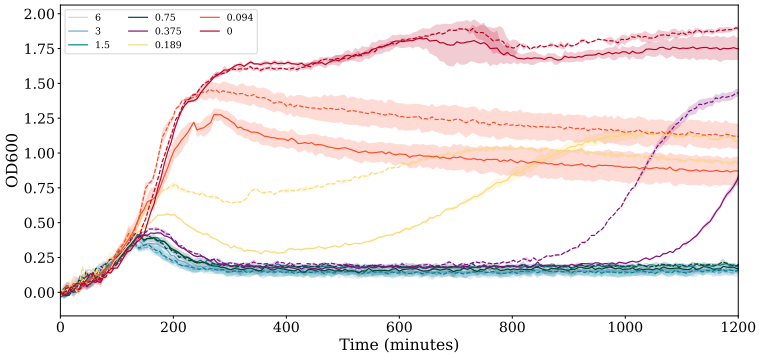

MOPSgluRDM at 34°C and pH 6.5: no delay versus 3 hours delay

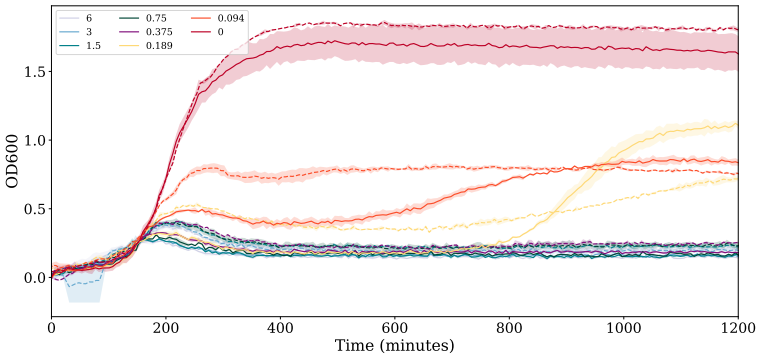

Figure B.8: Supplementary delay-time bioassay growth curves for *E. coli* RJA002 growing in LB and MOPSgluRDM with mecillinam (concentrations in legend in μg/ml). The dashed curves are from the delayed inoculate where time has been re-scaled by the delay time so that the antibiotic-free growth curves align.

B.5 Full data from genome sequencing

Condition	Gene Mutation Frequency																		
	gloB	stfP	hycB	gudB	rpoD	rffG	sdhA	yeaJ	rfbC	yjgL	stfE	paaX	glpT	yciH	pykF	wbbI	ptsI	ddlA	waaL	lysS
No antibiotic	0.9655	0.1014	1.0	1.0	0.1410	0.1081														
0.5MIC Fos.	1.0	0.19	1.0	0.9907	0.1471		0.1149	1.0	0.1449	0.4371	0.4320									
0.25MIC Fos.	1.0	0.1944	1.0	1.0	0.1795				0.3279					0.1111	0.3934	0.1071	1.0			
0.25MIC Ctx.	1.0	0.1061	1.0	1.0	0.1370		0.1359	0.1096	1.0	0.1667										
2MIC Mec.	1.0		1.0	1.0					1.0		0.1429									0.9527
0.0625MIC Mec	1.0	0.1136	1.0					0.1148	0.9828									0.1089	0.1111	

Table B.1: Full table of significant gene mutation frequencies as derived by Dr. Bartek Waclaw.

Appendix C

Extra MACS data analysis

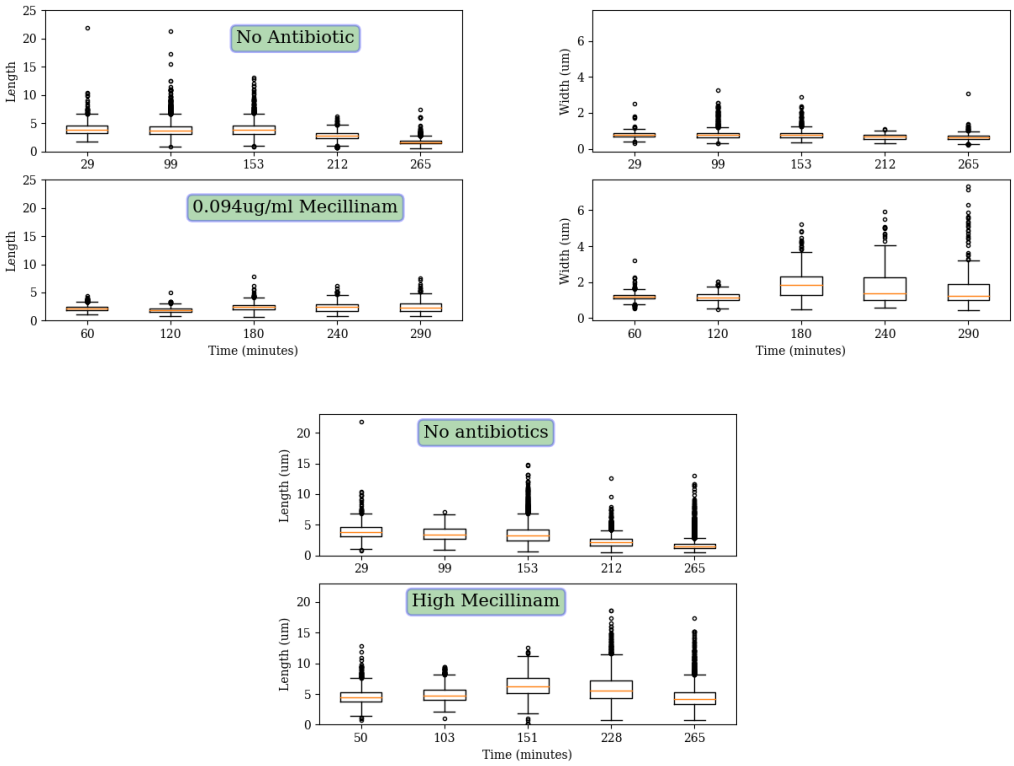

Figure C.1: Box plots with and without mecillinam derived from the MACS data in order to better visualise the length and width distributions (Top) MACS data for the low mecillinam condition at fast growth rate. Cell length (left) and width(right) are presented over time with and without mecillinam. (Bottom) MACS data for the high mecillinam condition in MOPSgluRDM, showing cell length only.

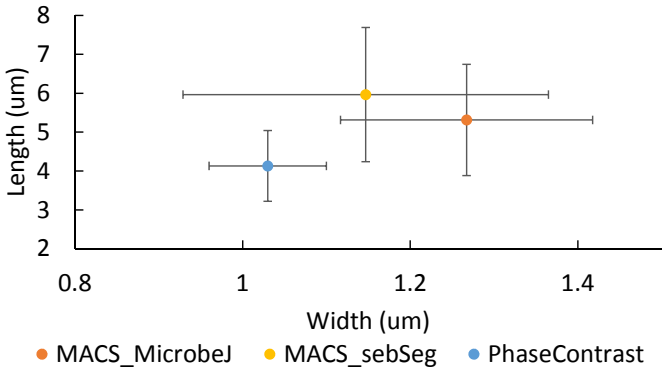

Figure C.2: Comparing the antibiotic-free morphologies measured using phase contrast and MACS microscopy in MOPSgluRDM 37°C, pH7.4. The MACS dataset was analysed with both MicrobeJ [31] and with a custom Matlab GUI [130] in conjunction with ImageJ.

Appendix D

Supplementary model results

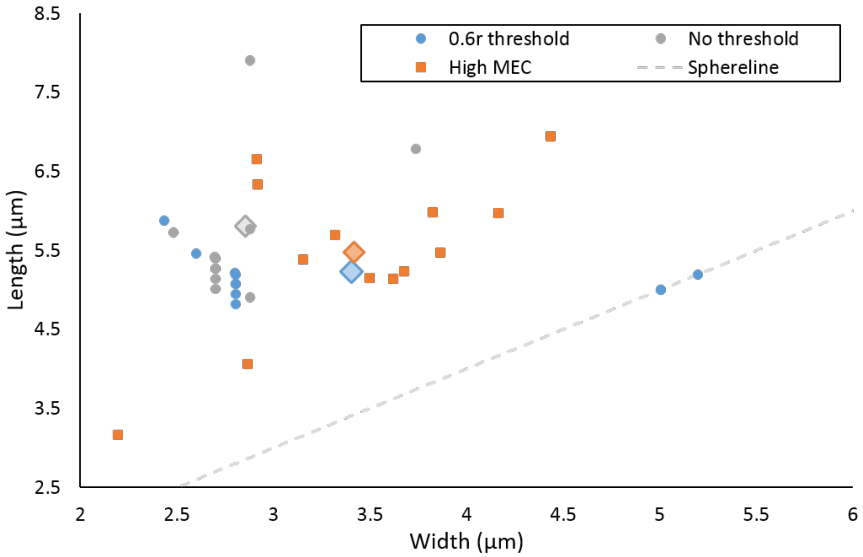

Figure D.1: Comparing the model (circles) and experimental (squares) length and width distributions after 240 minutes under the action of high mecillinam in MOPSgluRDM. Diamond markers indicate the experimental average and the weighted averages for the model results. The sphere line indicates where the cell length is equal to the width.

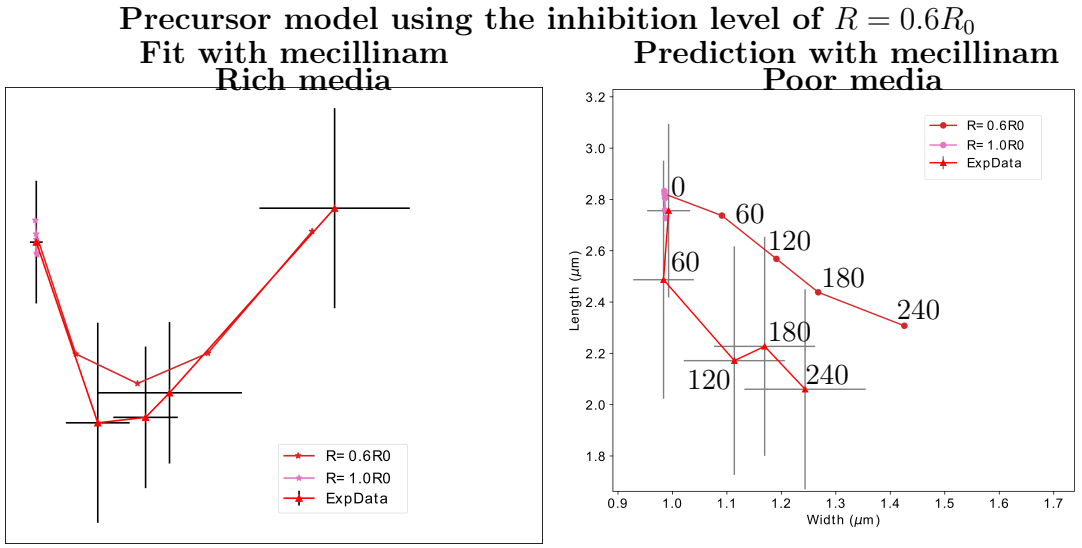

Figure D.2: Length and width dynamics. A comparison between experimental and simulated results using the precursor division model in poor growth conditions under mecillinam-like inhibition ($R = 0.6R_0$). The values in the legend indicate the inhibition level. Each marker corresponds to a single timepoint: 0, 60, 120, 180, and 240 minutes from the addition of mecillinam, going roughly from left to right.

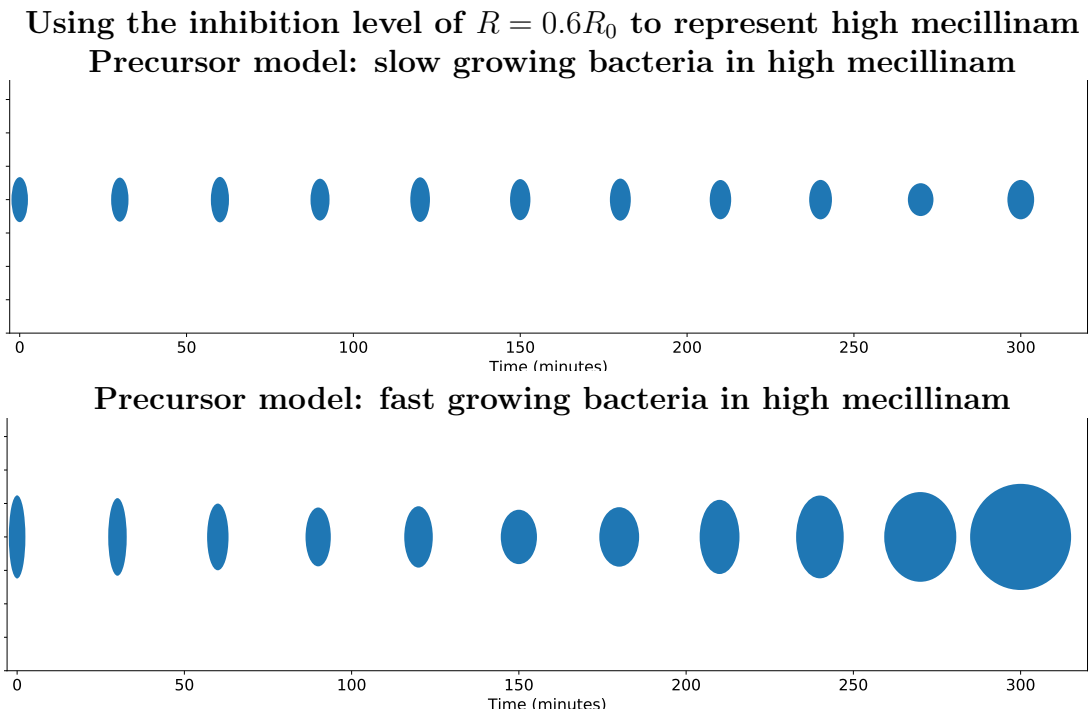

Figure D.3: Ellipse trajectories based on the average length and width every thirty simulation minutes for $R = 0.6R_0$. Tables 7.1 and 6.4 for parameter values.

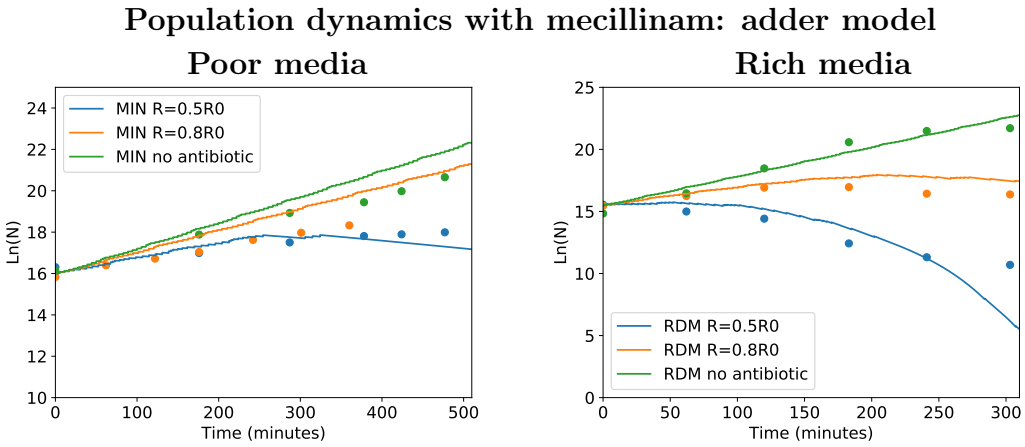

Figure D.4: Solid lines: The log cell number dynamics in the model at high ($R = 0.5R_0$) and low ($R = 0.8R_0$) mecillinam-like inhibition for slow growing cells using the adder division model. Filled circles: The experimental data for colony forming units in the presence of high (1.5μg/ml Mec.) and low (0.094μg/ml Mec.) for slow growing cells in MOPSgluMIN.

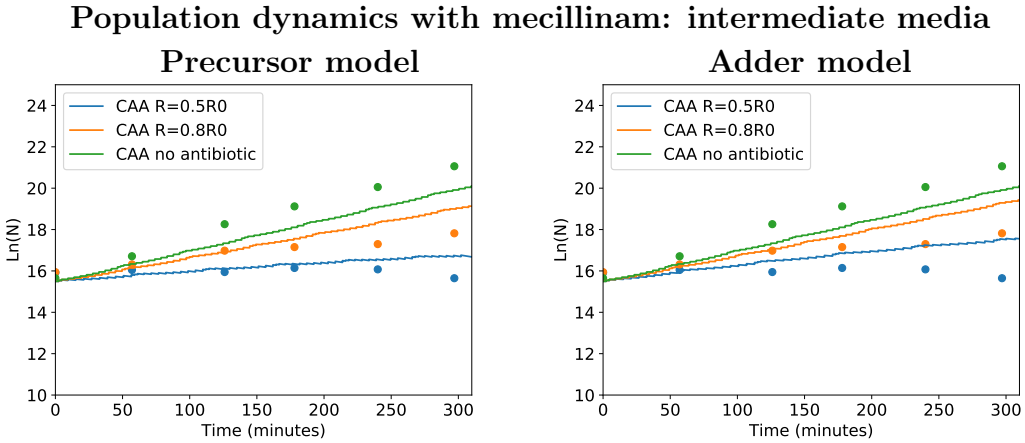

Figure D.5: Solid lines: The log cell number dynamics in the model at high ($R = 0.5R_0$) and low ($R = 0.8R_0$) mecillinam-like inhibition for intermediate growing cells. Filled circles: The experimental data for colony forming units in the presence of high (1.5μg/ml Mec.) and low (0.094μg/ml Mec.) for cells growing in MOPSgluCAA.

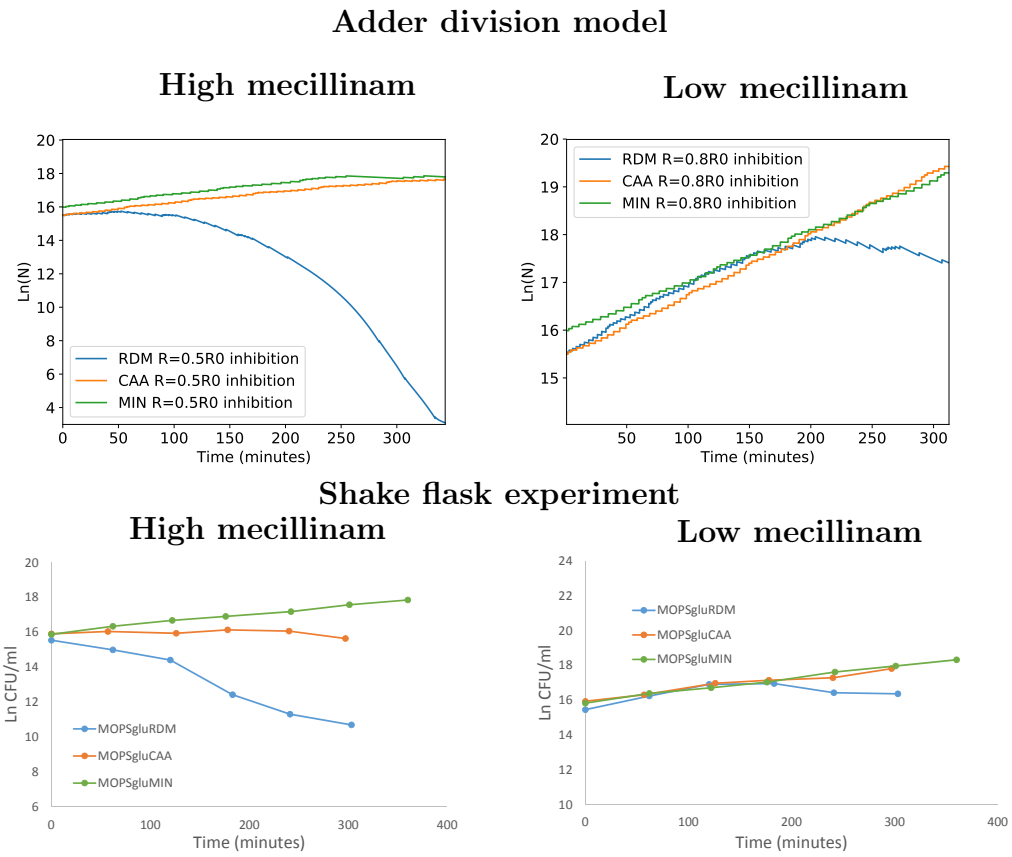

Figure D.6: Comparison between cell number dynamics in three different growth conditions: rich, medium and poor, in a high (1.5μg/ml) mecillinam-like inhibition (left) and a low (0.094μg/ml) mecillinam-like inhibition (right).

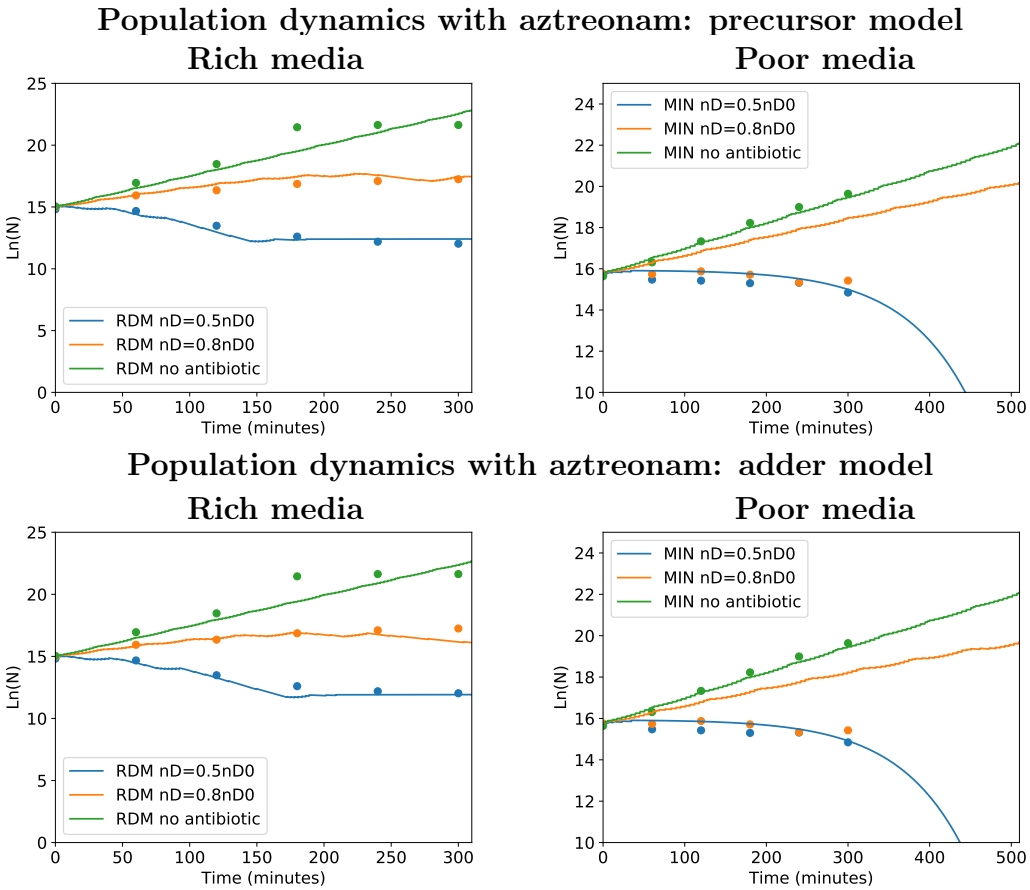

Figure D.7: Population dynamics with no elongation during pole formation. Solid lines: The log cell number dynamics in the model at high ($n_D = 0.4n_{D0}$) and low ($n_D = 0.5n_{D0}$) aztreonam-like inhibition for both fast growing (left) and slow growing (right) cells. Filled circles: The experimental data for colony forming units in the presence of high (0.5μg/ml Azt.) and low (0.0313μg/ml Azt.) for both fast and slow growing cells. In this example $\phi_D = 1.7$ and $\psi_D = 0.01$.

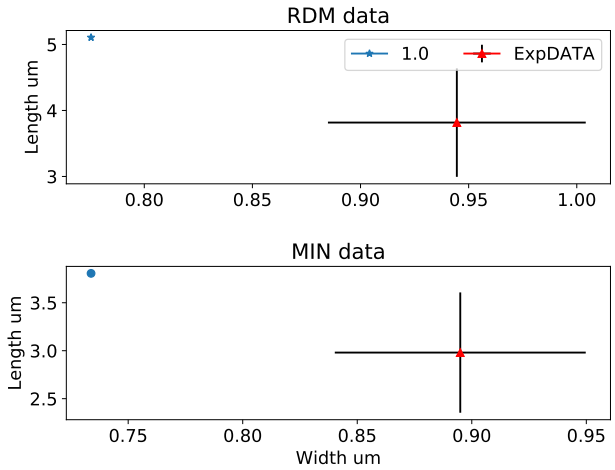

Figure D.8: A comparison between the antibiotic-free morphology from the experiments and the model when using the parameters fit without elongation during pole formation (Tables 6.4 and 7.1), applied when elongation is included during pole formation. This poor fit highlights the need to perform a parameter search with elongation included during pole formation.

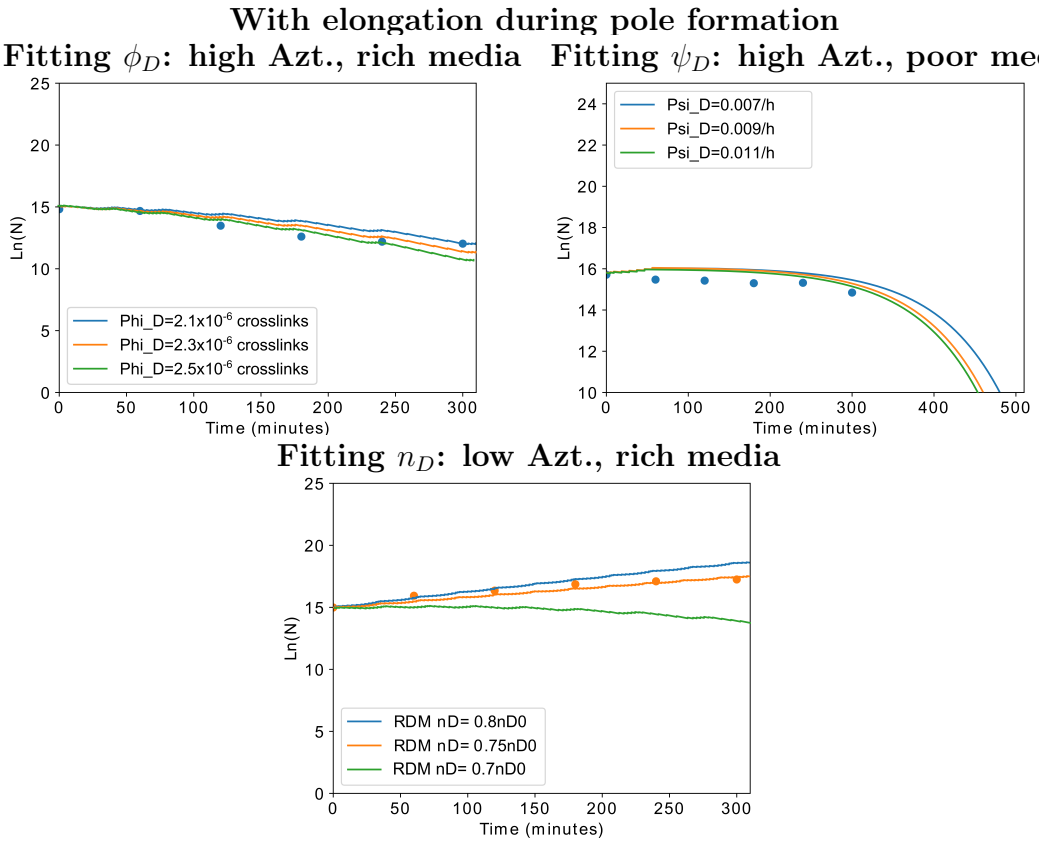

Figure D.9: Plots demonstrating the fitting for the lysis rate constants (ϕ_D and ψ_D) under high aztreonam-like inhibition, and for the inhibition level (n_D) under low aztreonam inhibition, using the parameters found when elongation is included during pole formation (Table 8.2). $\phi_D = 2.3 \times 10^{-6}$ disaccharides, $\psi_D = 0.011/\text{h}$ and $n_D = 0.75 n_{D0}$ were chosen as the best fits.

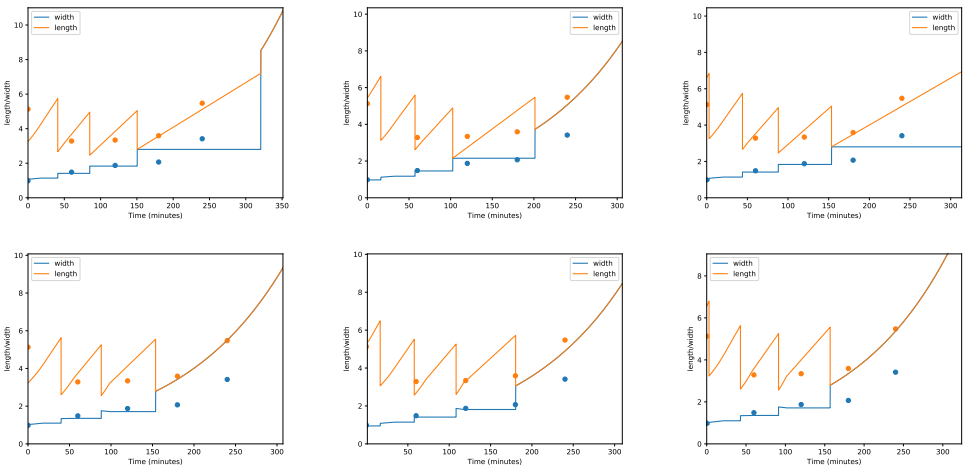

Figure D.10: Comparing the transition to spherical morphology between the precursor threshold division model (top row) and the adder division mode (bottom row), when mecillinam like inhibition is applied at the beginning (1st column), midway (2nd column) or at the end (3rd column) of the cell cycle for fast-growing bacteria.

Appendix E

Additional data analysis for the combination of fosfomycin and mecillinam

-0.98216	-1.02985	-0.83957	-0.83817	1.017903	-0.83026
-0.97844	-0.99638	-0.57226	-0.43648	-0.6914	-3.44598
-1.01104	-0.97952	-6.39422	36.6605	-3.69779	0.478315
-0.95312	-0.74747	-8.60866	8.441226	-1.17124	-3.5953
-1.09981	1.113369	-0.0172	-0.18693	-0.02709	0.060307
-1.01354	1.185749	-0.06893	2.942705	1.122455	2.180945

Figure E.1: Analysis of the growth rate in the presence of both fosfomycin and mecillinam to determine the interaction type using the formula in [97]. Red signifies synergy, purple additive behaviour and blue antagonism.

Bibliography

[1] Amir, A. "Is cell size a spandrel?" *eLife* 6: (2017) 1–8.

[2] Andrews, J. M. "Determination of minimum inhibitory concentrations." *Journal of Antimicrobial Chemotherapy* 48, Suppl. S1: (2001) 5–16.

[3] Arends, S. J. R., and D. S. Weiss. "Inhibiting Cell Division in *Escherichia coli* Has Little If Any Effect on Gene Expression." *Journal of Bacteriology* 186, 3: (2004) 880–884.

[4] Aronson, J. "Monobactams." In *Meyler's Side Effects of Drugs*, 2016, 1097–1099.

[5] Baltzer, B., F. Lund, and N. Rastrup-Andersen. "Degradation of Mecillinam in Aqueous Solution." *Journal of Pharmaceutical Sciences* 68, 10: (1979) 1207–1215.

[6] Banerjee, S., K. Lo, M. K. Daddysman, A. Selewa, T. Kuntz, A. R. Dinner, and N. F. Scherer. "Biphasic growth dynamics control cell division in *Caulobacter crescentus*." *Nature Microbiology* 2, 9: (2017) 6–11.

[7] Barbour, A. G., L. W. Mayer, and B. G. Spratt. "Mecillinam Resistance in *Escherichia coli*: Dissociation of Growth Inhibition and Morphologic Change." *Journal of Infectious Diseases* 143, 1: (1981) 114–121.

[8] Bollenbach, T., and R. Kishony. "Resolution of gene regulatory confilicts caused by combinations of antibiotics." *Molecular Cell* 42, 4: (2011) 413–425.

[9] Bremer, H., and P. P. Dennis. "Modulation of Chemical Composition and Other Parameters of the Cell at Different Exponential Growth Rates." *EcoSal Plus* , 1.

[10] Burdett, I. D. J., and R. G. E. Murray. "Septum formation in *Escherichia coli*: characterization of septal structure and the effects of antibiotics on cell division." *Journal of Bacteriology* 119, 1: (1974) 303–324.

[11] Bush, K. "Introduction to Antimicrobial Therapeutics Reviews: the bacterial cell wall as an antimicrobial target." *Annals of the New York Academy of Sciences* 1277: (2013) v–vii.

[12] Campos, M., I. V. Surovtsev, S. Kato, A. Paintdakhi, B. Beltran, S. E. Ebmeier, and C. Jacobs-Wagner. "A constant size extension drives bacterial cell size homeostasis." *Cell* 159, 6: (2014) 1433–1446.

[13] CDDEP. *The State of the World's Antibiotics, 2015.* Washington, DC: CDDEP, 2015.

[14] Chevereau, G., and T. Bollenbach. "Systematic discovery of drug interaction mechanisms." *Molecular Systems Biology* 11, 4: (2015) 807.

[15] Chien, A.-C., N. S. Hill, and P. A. Levin. "Cell Size Control in Bacteria." *Current Biology* 22, 9: (2012) R340–R349.

[16] Cho, H., T. Uehara, and T. G. Bernhardt. "Beta-Lactam Antibiotics Induce a Lethal Malfunctioning of the Bacterial Cell Wall Synthesis Machinery." *Cell* 159, 6: (2014) 1300–1311.

[17] Cho, H., C. N. Wivagg, M. Kapoor, Z. Barry, P. D. A. Rohs, H. Suh, J. A. Marto, E. C. Garner, and T. G. Bernhardt. "Bacterial cell wall biogenesis is mediated by SEDS and PBP polymerase families functioning semi-autonomously." *Nature Microbiology* 1, October: (2016) 16,172.

[18] Chung, H. S., Z. Yao, N. W. Goehring, R. Kishony, J. Beckwith, and D. Kahne. "Rapid beta-lactam-induced lysis requires successful assembly of the cell division machinery." *Proceedings of the National Academy of Sciences of the United States of America* 106, 51: (2009) 21,872–21,877.

[19] CLSI. *Performance Standards for Antimicrobial Susceptibility Testing; Twenty-Second Informational Supplement*, volume 32. Clinical and Laboratory Standards Institute, 2013.

[20] Cooper, S., and C. E. Helmstetter. "Chromosome replication and the division cycle of *Escherichia coli* B/r." *Journal of Molecular Biology* 31, 1: (1968) 519–540.

[21] Cooper, S., and M. L. Hsieh. "The Rate and Topography of Cell Wall Synthesis during the Division Cycle of *Escherichia coli* Using N-Acetylglucosamine as a Peptidoglycan Label." *Journal of General Microbiology* 134: (1988) 1717–1721.

[22] Cozens, R. M., E. Tuomanen, W. Tosch, O. Zak, J. Suter, and A. Tomasz. "Evaluation of the bactericidal activity of beta-lactam antibiotics on slowly growing bacteria cultured in the chemostat." *Antimicrobial Agents and Chemotherapy* 29, May: (1986) 797–802.

[23] Delcour, A. H. "Outer Membrane Permeability and Antibiotic Resistance." *Biochim Biophys Acta.* 1794, 5: (2009) 808–816.

[24] Demain, A. L., and S. Sanchez. "Microbial drug discovery: 80 Years of progress." *Journal of Antibiotics* 62, 1: (2009) 5–16.

[25] den Blaauwen, T., M. E. G. Aarsman, N. O. E. Vischer, and N. Nanninga. "Penicillin-binding protein PBP2 of *Escherichia coli* localizes preferentially in the lateral wall and at mid-cell in comparison with the old cell pole." *Molecular Microbiology* 47, 2: (2003) 539–547.

[26] Dion, M. F., M. Kapoor, Y. Sun, S. Wilson, J. Ryan, A. Vigouroux, S. van Teeffelen, R. Oldenbourg, and E. C. Garner. "Bacillus subtilis cell diameter is determined by the opposing actions of two distinct cell wall synthetic systems." *Nature Microbiology* .

[27] Dörr, T., B. M. Davis, and M. K. Waldor. "Endopeptidase-Mediated Beta Lactam Tolerance." *PLoS Pathogens* 11, 4: (2015) 1–16.

[28] Dougherty, T. J., K. Kennedy, R. E. Kessler, and M. J. Pucci. "Direct quantitation of the number of individual penicillin-binding proteins per cell in *Escherichia coli*." *Journal of Bacteriology* 178, 21: (1996) 6110–5.

[29] Doumith, M., S. Mushtaq, D. M. Livermore, and N. Woodford. "New insights into the regulatory pathways associated with the activation of the stringent response in bacterial resistance to the PBP2-targeted antibiotics, mecillinam and OP0595/RG6080." *Journal of Antimicrobial Chemotherapy* 1–5.

[30] Doyle, R. J., and R. Dziarski. "The bacterial cell: Peptidoglycan." In *Bacterial Structure*, 2001, 137–154.

[31] Ducret, A., E. M. Quardokus, and Y. V. Brun .

[32] Duetz, W. A., L. Rüedi, R. Hermann, K. O'connor, J. Büchs, and B. Witholt. "Methods for Intense Aeration, Growth, Storage, and Replication of Bacterial Strains in Microtiter Plates." *Applied and Environmental Microbiology* 66, 6: (2000) 2641–2646.

[33] Egan, A. J. F., and W. Vollmer. "The physiology of bacterial cell division." *Annals of the New York Academy of Sciences* 1277, 1: (2013) 8–28.

[34] Elowitz, M. B., A. J. Levine, E. D. Siggia, and P. Swain. "Stochastic gene expression in a single cell." *Science* 297, August: (2002) 1183–1186.

[35] Ercan, O., M. M. M. Bisschops, W. Overkamp, T. R. Jørgensen, A. F. Ram, E. J. Smid, J. T. Pronk, O. P. Kuipers, P. Daran-Lapujade, and M. Kleerebezem. "Physiological and Transcriptional Responses of Different Industrial Microbes at Near-Zero Specific Growth Rates." *Applied and Environmental Microbiology* 81, 17: (2015) 5662–5670.

[36] Esener, A. A., T. Veerman, J. A. Roels, and N. W. F. Kossen. "Modeling of Bacterial Growth; Formulation and Evaluation of a Structured Model." *Biotechnology and Bioengineering* XXIV: (1982) 1749–1764.

[37] EUCAST. "Determination of minimum inhibitory concentrations (MICs) of antibacterial agents by broth dilution." *European Committee for Antimicrobial Susceptibility Testing Discussion Document* E.DIs 5.1, 8: (2003) 1–7.

[38] Falagas, M. E., E. K. Vouloumanou, G. Samonis, and K. Z. Vardakas. "Fosfomycin." *Clinical Microbiology Reviews* 29, 2: (2016) 321–347.

[39] Ferrández, A., J. L. García, and E. Díaz. "Transcriptional regulation of the divergent paa catabolic operons for phenylacetic acid degradation in *Escherichia coli*." *Journal of Biological Chemistry* 275, 16: (2000) 12,214–12,222.

[40] Ferraro, J. R., K. Nakamoto, and C. W. Brown. "Basic Theory." In *Introductory Raman Spectroscopy*, Elsevier Science (USA), 1994, 1–94. Second edition.

[41] ———. "Biochemical and Medical Applications." In *Introductory Raman Spectroscopy, Second Edition*, Elsevier Science (USA), 2003, 1, chapter 6, 295–324.

[42] Gitai, Z., N. A. Dye, A. Reisenauer, M. Wachi, and L. Shapiro. "MreB actin-mediated segregation of a specific region of a bacterial chromosome." *Cell* 120, 3: (2005) 329–341.

[43] Gould, I., and F. MacKenzie. "The response of Enterobacteriaceae to Beta-lactam antibiotics – 'round forms, filaments and the root of all evil'." *Journal of Antimicrobial Chemotherapy* 40: (1997) 495–499.

[44] Greenwood, D., and F. O'Grady. "FL 1060: a new beta-lactam antibiotic with novel properties." *Journal of Clinical Pathology* 26, 1: (1973) 1–6.

[45] Greenwood, D., N. Pearson, A. Eley, and F. O'Grady. "Comparative in vitro activities of cefotaxime and ceftizoxime (FK749): New cephalosporins with exceptional potency." *Antimicrobial Agents and Chemotherapy* 17, 3: (1980) 397–401.

[46] Greenwood, D. "Effect of Osmolality on the Response of *Escherichia coli* to Mecillinam." *Antimicrobial Agents and Chemotherapy* 10, 5: (1976) 824–826.

[47] Greenwood, D., and F. O. Grady. "Comparison of the Responses of *Escherichia coli* and *Proteus mirabilis* to Seven Beta-Lactam Antibiotics." *The Journal of Infectious Diseases* 128, 2: (1973) 211–222.

[48] Greulich, P., M. Scott, M. R. Evans, and R. J. Allen. "Growth-dependent bacterial susceptibility to ribosome-targeting antibiotics." *Molecular Systems Biology* 11, 1: (2015) 796.

[49] Grover, N. B., and C. L. Woldringh. "Dimensional regulation of cell-cycle events in *Escherichia coli* during steady-state growth." *Microbiology* 147: (2001) 171–181.

[50] Hall, B. G., H. Acar, A. Nandipati, and M. Barlow. "Growth Rates Made Easy." *Molecular Biology and Evolution* 31, 1: (2014) 232–238.

[51] Harris, L. K., and J. A. Theriot. "Relative Rates of Surface and Volume Synthesis Set Bacterial Cell Size." *Cell* 165, 6: (2016) 1479–1492.

[52] Heidari Torkabadi, H., C. R. Bethel, K. M. Papp-Wallace, P. A. J. De Boer, R. A. Bonomo, and P. R. Carey. "Following Drug Uptake and Reactions inside *Escherichia coli* Cells by Raman Microspectroscopy." *Biochemistry* 53, 25: (2014) 4113–4121.

[53] Heidrich, C., M. F. Templin, A. Ursinus, M. Merdanovic, H. Schwarz, M. A. D. Pedro, and J.-V. Holtje. "Involvement of N -acetylmuramyl-L -alanine amidases in cell separation and antibiotic-induced autolysis of *Escherichia coli*." *Molecular Microbiology* 41, 1: (2001) 167–178.

[54] Henderson, T. A., K. D. Young, S. A. Denome, and P. K. Elf. "AmpC and AmpH, proteins related to the class C β-lactamases, bind penicillin and contribute to the normal morphology of *Escherichia coli*." *Journal of Bacteriology* 179, 19: (1997) 6112–6121.

[55] Herigstad, B., M. Hamilton, and J. Heersink. "How to optimize the drop plate method for enumerating bacteria." *Journal of Microbiological Methods* 44, 2: (2001) 121–129.

[56] Hobro, A. J., M. Rouhi, E. W. Blanch, and G. L. Conn. "Raman and Raman optical activity (ROA) analysis of RNA structural motifs in Domain I of the EMCV IRES." *Nucleic Acids Research* 35, 4: (2007) 1169–1177.

[57] Holtje, J. V. "Growth of the stress-bearing and shape-maintaining murein sacculus of *Escherichia coli*." *Microbiology and Molecular Biology Reviews* 62, 1: (1998) 181–203.

[58] Huang, K. C., R. Mukhopadhyay, B. Wen, Z. Gitai, and N. S. Wingreen. "Cell shape and cell-wall organization in Gram-negative bacteria." *PNAS* 105, 49: (2008) 19,282–19,287.

[59] Iliescu, T., M. Baia, and I. Pavel. "Raman and SERS investigations of potassium benzylpenicillin." *Journal of Raman Spectroscopy* 37, 1-3: (2006) 318–325.

[60] Ishino, F., S. Tamaki, B. G. Spratt, and M. Matsuhashi. "A mecillinam-sensitive peptidoglycan crosslinking reaction in *Escherichia coli*." *Biochemical and Biophysical Research Communications* 109, 3: (1982) 689–696.

[61] Jepson, A. *E. coli motility and growth: a biophysical study.* Doctor of philosphy, University of Edinburgh, 2014.

[62] Jiang, H., F. Si, W. Margolin, and S. X. Sun. "Mechanical control of bacterial cell shape." *Biophysical Journal* 101, 2: (2011) 327–335.

[63] Jiang, X., X. Qin, D. Yin, M. Gong, L. Yang, B. Zhao, and W. Ruan. "Rapid monitoring of benzylpenicillin sodium using Raman and surface enhanced Raman spectroscopy." *Spectrochimica Acta - Part A: Molecular and Biomolecular Spectroscopy* 140: (2015) 474–478.

[64] Johnson, J. W., J. F. Fisher, and S. Mobashery. "Bacterial cell-wall recycling." *Annals of the New York Academy of Sciences* 1277, 1: (2013) 54–75.

[65] Justice, S. S., D. A. Hunstad, P. C. Seed, and S. J. Hultgren. "Filamentation by *Escherichia coli* subverts innate defenses during urinary tract infection." *PNAS* 103, 52: (2006) 19,884–19,889.

[66] Karageorgopoulos, D. E., R. Wang, X.-H. Yu, and M. E. Falagas. "Fosfomycin: evaluation of the published evidence on the emergence of antimicrobial resistance in Gram-negative pathogens." *The Journal of Antimicrobial Chemotherapy* 67, 2: (2012) 255–68.

[67] Karp, P. D., D. Weaver, S. Paley, C. Fulcher, A. Kubo, A. Kothari, M. Krummenacker, P. Subhraveti, D. Weerasinghe, S. Gama-Castro, A. M. Huerta, L. Muñiz-Rascado, C. Bonavides-Martinez, V. Weiss, M. Peralta-Gil, A. Santos-Zavaleta, I. Schröder, A. Mackie, R. Gunsalus, J. Collado-Vides, I. M. Keseler, and I. Paulsen. "The EcoCyc Database." *EcoSal Plus* 6, 1: (2014) 1–19.

[68] Kennard, A. S., M. Osella, A. Javer, J. Grilli, P. Nghe, S. J. Tans, P. Cicuta, and M. Cosentino Lagomarsino. "Individuality and universality in the growth-division laws of single *E. coli* cells." *Physical Review E - Statistical, Nonlinear, and Soft Matter Physics* 93, 1.

[69] Kjeldsen, T., M. Sommer, and J. E. Olsen. "Extended spectrum β-lactamase-producing *Escherichia coli* forms filaments as an initial response to cefotaxime treatment." *BMC Microbiology* 15, 1: (2015) 6.

[70] Klumpp, S., and T. Hwa. "Bacterial growth: global effects on gene expression, growth feedback and proteome partition." *Current Opinion in Biotechnology* , 0: (2014) 96–102.

[71] Knierim, E., B. Lucke, J. M. Schwarz, M. Schuelke, and D. Seelow. "Systematic comparison of three methods for fragmentation of long-range PCR products for next generation sequencing." *PLoS ONE* 6, 11.

[72] Kocaoglu, O., and E. E. Carlson. "Profiling of β-lactam selectivity for penicillin-binding proteins in Escherichia coli strain DC2." *Antimicrobial Agents and Chemotherapy* 59, 5: (2015) 2785–2790.

[73] Koch, A. L. "Shrinkage of growing Escherichia coli cells by osmotic challenge." *Journal of Bacteriology* 159, 3: (1984) 919–924.

[74] Koch, A. L., and M. Crandall. "Photometric Measurement of Bacterial Growth." *The American Biology Teacher* 30, 6: (1968) 481–485.

[75] Kong, K.-F., L. Schneper, and K. Mathee. "Beta-lactam antibiotics: From antibiosis to resistance and bacteriology." *APMIS* 118, 1: (2010) 1–36.

[76] Kurabayashi, K., Y. Hirakawa, K. Tanimoto, H. Tomita, and H. Hirakawa. "Role of the CpxAR Two-Component Signal Transduction System in Control of Fosfomycin Resistance and Carbon Substrate Uptake." *Journal of Bacteriology* 196, 2: (2014) 248–256.

[77] Leber, A. L. "Synergism Testing : Broth Microdilution Checkerboard and Broth Macrodilution Methods." In *Antimicrobial Susceptibility Testing*, ASMscience, 2016, chapter 5.16, 5.16.1–5.16.23.

[78] Lee, T. K., C. Tropini, J. Hsin, S. M. Desmarais, T. S. Ursell, E. Gong, Z. Gitai, R. D. Monds, and K. C. Huang. "A dynamically assembled cell wall synthesis machinery buffers cell growth." *Proceedings of the National Academy of Sciences* 111, 12: (2014) 4554–4559.

[79] Leon, J., J. M. Garcia-Lobo, J. Navas, and J. M. Ortiz. "Fosfomycin causes transient lysis in *Escherichia coli* strains carrying fosfomycin-resistance plasmids." *Journal of General Microbiology* 131, 12: (1985) 3255–3260.

[80] Levin, B. R., and K. I. Udekwu. "Population dynamics of antibiotic treatment: a mathematical model and hypotheses for time-kill and continuous-culture experiments." *Antimicrobial Agents and Chemotherapy* 54, 8: (2010) 3414–3426.

[81] Levin, P. A., I. G. Kurtser, and A. D. Grossman. "Identification and characterization of a negative regulator of FtsZ ring formation in *Bacillus subtilis*." *Proceedings of the National Academy of Sciences of the United States of America* 96, 17: (1999) 9642–9647.

[82] Li, G.-W., D. Burkhardt, C. Gross, and J. S. Weissman. "Quantifying absolute protein synthesis rates reveals principles underlying allocation of cellular resources." *Cell* 157, 3: (2014) 624–635.

[83] Lloyd, D. P., and R. J. Allen. "Competition for space during bacterial colonization of a surface." *Journal of the Royal Society Interface* 12, 110.

[84] Luria, S. E., and M. Delbruck. "Mutations of Bacteria from Virus Sensitivity to Virus Resistance." *Genetics* , November: (1943) 491–511.

[85] Lutkenhaus, J., and S. G. Addinall. "Bacterial Cell Division and the Z ring." *Annual Review of Biochemistry* 66, 1: (1997) 93–116.

[86] Master, R. N., J. Deane, C. Opiela, and D. F. Sahm. "Recent trends in resistance to cell envelope-active antibacterial agents among key bacterial pathogens." *Annals of the New York Academy of Sciences* 1277, 1: (2013) 1–7.

[87] Mcvey, A. F., I. B. N. Clark, K. Stevenson, A. F. Mcvey, I. B. N. Clark, P. S. Swain, and T. Pilizota. "General calibration of microbial growth in microplate readers." *Scientific Reports* 6, 38828: (2016) 1–7.

[88] Mengin-Lecreulx, D., and J. van Heijenoort. "Effect of growth conditions on peptidoglycan content and cytoplasmic steps of its biosynthesis in *Escherichia coli*." *Journal of Bacteriology* 163, 1: (1985) 208–212.

[89] Micali, G., J. Grilli, M. Osella, and M. Cosentino Lagomarsino. "Concurrent processes set E. coli cell division." *Science Advances* 4, 11.

[90] Michalopoulos, A. S., I. G. Livaditis, and V. Gougoutas. "The revival of fosfomycin." *International Journal of Infectious Diseases* 15, 11: (2011) e732–e739.

[91] Miller, J. H. *A short course in bacterial genetics : a laboratory manual and handbook for Escherichia coli and related bacteria.* Plainview, N.Y.: Cold Spring Harbor Laboratory Press, 1992.

[92] Molina-Quiroz, R. C., C. M. Muñoz-Villagrán, E. de la Torre, J. C. Tantaleán, C. C. Vásquez, and J. M. Pérez-Donoso. "Enhancing the antibiotic antibacterial effect by sub lethal tellurite concentrations: tellurite and cefotaxime act synergistically in *Escherichia coli*." *PLoS ONE* 7, 4: (2012) 1–6.

[93] Monod, J. "The Growth of Bacterial Cultures." *Annual Review of Microbiology* 3, 1: (1949) 371–394.

[94] Mouton, J. W., R. A. A. Mathot, A. A. Vinks, R. N. van Rossem, and H. G. M. Heijerman. "Pharmacokinetics of Aztreonam in Healthy Subjects and Patients with Cystic Fibrosis and Evaluation of Dose-Exposure Relationships Using Monte Carlo Simulation." *Antimicrobial Agents and Chemotherapy* 51, 9: (2007) 3049–3055.

[95] Neidhardt, F. C., P. L. Bloch, and D. F. Smith. "Culture medium for Enterobacteria." *Journal of Bacteriology* 119, 3: (1974) 736–747.

[96] Neidhardt, F. C., J. L. Ingraham, and M. Schaechter. *Physiology of the Bacterial Cell.* Sunderland, Massachusetts: Sinauer Associates, Inc., 1990.

[97] Nguyen, C., A. Zhou, A. Khan, J. H. Miller, and P. Yeh. "Pairwise antibiotic interactions in *Escherichia coli*: triclosan, rifampicin and aztreonam with nine other classes of antibiotics." *The Journal of Antibiotics* , October 2015: (2016) 1–7.

[98] Nguyen, L. T., J. C. Gumbart, M. Beeby, and G. J. Jensen. "Coarse-grained simulations of bacterial cell wall growth reveal that local coordination alone can be sufficient to maintain rod shape." *Proceedings of the National Academy of Sciences* 112, 28: (2015) E3689–E3698.

[99] Nikolaidis, I., S. Favini-Stabile, and A. Dessen. "Resistance to antibiotics targeted to the bacterial cell wall." *Protein Science* 23, 3: (2014) 243–259.

[100] Ocampo, P. S., V. Lázár, B. Papp, M. Arnoldini, P. A. Zur Wiesch, R. Busa-Fekete, G. Fekete, C. Pál, M. Ackermann, and S. Bonhoeffer. "Antagonism between bacteriostatic and bactericidal antibiotics is prevalent." *Antimicrobial Agents and Chemotherapy* 58, 8: (2014) 4573–4582.

[101] Okumus, B., D. Landgraf, G. C. Lai, S. Bakshi, J. C. Arias-castro, S. Yildiz, D. Huh, R. Fernandez-lopez, C. N. Peterson, E. Toprak, M. E. Karoui, and J. Paulsson. "Mechanical slowing-down of cytoplasmic diffusion allows in vivo counting of proteins in individual cells." *Nature Communications* 7, 11641: (2016) 1–10.

[102] Ouzounov, N., J. P. Nguyen, B. P. Bratton, D. Jacobowitz, Z. Gitai, and J. W. Shaevitz. "MreB Orientation Correlates with Cell Diameter in *Escherichia coli*." *Biophysical Journal* 111, 5: (2016) 1035–1043.

[103] Pamp, S. J., M. Gjermansen, H. K. Johansen, and T. Tolker-Nielsen. "Tolerance to the antimicrobial peptide colistin in *Pseudomonas aeruginosa* biofilms is linked to metabolically active cells, and depends on the pmr and mexAB-oprM genes." *Molecular Microbiology* 68, 1: (2008) 223–240.

[104] Park, J. T., and T. Uehara. "How Bacteria Consume Their Own Exoskeletons (Turnover and Recycling of Cell Wall Peptidoglycan)." *Microbiology and Molecular Biology Reviews* 72, 2: (2008) 211–227.

[105] Pazos, M., K. Peters, and W. Vollmer. "Robust peptidoglycan growth by dynamic and variable multi-protein complexes." *Current Opinion in Microbiology* 36: (2017) 55–61.

[106] de Pedro, M., J. Höltje, and W. Löffelhardt, editors. *Bacterial Growth and Lysis: Metabolism and Structure of the Bacterial Sacculus*. New York: Springer US, 1992, first edition.

[107] Pisabarro, A. G., R. Prats, D. Váquez, and A. Rodríguez-Tébar. "Activity of penicillin-binding protein 3 from *Escherichia coli*." *Journal of Bacteriology* 168, 1: (1986) 199–206.

[108] Prats, R., and M. de Pedro. "Normal Growth and Division of *Escherichia coli* With a Reduced Amount of Murein." *Journal of Bacteriology* 171, 7: (1989) 3740–3745.

[109] Presser, K. A., D. A. Ratkowsky, and T. Ross. "Modelling the Growth Rate of *Escherichia coli* as a Function of pH and Lactic Acid Concentration." *Applied and Environmental Microbiology* 63, 6: (1997) 2355–2360.

[110] Purich, D. L. *Enzyme kinetics: catalysis & control. A reference of theory and best-practice methods.* San Diego, Calif. : Oxford: Elsevier Academic ; Elsevier Science, 2010.

[111] Rizzuto, T. "Technical Application Note: The Raman Spectrum of Water." *StellarNet Inc.* .

[112] Rohs, P. D., J. Buss, S. I. Sim, G. R. Squyres, V. Srisuknimit, M. Smith, H. Cho, M. Sjodt, A. C. Kruse, E. C. Garner, S. Walker, D. E. Kahne, and T. G. Bernhardt. "A central role for PBP2 in the activation of peptidoglycan polymerization by the bacterial cell elongation machinery." *PLoS Genetics* 14, 10: (2018) 1–25.

[113] Rosenberger, R. F., N. B. Grover, A. Zaritsky, and C. L. Woldringh. "Control of microbial surface-growth by density." *Nature* 271, 5642: (1978) 244–245.

[114] Satta, G., G. Cornaglia, A. Mazzariol, G. Golini, S. Valisena, and R. Fontana. "Target for Bacteriostatic and Bactericidal Activities of Beta-Lactam Antibiotics against *Escherichia coli* Resides in Different Penicillin-Binding Proteins." *Antimicrobial Agents and Chemotherapy* 39, 4: (1995) 812–818.

[115] Sauvage, E., F. Kerff, M. Terrak, J. A. Ayala, and P. Charlier. "The penicillin-binding proteins: Structure and role in peptidoglycan biosynthesis." *FEMS Microbiology Reviews* 32, 2: (2008) 234–258.

[116] Scheffers, D., and M. Pinho. "Bacterial cell wall synthesis: new insights from localization studies." *Microbiology and Molecular Biology Reviews* 69, 4: (2005) 585–607.

[117] Schirner, K., Y.-j. Eun, M. Dion, Y. Luo, J. D. Helmann, E. C. Garner, and S. Walker. "Lipid-linked cell wall precursors regulate membrane association of bacterial actin MreB." *Nature Chemical Biology* 11, 1: (2015) 38–45.

[118] Scott, M., E. M. Mateescu, Z. Zhang, and T. Hwa. "Interdependence of Cell Growth Origins and Consequences." *Science* 330, November: (2010) 1099–1102.

[119] Sezonov, G., D. Joseleau-Petit, and R. D'Ari. "*Escherichia coli* Physiology in Luria-Bertani Broth." *Journal of Bacteriology* 189, 23: (2007) 8746–8749.

[120] Shendure, J., and H. Ji. "Next-generation DNA sequencing." *Nature Biotechnology* 26, 10: (2008) 1135–1145.

[121] Shlaes, D. M. "New beta-lactam-beta-lactamase inhibitor combinations in clinical development." *Annals of the New York Academy of Sciences* 1277: (2013) 105–114.

[122] Siddiquee, K. A. Z., M. J. Arauzo-Bravo, and K. Shimizu. "Effect of a pyruvate kinase (*pykF*-gene) knockout mutation on the control of gene expression and metabolic fluxes in *Escherichia coli*." *FEMS Microbiology Letters* 235, 1: (2004) 25–33.

[123] Small, E. W., and W. L. Peticolas. "Conformational Dependence of the Raman Scattering Intensities from Polynucleotides. III. Order-disorder Changes in Helical Structures." *Biopolymers* 10, 8: (1971) 1377–1418.

[124] Spalding, C., E. Keen, D. J. Smith, A. M. Krachler, and S. Jabbari. "Mathematical modelling of the antibiotic-induced morphological transition of *Pseudomonas aeruginosa*." *PLoS Computational Biology* 14, 2: (2018) 1–28.

[125] Spratt, B. G. "Distinct penicillin binding proteins involved in the division, elongation, and shape of *Escherichia coli* K12." *Proceedings of the National Academy of Sciences of the United States of America* 72, 8: (1975) 2999–3003.

[126] ———. "The Mechanism of Action of Mecillinam." *Journal of Antimicrobial Chemotherapy* 3: (1977) 13–19.

[127] Sumayya, A., C. Y. Panicker, H. T. Varghese, and B. Harikumar. "Vibrational spectroscopic studies and ab initio calculations of l-glutamic acid 5-amide." *RJC Rasayan J. Chem* 1, 3: (2008) 548–555.

[128] Taheri-Araghi, S., S. Bradde, J. T. Sauls, N. S. Hill, P. A. Levin, J. Paulsson, M. Vergassola, and S. Jun. "Cell-size control and homeostasis in bacteria." *Current Biology* 25, 3: (2015) 385–391.

[129] Talbot, G. H. "β-Lactam antimicrobials: what have you done for me lately?" *Annals of the New York Academy of Sciences* 1277, 1: (2013) 76–83.

[130] Talyor, H., A. Lepore, D. Landgraf, B. Okumus, S. Jaramillo-Riveri, L. McLaren, J. Paulsson, and M. E. Karoui. "Quantification of very low-abundant proteins in bacteria using the HaloTag and epi-fluorescence microscopy." *bioRxiv* 237248.

[131] van Teeffelen, S., S. Wang, L. Furchtgott, K. C. Huang, N. S. Wingreen, J. W. Shaevitz, and Z. Gitai. "The bacterial actin MreB rotates, and rotation depends on cell-wall assembly." *Proceedings of the National Academy of Sciences* 108, 38: (2011) 15,822–15,827.

[132] Thulin, E., M. Sundqvist, and D. I. Andersson. "Amdinocillin (mecillinam) resistance mutations in clinical isolates and laboratory-selected mutants of *Escherichia coli*." *Antimicrobial Agents and Chemotherapy* 59, 3: (2015) 1718–1727.

[133] Tomasz, A. "The mechanism of the irreversible antimicrobial effects of penicillins: how the beta-lactam antibiotics kill and lyse bacteria." *Annual Review of Microbiology* 33: (1979) 113–137.

[134] Tuomanen, E., R. M. Cozens, W. Tosch, O. Zak, and A. Tomasz. "The Rate of Killing of *Escherichia coli* by β-Lactam Antibiotics Is Strictly Proportional to the Rate of Bacterial Growth." *Microbiology* 132, 5: (1986) 1297–1304.

[135] Tuomanen, E., K. Gilbert, and A. Tomasz. "Modulation of bacteriolysis by cooperative effects of penicillin-binding proteins 1a and 3 in *Escherichia coli*." *Antimicrobial Agents and Chemotherapy* 30, 5: (1986) 659–663.

[136] Tybring, L. "Mecillinam (FL 1060), a 6β-Amidinopenicillanic Acid Derivative: In Vitro Evaluation." *Antimicrobial Agents and Chemotherapy* 8, 3: (1975) 266–270.

[137] ———. "Special aspects of laboratory investigations with mecillinam." *Journal of Antimicrobial Chemotherapy* 3: (1977) 23–27.

[138] Typas, A., M. Banzhaf, C. A. Gross, and W. Vollmer. "From the regulation of peptidoglycan synthesis to bacterial growth and morphology." *Nature Reviews Microbiology* 10, 2: (2012) 123–136.

[139] Udekwu, K. I., N. Parrish, P. Ankomah, F. Baquero, and B. R. Levin. "Functional relationship between bacterial cell density and the efficacy of antibiotics." *The Journal of Antimicrobial Chemotherapy* 63, 4: (2009) 745–757.

[140] Uehara, T., and T. G. Bernhardt. "More than just lysins: peptidoglycan hydrolases tailor the cell wall." *Current Opinion in Microbiology* 14, 6: (2011) 698–703.

[141] Uehara, T., and J. T. Park. "Growth of *Escherichia coli*: Significance of peptidoglycan degradation during elongation and septation." *Journal of Bacteriology* 190, 11: (2008) 3914–3922.

[142] Vadia, S., and P. A. Levin. "Growth rate and cell size: A re-examination of the growth law." *Current Opinion in Microbiology* 24: (2015) 96–103.

[143] van Krimpen, P., W. van Bennekom, and A. Bult. "Penicillins and cephalosporins: Physicochemical properties and analysis in pharmaceutical and biological matrices." *Pharmaceutisch Weekblad Scientific Edition* 9, 1: (1987) 1–23.

[144] Vinella, D., R. D'Ari, A. Jaffé, and P. Bouloc. "Penicillin binding protein 2 is dispensable in *Escherichia coli* when ppGpp synthesis is induced." *The EMBO Journal* 11, 4: (1992) 1493–1501.

[145] Vinella, D., D. Joseleau-Petit, D. Thevenet, P. Bouloc, and R. D'Ari. "Penicillin-binding protein 2 inactivation in *Escherichia coli* results in cell division inhibition, which is relieved by FtsZ overexpression." *Journal of Bacteriology* 175, 20: (1993) 6704–6710.

[146] Volkmer, B., and M. Heinemann. "Condition-Dependent Cell Volume and Concentration of *Escherichia coli* to Facilitate Data Conversion for Systems Biology Modeling." *PLoS ONE* 6, 7: (2011) 1–6.

[147] Vollmer, W., and U. Bertsche. "Murein (peptidoglycan) structure, architecture and biosynthesis in *Escherichia coli*." *Biochimica et Biophysica Acta - Biomembranes* 1778, 9: (2008) 1714–1734.

[148] Wallden, M., D. Fange, E. G. Lundius, Ö. Baltekin, and J. Elf. "The Synchronization of Replication and Division Cycles in Individual *E. coli* Cells." *Cell* 166, 3: (2016) 729–739.

[149] Weart, R. B., and P. A. Levin. "Growth rate dependent regulation of medial FtsZ ring formation in *Bacillus subtilis*." *Journal of Bacteriology* 185, 9: (2003) 2826.

[150] Weiss, D. S., J. C. Chen, J.-M. Ghigo, D. Boyd, and J. O. N. Beckwith. "Localization of FtsI (PBP3) to the septal ring requires its membrane anchor, the Z ring, FtsA, FtsQ, and FtsL." *Journal of Bacteriology* 181, 2: (1999) 508–520.

[151] Wientjes, F. B., E. Pas, P. E. M. Taschner, and C. L. Woldringh. "Kinetics of uptake and incorporation of meso-diaminopimelic acid in different *Escherichia coli* strains." *Journal of Bacteriology* 164, 1: (1985) 331–337.

[152] Woldringh, C. L., P. Huls, E. Pas, G. J. Brakenhoff, and N. Nanninga. "Topography of Peptidoglycan Synthesis during Elongation and Polar Cap Formation in a Cell Division Mutant of *Escherichia coli* MC4100." *Microbiology* 133, 3: (1987) 575–586.

[153] Wu, X., and J. G. Hurdle. "The Membrane as a Novel Target Site for Antibiotics to Kill Persisting Bacterial Pathogens." In *Antibiotics: Targets, Mechanisms and Resistance*, edited by Claudio O. Gualerzi, Letizia Brandi, Attilio Fabbretti, and Cynthia L. Pon, Wiley-VCH Verlag CmbH & Co. KGaA, 2014, chapter 8, 183–216. First edition.

[154] Yao, Z., D. Kahne, and R. Kishony. "Distinct single-cell morphological dynamics under beta-lactam antibiotics." *Molecular Cell* 48, 5: (2012) 705–712.

[155] Yeh, P., A. I. Tschumi, and R. Kishony. "Functional classification of drugs by properties of their pairwise interactions." *Nature Genetics* 38, 4: (2006) 489–494.

[156] Zaritsky, A., C. L. Woldringh, and D. Mirelman. "Constant peptidoglycan density in the sacculus of escherichia coli B/r growing at different rates." *FEBS Letters* 98, 1: (1979) 29–32.

[157] Zervosen, A., E. Sauvage, J.-m. Frère, P. Charlier, and A. Luxen. "Development of New Drugs for an Old Target - The Penicillin Binding Proteins." *Molecules* 17: (2012) 12,478–12,505.

[158] Zhang, L., Y. Jin, H. Mao, L. Zheng, J. Zhao, Y. Peng, S. Du, and Z. Zhang. "Structure-selective hot-spot Raman enhancement for direct identification and detection of trace penicilloic acid allergen in penicillin." *Biosensors and Bioelectronics* 58: (2014) 165–171.